

A thesis submitted to the University of East Anglia for the Degree of Doctor of  
Philosophy

# Cellular patterns during leaf development

Yara E. Sánchez-Corrales

Department of Computational & Systems Biology and

Department of Cell & Developmental Biology

The John Innes Centre - Norwich, United Kingdom

This copy of the thesis has been supplied on condition that anyone who consults it  
it understood to recognise that its copyright rest with the author and that no quotation  
from the thesis, nor any information derived therefrom, may be published without the  
author's prior written consent.

A CD-ROM is enclosed in this thesis. The CD-ROM contains the Movies in AVI format. The information can be viewed using a default web-browser.

*Supervisors:*

**Dr. Veronica Grieneisen**  
**Prof. Enrico Coen**

*To my parents*





# Contents

<b>1</b>	<b>General Introduction</b>	<b>3</b>
1.1	Introduction . . . . .	3
1.2	Leaf development . . . . .	5
1.2.1	Cell division and cell growth regulation during leaf development . .	6
1.2.2	Polarity and leaf shape regulation . . . . .	10
1.3	Cell polarity . . . . .	11
1.4	Quantification of cell behaviour . . . . .	13
1.4.1	The kinematic analysis . . . . .	13
1.4.2	Live imaging . . . . .	14
1.5	About this work . . . . .	15
<b>2</b>	<b>Getting quantitative in cell shape studies: LOCO-EFA</b>	<b>17</b>
2.1	Introduction . . . . .	18
2.2	Problems of traditional methods to quantify cell shape. . . . .	19
2.3	Decomposing Shape: Lobe Contribution Elliptical Fourier Analysis (LOCO-EFA) . . . . .	20
2.3.1	Elliptical Fourier Analysis . . . . .	21
2.3.2	Contouring the Limitations: Lobe Contribution Elliptical Fourier Analysis (LOCO-EFA) . . . . .	28
2.4	Quantitative characterization of cell shape using LOCO-EFA . . . . .	37
2.4.1	Interpreting geometrical shapes with $L_n$ . . . . .	38
2.4.2	$L_n$ in real Pavement Cells . . . . .	42
2.5	Applying the LOCO-EFA to <i>in silico</i> populations and the effect of cell interactions on single cell shapes . . . . .	44
2.6	Discussion and concluding remarks . . . . .	47
2.7	Materials and Methods . . . . .	50
2.A	Appendix: Movies . . . . .	53
2.B	Appendix: Other LOCO-EFA features . . . . .	54
2.C	Appendix: Supplementary Figures . . . . .	55
<b>3</b>	<b>Time-lapse and imaging analysis</b>	<b>61</b>
3.1	Introduction . . . . .	62
3.2	Time-lapse Imaging . . . . .	63
3.2.1	Plant preparation prior to imaging . . . . .	63
3.2.2	Confocal microscope live-imaging . . . . .	66
3.3	Image processing . . . . .	68
3.3.1	2D projection . . . . .	68
3.4	Segmentation . . . . .	69

3.4.1	Segmentation Potts Model (SPM) . . . . .	70
3.5	Automatic cell tracking . . . . .	72
3.6	Discussion and concluding remarks . . . . .	74
3.A	Appendix . . . . .	76
3.A.1	DNA extraction protocol** . . . . .	76
<b>4</b>	<b>Dissecting spatial and temporal scales during leaf development at the cellular level</b>	<b>85</b>
4.1	Introduction . . . . .	86
4.2	Are cells growing and changing shape according to their position? . . . . .	88
4.2.1	Different spatial scales . . . . .	88
4.2.2	Cells grow and change shape differently according to their position . . . . .	94
4.2.3	Cell growth and cell shape taking a Lagrangian frame of reference: following groups of cells. . . . .	96
4.2.4	Different temporal scales . . . . .	98
4.3	Dynamics of cell divisions within the leaf . . . . .	104
4.3.1	Spatial and temporal dynamics of cell division: revisiting the cell cycle arrest front . . . . .	105
4.4	Perturbation of the system: auxin treatments . . . . .	107
4.5	Discussion and concluding remarks . . . . .	109
4.6	Materials and Methods . . . . .	118
4.A	Appendix: . . . . .	119
<b>5</b>	<b>Cell shape influence on intracellular dynamics</b>	<b>131</b>
5.1	Introduction . . . . .	132
5.2	Influence of cell shape changes during development . . . . .	132
5.2.1	Role of cell shape in cell differentiation . . . . .	133
5.2.2	Role of cell shape in cell division . . . . .	135
5.2.3	Examples of the influence of cell shape in intracellular patterning in plants . . . . .	138
5.3	How the cell shape could influence intracellular patterning? . . . . .	138
5.3.1	Mechanical influence . . . . .	138
5.3.2	Biochemical influence . . . . .	139
5.3.2.1	Effects of the cell geometry on the isocline of a reaction-diffusion system . . . . .	140
5.3.2.2	Effects of the cell shape through its influence in the surface/volume ratio in intracellular gradients. . . . .	142
5.4	Potential of the pavement cell shape to influence intracellular dynamics . . . . .	144
5.4.1	Curvature effects during pavement cell morphogenesis . . . . .	145
5.4.1.1	Secondary lobe formation: dynamical intracellular patterning . . . . .	147
5.5	Discussion and concluding remarks . . . . .	150
<b>6</b>	<b>General Discussion</b>	<b>153</b>
6.1	Introduction . . . . .	153
6.2	From a “static” to a “dynamic” view of development: new methods and importance of quantitative descriptions . . . . .	154
6.3	How is the division zone in the leaf regulated? . . . . .	156
6.4	Coordination of cell growth and cell division: compensation . . . . .	159
6.5	Limits of cell growth . . . . .	162
6.6	Cell polarity and growth . . . . .	163

6.7 Final remarks . . . . .	167
<b>Bibliography</b>	<b>173</b>



# List of Figures

1.1	Metamorphosis II by Escher resembles the epidermis of the leaf of <i>Arabidopsis thaliana</i> . . . . .	4
2.1	Pavement cells on the epidermis of leaves of many plants are characterized by jigsaw puzzle-like shapes consisting of multiple alternating protrusions (also called lobes) and indentations. . . . .	19
2.2	Traditional shape quantifiers can be misleading when applied to complex shapes. . . . .	21
2.3	Misleading measurements of lobe and neck length and skeleton. . . . .	22
2.4	Holomorphic and nonholomorphic shape outlines. . . . .	22
2.5	Elliptical Fourier approximation to a cell contour. . . . .	25
2.6	Relative rotation effect on the frequency and harmonic number. . . . .	26
2.7	The number of morphological protrusions (lobes) specified by a $n$ th harmonics of EFA is influenced by the direction of rotation. . . . .	27
2.8	Schematic diagram summarizing the LOCO-EFA method. . . . .	29
2.9	Temporal and spatial transformations are performed to calculate the precise contribution of each $n$ th harmonic. . . . .	30
2.10	Effect of the rotation-starting point of each pair of circles for shape reconstruction. . . . .	36
2.11	Each EFA-harmonic is decomposed into two circles to obtain the contribution of the $L_n$ mode. . . . .	37
2.12	Comparison of approximation of closed contour using EFA and LOCO-EFA. . . . .	38
2.13	LOCO-EFA is invariant to different rotations of the image, but it is sensitive to the image resolution. . . . .	39
2.14	Interpreting LOCO-EFA derived measures for geometrical shapes. . . . .	40
2.15	Interpreting LOCO-EFA derived measures for similar shapes of different protrusion amplitudes and asymmetrical shapes. . . . .	41
2.16	Other measures extracted from the LOCO-EFA coefficients can provide additional information about the complexity of the cell shape. . . . .	42
2.17	LOCO-EFA on pavement cells of <i>Arabidopsis thaliana</i> reveals that very few cell shapes can be well captured through a single $L_n$ mode. . . . .	43
2.18	LOCO-EFA quantifiers in real populations of pavement cells. . . . .	44
2.19	Cell shape modifications due to tissue interactions. . . . .	46
2.20	Cell shape analysis on cell-cell interactions in <i>in silico</i> tissues using LOCO-EFA. . . . .	47

2.21	LOCO-EFA analysis of <i>in silico</i> Pavement cells reveal the degree of divergence that interacting cells within a tissue experience from their specified shape. . . . .	48
2.22	Cell-cell interactions diverge the specified shape of single pavement-like cells and do not depend on interactions with a second cell type. . . . .	56
2.23	The divergence between single specified cell and their populations do not depend on the specific number of lobes specified (Lobe 2-4). . . . .	57
2.24	The divergence between single specified cell and their populations do not depend on the specific number of lobes specified (Lobe 5-7). . . . .	58
2.25	The divergence between single specified cell and their populations do not depend on the specific number of lobes specified (Lobe 8-10). . . . .	59
3.1	General pipeline to capture dynamic shape and size changes during leaf development at cellular level. . . . .	63
3.2	Custom-made perfusion chamber allows live-imaging of leaf development for long time periods. . . . .	65
3.3	3D width over time of wild type and <i>spch4-pmCherry</i> is similar. . . . .	66
3.4	Projections of the leaf epidermis using confocal optical sections require a special algorithm because the surface is curved. . . . .	78
3.5	Segmentation Potts Model is used to find cells in the confocal image. . . . .	79
3.6	Cell tracking algorithm. . . . .	80
3.7	Cell tracking algorithm enables the extraction of quantitative and dynamic data at the cell and tissue level. . . . .	81
3.8	Details of the tracking experiments (I). . . . .	82
3.9	Details of the tracking experiments (II). . . . .	83
4.1	Schematic representation of different spatial scales. . . . .	90
4.2	Cell growth rate and relative cell shape complexity. . . . .	95
4.3	Cell area varies in a graded-fashion from the base to the tip of the leaf. . . . .	96
4.4	Cell shape is changing in a graded-fashion from the base to the tip of the leaf. . . . .	97
4.5	Number of cells analysed taking an Eulerian frame of reference in absolute and relative position. . . . .	98
4.6	Cells in the leaf are changing position during development. . . . .	99
4.7	Cell growth and cell shape dynamics taking Lagrangian frame of reference still show a gradient according to the position. . . . .	100
4.8	Number of cells considering a Lagrangian frame of reference. . . . .	101
4.9	Schematic representation of different temporal scales. . . . .	102
4.10	Alternative hypothesis of the effect of the cell age in cell dynamics when the position is taken into account. . . . .	103
4.11	Cell growth and Eulerian reference when cells are aligned by their age does not show strong differences depending on the position. . . . .	103
4.12	Cell shape dynamics and Eulerian reference when cells are aligned by age does not show strong differences depending on the position. . . . .	104
4.13	Number of cells considering a Eulerian frame of reference when cells are aligned by age. . . . .	105
4.14	Cell area and cell shape dynamics taking a Lagrangian frame of reference when cells are aligned by their age does not show strong differences depending on the position. . . . .	106
4.15	Number of cells considering a Lagrangian frame of reference when cells are aligned by age. . . . .	107

4.16	The overall growth and shape dynamics follows a very similar trend when the cell age is taken into account. . . . .	108
4.17	Cell growth and cell shape are correlated. . . . .	109
4.18	Cell area and cell shape dynamics change independently of the number of cell divisions pursued. . . . .	110
4.19	The zone where division takes place is not within a fixed distance. . . . .	111
4.20	Division rate decreases over time. . . . .	112
4.21	Auxin response is localized at the tip of the leaf. . . . .	112
4.22	Cell growth and cell shape under auxin treatments. . . . .	113
4.23	Cell growth and cell shape after cell division. . . . .	115
4.24	Gradients in cell growth are independent on the underlying model assumed. . . . .	119
4.25	Entropy follows a similar trend than cumulative difference. . . . .	120
4.26	Cell area and cell shape dynamics change independently of the number of cell divisions pursued (ExpID3078-PA). . . . .	121
4.27	Cell area and cell shape dynamics change independently of the number of cell divisions pursued (ExpID3148-PA). . . . .	122
4.28	Mesophyll divisions were tracked manually. . . . .	123
4.29	Time of the leaf (HAS) and Eulerian frame of reference showing the growth for auxin and its control (+DMSO). . . . .	124
4.30	Time of the leaf (HAS) and Eulerian frame of reference showing the cell shape for auxin and its control (+DMSO). . . . .	125
4.31	Time of the cell (cell age) and Eulerian coordinates of reference analysing the cell growth under auxin and its control (+DMSO). . . . .	126
4.32	Time of the cell (cell age) and Eulerian coordinates of reference analysing the cell shape for auxin and its control (+DMSO). . . . .	127
4.33	Time of the leaf (HAS) and Lagrangian frame of reference for the analysis of the cell growth and the cell shape for auxin and its control (+DMSO). . . . .	128
4.34	Time of the cell (cell age) and Lagrangian frame of reference for the analysis of the cell growth and the cell shape for auxin and its control (+DMSO). . . . .	129
4.35	Mutants involved in auxin biosynthesis and auxin transport present strong developmental defects. . . . .	130
5.1	Cell shape manipulation by changing the size of the substratum. . . . .	134
5.2	Cell fate acquisition in human mesenchymal stem cells (MSC) is influenced by the cell shape and mediated by Small GTPases and cytoskeleton. . . . .	136
5.3	Effects of the cell shape in the interface or isocline of steady states in a reaction diffusion system. . . . .	141
5.4	Effect of cell geometry in the formation of intracellular gradients. . . . .	144
5.5	Pavement cell morphogenesis. . . . .	146
5.6	Schematic representation of the molecular basis of pavement cell morphogenesis. . . . .	147
5.7	Pavement cell lobe bifurcations. . . . .	149
6.1	Cell division zone and displacement of cells during leaf growth. . . . .	157
6.2	Cell growth and cell division might be related in different manners to ensure a coordination during morphogenesis. . . . .	159
6.3	Cell size and overall leaf size when cell division is disrupted. . . . .	161
6.4	Different notions of cell polarity. . . . .	169
6.5	Growth parameters at the cellular level . . . . .	170
6.6	Cell shape present variations in different species. . . . .	171





# Chapter 1

## General Introduction

### 1.1 Introduction

A major problem in developmental biology is to understand how the behaviour of individual cells creates reproducible biological shapes. Moreover, the reproducibility of form happens not only at the level of the organism, but patterns at the cellular level are evident in the temporal as well as the spatial scales (Sachs, 1991). Understanding the basic principles underlying these cellular patterns constitutes a fundamental question to linking the individual cell (microscopic) dynamics to the collective (macroscopic) phenomenon of morphogenesis.

The relative flat shape, accessibility and the absence of cell migration and apoptosis makes the leaf of *Arabidopsis thaliana* an excellent system to study the process of morphogenesis at the cellular level. However, the information about the cellular dynamics that is available has just been inferred indirectly or restricted to few cells.

The rigorous labour of dissecting many leaves to observe cellular characteristics over time and space has generated an overall picture of different cellular patterns and a rough idea of the scales at which these patterns happen. Yet, it has been impossible to follow *in vivo* populations of cells during the morphogenesis of the organ. The studies undertaken so far have followed either small groups of cells (tens) at late stages (Asl *et al.*, 2011; Zhang *et al.*, 2011; Elsner *et al.*, 2012) or analysed growth at the tissue-level without cellular resolution (Avery, 1933; Schmundt *et al.*, 1998; Remmler & Rolland-Lagan, 2012; Kuchen *et al.*, 2012).

One of the most characteristic patterns at the cellular level is that the cell divisions are confined to particular regions in some plant organs. In roots, for instance, the meristematic region is located at the tip of the root and the division is maintained over long periods (often, referred to as an indeterminate organ). In contrast, within the leaf, divisions happen at the base and eventually disappear and the leaf reaches a particular size (determinate organ). In the specific case of the leaf, the pattern that cell division follows has been coined “cyclic arrest front”, because cells are “arresting” division from the tip

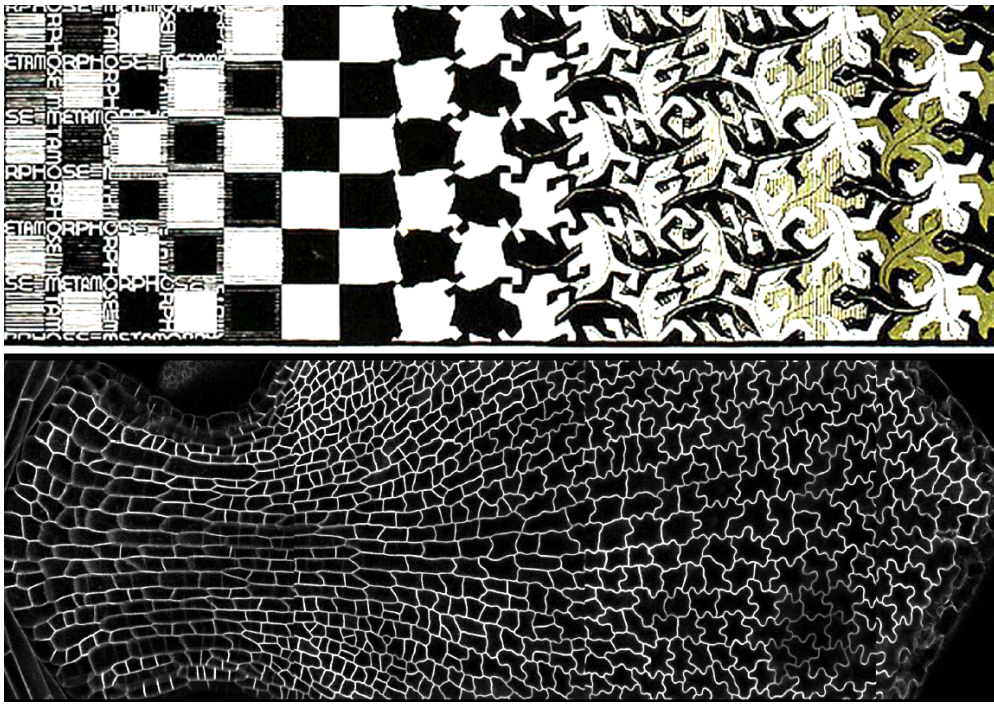


**Figure 1.1: Metamorphosis II by Escher resembles the epidermis of the leaf of *Arabidopsis thaliana*.**

progressing towards the base of the leaf (Donnelly *et al.*, 1999; Nath *et al.*, 2003; Kazama *et al.*, 2010).

Complementary to the spatial pattern of cell divisions, cells acquire the characteristic jigsaw puzzle-like shape in an opposite fashion: starting from the tip and continuing extending over time until reaching the base of the leaf (Donnelly *et al.*, 1999). This results in a gradient of developmental cell stages and geometries: rectangular and square cells are at the base of the leaf while jigsaw puzzle-like cells are recognized first at the tip of the leaf. This situation resembles the famous drawing by the Dutch artist M.C. Escher called *Metamorphosis II* (Figure 1.1). Here too, shapes develop gradually in a tessellated pattern (space filling with no overlaps or gaps).

Another cellular pattern important for the morphogenesis of the leaf that has received increased interest is the polarity. A prototypical example of polarity at the cellular level is the expression of the proteins PIN-FORMED in particular side of a cell (for example see Benkova *et al.*, 2003). However, cell polarity also involves internal asymmetry that confers changes in geometry (Nelson, 2003). The development of a jigsaw puzzle-like cell shape involves alternate patterns of lobe and indentations in a multi-polar fashion (similarly to Escher's interdigitating lizards, see Figure 1.1). Thus, the study of the shape dynamics provides us with an extraordinary system to study how cell polarity is established and coordinated among neighbours and how it relates to the overall tissue morphogenesis.

The cell shape change is accompanied by the increase in cell size. Unfortunately, a study of the dynamics of cell growth during leaf development has not been carried out directly to date. On one hand, cell growth has been extrapolated from a sample of re-

gions within the leaf over time, resulting in information about the average at the organ level, and hence, ignoring spatial differences. On the other hand, other studies analysing growth have focused on tissue scale patterns. For instance, a long tradition of placing marks in different leaf regions (i.e ink) and tracking those over time have reported a strong basipetal gradient of the growth rates in diverse species (Avery, 1933; Granier & Tardieu, 1998).

Nevertheless, using only tissue scale measurements, it is not possible to know whether a gradient of growth occurs at the cellular level as well. In the root of *Arabidopsis thaliana*, for instance, it is possible to distinguish regions at tissue scale with particular growth characteristics (division zone, elongation zone and differentiation zone) at almost fixed distances from the tip. The cells, however, are not fixed, but they are elongating and transiting through the root (Beemster & Baskin, 1998). The difference in behaviour at the tissue and cellular level in this system highlights also the importance of the analysis of the cellular data to understand the macroscopic behaviour at the organ-level.

What regulates the characteristic cellular patterns, so that they can lead to reproducible organ shapes is an exciting open question. Although, many genes have been involved in different aspects of cellular behaviour, there is just a scattered picture of the underlying mechanism. In parallel, theoretical considerations have proposed the existence of putative gradients at the tissue level that could control cellular behaviour at the organ scale (Wolpert, 1994; Grieneisen *et al.*, 2007; Kazama *et al.*, 2010; Kennaway *et al.*, 2011; Remmler & Rolland-Lagan, 2012; Grieneisen *et al.*, 2012). In my opinion, any of those approaches by their own can lead to satisfactory answers in the absence of information about the dynamics at the cellular level: mutant phenotypes could be explained by different cellular dynamics and theoretical hypothesis if unconstrained by real data at the cellular level can lead to wrong interpretations of a biological phenomenon.

In this thesis, I present some methods that allowed the characterisation of the cellular dynamics (Chapter 2 and 3). In fact, the analysis of cell division, cell growth and cell shape over relevant spatial and temporal scales required the synergy of experimental and computational tools. Altogether, it was possible to capture cell dynamics with an unique spatial and temporal resolution, permitting me to revisit and propose new hypothesis for the regulation of cellular dynamics during leaf morphogenesis (Chapter 4, 5 and 6).

## 1.2 Leaf development

Multicellularity demands the coordinated activity of cellular processes over time and space. The outgrowth of an appendage in plants and animals is not an exception. During the vertebrate limb development, a strong distal pattern of higher cell division rates together with directed cell movement and oriented cell division promote its outgrowth (Boehm *et al.*, 2010). In the leaf, cells are restricted to move and it is easier to distinguish a trend in cell divisions and cell growth. Cell proliferation is concentrated in the proximal end of the leaf while the cell growth and the development of complex cell shapes

(pavement cells) is strongly marked at the other end of the organ (Donnelly *et al.*, 1999). However, unlike limb development (Boehm *et al.*, 2010), the dynamics of cell behaviour has not been analysed *in vivo* during leaf development but it has been inferred from series of static pictures, and the role of cell polarity (if any) has not been investigated in the context of leaf growth.

In contrast to the lack of dynamic data at cellular resolution, there has been an enormous progress in disentangling the molecular and genetical basis of leaf development. I start by summarizing the current molecular aspects attributed to the coordination of cell division and cell growth during leaf morphogenesis.

Although leaf growth is often argued to result from the combined action of cell division and cell growth, it is important to mention that cell division represents just a partition of space and by itself cannot contribute to tissue growth (Su & O'Farrell, 1998). This distinction is important because it allows us to study cell division separately from cell growth, a conceptual separation that helps formulate hypothesis about its relation and coordination. Nevertheless, it is obvious that cell growth accompanies cell division because infinitely small cells have not been observed. Indeed, the cell growth follow a very characteristic pattern after cell division and will be discussed further in Chapter 4. Here, for simplicity, I refer as cell division or cell proliferation to the biological process that involves cell division and its simultaneous cell growth.

### 1.2.1 Cell division and cell growth regulation during leaf development

The first phase of leaf development is marked by an auxin maxima in the L1 of the meristem, created by a positive feedback loop between auxin and its transporter PINFORMED1 (PIN1) (Jonsson *et al.*, 2006; Smith *et al.*, 2006). The leaf primordium emerge from the flanks of the shoot apical meristem (SAM, Reinhardt *et al.*, 2000) and the PIN1 transporters are identified along the structure that will give raise to the vasculature system (Sawchuk *et al.*, 2013). Based on clonal analysis, the number of cells that gives raise to the leaf primordium has been estimated to be around 100 cells, but varies depending on the plant species (Efroni *et al.*, 2010; Gonzalez *et al.*, 2012). Subsequently, the leaf is partitioned into the adaxial and abaxial domains (Bowman *et al.*, 2002).

After this phase of early patterning, the leaf is recognized as an outgrowth and continues growing to acquire its final shape. In this work, I focus on the analysis of the cellular behaviour from the subsequent stages of leaf development but as early as when all the cells are recognized as rectangular or hexagonal shapes (at 6 days after stratification, when the first leaf is approximately 0.121 mm in width).

Leaves are determinate organs because the cell divisions are detected in a specific temporal window and eventually they disappear; subsequently, all cells in the organ differentiate (and saturate their growth) and the leaves acquire their final size and shape. Cell proliferation within the leaf is detected mainly at its base and it is only transiently maintained (Donnelly *et al.*, 1999; Kazama *et al.*, 2010; Lenhard, 2012). The reported dy-

namics of cell division is proposed to follow a “cyclic arrest front”, that separates a cell proliferative region from a region where cells exit the mitotic process and begin expansion and differentiation (Donnelly *et al.*, 1999; Nath *et al.*, 2003). The “front” starts from the proximal end and advances towards the distal part of the leaf, until divisions are “arrested”. Recently, it was proposed that the cyclic arrest front is maintained in a fixed location of about 100  $\mu\text{m}$  from the base of the leaf and that the exit of proliferation occurs drastically in time (Kazama *et al.*, 2010; Andriankaja *et al.*, 2012; Lenhard, 2012). Stomata differentiation seems to follow different dynamics and the arrest of division of stomata lineage occurs later (White, 2006).

Conversely, cell elongation coincides with the development of jigsaw puzzle-like cells and both of these cellular characteristics are detected first in the opposite extreme of the leaf (i.e. tip, Donnelly *et al.*, 1999). Regarding the dynamics of cell growth, it is known that cell size increases over time (De Veylder *et al.*, 2001; Andriankaja *et al.*, 2012) but a detailed analysis on the temporal and spatial dynamics has not been undertaken.

Although many regulators involved in the control of cell division and cell elongation have been identified (reviewed in Powell & Lenhard, 2012), how cell division and cell growth are coordinated remains unclear.

One theoretical proposal is that gradients could act as coordinators over the tissue scale regulating different cellular outcomes, including cell division and cell growth (Anastasiou *et al.*, 2007; Grieneisen *et al.*, 2007; Kazama *et al.*, 2010; Wartlick *et al.*, 2011; Kenaway *et al.*, 2011). Despite the theoretical importance of gradients to modulate cell dynamics, there has not been a single characterization of a gradient within the leaf (at least not at the level of quantitation comparable to some gradients in animals such as Decapentaplegic and Bicoid, see Kicheva *et al.*, 2007 and Gregor *et al.*, 2007a, respectively). However, I summarize some of the pathways that have been reported, emphasizing those that act non-cell autonomously in the leaf and that potentially could be implied in the formation of gradients. A detailed analysis of the molecular and genetic evidence available can be found in recent reviews (Johnson & Lenhard, 2011; Powell & Lenhard, 2012; Tsukaya, 2013).

Interestingly, some pathways seem to converge in the regulation of the cyclin-D3 (CYCD3) involved in the transition of G1-S phase during the cell cycle (Dewitte *et al.*, 2003). Overexpression of CYCD3 leads to leaf overgrowth and buckling (Dewitte *et al.*, 2003) and its loss of function causes premature termination of cell division (Dewitte *et al.*, 2007). Cytokinin, for instance, activates the expression of CYCD3 (Riou-Khamlichi *et al.*, 1999) and the triple *cycd3;1-3* showed impaired cytokinin response (Dewitte *et al.*, 2007). A link with other important phytohormone, auxin, was also established. Ectopic expression of AINTEGUMENTA (AN), regulated by auxin through ARGOS, led to extended CYCD3 expression (Hu *et al.*, 2003; Mizukami & Fischer, 2000).

Moreover, CYCDs participate in the well-conserved module that includes retinoblastoma-related protein (RBR) and E2F transcription factors to regulate entry to the S phase in the

cell cycle (Dewitte *et al.*, 2003, 2007). Recently, a gene regulatory network including auxin and SHORT ROOT (SHR), SCARECROW (SCR), RBR and its phosphorylation by CYCD6 was shown to play an important role in the asymmetric divisions in the root stem cell niche by using the interaction of two gradients (Cruz-Ramirez *et al.*, 2012). A similar network has been implied in the asymmetric division of stomata (Weimer *et al.*, 2012); it could be interesting to investigate whether similar components operate in the divisions independent of the stomata lineage. This is a plausible possibility, given that mutants of SHR and SCR also showed smaller leaves caused by a decrease in the overall cell division and SHR is proposed to be expressed in a graded fashion within the leaf (Dhondt *et al.*, 2010).

Another important module in leaf size regulation is composed by TCP transcription factors (Palatnik *et al.*, 2003; Martin-Trillo & Cubas, 2010). Although there are not reports of movement for TCPs, their downstream activity (i.e via cytokinin) and regulation (mediated by microRNA) might be non-cell autonomous (see below). There are two classes of TCP factors based on the sequence (reviewed in Martin-Trillo & Cubas, 2010) with antagonistic activities. Class I TCP genes positively regulate proliferation, whereas class II TCP genes, such as TCP2-4 in *Arabidopsis thaliana* and CINCINNATA (CIN) in *Antirrhinum majus*, negatively regulate proliferation (Kosugi & Ohashi, 1997; Palatnik *et al.*, 2003; Nath *et al.*, 2003; Li *et al.*, 2005).

The proliferative activity of TCPs might be mediated by their influence on cytokinin response. Recently, it was shown that class II TCPs transcription factors reduced cytokinin response by the induction of its inhibitor ARR4 (Efroni *et al.*, 2013) while the class I TCPs was proposed to enhance the responses to cytokinin (Steiner *et al.*, 2012).

Moreover, based on the analysis of binding promoter regions, TCP factors could coregulate cell cycle factors and translational machinery; thus, linking cell division and cell growth (Li *et al.*, 2005). In agreement, transient expression of TCPs in early stages resulted in small leaves and transient delay in their expression induced giant leaves with normal morphology (Palatnik *et al.*, 2003; Efroni *et al.*, 2008). Furthermore, mutants such as *cin*, resulted in crinkly and bended leaves because cell division was prolonged and ectopically maintained in the leaf margins of *Antirrhinum majus* (Nath *et al.*, 2003). Therefore, an interesting suggestion is that the antagonistic activities of class I and II TCP genes regulate leaf growth and perhaps the boundary of expression of members of these families coincides with the region where division takes place or is restricted, respectively (Li *et al.*, 2005; Efroni *et al.*, 2008). However, to my knowledge there is no study where the boundary of expression of the members of both classes have been analysed during leaf development.

In *Arabidopsis thaliana*, some TCP factors are negatively regulated by a microRNA (miR319), which guides the cleavage of their messenger RNA to maintain their domain of activity (Palatnik *et al.*, 2003). Overexpression of cleavage-resistant versions of TCPs resulted in crinkly leaves (Palatnik *et al.*, 2003), resembling *cin* mutants in *Antirrhinum*

*majus* (Nath *et al.*, 2003). An interesting observation is that microRNA could act non-cell-autonomously and potentially form gradients (Carlsbecker *et al.*, 2010), but this has not been shown in context of the leaf.

Another module regulated by microRNAs is constituted by the transcription factors of the family GROWTH REGULATING FACTOR (GRF). In this case, the miR396, which downregulates the GRF mRNA, is expressed in the distal part of leaf primordia initially, and increases its expression level over time (Horiguchi *et al.*, 2005; Rodriguez *et al.*, 2010). In contrast, GRF is expressed in the proximal side of the leaf, coinciding with cell divisions, in a graded fashion (accordingly with the GRF2:*wt*GRF2-GUS expression pattern) that depends on the correct activity of miR396 (Rodriguez *et al.*, 2010). Similarly, other member of the GRF family, GRF5 and its coactivator ANGUSTIFOLIA3 (AN3) are expressed in the proximal proliferation zone of the leaf and its expression is also limited by miR396 (Horiguchi *et al.*, 2005; Tsukaya, 2013). Overexpression of miR396 leads to narrow leaves, similarly to *angustifolia* mutant (Rodriguez *et al.*, 2010; Bai *et al.*, 2010). Recently, it was shown that AN3 can diffuse across leaf layers, but it cannot cross the midvein (Kawade *et al.*, 2013). It could be interesting to quantify the AN3 diffusion (and production, degradation, etc.) to explore the potential to form a gradient in relevant spatial and temporal scales.

Despite the theoretical importance of gradients in coordinating and regulating cellular behaviour, in leaves there are no reports of the dynamics of any gradient, as mentioned before. Auxin, for example is able to form a stable gradient along the root (Grieneisen *et al.*, 2007; Petersson *et al.*, 2009; Grieneisen *et al.*, 2012). In the context of the leaf, the auxin response marker (DR5, a synthetic promoter) shows a peak of expression at the tip of the leaf (Aloni *et al.*, 2003). Auxin transporters (PINs), however, are only detected at very early stages of leaf development (Benkova *et al.*, 2003; Guenot *et al.*, 2012); thus, it is not clear if a gradient of auxin is present in the leaf or if the maximum of DR5 is the result of their transport through the vasculature. Other hormones such as gibberellin and brassinosteroids have been also implied in the modulation of the organ size, and potentially could act non-cell autonomously (see for example, Achard *et al.*, 2009; Zhiponova *et al.*, 2013). In addition, other molecules reported as acting in a non-autonomous manner include KLUH (Anastasiou *et al.*, 2007; Eriksson *et al.*, 2010), SHR (Dhondt *et al.*, 2010), peptides such as ERECTA (Shpak *et al.*, 2004), microRNAs (Carlsbecker *et al.*, 2010; Rodriguez *et al.*, 2010) and AN3 (Kawade *et al.*, 2013).

Leaf growth can also be transiently arrested in response to environmental stimuli (Wolters & Jurgens, 2009). When plants are growing in overcrowded environments, the growth of the leaf blade stops transiently while the petiole accelerates its growth, to overcome the shade imposed by the neighbours (Carabelli *et al.*, 2007). This phenomenon is called shade avoidance syndrome (SAS) and it involves auxin production by the tryptophan aminotransferase TAA1 (Tao *et al.*, 2008). The increased auxin levels, in turn, trigger the induction of the enzyme oxidase CKX6, which breakdowns cytokinin, resulting in

transient growth arrest (Carabelli *et al.*, 2007). This suggests that the developmental programs that control cellular activity are flexible and might operate in different contexts.

How the final size of a leaf, or in fact any organ, is determined is poorly understood (Day & Lawrence, 2000). An interesting feature of leaf development is that when cell proliferation is reduced, cells elongate over the wild type limits of cell size, such as the overall leaf size is not dramatically altered (Tsukaya, 2013). This phenomenon is not exclusive to plants but has been reported in other multicellular organisms, including *Drosophila* (see some reviews of the topic, Day & Lawrence, 2000; Su & O'Farrell, 1998). In plants, this phenomenon is called compensation (Tsukaya, 2002). Different mutants that show this behaviour have reported (reviewed in Horiguchi & Tsukaya, 2011), but to date, this phenomenon remains mysterious.

A complication in unravelling how cell growth and cell division are related and modulated during development (i.e regulation by a gradient) is that it has been impossible to directly assess the dynamics of these processes at the cellular level at relevant spatial (within the leaf) and temporal (from early stages to leaf maturation) scales.

### 1.2.2 Polarity and leaf shape regulation

Final leaf shape arises from a bud-like structure that over time, becomes flat. Final leaf form is defined by interaction of orthogonal systems that regulate the shape along the dorsiventral, mediolateral, and proximodistal axes (Tsuge *et al.*, 1996; Efroni *et al.*, 2010; Kuchen *et al.*, 2012). In accordance, there are several reported mutants that showed alteration in these axes (long and narrow leaves or rounded leaves, for instance. See a detailed review about mutants altered in leaf shape in Micol, 2009).

Almost ten years ago, it was proposed that the shape of an organ during development could be described by four simple local growth parameters: growth rate, anisotropy, direction and rotation (Coen *et al.*, 2004). The variation of these parameters over time and space in the context of a connected tissue could give rise to diverse biological forms (Coen *et al.*, 2004).

Recently, these ideas were linked to underlying factors to include the interplay of modulators of growth (growth rate regulatory network) and directions (polarizer regulatory network) that interact with gene regulatory networks (GRN) to specify complex shapes (Kennaway *et al.*, 2011). This framework allows specifying a pattern of growth rates that occur parallel or perpendicular to hypothetical gradients (*specified growth*). The *resultant growth*, however, can diverge from the *specified growth* due to interactions between the connected tissue regions and the direction of growth (polarity, in this context). A remarkable feature of this framework is the possibility of establishing local feedbacks among the growth parameters and the orientations of preferential growth (Kennaway *et al.*, 2011)

Using this scheme, a computational model of the leaf showed that feedbacks between early patterning of directed growth and tissue deformation might underlie leaf shape development (Kuchen *et al.*, 2012). This hypothesis for leaf morphogenesis proposes the

existence of a PGRAD factor that promotes growth along the proximodistal axis (i.e. it determines a growth rate constant  $k$ ). The expression of this factor declines from the proximal to distal ends of the leaf, such as the growth rates decline towards the tip of the leaf, according to the *in vivo* confocal data. Another hypothetical factor, LAM, contributes to the growth rate in the mediolateral axis.

Interestingly, this model proposes the existence of local polarity to specify directed growth within the leaf (Kuchen *et al.*, 2012), raising the questions of what substance underlies the tissue polarity and if this system acts at the cellular level as well. Cell polarity in a broader context is discussed next.

### 1.3 Cell polarity

Cell polarity or asymmetry in cell shape, protein distribution or cell functions (Nelson, 2003) is crucial in many biological processes such as asymmetric cell division, cell fate determination, cell function, and cell morphology to name a few (Etienne-Manneville & Hall, 2002; Yang, 2008).

In plants, for example the asymmetric distribution of BASL has been implied in cell divisions within the stomatal lineage (Dong *et al.*, 2009; Robinson *et al.*, 2011); the polar localization of the auxin-efflux transporters PIN has been involved in apical and basal identity in embryos (Steinmann *et al.*, 1999) and directional transport of auxin in the root (Blilou *et al.*, 2005; Grieneisen *et al.*, 2007); and polar distribution of the small GTPases has been involved in asymmetric elongation of cell surface as in the case of root hairs and pavement cells (Fu & Yang, 2001; Fu *et al.*, 2002, 2005, 2009).

Despite the fact that many of the underlying molecular determinants of these asymmetries have been identified in animals and plants, the mechanism(s) by which cell polarity is established, maintained and coordinated in multicellular systems during development remains unknown.

A theoretical possibility is that cell polarity or cell asymmetries can arise spontaneously. In 1952, Turing showed that diffusible chemical substances, which he called morphogens (to convey the idea of “form producers”), could self-organize into spatial patterns, starting from homogeneous distributions (Turing, 1952). Turing’s reaction–diffusion model shows that two (or more) morphogens with different diffusion properties that react by auto- and cross-catalyzing or inhibiting their production, can generate spatial patterns of morphogen concentration (Turing, 1952). The reaction–diffusion formalism was used to model diverse systems such as regeneration in hydra (Turing, 1952), pigmentation of fish (Kondo & Miura, 2010), and patterns on the shells of snails (Meinhardt & Gierer, 1974).

Using a similar mechanism, a recent hypothesis involving an intracellular partitioning system able to generate spontaneous cell polarity was proposed as a fundamental element to account for tissue polarity (Abley *et al.*, 2013). It was proposed that auxin acts as a mediator in the coordination of cell polarity among neighbours in plants, where direct

protein-protein interactions are not possible due to the presence of cell walls (Abley *et al.*, 2013).

Candidates components for the intracellular partitioning are the well-conserved proteins Rho-GTPases, in plants called ROPs (Rho-GTPases of Plants). The switch-behaviour of the active-inactive small GTPases proteins and the spatial differences of these alternative forms make them ideal as candidates of molecular components underlying cell polarity (Marée *et al.*, 2012; Grieneisen *et al.*, 2013b). The active form or GTP-bound form recognizes target proteins and generates a response until GTP hydrolysis returns it to the inactive form or GDP-bound state. The cycling of inactive and active and vice versa is mediated by Guanine Nucleotide Exchange factor (GEF) and GTPase-activating proteins (GAPs), respectively. The active form is attached to the membrane while the inactive form can be unattached to the cytosol by Guanosine Nucleotide Dissociation Inhibitors (GDI) (Takai *et al.*, 2001). Thus, the GEFs, GAPs and GDI proteins modulate the behaviour of small GTPases that, in turn, could influence their dynamics in the generation of intracellular patterning (i.e cell polarity) through Turing instabilities (Turing, 1952) or any other pattern formation mechanism (see for example, the wave-pinning mechanism described in Mori *et al.*, 2008).

In animals, there are well-characterized GEF, GAP and GDI (review in Etienne-Manneville & Hall, 2002). In contrast, in plants the effects and specific roles of GEF, GAP and GDI are not widely documented but the available evidence suggests that their function is conserved in plants (Berken *et al.*, 2005; Yang, 2008). The only homolog of RhoGEF reported so far is SPIKE, which in addition to binding to ROP2 has been involved in actin filament assembly as part of SCAR/WAVE complex (Qiu *et al.*, 2002; Uhrig *et al.*, 2007; Basu *et al.*, 2008). In addition, the existence of a family of plant-RhoGEFs has been reported and the RhoGEF activity was shown *in vitro* (Ben-Zvi *et al.*, 2008). There is also evidence of the functional role of GDI in plants. Knocking out RhoGDI1 induces multiple root hairs in a single cell, most probably due to the sequestration of ROP2 in the cytosol, in agreement with the role of GDI reported previously (Carol *et al.*, 2005). Moreover, overexpression of RhoGDI1 suppresses the defective growth caused by overexpression of ROP1 in tobacco pollen tubes (Fu & Yang, 2001). Less is known about the function of GAPs in plants. But it has been related with suppression of depolarization induced by overexpression of ROP1 in pollen tubes (Fu & Yang, 2001; Klahre & Kost, 2006).

Moreover, a link between auxin and ROPs required for the intracellular partitioning that generates cell polarity (Abley *et al.*, 2013) has been implied in the development of the jigsaw puzzle-like cell shapes in the epidermis of leaves and PIN2 polarity in roots (see a recent review in Grieneisen *et al.*, 2013b). Importantly, ROPs also link a possible intracellular patterning formation with the cytoskeleton, enabling for an additional level of feedback between the polarity and mechanics (Asnacios & Hamant, 2012).

An interesting possibility is that a similar mechanism of intracellular partitioning coupled by auxin could underlie asymmetries in cell shape (Grieneisen *et al.*, 2013a) and per-

haps also principal directions of growth and anisotropy at the cellular level. Due to their multipolar pattern of lobes and indentations, the puzzle-like pavement cells in the epidermis of the leaf of *Arabidopsis thaliana* represent an ideal system to address this question.

Indeed, ROP proteins are asymmetrically expressed in lobes and indentations within the pavement cells and there is experimental evidence supporting their influence to the downstream cell cytoskeleton, which ultimately enables differential membrane elongation (Fu *et al.*, 2005, 2009). Moreover, constitutive active (CA) and dominant negative (DN) mutants of these proteins showed alterations in the characteristic pavement cell shape, suggesting that an intracellular partitioning mediated by ROPs can be important for the cell polarity that underlies their complex shape (Fu *et al.*, 2002, 2005, 2009; Grieneisen *et al.*, 2013a). In addition, auxin also has been involved in modulating the “waviness” of pavement cells shape in a concentration-dependent manner (Xu *et al.*, 2010; Grieneisen *et al.*, 2013a). Thus, the study of the cell shape progression in individual cells is likely to provide insights into the cell polarity mechanism that creates complex geometries.

## 1.4 Quantification of cell behaviour

Cellular behaviour is constantly changing during development. Studies aimed to investigate the dynamics of cellular patterns have used different methods, ranging from tracking growth by placing ink dots on the leaf surface to using microscopes and fluorescent marked cell outlines to study cell behaviour. Other studies have used the relation between cell size (or length), cell number, and overall tissue length to infer the cellular growth and the division rates (Nelissen *et al.*, 2013). In contrast, quantification of complex cell shapes (and its dynamics) is very challenging to assess (Pincus & Theriot, 2007), and will be discussed in detail in Chapter 2.

### 1.4.1 The kinematic analysis

Often in plants, the growth within a tissue is not homogeneous (Beemster & Baskin, 1998). Due to differential growth, cells change their position and displace. When there are parts of the tissue that grow at different speeds (different strain rates), the displacement each cell experiences is also different. Early efforts to study the dynamics of plant cells recognized the difficulty to study a system in which elements are both “moving” and expanding. To capture the dynamics of cellular behaviour, the kinematic analysis in plants borrowed some terms from fluid dynamics: “Like a flame or the wake of a boat, the form of a plant changes slowly but the components are in continual flux. The motion of the components can therefore be analysed in terms of fluid flow”, Erickson & Silk, 1980.

In the root of *Arabidopsis thaliana*, it is possible to distinguish different regions described in terms of the cellular characteristics as division zone, expansion zone and differentiation zone (Beemster & Baskin, 1998; Perilli *et al.*, 2012) that can be found at almost fixed distances from the tip after 6 days (Eulerian system of reference, discussed in Chapter 4). The cells, however, are continually being displaced and transiting through zones; they can be said to flow through the growing region (Lagrangian system of reference, discussed in Chapter 4). Thus, the unchanging root geometry is made of elements (the cells) that are constantly changing (Erickson & Silk, 1980).

The kinematic method allows quantifying production and expansion rates in an organ as well as the rate of cell division and flux of cells in a particular region using the continuity equation (see details in Silk & Erickson, 1979; Beemster & Baskin, 1998). This method has been applied to leaves (Granier & Tardieu, 1998; Nelissen *et al.*, 2013) and roots (see an example in Beemster & Baskin, 1998).

Early efforts to measure leaf growth involved drawing ink dots or using the vein intersections on the leaf surface to delineate a grid whose deformation over time could be used to calculate regional growth rates (Avery, 1933; Granier & Tardieu, 1998; Schmundt *et al.*, 1998). Although, these studies were informative, they were limited to late stages of development when the leaf has grown enough to place landmarks. Besides, the relatively big size of the segments made it difficult to achieve good estimates for the behaviour of the cells.

To access the cellular level, other studies proposed to measure the overall leaf area and sample cells at two (or more) positions of the leaf (for instance, at about a quarter from the tip and bottom of the leaf and halfway between the leaf margin and the mid-vein). Then, the mean area and the number of cells in those regions were extrapolated to all the leaf to infer cell division and cell expansion rates. In many occasions, it was necessary to dissect many leaves at specific time intervals throughout development (Nelissen *et al.*, 2013); thus, it is not possible to follow the same regions over time using this approach.

Other studies have used the replica-method that involves making impressions of the leaf surface for several days (see for example, see Elsner *et al.*, 2012). This method permits better cellular resolution; however, it is limited to a small sample size (hence, it is not possible to study spatial differences within the leaf). Moreover, as it involves direct manipulation of the leaf, it cannot be performed for long periods without damaging the tissue, limiting the temporal resolution of the time-lapse (see for example, Zhang *et al.*, 2011; Asl *et al.*, 2011; Elsner *et al.*, 2012).

### 1.4.2 Live imaging

Recently, the use of confocal microscopy combined with fluorescent proteins to label membranes or molecular activity has enabled the study of developmental processes in an unprecedented manner (Megason & Fraser, 2007).

In plants, sophisticated microscopes and fluorescent protein tags to track cellular behaviour have been developed (Reddy *et al.*, 2007). Examples of quantitative extraction of cellular features obtained using time-lapse include the imaging of the shoot apical meristem (Grandjean *et al.*, 2004; Uyttewaal *et al.*, 2012; Kierzkowski *et al.*, 2012), sepal primordia (Schiessl *et al.*, 2012), and sepals (Roeder *et al.*, 2010), to mention just few recent examples.

For the leaf, the perfusion chamber developed to track early leaf development has been used to analyse patterns of cell divisions in the stomatal lineage (Robinson *et al.*, 2011), gibberellin response in hypocotyl cells (Sauret-Gueto *et al.*, 2012) and leaf growth (Kuchen *et al.*, 2012). Thus, live imaging is a powerful approach to study dynamical aspects of development at the cellular level.

However with live imaging we face a trade-off between preserving the integrity of the tissue and acquiring images at high resolution at relevant spatial (tissue level) and temporal scales (in the order of days for leaves). Tracking leaf growth, for example, can be achieved only for a couple of days because the leaves develop curvature and reach sizes that make impossible to capture cells at good resolution in reasonable scanning times. Thus, *in vivo* leaf tracking for long periods required the modification of the standard procedure of acquiring images.

Together with time-lapse techniques, it was necessary to develop computational tools to extract cellular features (Roeder *et al.*, 2012a). Many of the previous time lapse studies were limited to tens of cells because they required manual intervention to track cellular behaviour. To overcome these limitations, automatic and semi-automatic tools were developed and will be discussed in detail in Chapter 3.

## 1.5 About this work

Although much progress has been made in understanding the molecular basis that modify different aspects of the cellular behaviour, there is not a single study where the cellular dynamics have been followed for long periods of time together with the organ level. The information about the cellular dynamics that is available has just been inferred indirectly or restricted to few cells. This has limited our understanding on how the cellular behaviour is regulated during development and how it relates with the overall organ morphogenesis.

To evaluate cellular patterns during leaf development, first it was necessary to develop quantitative tools to characterize the dynamics of cellular behaviour over time. The complexity of pavement cell geometry rendered it impossible to use traditional metrics to capture the essence of the cell shape and their dynamics. In Chapter 2, I present a new method, the Lobe Contribution Elliptical Fourier Analysis (LOCO-EFA), that was developed with this purpose. Quantifiers obtained using this method permitted the char-

acterization of the cell shape complexity and provide a shape profile for individual cells that can be used to evaluate characteristics of populations of cells.

Remarkably, the shape profile of single cells changes only slightly from one time interval to the next in a fashion unique to each cell. This characteristic was used to develop a tracking algorithm that, integrated with an algorithm to identify cells within an image (SPM), results in a powerful tool to recognize cells in a succession of images and extract not only their cell shape, but also cell area, cell position and, importantly, cell lineages (Chapter 3).

The synergy between *in vivo* imaging and computational tools to extract efficiently the cell dynamics enabled the study of cellular patterns at temporal and spatial resolutions that were not achieved before. The analysis of diverse spatial (Eulerian and Lagrangian) and temporal scales (at the cellular and the leaf level) were needed to disentangle the behaviour related with the position from the behaviour related with the age of the cell (taking as a reference the moment of cell division) and it is presented in Chapter 4. The cell dynamics of growth, shape and divisions using long time-lapse enabled to revisit and propose new hypothesis about the regulation of the cellular behaviour during leaf morphogenesis.

Long time-lapse also enabled to study the dynamics of complex cell geometries. In Chapter 5, I focus on the development of the characteristic jigsaw puzzle-like shape of pavement cells and speculate from the data about the intracellular patterning and possible feedbacks that might account for it.

Finally, in Chapter 6, I discuss some outstanding open questions that can be addressed using the pipeline presented here. I also envision possible new directions, based on the results obtained in this thesis, that can guide us closer to understanding the mechanisms underlying morphogenesis.

## Chapter 2

# Getting quantitative in cell shape studies: Lobe Contribution Elliptical Fourier Analysis

### Abstract

Outstanding advances in microscopy techniques have allowed us to get access to considerable amount of data on cell morphology. However, there are very few methods to extract quantitative information of cell geometry, specially for complex cell shapes (such as pavement cells). The lack of quantitative criteria to assess the cell geometry limits the study of populations (i.e mutants, within an organ, cell shape over time) and make cell morphogenesis studies a very time consuming activity. In this chapter, I present a new method for the quantification of the cell shape, the Lobe Contribution Elliptical Fourier Analysis (LOCO-EFA). It takes into account the information of the whole cell outline and provides meaningful descriptors that are directly matched to morphological features of a cell. To validate the proposed method, I applied it to geometrical shapes and *in silico* tissues, where cells have a controlled specified shape that prevails when the simulated cells are alone but diverges when they are allowed to interact in a tissue context. These differences due to cell-to-cell interactions are fully quantified using the LOCO-EFA. Besides providing a quantification of the cell geometry, the LOCO-EFA method was used to identify the same cell over time (cell tracking algorithm, discussed in the next chapter).

## 2.1 Introduction

The geometry of a cell is a complex output of cell polarity (or asymmetries within a cell), cytoskeleton and other downstream processes that altogether shape cells according to a particular developmental context. For example, during the development of a root hair cell, the shape changes are preceded by the formation of a polar domain of a small GTPase ROP2, that leads to the reorganization of the cytoskeleton (ie. microtubules and actin filaments). In turn, this triggers local growth at one particular extreme of a cell leading to the formation of this specialized cell type (Jones *et al.*, 2002). Thus, the cell shape itself can be considered the read out of the patterning that underlies cell polarity and internal machinery that leads to the final cell shape. Importantly, this implies that studying how the cell shape changes quantitatively during its development and in the context of a growing tissue, can provide a mechanistic insight into how the cell polarity is established and maintained.

The quantitative assessment of cell shape (and its dynamics) is, however, not a trivial task. Especially difficult are cells with complex shapes, such as pavement cells (Figure 2.1). Indeed, their intricate form makes them a paradigmatic example that illustrates the challenges of the quantitative characterization of any cell shape, such as 1) complex geometry and, thus impossibility to describe their shape meaningfully with traditional metrics and 2) lack of recognizable landmarks, making it impossible to apply the myriad of shape statistics (i.e principal component analysis and procrustes analysis) that have been developed in other fields.

In this chapter, I discuss how traditional metrics can be misleading when applied to complex geometries. Then, I review previous work aimed to use the information of the whole contour of the cell to quantify cell shape using the Elliptical Fourier Analysis, pointing out the shortcomings of this method. Finally, I present a new method to quantify the cell shape (Lobe Contribution Elliptical Fourier Analysis) that is validated using simple geometrical shapes and *in silico* pavement-like shapes.

Interestingly, the analysis of computer-generated tissues where pavement-like cells have a parametrized specified shape also permits to address the fundamental question of how the resultant cell shape, when cells cannot move to accommodate or migrate, is influenced by cell-to-cell interactions within a packed tissue. Specifically, I explore the influence of cell neighbours on morphogenesis of individual cells by measuring the divergence of a specified cell shape when it is alone as compared to when it is immersed in the *in silico* tissue. This analysis, performed on *in silico* tissues allows to quantify such differences for a generic situation. These results validate the proposed method and show that local interactions at the level of individual cells could deviate the symmetric specified shapes towards very asymmetrical forms, an attractive hypothesis that awaits to be tested experimentally.

In the context of this work, LOCO-EFA provides a quantitative manner to evaluate cell morphogenesis of pavement cells (that can be well-described in two-dimensions, see

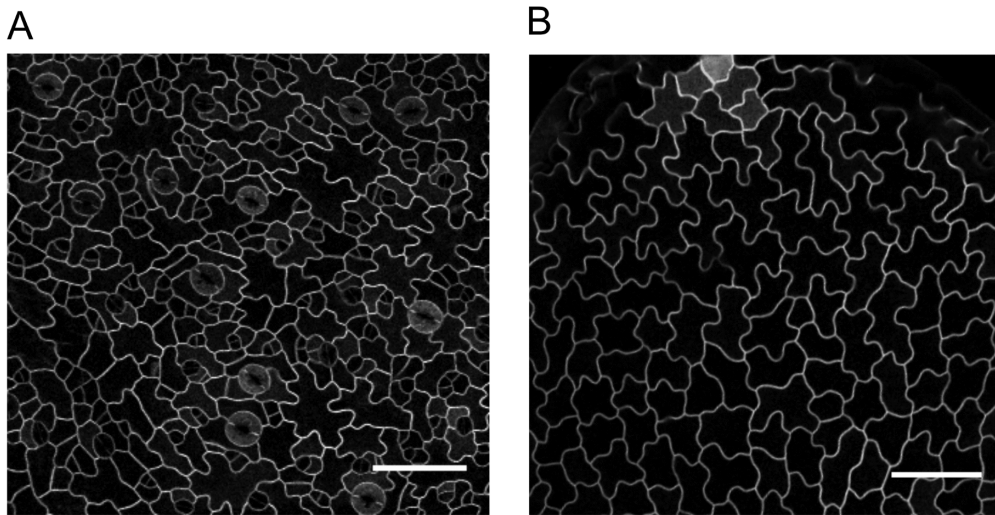


**Figure 2.1: Pavement cells.** These epidermal cells of the leaves of many plants are characterized by jigsaw puzzle-like shapes consisting of multiple alternating protrusions (also called lobes) and indentations. Due to the complexity of its shape, it is not trivial to capture the relevant cell shape features in a quantitative and robust manner. A) Pavement cells of *Arabidopsis thaliana* wild type pavement cells and B) *speechless* mutant are shown. Scale bar corresponds to 50  $\mu m$  in both captions.

Figure 3.4) during leaf development (Chapter 4) and, it is used in the algorithm to track individually cells over time (Chapter 3). Moreover, the the LOCO-EFA derived metrics can be used as criteria to quantify populations of cells from different treatments or mutants; thus, it also provides a quantitative manner to statistically assess populations.

## 2.2 Problems of traditional methods to quantify cell shape.

Some approaches classically used to quantify pavement cells are summarized in Table 1.1. Traditional metrics such as cell area, perimeter, aspect ratio and form factor are useful as general descriptors but the shape information that is possible to extract from them is limited and redundant: very different shapes may have a very similar aspect ratio and form factor (Figure 2.2). Thus, they are not unique and do not provide information about the shape features that are biologically relevant.

Some algorithms are highly sensitive to noise in the image (i.e skeleton) and others completely depend on human decisions to judge what is a lobe or indentation, such as the average lobe length and neck width (Figure 2.3), making this measure highly variable from cell to cell and from human to human. Thus, traditional metrics fail to quantitatively characterize general aspects of cell shape or specific features of pavement cell form such as quantity and quality of lobes.

Measure	Description	Reference
Average lobe length and neck width	Length of each lobe and the distance between opposite indentations within a cell (also called necks). The final measures for a cell is the average of lobe lengths and the average of all the neck widths. These measurements depends on the human criteria to identify lobes and necks.	Fu <i>et al.</i> , 2005
Form factor (or circularity)	Defined as: $\frac{P^2}{4A\pi}$ Where $P$ is the perimeter and $A$ is cell area. A circle will have a form factor 1, the lowest value possible.	Bai <i>et al.</i> (2010); Russ (2000); Andriankaja <i>et al.</i> (2012)
Skeleton	This method constructs a skeleton representation of the cell shape by removing certain pixels of cell in an iterative manner such that only an underlying branched one-dimensional structure remains. There are different variants of this algorithm to skeletonise cell shapes. This method is highly dependent on the parameters used to find the skeleton and it is very sensitive to the image resolution.	Le <i>et al.</i> (2006); Russ (2000)
Average polarity score	Defined as: $\frac{c+s}{2}$ Where $c$ is circularity and $s$ is the number of skeleton end points.	Sorek <i>et al.</i> (2011)

**Table 2.1:** Distinct shape descriptors have been used to quantify pavement cells.

### 2.3 Decomposing Shape: Lobe Contribution Elliptical Fourier Analysis (LOCO-EFA)

To quantitatively capture cell shape is not a trivial task. Elliptical Fourier analysis (EFA) provides a tool to simplify the contour of a cell through a set of coefficients that can be used as shape descriptors. However, EFA by its own has two major problems that compromise its use in cell shape studies: 1) it does not provide a manner to relate such coefficients to features of a cell (for example, protrusions or lobes) and 2) it allows multiple descriptions for a given shape. In this section, I briefly summarize previous efforts to make the EFA-coefficients biologically interpretable. Next, I discuss why the previous attempt to match EFA-coefficients with shape features do not work for all shapes. Finally, I present a new method, Lobe Contribution Elliptical Fourier Analysis (LOCO-EFA), that produces quantitative measurements that are biologically interpretable and unique for a given shape, overcoming the shortcomings of the previous methods.

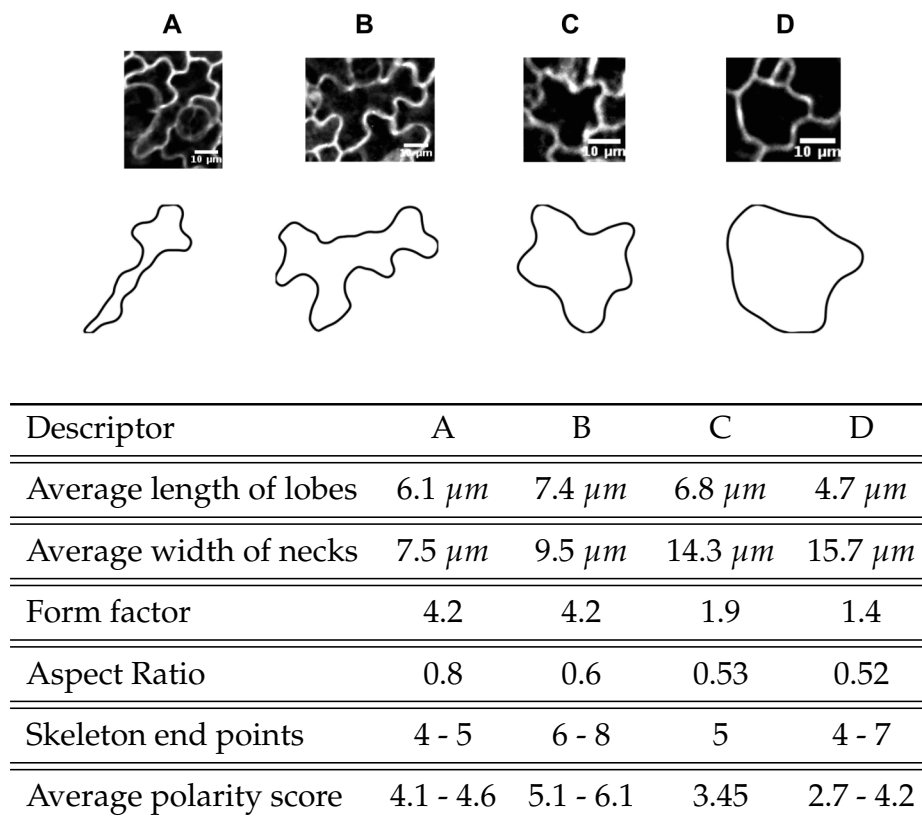


**Figure 2.2: Traditional shape quantifiers can be misleading when applied to complex shapes.** (A-D) Pavement cells imaged using confocal microscopy (upper panel) and its corresponding segmented images (lower panel). Traditional metrics to quantify cell shape can lead to very similar values for very different shapes (form factor and aspect ratio) or can be very sensitive to the parameters (skeleton) and image conditions chosen. Scale bars correspond to 10  $\mu m$ . See also Figure 2.3.

### 2.3.1 Elliptical Fourier Analysis

Fourier analysis has been widely used to analyse cell morphology when cells have a simple holomorphic shape, i.e when the radii emanating from the centroid of a cell intersect the outline only once (Figure 2.4A and Pincus & Theriot, 2007). When the geometry of a cell is more complex and the radii emanating from the centroid intersect the outline more than once it ceases to be possible to use the Fourier expansion based on polar coordinates (Figure 2.4B and Schmittbuhl *et al.*, 2003).

A solution to this limitation was presented in 1982, when Kuhl & Giardina proposed the Elliptical Fourier Analysis to describe the outline of any two-dimensional shape from the coordinates of the points of its outline. However, in contrast to the Fourier analysis, the EFA by its own cannot retrieve information that directly relates to morphological features of a cell, making the biological interpretation of this analysis very difficult. Another disadvantage is that EFA, in its current state, allows multiple descriptions for a given shape, endangering the statistical study of populations of cells, as explained further on.

In short, EFA takes the displacements of both  $x$  and  $y$  coordinates of a closed contour

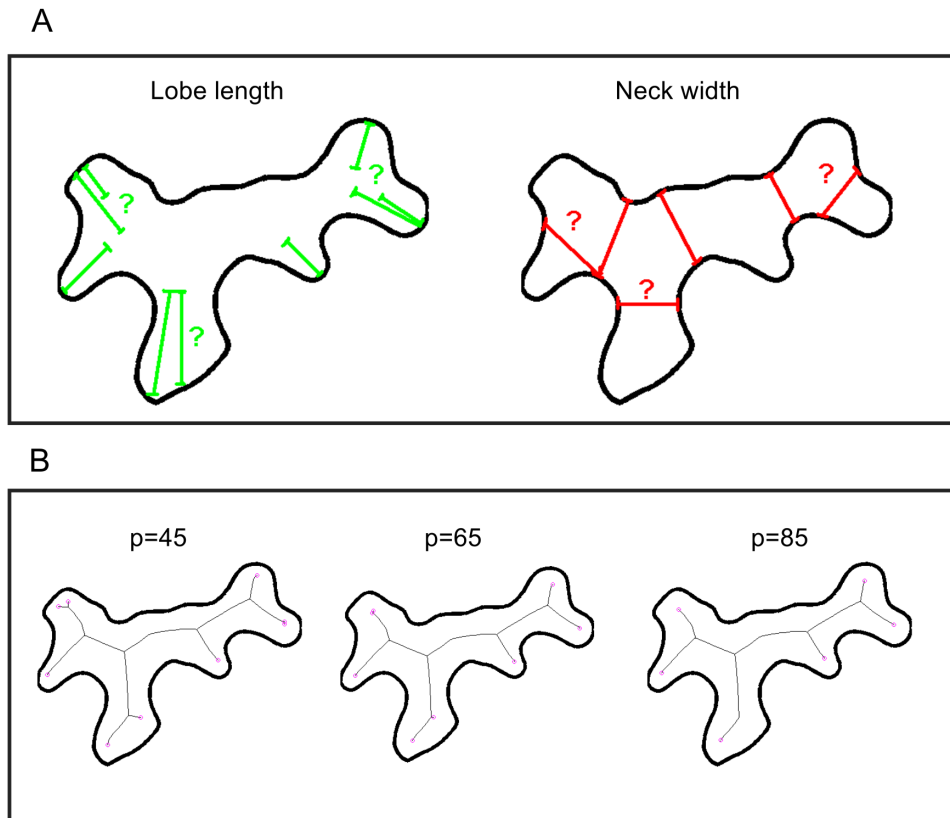


**Figure 2.3: Misleading measurements of lobe and neck length and skeleton.** (A) Neck width and lobe length depend on the human criteria for identifying such structures and (B) skeleton-end-points depend on the parameters chosen to find the skeleton. One parameter ( $p$ ) was varied from 45 (left), 65 (middle) and 85 (right) could give as an output 8-6 lobes.

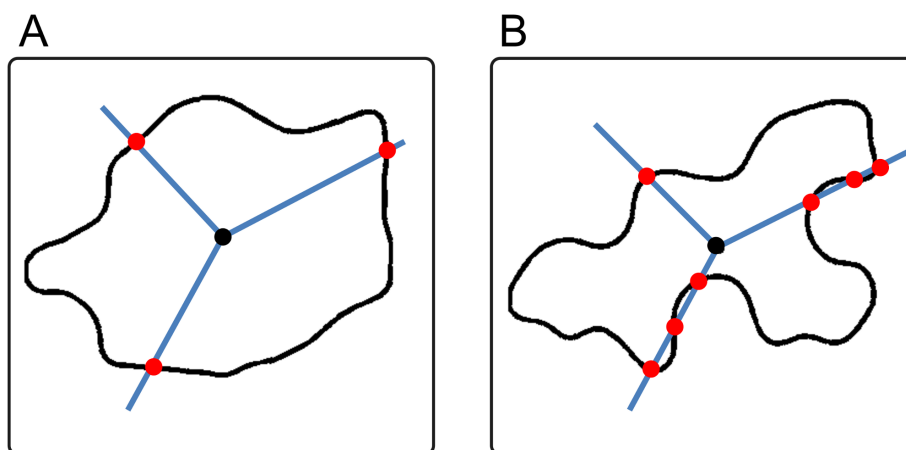


**Figure 2.4: Holomorphic and nonholomorphic shape outlines.** (A) The radii from the centroid to the outline of an holomorphic shape intersect only once whereas in a (B) non-holomorphic shape the same radii can intersect more than once. Few pavement cells (A) have an holomorphic shape but the majority contains a very complex non-holomorphic outline (B) that does not allow their outline to be represented in polar coordinates .

independently and decomposes it into an infinite summation of related ellipses:

$$x(t) = A_0 + \sum_{n=1}^{\infty} \left[ \alpha_n \cos \left( \frac{2n\pi t}{T} \right) + \beta_n \sin \left( \frac{2n\pi t}{T} \right) \right] \quad (2.1a)$$

$$y(t) = C_0 + \sum_{n=1}^{\infty} \left[ \gamma_n \cos \left( \frac{2n\pi t}{T} \right) + \delta_n \sin \left( \frac{2n\pi t}{T} \right) \right] \quad (2.1b)$$

where  $\alpha_n$ ,  $\beta_n$ ,  $\gamma_n$  and  $\delta_n$  are the EFA-coefficients and each four  $n$ th coefficients account for an ellipse (also referred to as 'mode' or 'harmonic') with a certain orientation and rotation;  $A_0$  and  $C_0$  are the offsets of the initial contour. Note that  $x(t)$  and  $y(t)$  are periodic functions with period equal to  $T$  (more below on the interpretation of  $t$  and  $T$ ).

The detailed derivation of the EFA coefficients can be found in Kuhl & Giardina, 1982. Briefly, the elliptic Fourier coefficients can be obtained as:

$$\alpha_n = \frac{T}{2n^2\pi^2} \sum_{i=1}^K \frac{\Delta x_i}{\Delta t_i} \left[ \cos \frac{2n\pi t_i}{T} - \cos \frac{2n\pi t_{i-1}}{T} \right] \quad (2.2a)$$

$$\beta_n = \frac{T}{2n^2\pi^2} \sum_{i=1}^K \frac{\Delta x_i}{\Delta t_i} \left[ \sin \frac{2n\pi t_i}{T} - \sin \frac{2n\pi t_{i-1}}{T} \right] \quad (2.2b)$$

$$\gamma_n = \frac{T}{2n^2\pi^2} \sum_{i=1}^K \frac{\Delta y_i}{\Delta t_i} \left[ \cos \frac{2n\pi t_i}{T} - \cos \frac{2n\pi t_{i-1}}{T} \right] \quad (2.2c)$$

$$\delta_n = \frac{T}{2n^2\pi^2} \sum_{i=1}^K \frac{\Delta y_i}{\Delta t_i} \left[ \sin \frac{2n\pi t_i}{T} - \sin \frac{2n\pi t_{i-1}}{T} \right] \quad (2.2d)$$

where  $K$  is the total number of points  $x_i, y_i$  of the closed contour. The "time" passed while "tracing" the contour or distance along the contour for each pair of  $x_i$  and  $y_i$  coordinates is referred as  $t_i$ , and  $T$  is the "total time" or perimeter length. Imagine drawing the contour of the cell, then  $\Delta t_i$  is the time spent drawing the segment of the contour that links each  $x_{i-1}$  and  $y_{i-1}$  pair to  $x_i$  and  $y_i$ ; similarly,  $T$  is the total time spent to draw the whole contour (Figure 2.5). Note that  $\Delta t_i$  is not fixed but can be different for each interval while  $T = \sum_{i=1}^K \Delta t_i$ ; and  $t_0 = 0$ ;  $t_K = T$ . Also note that  $x(0) = x(T)$  and  $y(0) = y(T)$ ; accordingly,  $x_0 = x_K$ ,  $y_0 = y_K$ , because it is an enclosed contour. Importantly, EFA does not require equal spacing between the points, so it is easy to sample the  $K$  observation points from a cell contour. The only requirements are that the contour is closed and the  $xy$ -coordinates are presented in a sequential order.

The offsets of the contour are given by:

$$A_0 = \frac{1}{T} \sum_{i=1}^K \left[ \frac{\Delta x_i}{2\Delta t_i} (t_i^2 - t_{i-1}^2) + \xi_i(t_i - t_{i-1}) \right] + x_0 \quad (2.3a)$$

$$C_0 = \frac{1}{T} \sum_{i=1}^K \left[ \frac{\Delta y_i}{2\Delta t_i} (t_i^2 - t_{i-1}^2) + \varepsilon_i(t_i - t_{i-1}) \right] + y_0 \quad (2.3b)$$

where  $\xi_i = \sum_{j=1}^{i-1} \Delta x_j - \frac{\Delta x_i}{\Delta t_i} \sum_{j=1}^{i-1} \Delta t_j$ ;  $\varepsilon_i = \sum_{j=1}^{i-1} \Delta y_j - \frac{\Delta y_i}{\Delta t_i} \sum_{j=1}^{i-1} \Delta t_j$  and  $\xi_1 = \varepsilon_1 = 0$  (see details in Kuhl & Giardina, 1982).

The way by which the combination of progressive  $n$ -ellipses give rise to the final shape is as follows: each  $n$ th elliptic harmonic traces  $n$  clockwise or counter-clockwise revolutions while rotating around the previous harmonic ellipse (and so forth, see Figure 2.5 and Appendix 2.A Movie 2.1). The direction of rotation of the  $n$ th harmonic ellipse is given by the determinant of the EFA-coefficients matrix,  $\det[\alpha_n \beta_n; \gamma_n \delta_n]$ , thus the direction of rotation is given by the sign of

$$r_n = \alpha_n \delta_n - \beta_n \gamma_n. \quad (2.4)$$

If  $r_n < 0$ , the elliptic harmonic is rotating clockwise; if  $r_n > 0$  the elliptic rotator is rotating counter-clockwise.

An expected result (but not so obvious) of the approximation of the shape using EFA is that, as the elliptical harmonics rotate around the others, each mode contribute to  $n + 1$  or  $n - 1$ 'th shape features (such as lobes) depending on their relative rotation to the first harmonic (Diaz *et al.*, 1990). As a result of this rotatory effect, there is no direct or clear relation between EFA-coefficients and morphological features (such as protrusions, lobes and filipodias) rendering the biological interpretation of the results unclear and ambiguous.

To solve this problem and find a correspondence between EFA-coefficients and the shape, Diaz *et al.* (1990) proposed a heuristic solution consisting of obtaining the contribution of each harmonic to the shape through an approximation of the perimeter of each ellipse multiplied by its harmonic number  $n$ ,

$$P_n = n2\pi \sqrt{\frac{\lambda_{1n}^2 + \lambda_{2n}^2}{2}} \quad (2.5)$$

where  $\lambda_{1n}$  and  $\lambda_{2n}$  are the two semi-axes corresponding to the  $n$ th ellipse.

To align the contribution of each harmonic to its correspondent morphological feature of "protrusions" (for example that a hexagon has its maximum EFA-contribution at  $P_6$ , see Figure 2.6) they noted that when an elliptic harmonic was rotating in the same direction as the first harmonic, its main contribution (in the hexagon example, the sixth mode) was shifted backwards a position, resulting in a peak at the  $n - 1$  mode (fifth mode, in this case); inversely, when the rotatory direction of a given mode was opposite to the first

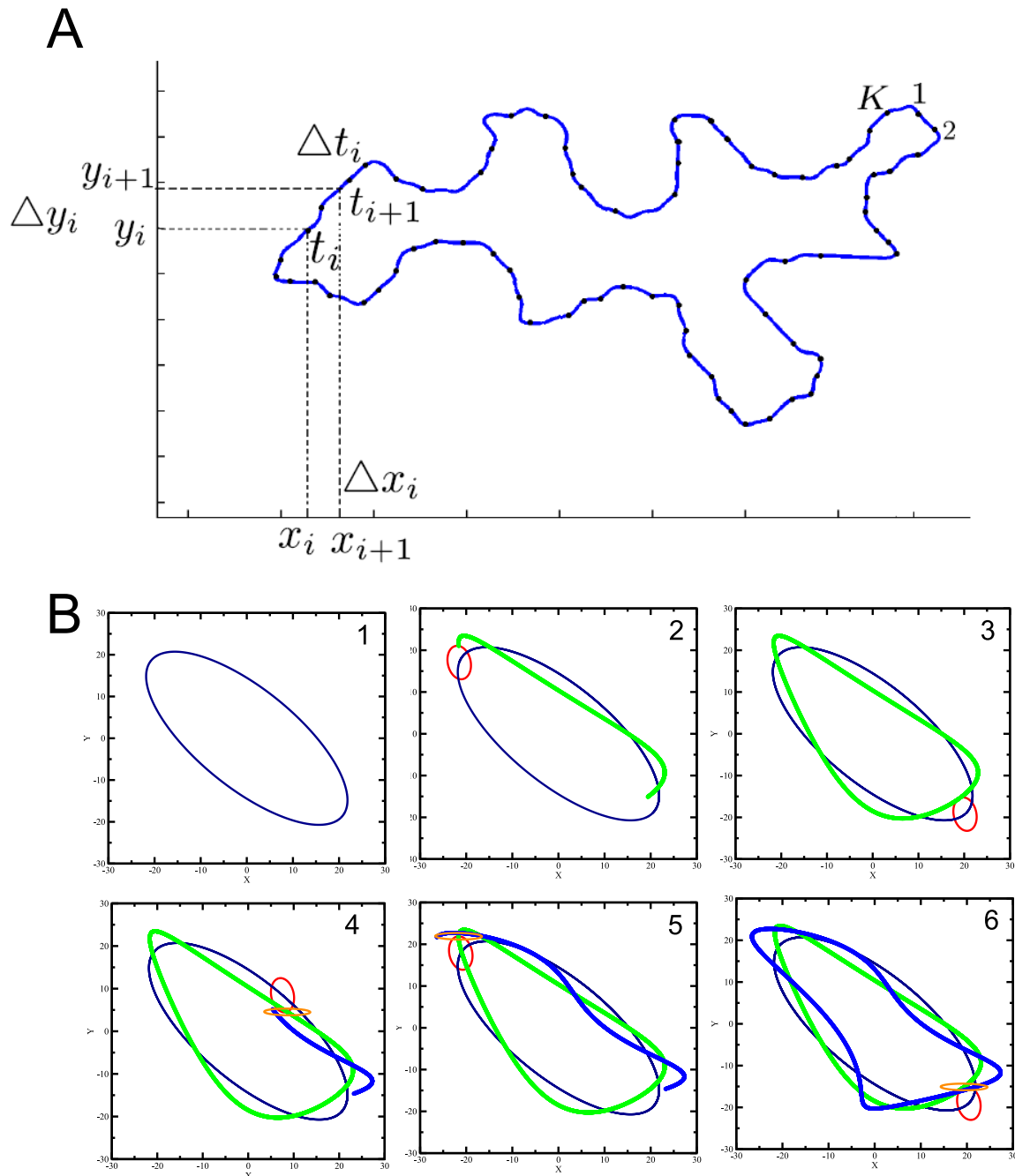


**Figure 2.5: Elliptical Fourier approximation to a cell contour.** (A) Cell contour and discretized displacements used to calculate the EFA-coefficients. (B) Sequential approximation of the cell's contour is shown: the first harmonic is an ellipse shown in blue (1), the second harmonic (2, red) rotates around the first and the summation of the them is shown in green; the third harmonic (4, orange) rotates around the second and the summation of the three is shown in a bold blue line (5-6). Also see Movie 1.1

harmonic, the main contribution was moved upwards one position (seventh mode, see Figure 2.6 and Figure 2.7). Indeed, this effect of presenting contributions on either the  $n + 1$ 'th or  $n - 1$ 'th mode depending on the relative direction of rotation of the first harmonic is a common phenomenon of objects that rotate around themselves while orbiting others

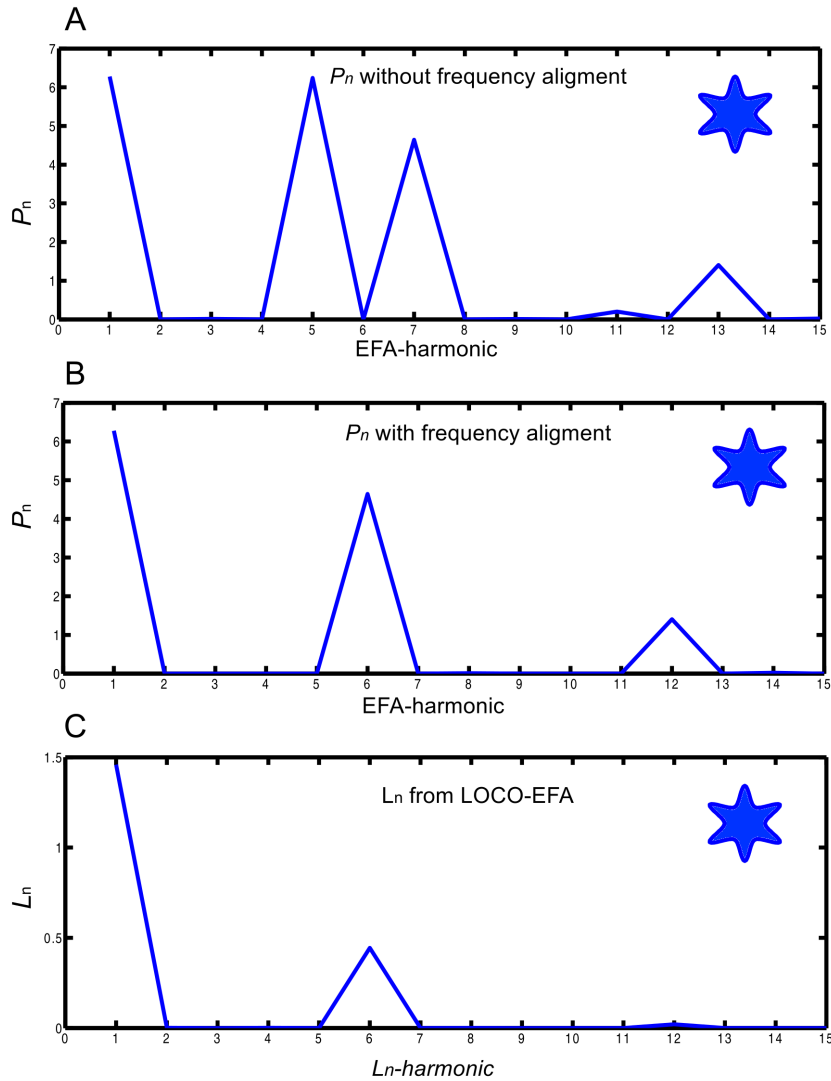


**Figure 2.6: Relative rotation effect on the frequency and harmonic number.** To align the frequency of the EFA-reconstruction and the real shape features, Diaz *et al.*, 1990 proposed to move the contribution of each harmonic ( $P_n$ ) to the  $n + 1$  or  $n - 1$  positions according with their rotatory direction. (A) Without alignment a sixth-sided shape (shown as an inset) has its  $P_n$  main contribution in the 5th and 7th harmonics ( $n - 1$  and  $n + 1$  sides). (B) Moving each  $P_n$  contribution  $n + 1$  or  $n - 1$  positions according with their rotatory direction aligns the 6th harmonic with the main frequency (this does not always holds, see main text). (C) LOCO-EFA method also aligns the main contribution with the corresponding harmonic number (for any shape, see main text).

(referred as rotatory effect hereafter). For example, the fact that our planet rotates around its axis in the opposite direction it rotates around the Sun makes the number of days we perceive in a year (from “sunrise to sunrise”, called sidereal days) not be the actual number of rotations it performs 365 (observed from “star-rise to star-rise”), but instead, 366.

The solution proposed in Diaz *et al.* (1990) for this discrepancy between harmonic frequency and morphological periodicities, was to displace each frequency by one position according to their rotatory direction with respect to the first harmonic. Then, if the ro-

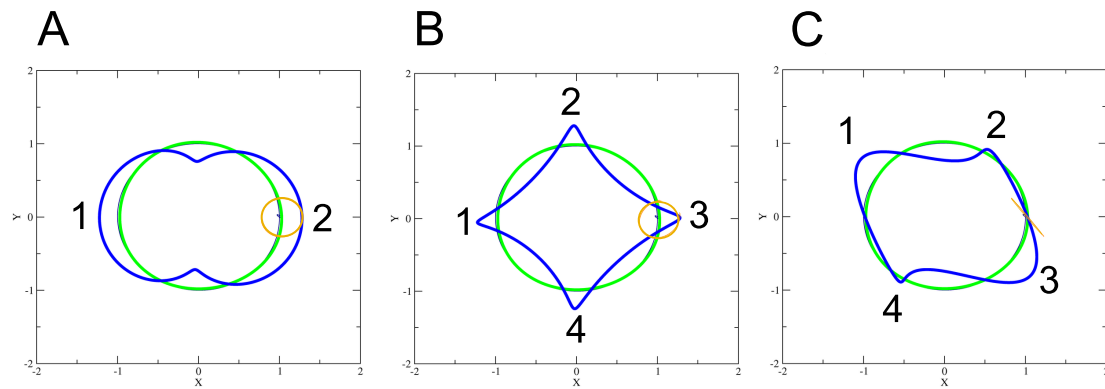


**Figure 2.7: The number of morphological protrusions (lobes) specified by a  $n$ th harmonics of EFA is influenced by the direction of rotation.** As an heuristic rule, it has been suggested that if the first harmonic and the  $n$ th harmonic are rotating in the same direction, they will generate a contour with  $n - 1$  protrusions; if the direction of rotation is opposite, a  $n + 1$  sided shape is generated. (A-C) Final shape generated (blue) from the sum of the first (green) and the third harmonic (orange). The third harmonic generates a shape with either 2 (A) or 4 lobes (B), depending on its direction of rotation in respect to the first mode. However, this heuristic rule of an  $n$ th-mode harmonic contributing solely to  $n + 1$  or  $n - 1$  (Diaz *et al.*, 1990) does not apply when the harmonic elliptic has a higher eccentricity: the final shape has  $n + 1$  protrusions (4 lobes) although the direction of rotation of the first and third harmonics were opposite (C). See also Movie 2.2-Movie 2.4.

tatory direction  $r_n$  of the  $n$ th elliptic harmonic (for  $n > 1$ ) coincides with the rotatory direction of the first ellipse  $r_1$  (i.e. when  $r_n$  and  $r_1$  have the same sign), the corresponding  $P_n$  value was shifted to the  $n - 1$ 'th position. Conversely, if the rotation  $r_n$  of  $n$ th (for  $n > 1$ ) mode was opposite to  $r_1$ , then  $P_n$  was moved to the  $n + 1$ 'th position (Figure 2.6). In other words, each EFA-coefficients ( $\alpha_n, \beta_n, \gamma_n, \delta_n$ ) were contributing to either  $n + 1$  or  $n - 1$  morphological periodical features (for example, 5 lobes).

However, this simple and heuristic solution is not satisfactory for interpreting shapes. In fact, an elliptical harmonic only contributes in such a pure fashion to either one or the other mode when the  $n$ th harmonic is a perfect circle (Figure 2.7A,B and Movie 2.2-Movie 2.4). However, when the aspect ratio of a harmonic ( $\lambda_{1n}/\lambda_{2n}$ ) is large (i.e the elliptical harmonic is very flat, deviating significantly from circular) the proposed rule fails to apply. Figure 2.7c illustrates this for the situation when the first harmonic and the third are rotating in the opposite direction (in relation to the first), yet instead of generating a contour of  $n - 1$  (2 protrusions as expected from the proposed rule), a 4-sided outline is generated. Thus, the proposed solution of moving the contribution of the  $n$ th mode ( $P_n$ ), to the  $n + 1$  or  $n - 1$  position, clearly does not work. This shortfall, threatens to render EFA unsuitable for biological shape interpretations, and as a consequence, renders its coefficients unusable for further statistical analysis. Surprisingly, the rotatory effect has never been taken into account in the standard normalization procedures when EFA was used in population analysis (Yoshioka *et al.*, 2005; Friess & Baylac, 2003; Neto *et al.*, 2006; Iwata *et al.*, 1998, 2010).

### 2.3.2 Contouring the Limitations: Lobe Contribution Elliptical Fourier Analysis (LOCO-EFA)

To capture the biologically relevant cell shape features overcoming the limitations of using  $P_n$  and the adjustments  $(n + 1, n - 1)$  depending on the direction of rotation, an alternative method coined Lobe Contribution Elliptical Fourier Analysis (LOCO-EFA) was developed. As the name suggests, it correctly maps the contribution of each harmonic to its morphological features. This is done by splitting each elliptic harmonic into two circles rotating in opposite direction as described below. Indeed, the previous and only available method (Diaz *et al.*, 1990) results in an overestimation or underestimation of a given harmonic contribution because it assumes that each harmonic is contributing solely to  $n + 1$  or  $n - 1$  morphological periodicities. Given that they can contribute to both  $n + 1$  and  $n - 1$  simultaneously, it is necessary to evaluate the contribution of each elliptic harmonic to these different modes to correctly assign it to the actual shape. Importantly, the LOCO-EFA method also eliminates the rotatory effect that was not considered before, ensuring an unique representation of a given shape.

For simplicity, it is useful to rewrite the EFA Eq. 2.1 in matrix form as

$$\begin{bmatrix} x(t) \\ y(t) \end{bmatrix} = \begin{bmatrix} \alpha_0 \\ \gamma_0 \end{bmatrix} + \sum_{n=1}^N \begin{bmatrix} \alpha_n & \beta_n \\ \gamma_n & \delta_n \end{bmatrix} \begin{bmatrix} \cos\left(\frac{2n\pi t}{T}\right) \\ \sin\left(\frac{2n\pi t}{T}\right) \end{bmatrix}, \quad (2.6)$$

where the infinite sum is truncated to the  $N$ th order harmonic.

Then, the EFA (2.6) can be expressed in matrix notation as

$$[X(t)] = [A_0] + \sum_{n=1}^N [A_n] [M_n(t)] \quad (2.7)$$

where:  $[X(t)]$  corresponds to the column  $\begin{bmatrix} x(t) \\ y(t) \end{bmatrix}$ ,

$[A_0]$  is the offset  $\begin{bmatrix} \alpha_0 \\ \gamma_0 \end{bmatrix}$ ,

$[A_n]$  corresponds to the elliptical coefficients  $\begin{bmatrix} \alpha_n & \beta_n \\ \gamma_n & \delta_n \end{bmatrix}$ , and

$[M_n(t)]$  refers to the column  $\begin{bmatrix} \cos\left(\frac{2n\pi t}{T}\right) \\ \sin\left(\frac{2n\pi t}{T}\right) \end{bmatrix}$ .

In summary, the LOCO-EFA method consists of three steps: 1) eliminate multiple representations of the same outline, 2) decompose each  $n$ th elliptic harmonic into two circles rotating in opposite directions and 3) find the  $L_n$  contribution for the  $N$  modes (Figure 2.8). These steps are described in the following.

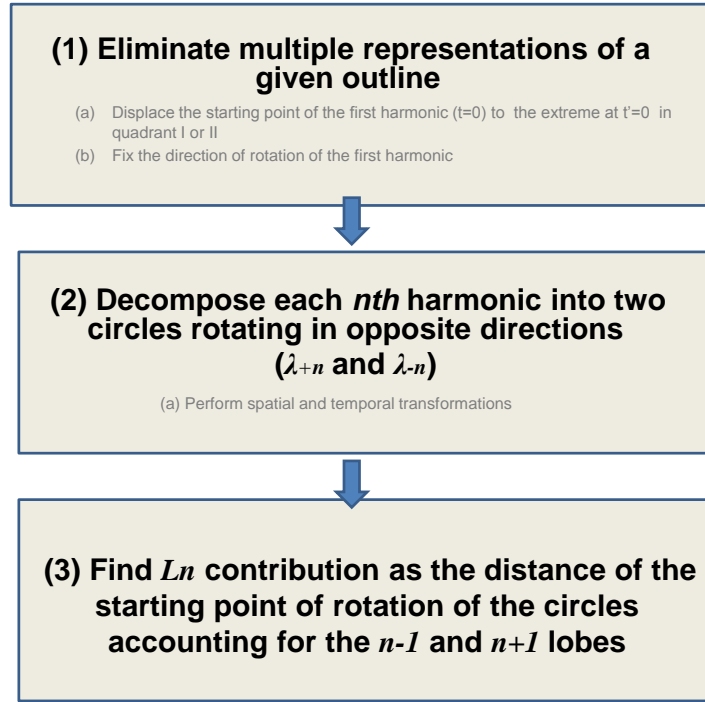


**Figure 2.8: Schematic diagram summarizing the LOCO-EFA method.**

### (1) Eliminate multiple representations of the same outline

There are three important sources of degeneracy in the EFA-coefficients that are eliminated before splitting the contribution of the EFA-harmonics into the  $n + 1$  and  $n - 1$  number of lobes. The first is that any contour can be drawn from any arbitrary starting point; thus, the approximation to the shape from different starting points will produce different sets of coefficients for the same shape because the elliptic harmonics will take different orientations (Kluh & Giardina, 1982). Therefore, the EFA-coefficients are transformed such that the starting point is aligned to one extreme of the semi-major axis (explained below). However, such normalization still renders two possible representations of the outline depending on which of the extremes of the semi-major axis the starting point is located at. The third source of degeneracy is that an outline can be drawn clockwise or counter-clockwise. Therefore, before decomposing the harmonics into its two contributing circular orbits, first it is ensured that there is no source of degeneracy remaining.

The process starts by first adjusting the starting point of the first harmonic. The starting point needs to be displaced by a certain temporal angle ( $\tau_1$ ) to coincide with  $t' = 0$  at the extreme of one of the semi-axis of the first harmonic (Figure 2.9). This temporal angle  $\tau_1$  is determined from the point  $(x_1, y_1)$ , determined by:

$$x_1 = \alpha_1 \cos \tau + \beta_1 \sin \tau \quad (2.8)$$

$$y_1 = \gamma_1 \cos \tau + \delta_1 \sin \tau \quad (2.9)$$

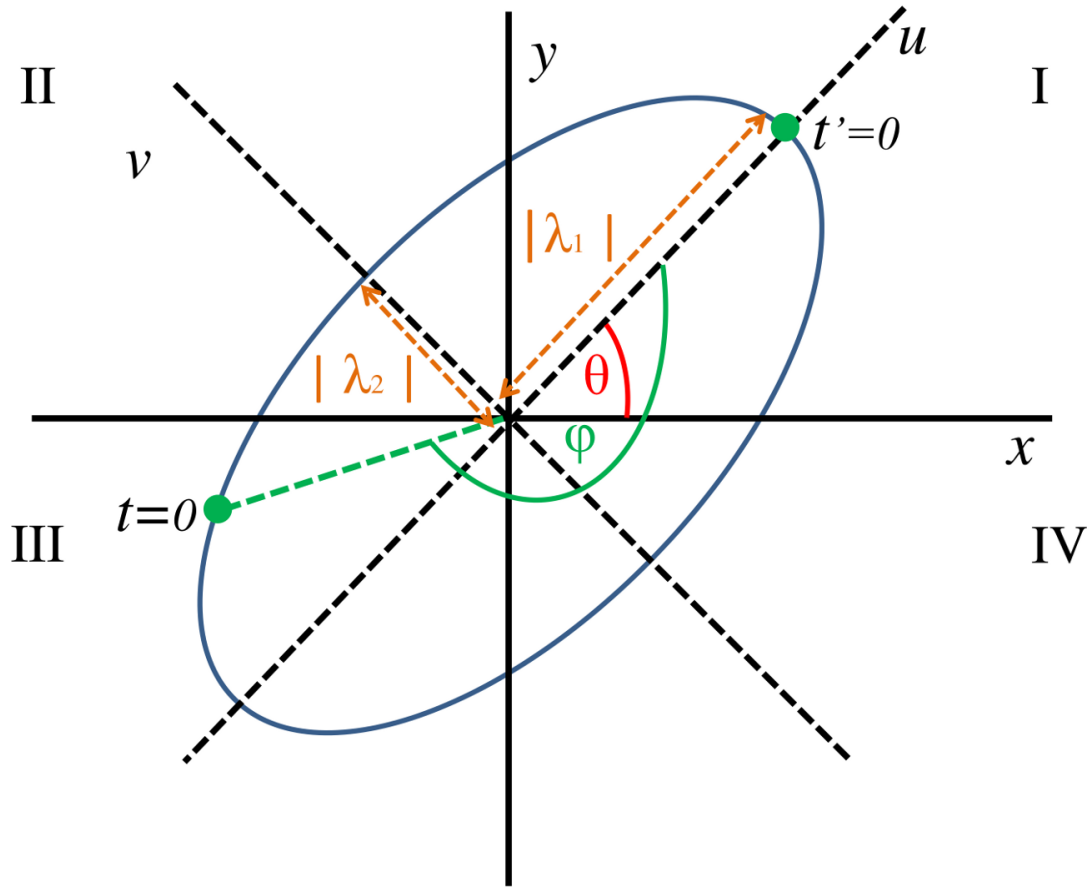


**Figure 2.9: Temporal and spatial transformations are performed to calculate the precise contribution of each  $n$ th harmonic.** The temporal angle ( $\varphi$ ) moves the starting point at  $t = 0$  within the outline to one extreme of the semi-major axis at  $t' = 0$ . The spatial angle ( $\theta$ ) gives the inclination of the  $n$ th harmonic. The EFA equation can be rewritten using the geometrical interpretation of the  $n$ th harmonics (semi-major and semi-minor axis  $\lambda_1$  and  $\lambda_2$ ) applying appropriate spatial and temporal transformations. The starting point of the first harmonic is moved accordingly with a temporal angle  $\tau_1^*$ . In contrast to  $\varphi$ , the temporal angle is fixed to the quadrants I and II to avoid multiple representations of the same outline (starting from one or the other extreme of the first harmonic).

Kuhl & Giardina, 1982 calculated  $\tau_1$  by differentiating the magnitude of the first harmonic ellipse  $E=(x_1^2 + y_1^2)^{0.5}$  and setting its derivative to zero, giving

$$\tau_1 = \frac{1}{2} \arctan \left( \frac{2(\alpha_1\beta_1 + \gamma_1\delta_1)}{\alpha_1^2 + \gamma_1^2 - \beta_1^2 - \delta_1^2} \right), \quad (2.10)$$

for  $-\pi < \tau_1 < \pi$ . An important remark is that in order to guarantee that this expression corresponds to an extreme of the semi-major axis (and not the semi-minor axis), it is necessary to permit different representations depending on the quadrant of the angle  $\tau_1$ . The function  $\arctan$  is limited to the interval  $[-\pi/2, \pi/2]$  and cannot uniquely define any possible angle. For this reason, it is necessary to implement the function four-quadrant inverse tangent ( $\text{atan2}$ ) used in a variety of computer languages (i.e, such that  $\text{atan2}(1,1) = \pi/4$  is different from  $\text{atan2}(-1,-1) = -3\pi/4$ ). This ensures that the tem-

poral angle  $\tau_1$  is located at the extreme of the semi-major axis, unambiguously.

However, there are still two ways to locate  $\tau = 0$  (one at each of the extremes of the semi-major axis of the first harmonic, at  $t' = 0$  and  $t' = \pi$ ) and therefore two distinct representations of the same outline. To avoid this dual representation that leads to degeneracy of the coefficients, the  $t'=0$  is always located in the first or second quadrant (I, II, Figure 2.9). This is achieved by adding  $\pi$  whenever the starting point  $\tau_1$  is located in the quadrants III and IV. To assess if the starting point is in those quadrants, the angle  $\varrho$  going from  $x$ -axis to  $\tau_1$  is calculated. This angle depends on the point  $x_1, y_1$  and can be calculated as

$$\varrho = \arctan\left(\frac{\gamma_1}{\alpha_1}\right), \quad (2.11)$$

for  $-\pi < \varrho < \pi$ . The starting point  $\tau_1$  is in the III or IV quadrant when  $(\tau_1 + \varrho) > \pi$  or  $0 > (\tau_1 + \varrho) > -\pi$ . In this case, the starting point angle becomes

$$\tau_1^* = \tau_1 + \pi, \quad (2.12)$$

otherwise,  $\tau_1^* = \tau_1$  (when the starting point is already located in the quadrants I or II).

Thus, the new EFA coefficients corrected for the starting point become

$$\begin{bmatrix} \alpha_n^* & \beta_n^* \\ \gamma_n^* & \delta_n^* \end{bmatrix} = \begin{bmatrix} \alpha_n & \beta_n \\ \gamma_n & \delta_n \end{bmatrix} \begin{bmatrix} \cos(n\tau_1^*) & -\sin(n\tau_1^*) \\ \sin(n\tau_1^*) & \cos(n\tau_1^*) \end{bmatrix}. \quad (2.13)$$

Finally, the direction of rotation of the first harmonic is fixed to rotate counter-clockwise ( $r_1 > 0$ ). Besides removing redundancy by restricting the freedom of the choice of the overall rotation of the contour, this transformation likewise guarantees a unique correspondence between the contribution of each subsequent harmonic and the morphological features. When the direction of the first harmonic is clockwise ( $r_1 < 0$ ), we thus invert the direction of rotation of all the ellipses in order to maintain their inter-relationships. This can be done by running "time" backwards,

$$\begin{bmatrix} x(-t) \\ y(-t) \end{bmatrix} = \begin{bmatrix} \alpha_n^* & \beta_n^* \\ \gamma_n^* & \delta_n^* \end{bmatrix} \begin{bmatrix} \cos\left(\frac{2n\pi(-t)}{T}\right) \\ \sin\left(\frac{2n\pi(-t)}{T}\right) \end{bmatrix} \Rightarrow \begin{bmatrix} \alpha_n^* & \beta_n^* \\ \gamma_n^* & \delta_n^* \end{bmatrix} \begin{bmatrix} \cos\left(\frac{2n\pi t}{T}\right) \\ -\sin\left(\frac{2n\pi t}{T}\right) \end{bmatrix} \Rightarrow \begin{bmatrix} \alpha_n^* & -\beta_n^* \\ \gamma_n^* & -\delta_n^* \end{bmatrix} \begin{bmatrix} \cos\left(\frac{2n\pi t}{T}\right) \\ \sin\left(\frac{2n\pi t}{T}\right) \end{bmatrix}. \quad (2.14)$$

Note that, as the proposed method uses information of the semi-axis of each harmonic, it is invariant to the orientation of the elliptic harmonic and offset of the contour. However, if desired, it is possible to rotate the contour to be parallel to the  $x$ -axis as described in the appendix.

For simplicity of notation in the rest of the manuscript I refer to the  $[A_n]$  matrix, which elements have been normalized for starting point and direction of rotation of the first harmonic as follows:

$$\begin{bmatrix} \alpha_n^* & \beta_n^* \\ \gamma_n^* & \delta_n^* \end{bmatrix} \equiv \begin{bmatrix} a_n & b_n \\ c_n & d_n \end{bmatrix} \equiv [A_n]. \quad (2.15)$$

The corrections for the starting point and direction of rotation of the first harmonic discussed in this first step are aimed to eliminate multiple representations of the same outline. After all possible sources of redundancy have been eliminated, the next step of the LOCO-EFA method is aimed to decompose each elliptic harmonic into two circles rotating in opposite directions.

## (2) Decompose each $n$ th elliptic harmonic into two circles rotating in opposite directions

In order to explain how the contribution of  $n$ th harmonic to a given morphological mode was achieved, it is useful to rewrite the EFA matrix (Eq. 2.6) substituting the normalized coefficients  $(a_n, b_n, c_n, d_n)$  by the axes of the  $n$ th ellipse ( $\lambda_{1n}$  and  $\lambda_{2n}$ ). This corresponds to the diagonalization of the  $[A_n]$  matrix, explained below.

For this purpose, it is necessary to introduce spatial and temporal transformations given by the operators  $[\psi_S]$  and  $[\psi_T]$ , respectively. The temporal operator is defined as

$$[\psi_T] = \begin{bmatrix} \cos \phi & -\sin \phi \\ \sin \phi & \cos \phi \end{bmatrix}, \quad (2.16)$$

and correspondingly, the spatial operator is

$$[\psi_S] = \begin{bmatrix} \cos \theta & -\sin \theta \\ \sin \theta & \cos \theta \end{bmatrix}, \quad (2.17)$$

where  $\phi$  is the temporal angle and  $\theta$  corresponds to the spatial angle (Figure 2.9).

The temporal angle,  $\phi_n$  (similarly to Eq. 2.10), corresponds to:

$$\phi_n = \frac{1}{2} \arctan \left( \frac{2(a_n b_n + c_n d_n)}{a_n^2 + c_n^2 - b_n^2 - d_n^2} \right). \quad (2.18)$$

The spatial angle  $\theta_n$  (see Figure 2.9) can be calculated only after the temporal modification as:

$$\theta_n = \arctan \frac{c'_n}{a'_n}, \quad (2.19)$$

where  $c'_n$  and  $a'_n$  are the coefficients after temporal transformation, see below.

Continuing with the diagonalization procedure, Eq. 2.7 can also be rewritten as:

$$[X(t)] = [A_0] + \sum_{n=1}^N [\psi_{S_n}] [\psi_{S_n}^{-1}] [A_n] [\psi_{T_n}] [\psi_{T_n}^{-1}] [M_n(t)] \quad (2.20)$$

where  $[\psi_{S_n}] [\psi_{S_n}^{-1}]$  and  $[\psi_{T_n}] [\psi_{T_n}^{-1}]$  correspond to the identity matrix. For simplicity, as the term  $[A_0]$  represent just the offset of the initial contour, it will be omitted in the rest of

the description.

Likewise, Eq. 2.20 can be rewritten as:

$$[X(t)] = \sum_{n=1}^N [\psi_{S_n}] [\Lambda_n] [\psi_{T_n}^{-1}] [M_n(t)]; \quad (2.21)$$

from where we can identify the diagonal matrix which its non-zero entries correspond to the semi-axes of the  $n$ th ellipse as:

$$[\Lambda_n] = [\psi_{S_n}^{-1}] [A_n] [\psi_{T_n}] = \begin{bmatrix} \lambda_{1n} & 0 \\ 0 & \lambda_{2n} \end{bmatrix}, \quad (2.22)$$

The temporal transformation (given by  $\psi_{T_n}$ ) displaces the starting point of each harmonic at  $t' = 0$  ( $a'_n, b'_n, c'_n, d'_n$ ) to coincide with the extreme of the semi-major axis of each elliptic harmonic while the spatial transformation ( $\psi_{S_n}^{-1}$ ) yields the length of the semi-major  $\lambda_{1n}$  and semi-minor axis  $\lambda_{2n}$  (Eq. 2.22).

The diagonalization rewrites the EFA Eq. 2.7 in a manner that the contribution of each harmonic can be easily separated to correctly map to morphological features as shown below. Eq. 2.21 corresponds to:

$$\begin{bmatrix} x(t) \\ y(t) \end{bmatrix} = \sum_{n=1}^N \begin{bmatrix} \cos \theta & -\sin \theta \\ \sin \theta & \cos \theta \end{bmatrix} \begin{bmatrix} \lambda_{1n} & 0 \\ 0 & \lambda_{2n} \end{bmatrix} \begin{bmatrix} \cos \phi & \sin \phi \\ -\sin \phi & \cos \phi \end{bmatrix} \begin{bmatrix} \cos \left( \frac{2n\pi\tau}{T} \right) \\ \sin \left( \frac{2n\pi\tau}{T} \right) \end{bmatrix}. \quad (2.23)$$

The diagonal matrix containing the length of the semi-axes of each  $n$ th mode, can be decomposed into two diagonal matrices that correspond to circular orbits of opposite direction of rotation that, in turn, account for the contribution of  $n + 1$  and  $n - 1$  morphological features :

$$\begin{bmatrix} x(t) \\ y(t) \end{bmatrix} = \sum_{n=1}^N \begin{bmatrix} \cos \theta & -\sin \theta \\ \sin \theta & \cos \theta \end{bmatrix} \left( \begin{bmatrix} \lambda_{+n} & 0 \\ 0 & \lambda_{+n} \end{bmatrix} + \begin{bmatrix} \lambda_{-n} & 0 \\ 0 & -\lambda_{-n} \end{bmatrix} \right) \begin{bmatrix} \cos \phi & \sin \phi \\ -\sin \phi & \cos \phi \end{bmatrix} \begin{bmatrix} \cos \left( \frac{2n\pi\tau}{T} \right) \\ \sin \left( \frac{2n\pi\tau}{T} \right) \end{bmatrix}, \quad (2.24)$$

where  $\lambda_{+n}$  and  $\lambda_{-n}$  are the radii of each circle (Figure 2.11).

Summing up the diagonal matrices in Eq. 2.24, yields

$$\begin{bmatrix} x(t) \\ y(t) \end{bmatrix} = \sum_{n=1}^N \begin{bmatrix} \cos \theta & -\sin \theta \\ \sin \theta & \cos \theta \end{bmatrix} \begin{bmatrix} \lambda_{+n} + \lambda_{-n} & 0 \\ 0 & \lambda_{+n} - \lambda_{-n} \end{bmatrix} \begin{bmatrix} \cos \phi & \sin \phi \\ -\sin \phi & \cos \phi \end{bmatrix} \begin{bmatrix} \cos \left( \frac{2n\pi\tau}{T} \right) \\ \sin \left( \frac{2n\pi\tau}{T} \right) \end{bmatrix}. \quad (2.25)$$

in which the major and minor axes of each elliptic harmonic are:

$$\lambda_{1n} = \lambda_{+n} + \lambda_{-n} \quad (2.26a)$$

$$\lambda_{2n} = \lambda_{+n} - \lambda_{-n} \quad (2.26b)$$

and hence, the radii of each opposite-rotating circle is given by

$$\lambda_{+n} = (\lambda_{1n} + \lambda_{2n}) / 2 \quad (2.27)$$

$$\lambda_{-n} = (\lambda_{1n} - \lambda_{2n}) / 2. \quad (2.28)$$

To find the radii of each rotating circle  $\lambda_{+n}$  (counter-clockwise) and  $\lambda_{-n}$  (clockwise), a new set of coefficients ( $a_{+n}, b_{+n}, c_{+n}, d_{+n}$  and  $a_{-n}, b_{-n}, c_{-n}, d_{-n}$ , respectively) is calculated. As they are circles, the length of the radii are the same:

$$a_{jn} = d_{jn} = \lambda_{jn}, \text{ for } j = +, - \quad (2.29)$$

and

$$b_{jn} = c_{jn} = 0, \quad (2.30)$$

where  $j = +, -$  accounts for the two rotating circles (counter-clockwise and clockwise, respectively).

To find the contribution of each circle to a given shape, it is necessary to approximate the original outline,  $x(t), y(t)$ , using the circles  $\lambda_{n+}$  and  $\lambda_{n-}$ . For this purpose, it is required to complete the transformations using the spatial ( $\theta_n$ ) and temporal angle ( $\phi_n$ ) calculated before. Such transformations are clearly seen when Eq. 2.24 is rewritten in matrix form as:

$$[X(t)] = \sum_{n=1}^N [\psi_{S_n}] [\Lambda_{+n} + \Lambda_{-n}] [\psi_{T_n}^{-1}] [M_n(t)], \quad (2.31)$$

and

$$[X(t)] = \sum_{n=1}^N [\psi_{S_n}] [\Lambda_{+n}] [\psi_{T_n}^{-1}] [M_n(t)] + \sum_{n=1}^N [\psi_{S_n}] [\Lambda_{-n}] [\psi_{T_n}^{-1}] [M_n(t)], \quad (2.32)$$

where the first term on the right side refers to the contribution of the shape approximation coming from  $n + 1$  "lobes" and the second term is the contribution of  $n - 1$  "lobes".

Then, the next steps in the LOCO-EFA method corresponds to the operations  $[\psi_{S_n}] [\Lambda_{+n}] [\psi_{T_n}^{-1}]$  and  $[\psi_{S_n}] [\Lambda_{-n}] [\psi_{T_n}^{-1}]$ , that for clarity are done in two steps.

First, rotate  $\theta_n$  to get back the original spatial angle,

$$\begin{bmatrix} a'_{jn} & b'_{jn} \\ c'_{jn} & d'_{jn} \end{bmatrix} = \begin{bmatrix} \cos \theta_n & -\sin \theta_n \\ \sin \theta_n & \cos \theta_n \end{bmatrix} \begin{bmatrix} a_{jn} & b_{jn} \\ c_{jn} & d_{jn} \end{bmatrix} \text{ for } j = +, -. \quad (2.33)$$

Secondly, to complete the rotational operations, rotate by  $\phi_n$  original temporal angle, that is:

$$\begin{bmatrix} a''_{j_n} & b''_{j_n} \\ c''_{j_n} & d''_{j_n} \end{bmatrix} = \begin{bmatrix} a'_{j_n} & b'_{j_n} \\ c'_{j_n} & d'_{j_n} \end{bmatrix} \begin{bmatrix} \cos \phi_n & \sin \phi_n \\ -\sin \phi_n & \cos \phi_n \end{bmatrix} \text{ for } j = +, -. \quad (2.34)$$

Thus, a new set of coefficients  $(a''_{j_n}, b''_{j_n}, c''_{j_n}, d''_{j_n})$  that account for two circles rotating in opposite directions are obtained (these coefficients can be used to approximate the original contour, as shown below).

**(3) Find the  $L_n$  contribution as the distance of the starting point of the  $n - 1$  and  $n + 1$  rotating circles**

Finally, we can obtain the  $n$ th morphological contribution of each mode,  $L_n$ , which originate from the two circles rotating in opposite directions, one from the  $n$ th + 1 mode ( $\lambda_{+n+1}$ ) and the other from the  $n$ th - 1 mode ( $\lambda_{-n-1}$ )(see Figure 2.11).

Obviously, there are three exceptions to this: 1)  $L_1$ , whose contribution comes solely from  $\lambda_{+1}$ , 2) the last  $L_N$ , that comes solely from  $\lambda_{-N-1}$  and 3)  $L_{N+1}$  that comes from  $\lambda_{-N}$ , where  $N$  accounts for the total number of harmonics considered.

The exact contribution of each circle to  $L_n$ -th morphological features is related to the starting position of both circles, which is calculated as,

$$\phi_{j_n} = \arctan \left( \frac{c''_{j_{m+1}}}{a''_{j_{m+1}}} \right) \text{ for } j = +, \quad (2.35)$$

and

$$\phi_{j_n} = \arctan \left( \frac{c''_{j_{m-1}}}{a''_{j_{m-1}}} \right) \text{ for } j = -, \quad (2.36)$$

The contribution of the two counter-rotating circles to the reconstruction of the outline will depend on their starting points. Figure 2.10 illustrates the effect of the starting point of rotation of the pair of circles in polar coordinates. For example, if the starting point of each circle is  $180^\circ$  opposite they strengthen each other (Figure 2.10A). Conversely, if they start rotating at the same place, as their rotation is opposite, they cancel each other (Figure 2.10B).

Therefore,  $L_n$  is given by the distance of  $\lambda_{+n+1}$  and  $\lambda_{-n-1}$  starting points of rotation, illustrated in Figure 2.11 (yellow line).

The expression of this relation is given from the Law of Cosines:

$$L_n = \sqrt{\lambda_{+n+1}^2 + \lambda_{-n-1}^2 + 2\lambda_{+n+1}\lambda_{-n-1}\cos(\phi_{+n} - \phi_{-n})}. \quad (2.37)$$

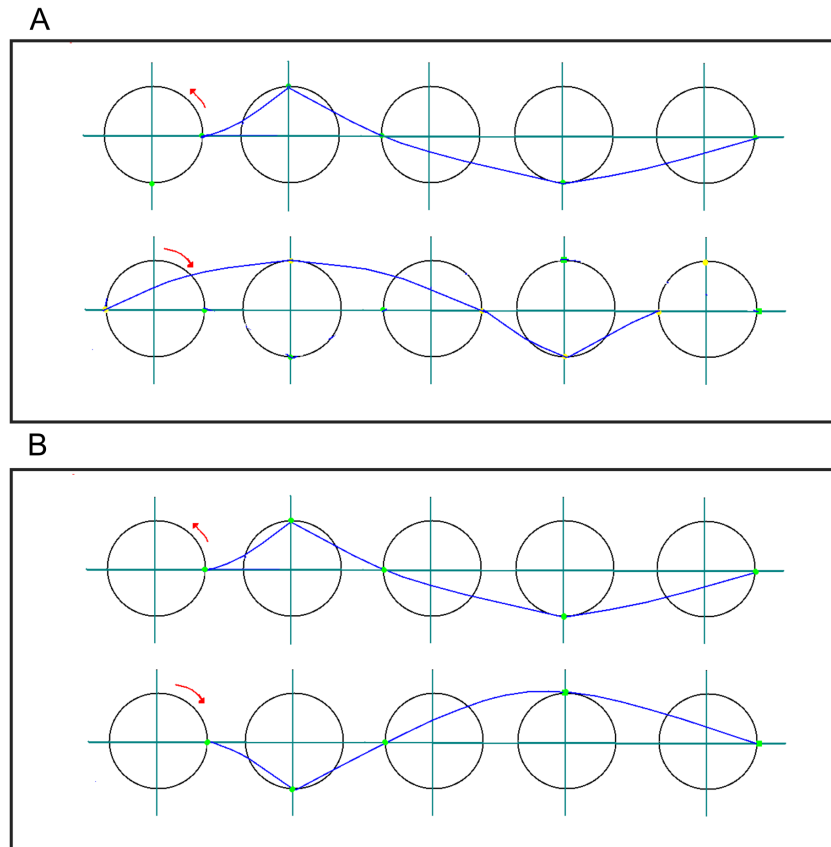


**Figure 2.10: Effect of the rotation-starting point of each pair of circles for shape reconstruction.** Polar coordinates are shown (in the x-axis is the arc-length and in the y-axis is the radius) for a pair of circles rotating in opposite directions. A) If the starting point of rotation of each circle is 180 degree opposite, they enhance each other. B) Conversely, if they start rotating at the same place they cancel each other.

In summary, the LOCO-EFA method consists in: 1) eliminating any source of degeneracy in the EFA-coefficients, 2) decomposing each elliptic harmonic into two circles rotating in opposite directions ( $\lambda_{+n}$  and  $\lambda_{-n}$ ), and therefore contributing to  $n + 1$  and  $n - 1$  number of lobes (i.e. morphological features), and 3) calculating the offset between starting points of these two circles derived from each ellipse to estimate the  $L_n$ th lobe-contribution. To eliminate the effect of cell area (for example, to compare populations of cells), it is desirable to normalize by the cell size by dividing each  $L_n$  value by the square root of the real cell area. In addition, it is possible to quantify not only the number of protrusions of a shape, and how significant they are for the shape, but also qualitative aspects, such as how “roundy” or “pointy” a protrusion is using the LOCO-EFA circles (see description in appendix).

Importantly, while the LOCO-EFA method continues to approximate the original shape by its coefficients, unlike the traditional EFA, it can also precisely indicate the correct shape contribution of each harmonic. This is exemplified in Figure 2.12, where an hexagon is approximated using both EFA and LOCO-EFA. Note that whereas EFA recovers an spurious shape using the first 5 modes and it is only when the 7th harmonic is added that

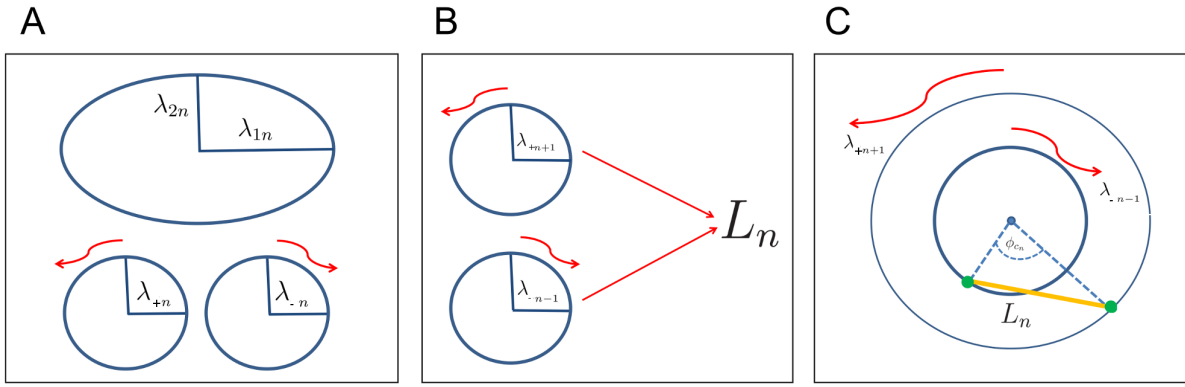


**Figure 2.11: Each EFA-harmonic is decomposed into two circles to obtain the contribution of the  $L_n$  mode.** (A) Each elliptic harmonic is decomposed into two circles rotating in opposite directions. (B) Each  $L_n$  is composed from the contribution of a  $n + 1$  circle rotating counter-clockwise and  $n - 1$  circle rotating clockwise. (C) The combined contribution of the two rotating circles with diameter  $\lambda_{+n+1}$  and  $\lambda_{-n-1}$  to  $L_n$  (yellow line), is given by the offset of their starting points (green dots).

it reconstructs the original hexagonal shape (Figure 2.12A), LOCO-EFA retrieve the correct shape at the 6th term (Figure 2.12B). The correct approximation of a shape outline achieved by the LOCO-EFA is calculated as:

$$\begin{bmatrix} x(t) \\ y(t) \end{bmatrix} = \begin{bmatrix} (a''_{+2}) & (b''_{+2}) \\ (c''_{+2}) & (d''_{+2}) \end{bmatrix} \begin{bmatrix} \cos\left(\frac{2n\pi t}{T}\right) \\ \sin\left(\frac{2n\pi t}{T}\right) \end{bmatrix} + \sum_{n=2}^N \begin{bmatrix} (a''_{+n+1} + a''_{-n-1}) & (b''_{+n+1} + b''_{-n-1}) \\ (c''_{+n+1} + c''_{-n-1}) & (d''_{+n+1} + d''_{-n-1}) \end{bmatrix} \begin{bmatrix} \cos\left(\frac{2n\pi t}{T}\right) \\ \sin\left(\frac{2n\pi t}{T}\right) \end{bmatrix} + \sum_{N+1}^{N+1} \begin{bmatrix} (a''_{-N-1}) & (b''_{-N-1}) \\ (c''_{-N-1}) & (d''_{-N-1}) \end{bmatrix} \begin{bmatrix} \cos\left(\frac{2n\pi t}{T}\right) \\ \sin\left(\frac{2n\pi t}{T}\right) \end{bmatrix} \quad (2.38)$$

where  $a''_{j_n}, b''_{j_n}, c''_{j_n}, d''_{j_n}$  are the coefficients specifying  $j = +, -$  opposite-rotating circles after appropriate temporal and spatial transformations that I will refer as LOCO-EFA coefficients or  $L_n$ -mode for short.

Importantly, the LOCO-EFA method permits to distinguish the contribution of each harmonic to  $n + 1$  and  $n - 1$  shape features (i.e. lobes) correctly. This provides a complete description of both the number of lobes and the degree of “waviness” (or amplitude) that can be used to fully characterize and quantify the intrinsic cell shape properties, irrespective of cell area, spacing between sampling points, different rotations of the cell (Figure 2.13A,B) or direction of the EFA approximation. However, it is important to consider that changes in the resolution of the image could lead to differences in the LOCO-EFA metrics (Figure 2.13C,D).

## 2.4 Quantitative characterization of cell shape using LOCO-EFA

In this section, I illustrate the characterization of the shape using  $L_n$  coefficients and introduce additional metrics derived from the LOCO-EFA method to help quantify different aspects of “cell shape complexity” (a notion that I will define more precisely below). First,

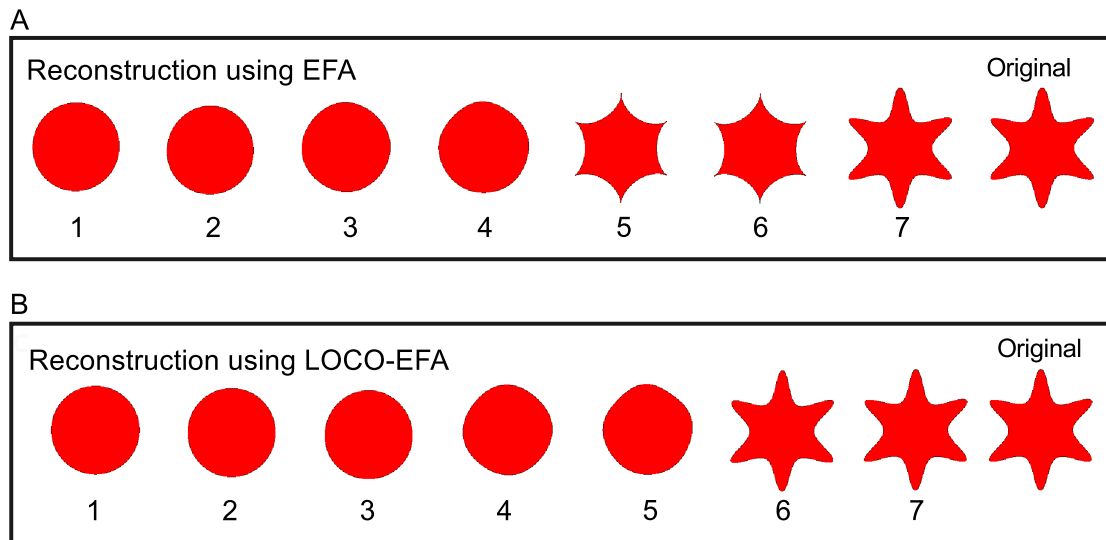


**Figure 2.12: Comparison of approximation of closed contour using EFA and LOCO-EFA.** Although both approximations converge to the original hexagonal shape, the reconstruction using EFA harmonics (A) recovers a spurious shape after adding the 5th harmonic and it is only when the 7th harmonic is summed that the original shape is recovered, whereas the reconstruction using LOCO-EFA modes (B) recalls the original shape precisely at the 6th mode, matching with the number of protrusions (lobes). The number of modes used in the reconstruction are indicated by the number below each shape (both reconstructions were truncated at  $N = 15$  modes, data not shown).

I apply the method to well characterized geometrical shapes. This illustrates how the coefficients relate to the shape. Next, I generate geometrical shapes of differing degrees of asymmetry, to gain an intuition on how the LOCO-EFA coefficients ( $L_n$ ) match those less well-defined shapes. Finally, I apply the LOCO-EFA method and its measures to confocal image outlines of real biological cells, which present much less symmetric and stereotypical geometrical shapes.

### 2.4.1 Interpreting geometrical shapes with $L_n$

The  $L_n$  coefficients provide information about the composition of each morphological periodicity contributing to the shape: for example, an hexagon will have the highest amplitude of  $L_n$  exactly at  $n = 6$ , i.e.  $L_6$ . Thus,  $L_n$  profiles reflect the geometrical nature of the shape being considered (Figure 2.14A-J).

Moreover, the  $L_n$  numbers provide information regarding the “degree of waviness” (or amplitude). Cells of similar shapes (in terms of number of lobes) but presenting different amplitudes in the extent of their protrusions, will also present different values in the main mode  $L_n$  corresponding to that  $n$ th-morphological periodicity. Figure 2.15 shows how different 6-sided shapes (A-F) present different  $L_6$  values (G), in accordance with the amplitude of its protrusions. Note that if the shapes are not symmetrical (Figure 2.15E-F), new peaks in the  $L_n$  profile appear. Real cells (such as pavement cells of *Arabidopsis*

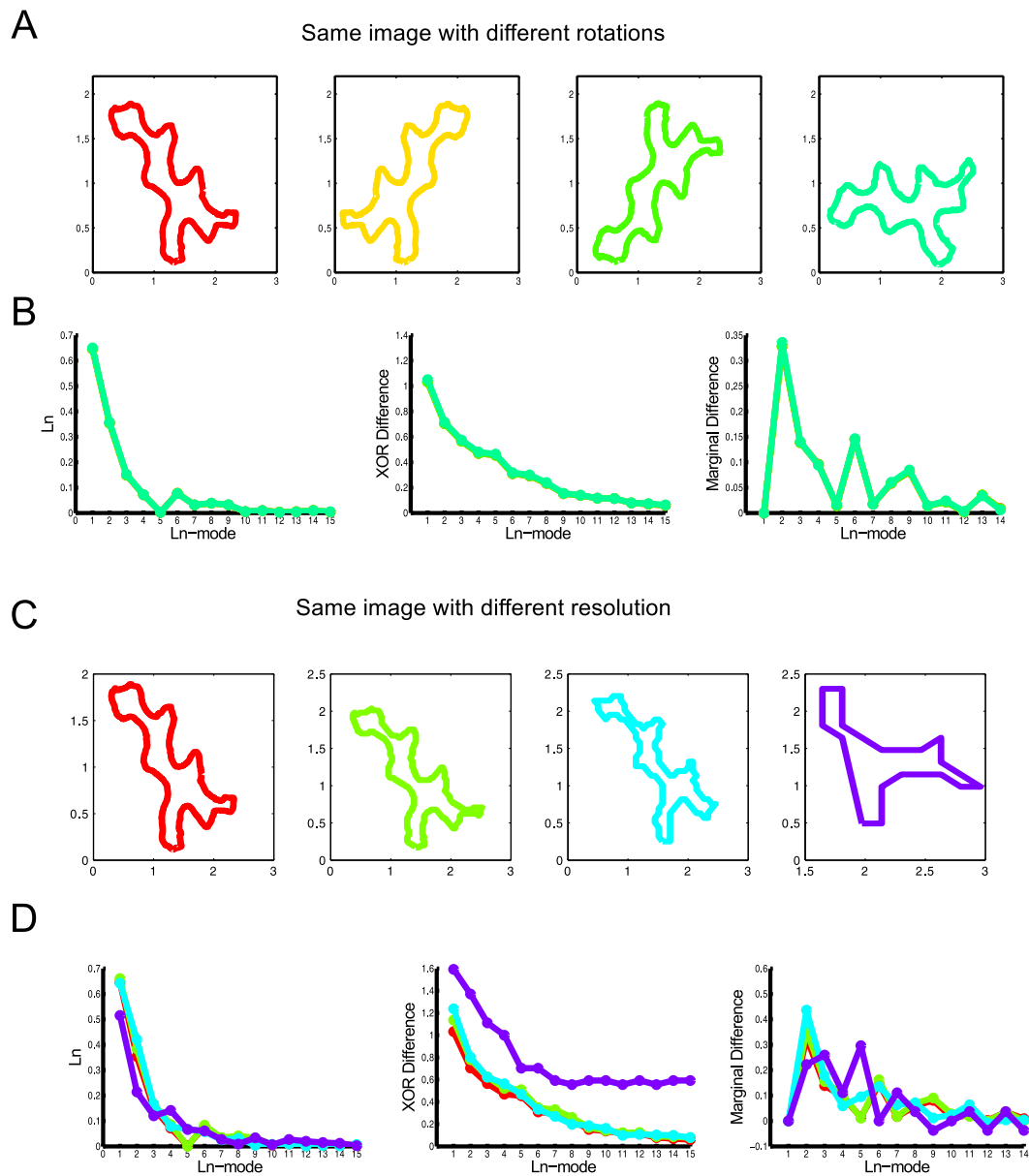


**Figure 2.13: LOCO-EFA is invariant to different rotations of the image, but it is sensitive to the image resolution.** A) An image of a real cell was rotated in different manners and the LOCO-EFA method was applied to each image separately. B) The  $L_n$  numbers and other derived metrics (see main text) showed invariance regarding these rotations. C) The resolution of the original image was modified, such that the number of points decreased from 1104 to 253, 108 and 27 (from left to right, respectively). D) The  $L_n$  numbers and the associate metrics can vary depending on the resolution. Note, however, that the coefficients differ more as the original shape gets more distorted (in accordance with the “new” shape).

*thaliana*, Figure 2.15F) more closely resemble this situation: their  $L_n$  landscape is typically characterized by multiple peaks (Figure 2.15G). This is because non-symmetrical cells with a given number of protrusions placed non-periodically can also be interpreted as different protrusion frequencies superimposed (i.e. one might count nine total biological lobes on a cell, which should correspond to a peak at  $L_9$ , if the lobes are distributed in

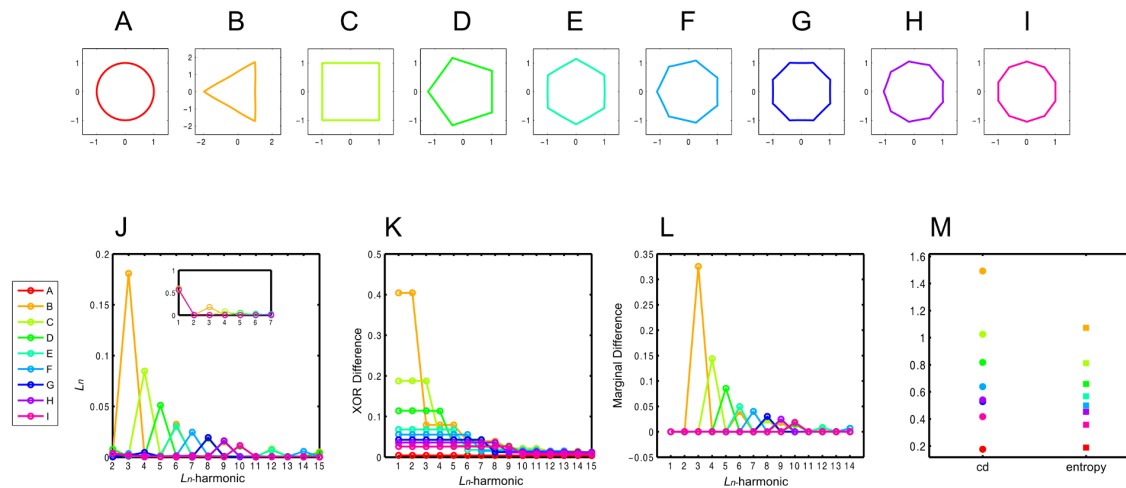


**Figure 2.14: Interpreting LOCO-EFA derived measures for geometrical shapes.** (A-I) Geometrical shapes with symmetrical and well defined shapes. Lower panel: the  $L_n$ , XOR, and Marginal difference profiles (J, K and L respectively) are shown. For each geometric shape, a clear peak appears in the Lobe-number ( $L_n$ ) and marginal difference profile (J and L) corresponding to the main contributor to the shape, which in the LOCO-EFA, coincides with the number of protrusions (sides or lobes). The rightmost panel (M) shows the cumulative difference (cd) and entropy of the circle and other shapes.

pentagonal clustered fashion, this would lead to an additional peak at  $L_5$ , whilst superimposed on a triangular shaped basis of a cell, leading to a  $L_3$  contribution, and so forth).

From the  $L_n$  profiles, a series of other informative measurements regarding shape can be derived (Figure 2.16) and are described next.

Complementary to the magnitude of each individual  $L_n$  number, the cell shape complexity can be estimated using the information of the approximation to the original shape using  $N$  LOCO-EFA modes. This can be done by addressing the question: how relevant is each higher order  $L_n$ -mode for explaining the shape? This can be answered by calculating the difference of the original shape with the reconstruction after  $N$  LOCO-EFA harmonics (XOR original and reconstructed, see Figure 2.16). Importantly, this measure is just meaningful when the reconstruction is performed using the  $L_n$ -modes, and not with the EFA alone (see discrepancy in the reconstruction in Figure 2.12). In this context, the more “complex” shape is the one in which higher order LOCO-EFA modes are needed to obtain a good match between the reconstitution and the real shape (i.e.  $XOR = 0$ ). Using this criteria, a circular cell, perfectly reconstituted with only the contribution of  $n = 1$  becomes the least complex shape (Figure 2.14A). While those presenting higher number of heterogeneous lobes, yield increasingly higher numbers for the  $XOR = 0$  measure (Figure 2.14B-I, K and Figure 2.15A-F, H).

Moreover, the area under the curve of the XOR in function of  $L_n$ -mode number, also

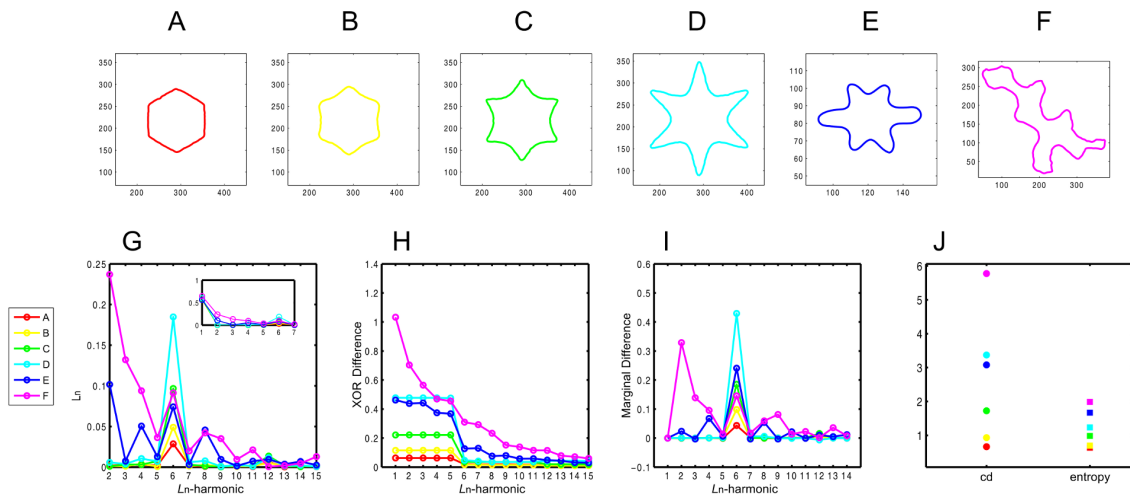


**Figure 2.15: Interpreting LOCO-EFA derived measures for similar shapes of different protrusion amplitudes and asymmetrical shapes.** Symmetrical shapes of increasing protrusion amplitude (A-D) also present an increasing  $L_n$ -amplitude value (here at  $L_6$ , G), XOR value (H) and marginal difference value (I) in the dominant mode. Non-symmetrical shapes (E,F) will have more than one peak in the  $L_n$  landscape and Marginal Difference profile and more modes will be needed to recapitulate the original shape, i.e XOR profiles are altered (G,H and I). Moreover, shapes presenting higher protrusion amplitudes and asymmetries will also present increased values in the cumulative difference (cd) and entropy measures (J).

called *cumulative difference* (cd), will be larger for more complex cells. Hence, the closer to a circle a shape is (described with the first mode), the lower the value of cumulative difference (Figure 2.14A, M and Figure 2.15A, J). Conversely, as the morphological protrusions increase in number (Figure 2.14B-I, M) or become higher in amplitude (Figure 2.15A-F, J), the cumulative difference also increases because higher order modes are required to approximate the shape.

Note that the XOR profile typically does not change smoothly, but there are some modes that contribute more in capturing the main features of the shape. Thus, the rate of change of XOR in relation to the addition of a new mode,  $\frac{d(XOR)}{dL_n}$ , coined *marginal difference*, gives information about the dominant modes (Figure 2.14L and Figure 2.15I). As mentioned before, cell shapes may consist of a combination of different modes (Figure 2.15E-F). This is directly reflected in the multiple peaks within the  $L_n$  landscape, and clearly seen in the marginal difference profiles (Figure 2.15I). The marginal difference helps identify which modes are the most relevant for the shape.

However, one can argue that the complexity of the shape should not be regarded as only proportional to the number of protrusions. For example, for two cells each presenting 5 lobes, the one which is most symmetric and star-shaped, would seem less complex, than a distorted cell with different amplitudes and distributions of its 5 lobes. Thus, we could define cell shape complexity as the tendency of a cell to deviate from geometric

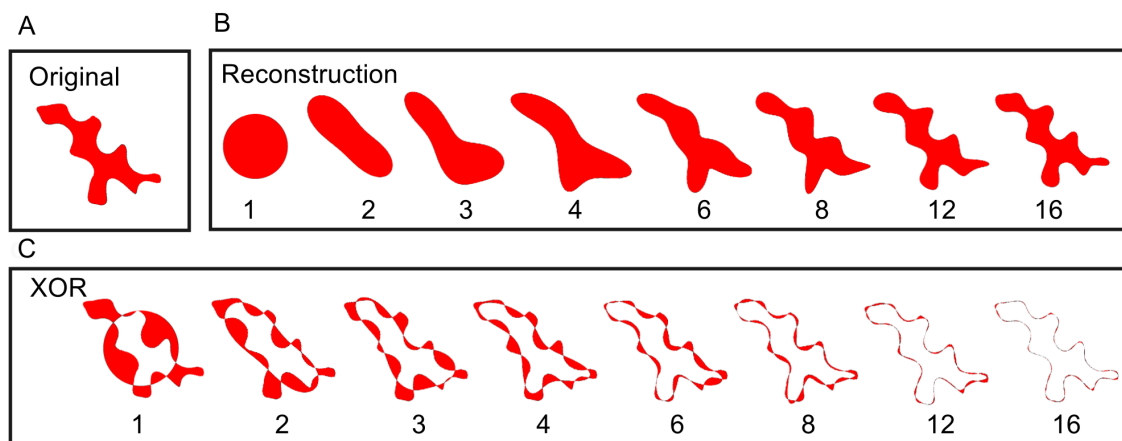


**Figure 2.16: Other measures extracted from the LOCO-EFA coefficients can provide additional information about the complexity of the cell shape.** A) Original cell contour to be analysed and B) LOCO-EFA reconstruction after the sum of  $n$ th  $L$ -modes (indicated by the number below each shape). C) By subtracting the area overlap of the original cell (A) and reconstructed shape after  $N$  number of  $L$ -modes (B, indicated by the number below), a measure of the mismatch between the truncated approximation of  $n$ th order to the actual shape (XOR) is obtained. For this measure, the more “complex” the shape, the more number of  $L$ -modes will be required to obtain the same XOR.

well-defined polygons. A useful measure for this second definition of “cell shape complexity”, now uses information about the distribution of  $L_n$  landscape calculating the entropy of the  $L_n$  spectrum, defined as:

$$E = \sum_{n=1}^N f_n \ln f_n, \quad (2.39)$$

where  $f_n$  refers to the relative proportion of each  $L_n$  for a given  $N$  number of modes analysed. In most cases, the entropy yields very similar results as the cumulative difference. However, they tend to diverge for those cases, in which there is a strong contribution of the lower harmonics, for which entropy values give more meaningful results. The reason for this is that lower modes (i.e high contribution for  $L_2$ , as when a cell is very elongated) will have a high value of cumulative difference (integral or area under the curve of the XOR original and reconstructed profile) that can be very similar to another cell where the XOR profile (and its integral) is more distributed among modes.

## 2.4.2 $L_n$ in real Pavement Cells

To validate the method on actual biological samples, and to further increase the understanding of the above introduced measures, I next analysed populations of real pavement cells by applying the LOCO-EFA method. To visualize the shape characteristics of a population of only pavement cells, I applied the analysis to an image of a mutant that does not generate other cell types of very divergent shapes, such as meristemoids or stomata

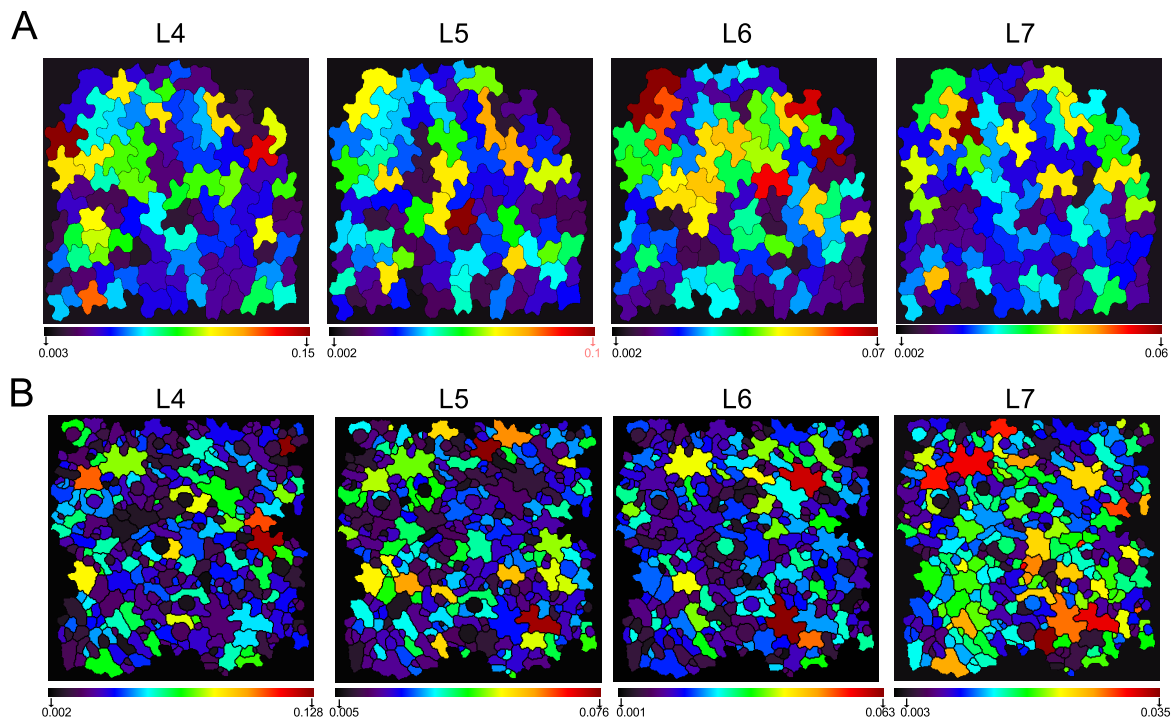


**Figure 2.17: LOCO-EFA on pavement cells of *Arabidopsis thaliana* reveals that very few cell shapes can be well captured through a single  $L_n$  mode.**  $L_n$  values are differentially contributing to the cell shapes within a piece of tissue of a *speechless* mutant (A) and a wild type (B) leaves. It is noteworthy that only few cells have a very high component in a particular mode, the majority are composed by a combination of different modes indicating the complexity (non-symmetry of the shapes).

(*speechless* mutant, MacAlister *et al.*, 2007, Figure 2.17A) as well as an image of wild type population of epidermal cells consisting of both pavement cells together with stomata and other cells from the stomatal lineage (Figure 2.1, Figure 2.17B).

Using LOCO-EFA, it is quickly possible to dissect the precise contribution of each mode for each cell in the population. Figure 2.17A-B shows color-coded populations according with a specific  $L_n$  mode. Interestingly, very few shapes show a high component for a single  $L_n$ , but the majority of the shapes are composed of high contributions stemming from different modes. In other words, very few cells can be characterized as a symmetrical shape. This indicates that for these biological cells, simply counting the number of lobes manually would lead to very incomplete information regarding the shape (it would be difficult to compare mutants for example, and the final result will be dependent on the human criterion of what is a lobe, as discussed before). Moreover, the data shows that when the contribution of a given mode is significant to the shape, there is not a preferential  $L_n$  where this occurs (Figure 2.17). Other LOCO-EFA shape measurements (Figure 2.18) also supports this observation.

Clearly, the heterogeneity of modes that composes real populations of pavement cells cannot be explained solely by the proposed molecular mechanisms underlying lobe and indentation. The existence of two counteracting pathways (one for lobe and other for

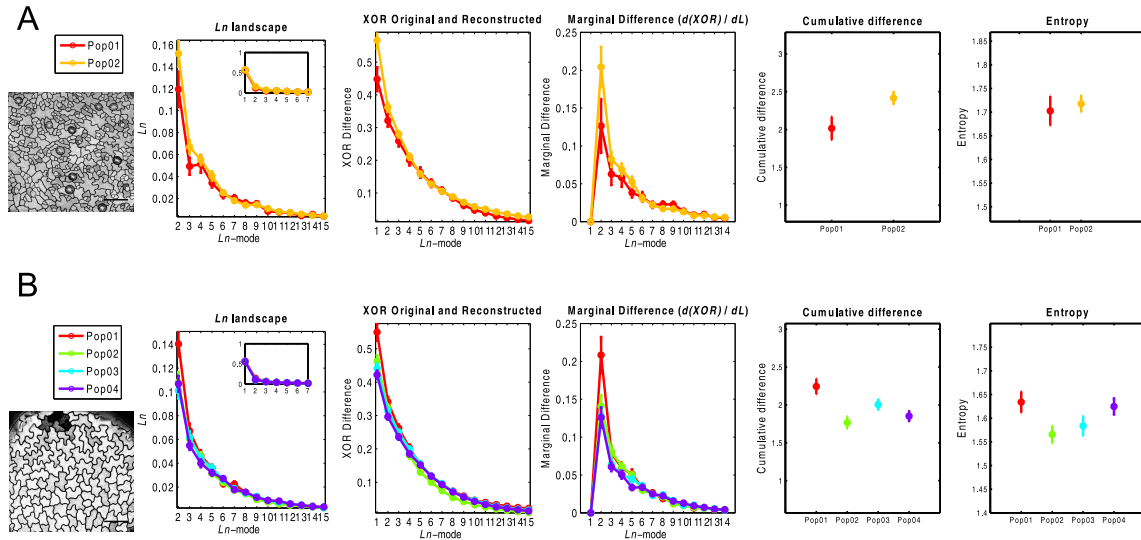


**Figure 2.18: LOCO-EFA quantifiers in real populations of pavement cells.** (A) Pavement cells from wild type populations (Columbia ecotype) were identified as cells with area bigger than  $400\mu m^2$  and (B) pavement cells from *speechless*. Pavement cell shapes are very heterogeneous and the mean LOCO-EFA measurements appears without a predominant mode. For cumulative difference and entropy 50  $L_n$ -harmonics were taken into consideration. Each population comes from different leaves from a comparable developmental stage and region within the leaf. Error bars correspond to 1+/- standard error, N=18,40 for wild type populations and *speechless* populations N=42,93,69,74.

indentation, see details in Xu *et al.*, 2010), in the more coarse of the cases, will give rise to a very symmetrical shapes (assuming that the cell shape results from the upstream distribution of initial alternate ROPs peaks) through Turing-like instabilities (Grieneisen *et al.*, 2013a). To gain insights in how this asymmetry could appear within a tissue, and to further validate the LOCO-EFA method on population of cells, I performed cell-based simulations of interacting cells using *in silico* cell shapes.

## 2.5 Applying the LOCO-EFA to *in silico* populations and the effect of cell interactions on single cell shapes

The *in silico* cells were created using the Cellular Potts model, an energy-based framework that enables the representation of cells and their dynamics through membrane extensions (see Methods section). While in its basic form, CPM cell shapes emerge due to surface tension (that can change according to their contacts) as well as internal pressure, here I use an extension of the CPM that allows more complex shapes to be generated. This extension consists in attributing to each cell a specified parametrized shape, in which differential effective surface tension along the cell changes its equilibrium shape (scripts to generate complex shapes were provided by Jop van Rooij and they are described in van Rooij *et al.*, 2013b). Specified individual cells were allowed to interact with each

other within a tissue-context, in a similar manner as in real tissues. In this way, I could analyse separately the shape of a single cell and the effect of cell-cell interactions within the population on the shape distributions using the LOCO-EFA.

Three distinct specified shapes (Figure 2.19A, see Table 1.2 for the specific parameters used), each consisting of 6-lobes and its population within the constrained tissue-context were evaluated (Figure 2.19B,C). It is noteworthy that although the cell shape specified is the same for each member within the population, cells acquire different shapes due to their interactions (Figure 2.19C). This divergence can be fully quantified using LOCO-EFA. For example, as a manner to assess the influence of neighbours in the final cell shapes within a population, one can retrieve and compare the contribution of a given  $L_n$  for the single specified cells and the resultant shapes on the cells within the population (Figure 2.19- Figure 2.21).

This divergence between a single specified cell and the resultant of the population when they interact is shown in Figure 2.19-Figure 2.20. To summarize this effect, the difference of the LOCO-EFA descriptors between the mean of the three populations of the same specified shape and the isolated *in silico* pavement cell can be calculated and it is shown in Figure 2.19D-G. To interpret the graphs note that, if the resultant single cell and the resultant mean population shapes were the same (or very similar) the difference will be very close to zero (and it would be straight line in these plots); conversely, any divergence of the single cell shape to the population mean shape will be shown as a positive (if the  $L_n$  mode and the other metrics are larger in the population than in the single cell) or negative values (when the single cell quantifiers are larger than the mean of the population).

Due to cell-cell interactions new peaks arise, as can be seen by the positive values of the amplitude differences (Figure 2.19D). Within the population, cells also become more complex, as is reflected by the increase of the average cumulative difference and entropy of the population (Figure 2.19F-G, last panel). Interestingly, the predominant specified peak ( $n = 6$  in this example) decreases in amplitude as other modes acquire more importance for the shape. Thus, while an individual isolated cell would be able to generate protrusions of a certain amplitudes, in the packed environment of a tissue, the periodical lobe formation is inhibited, and other symmetries and shape distortions appear as a consequence of tissue packing. This tendency was observed over all simulations performed irrespective of the initial specified shape, number of lobes and over a wide-range of parameter values defining cell-cell interactions (Appendix 2.C Figure 2.23- Figure 2.25 include the data for specified shapes and its populations with different number of protrusions).

Given that in real epidermal tissues of leaves several cell types coexist, I also evaluate if the difference between the specified shape and its population could be further influenced by the introduction of another cell type, smaller and round (for example, stomata; Figure 2.22A-G). Qualitatively, the results present similar behaviour: the main specified

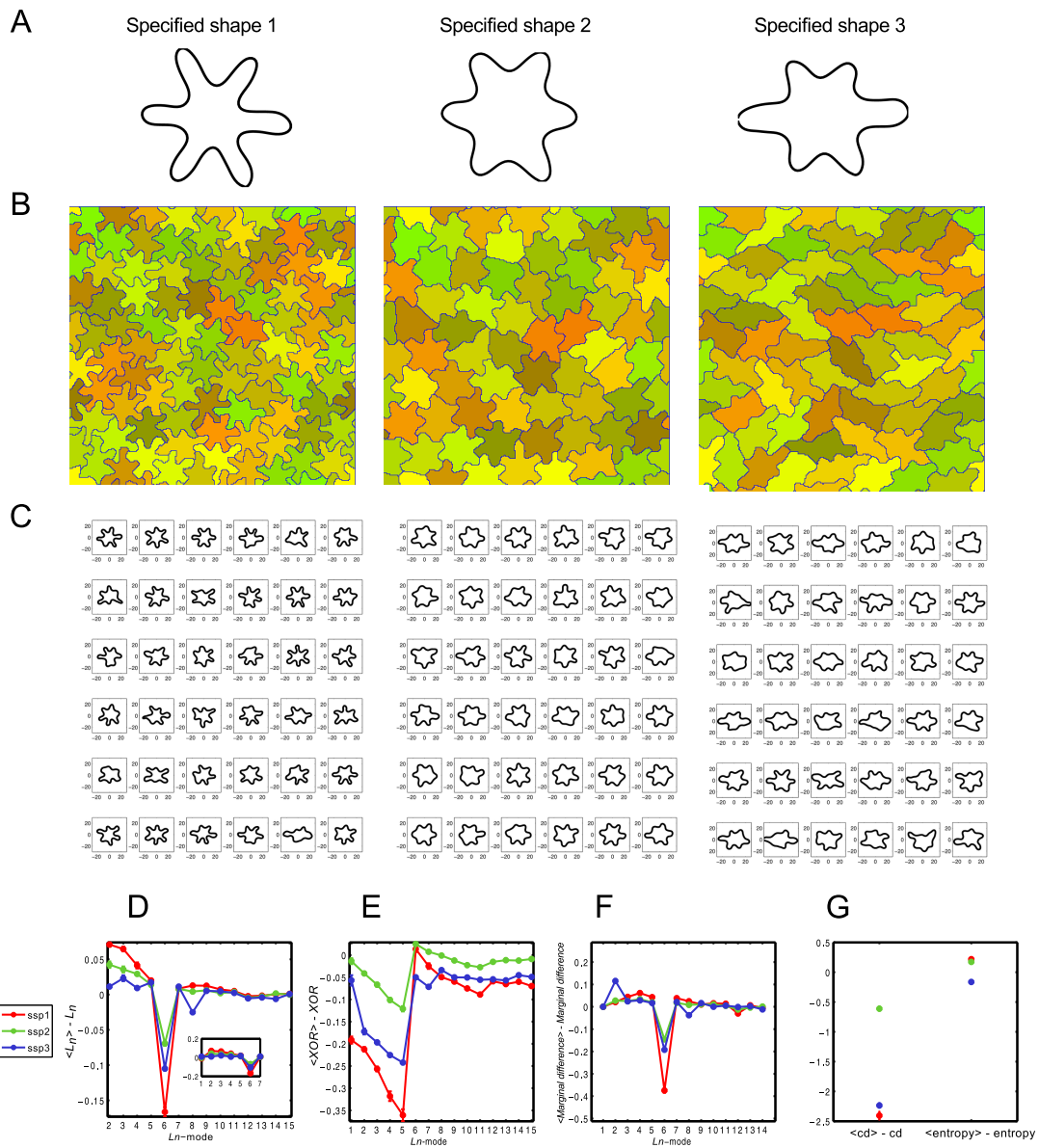


**Figure 2.19: Cell shape modifications due to tissue interactions.** A) Three *in silico* cells generated within the Cellular Potts Formalism, of different specified shapes (specified shape or ssp 1,2 and 3, respectively) and B) their corresponding *in silico* populations are shown. C) Note that the specified shape of each cell within a given population is the same, but the resultant cell shapes may be dramatically different due to cell-cell interactions and constraints within a tessellating tissue. D-G) To estimate the divergence between the single specified cells and their populations, the difference of the mean LOCO-EFA measurements between the individuals and population are shown. If the single cell and the mean of the population were the same, the difference will be zero. It is noteworthy that new peaks in addition of the specified (L6) appear and the specified peak decreases as shown by the negative values of the difference at the L6 (D,F). The difference of the average was calculated using 3 populations of same specified shape (different runs of the same model). The error bars show the standard error. The populations size for ssp1 were N=67,63,67; spp2, N=48,44,45 and spp3, N=47,46,47. See an example of a simulation in Movie 2.5.

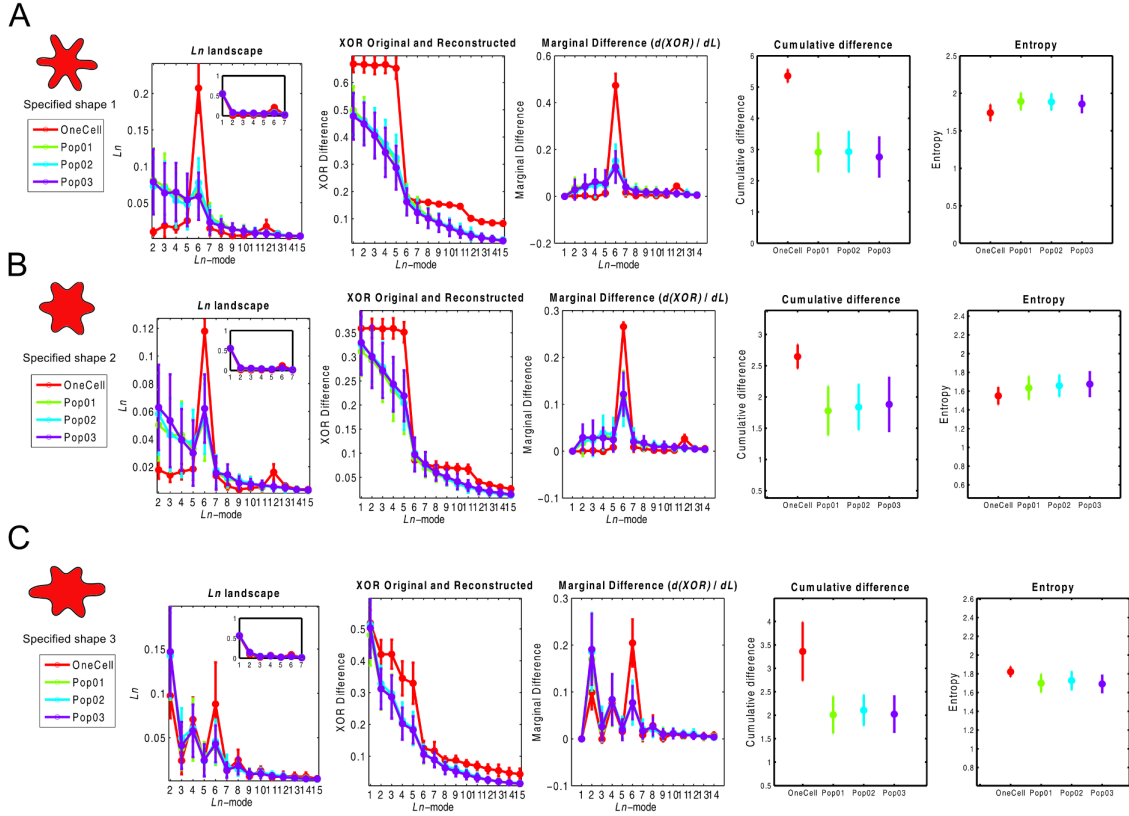


**Figure 2.20: Cell shape analysis on cell-cell interactions in *in silico* tissues using LOCO-EFA.** (A-C) One cell and 3 different populations for three different combinations of parameters (specified shapes or ssp) are shown. In the three cases, different peaks to the specified can appear in the  $L_n$  and Marginal difference profiles, and the contribution of different modes than the specified acquires more importance in the final cell shape approximation. In the same way, the cumulative difference decreases whereas the entropy tends to increase in the populations. Importantly, the variation of a multiple runs of the model for single cells (red) is generally smaller than the variation in the population and often it does not overlap. Error bars represent  $\pm 1$  standard deviation. Specified shape 1,  $N=67,63,67$ ; Specified shape 2,  $N=48,44,45$ ; Specified shape 3, populations of  $N=47,46,47$ . Single cells of 5 different simulations were used for each specified shape.

peak tends to decrease and new peaks form as a result of interactions within a population. Similar results were found when the round cell was allowed to vary in size (Figure 2.22H-N).

## 2.6 Discussion and concluding remarks

Quantitative analysis of pavement cells morphogenesis and how it relates with other cellular processes is important to gain understanding of the cellular basis of leaf development. Besides, a quantitative description of cell geometry also allows to compare and contrast the influence of mutations that affect the cell shape (and the cell polarity). Despite their importance, available methods to quantify pavement cell shape can be mis-

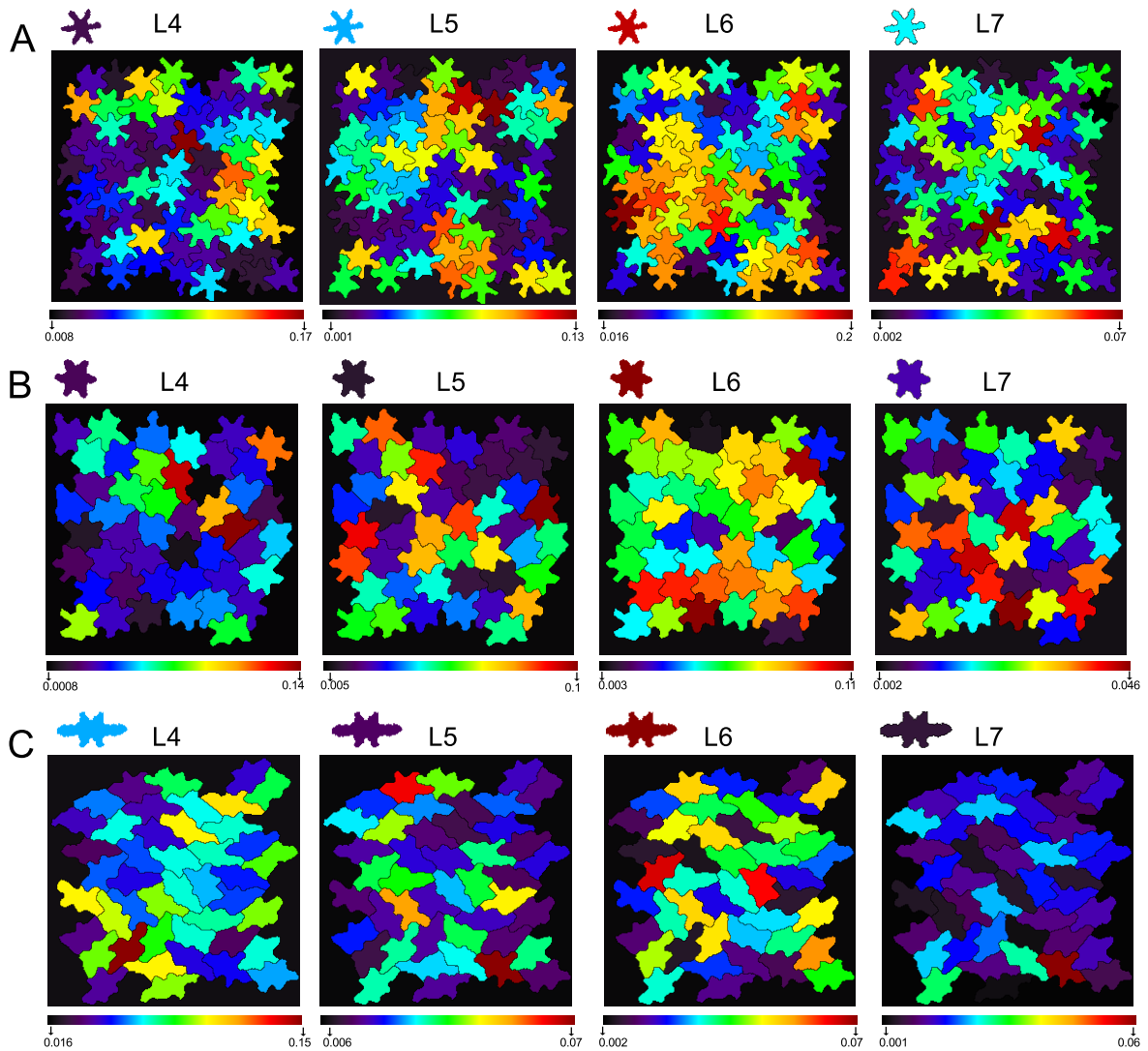


**Figure 2.21: LOCO-EFA analysis of *in silico* Pavement cells reveal the degree of divergence that interacting cells within a tissue experience from their specified shape.** (A-C) Different  $L_n$ -modes ( $n=4-7$ ) and their  $L$ -contributions (colour-coded) are shown for the three different specified shape populations. Single cells interacting within the tissue can present deviations of the contribution of a given  $L_n$  from the situation of them being isolated cells (shown at the top of each panel), as is shown by the divergences in their colour.

leading, very sensitive to specific parameters or depend on arbitrary criteria of what is a lobe and indentation. These shortcomings limit the scope of any conclusion based on cell shape and make cell shape phenotyping a very time-consuming activity.

A useful method to quantify cell shape must fulfil the following characteristics: 1) it should not discard meaningful shape features at the same time that 2) it simplifies the complexity of the cell shape, 3) it is biologically interpretable and 4) it provides a quantifiable manner to distinguish and compare shape traits among populations. I presented here a new method that collects these characteristics and overcomes the problems stated before. It takes the information of the whole contour of the cell and provides a measure

that directly relates to morphological features ( $L_n$ ) and the amplitude of them. It is not sensitive to cell orientation or cell size, providing a robust and meaningful way to extract quantitative information of cell shapes. Importantly,  $L_n$  and XOR profiles are unique for a particular geometry, providing not just with a quantitative assessment of cell shape but also with an identifier that can be seen as the “fingerprint” of a cell. This attribute is used as a pattern recognition tool for tracking cells in a temporal sequence of images (discussed in the next chapter).

To illustrate the interpretation of the different measurements obtained with LOCO-EFA, simple shapes (geometrical or symmetrical forms) were analysed. To assess the performance of the proposed method in realistic cell shapes, I extended the method to analyse populations of real pavement cells. It is noteworthy that very few cells have a symmetrical shape and, when the contribution of the shape is high in a particular mode, there is not a preferential  $L_n$ . Importantly, the composition of  $L_n$  in real cells cannot be explained just by the existence of two counteracting pathways specifying lobe and indentation identities (Xu *et al.*, 2010, Grieneisen *et al.*, 2013a), that in the more coarse of the cases will give rise to a very symmetrical cell form (assuming that they counteract each other with the same strength to generate an alternate patterning of ROPs, upstream the cytoskeleton activity that underlies the final cell shape).

To further test the LOCO-EFA method as a statistical tool and gain insights in possible mechanisms of the heterogeneity on the  $L_n$  profiles of real pavement cells, I used synthetically generated data, in which the output can be varied systematically because the specified, parametrized individual cell shape is controlled. I measure by the LOCO-EFA how cells diverge from their specified shape when they are allowed to interact with their neighbours. As a result of their interactions, the main specified mode decreases and new modes become important, altogether leading to asymmetrical resultant shapes even when a very symmetrical individual cell shape was initially specified. Interestingly, the divergence between specified and resultant shapes in populations was not dependent on the introduction of another cell type (circular, stomata-like) or when this cell type was allowed to vary in area.

Although synthetic data is just a phenomenological reconstruction of the real shapes, the results presented here suggest that the local influence of neighbours during pavement cell development is important for the acquisition of their final shape. Sectors of wild type and mutants cells defective in cell shape will be crucial for assessing this hypothesis. Further analysis of the the angle of divergence (spatial angle) can be extended in *in silico* tissues and compared with a time-lapse data of real pavement cells to study other aspects of tissue packing.

In short, I presented a new method to extract relevant quantitative cell shape information that was validated using *in silico* tissues. The LOCO-EFA can be applied to other cell types or organs in different species, as it is a reproducible and quantitative method to phenotype efficiently and objectively large 2D data sets. I also showed that syntheti-

cally generated shapes in addition to provide “grounds truths” to evaluate the proposed method, can be used to gain insights into real populations of pavement cells.

## 2.7 Materials and Methods

### 1. Confocal Images and Image Processing

Columbia wild type or *speechless* mutant leaves expressing pmCherry-aquaporin (Nelson *et al.*, 2007) were imaged using a confocal microscope Leica SP5 at comparable stages and at comparable regions. Further image processing was done using Fiji and images were segmented using the Segmentation Potts Model (see Chapter 3 and van Rooij *et al.*, 2013a).

### 2. Shape descriptors

Average lobe length and neck width were calculated using Image J (Analyse->Measure). The skeleton was calculated using a MATLAB file exchange files (Better Skeletonization by Nicholas Howe).

### 3. Geometrical shapes.

Geometrical shapes were generated using the superformula (described in Gielis, 2003) and the images were analysed as mentioned before for confocal images.

### 4. XOR and other measurements

The total number of pixels belonging to each real or synthetic pavement cell was compared successively with the total number of pixels of the reconstruction after  $N$  number of  $L_n$ -modes. The scripts to calculate the XOR and colour-code the real and synthetic cells were written in C, using the Excalib2d library of Stan Marée. The cumulative difference and entropy as well as the approximation to shapes were calculated using 50  $L_n$  modes.

### 5. Cellular Potts Model shape generator

The Cellular Potts Model is an energy-based formalism that represents cells within a lattice. Here, it is used to generate single cells with a specific shape that are allowed to interact. In short, at each step of the simulation a random sampling of the lattice (pixels in this case) is evaluated to change its state. To evaluate if such change of state (also called

“copying”) will occur, the Hamiltonian is calculated. It is defined by summing the energy contribution of each pixel over the entire field and over cells:

$$\mathcal{H} = \sum_{ij} J_{CM} + \sum_c \gamma_a (a - A)^2 + \gamma_b \sum_c (p - P)^2, \quad (2.40)$$

$J_{CM}$  refers to the coupling energy per boundary site (per  $ij$  pixels),  $a$  and  $p$  are the actual cell area and cell perimeter of each cell ( $c$ ), respectively. Similarly,  $A$  and  $P$  are the target cell area and target cell perimeter. The parameters  $\gamma_a$  and  $\gamma_b$  describe resistance to deviate from the target area or perimeter, respectively. The total change in the Hamiltonian due to a “copying” event before and after  $\Delta\mathcal{H} = \mathcal{H}_{after} - \mathcal{H}_{before}$  is calculated, and the event is accepted with probability

$$P = \begin{cases} 1 & \text{if } \Delta\mathcal{H} < -Y, \\ e^{-\frac{\Delta\mathcal{H}+Y}{T}} & \text{if } \Delta\mathcal{H} \geq -Y, \end{cases} \quad (2.41)$$

where  $Y$  corresponds to the yield or the ability of the membrane to resist a force and  $T$  introduce stochastic fluctuations. Copying events that decrease  $\mathcal{H}$  by at least  $Y$  will be always accepted, other changes will be accepted with Boltzmann probability (Eq. 2.41).

To generate cells with a particular number of protrusions, we modify the increase in the Hamiltonian (van Rooij *et al.*, 2013b) as a short-cut of the intracellular polarity of the cell. Simulated cells have a specified number of lobes, amplitude of lobes, overall elongation and roundness. Importantly, these characteristics are not fixed but are dynamically updated and they are allowed to vary to “accommodate” a favourable position.

This was implemented by modifying the increase of the Hamiltonian (for a copy event) as follows:

$$\Delta\mathcal{H}' = \Delta\mathcal{H} - \nu \cos(n\theta) - \chi \cos(2\alpha) - \mu(\sqrt{A/\pi} - \nu) \quad (2.42)$$

where  $\nu$  is the “propensity” to extend (amplitude or pointiness) and  $\theta$  is the angle between the target direction of growth and the vector determined by the coordinates of the position that is evaluated and the mean position of the cell (hereafter called copy vector). To create cells with a given number of lobes the angle  $\theta = \arctan(y, x)$  is expanded as many times as number of lobes. Afterwards, the mean angle corresponds to  $\theta = 360/n$ , where  $n$  is the number of lobes specified. To update the number of points or lobes, the preferred direction of extension is where they were most extended in.

Elongation is implemented in a similar way (third term in Eq. 2.42).  $\chi$  corresponds to the strength of elongation and  $\alpha$  is the angle between the elongation vector and copy

	SSP1	SSP2	SSP3	Round Cell
Target Area	858	1167	1197	600*
Pointiness	6912	5328	5207	0
Number of lobes	2 - 10	2 - 10	2 - 10	2
Roundness	382	518	434	4000
Elongation	4	28	5927	0

**Table 2.2:** Three combinations of different specified shapes of single and population cells.\*200-600 when it was allowed to vary in size. The population density of the circular cell was always 20%.

vector (as calculated by the cross product). Others alternatives for elongation such as  $\chi(-|\sin\alpha|)$  and  $\chi|\cos\alpha|$  showed similar results.

The strength of the roundness was implemented by  $\mu$  (fourth term in Eq. 2.42), and can be interpreted as the resistance for a cell to deviate from a circle ( $v$ , refers to the length of the copy vector). For a detail explanation see van Rooij *et al.*, 2013b .

Cell position within the field was randomly chosen. The elongation and position of the lobes were updated every 100 time steps from a total of 10000 time steps. The parameters used for each specified shape (ssp) are shown in Table 1.2.

## 2.A Appendix: Movies

**Movie 2.1: Approximation of a closed contour by Elliptic Fourier Analysis.**

A given 2-dimensional shape can be approximated using EFA by summing  $n$ -ellipses as follows: each  $n$ th elliptic harmonic traces  $n$  clockwise or counter-clockwise revolutions while rotating around the previous harmonic ellipse.

**Movie 2.2: Direction of rotation opposite to the first harmonic ellipse.**

A given mode  $n$  will generate an  $n + 1$  shape if its direction of rotation is opposite to the rotation of the first harmonic (for some special cases).

**Movie 2.3: Direction of rotation same as the first elliptic harmonic.**

Conversely, a given mode  $n$  will generate an  $n - 1$  shape if its direction of rotation is in the same direction than the rotation of the first harmonic (for some special cases).

**Movie 2.4: Exception of the rule of direction of rotation.**

If the eccentricity of an elliptical mode is very high (i.e an ellipse is very flat), it is not possible to predict the number of lobes according to the direction of rotation as before.

**Movie 2.5: Example of an *in silico* simulation for a population of specified shapes.**

CPM pavement-like cells for a given specified shape when they are allowed to interact with neighbours within a simulation.

## 2.B Appendix: Other LOCO-EFA features

### Adjustment the semi-major axis to be parallel to the x-plane

If desired to approximate the shape contour with its long axis parallel to, for example, the x-axis (i.e. if the orientation respect to an organ landmark coinciding with the x-axis is important such as the midvein or, if it is important to have a similar cell orientation), another matrix transformation involving its spatial angle can be applied. The spatial angle  $\rho_1$ , is found after adjusting the starting point at  $t' = 0$ .

$$\rho_1 = \arctan \frac{y_1'(0)}{x_1'(0)} = \arctan \frac{\gamma_1^*}{\alpha_1^*} \quad (2.43)$$

for  $0 \leq \rho_1 < 2\pi$ .

In this case, the first harmonic is rotated such that its semi-major axis is parallel to the x-axis by setting the spatial angle  $\rho_1 = 0$

$$\begin{bmatrix} \alpha_n^{**} & \beta_n^{**} \\ \gamma_n^{**} & \delta_n^{**} \end{bmatrix} = \begin{bmatrix} \cos(\rho_1) & \sin(\rho_1) \\ -\sin(\rho_1) & \cos(\rho_1) \end{bmatrix} \begin{bmatrix} \alpha_n^* & \beta_n^* \\ \gamma_n^* & \delta_n^* \end{bmatrix}, \quad (2.44)$$

Note that at difference of the EFA (Kuhl & Giardina, 1982) where the spatial angle transformation is always needed as a normalization step, for the calculation of the contribution of each harmonic  $L_n$ , this transformation is not mandatory. However, the spatial angle  $\rho_1$  can be informative for determined the preferred elongation of a cell in a tissue taking as a reference a particular landmark (for instance, the midvein in the leaf as illustrated in Chapter 6, Figure 6.4).

### Other features of LOCO-EFA

#### 1) Pointiness and Roundness

Notably,  $\lambda_{+n}$  will generate protrusions with roundy shape, whereas  $\lambda_{b-n}$  will generate pointy lobes.

The amount of 'roundness' or 'pointiness' of each shape is given by the proportion:

$$w_+ = (\lambda_{+n+1}) / (\lambda_{+n+1} + \lambda_{-n-1}) \quad (S1)$$

and,

$$w_- = (\lambda_{-n-1}) / (\lambda_{+n+1} + \lambda_{-n-1}) \quad (S2),$$

respectively.

## **2.C Appendix: Supplementary Figures**

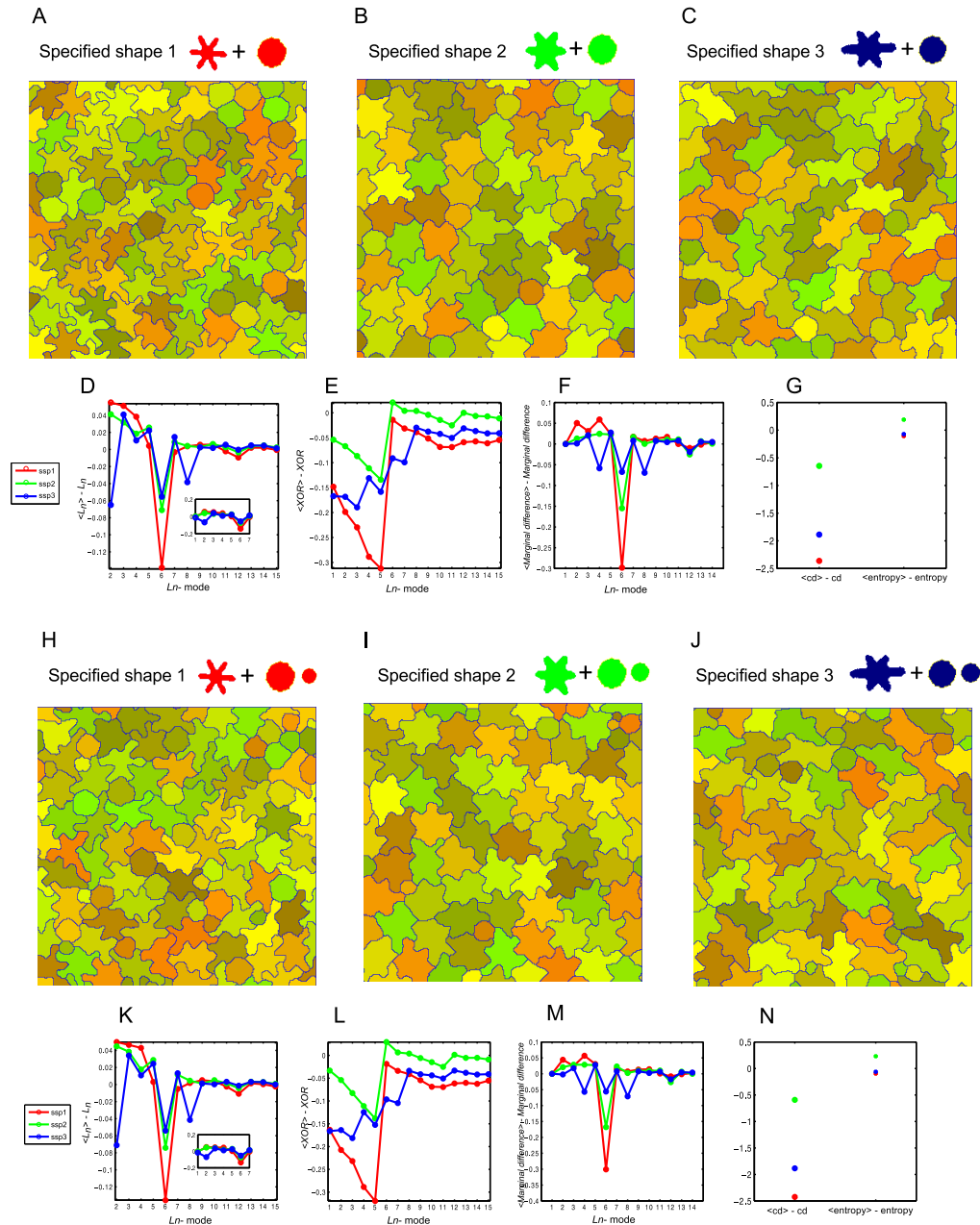


**Figure 2.22: Cell-cell interactions diverge the specified shape of single pavement-like cells and do not depend on interactions with a second cell type.** *in silico* individual pavement cells together with a sub-population of circular cell type stomata-like when fixed (A-C) and when it is allowed to vary in size (H-J) for three combinations (ssp) and an example of their populations. (D-G, K-N) Difference of the LOCO-EFA descriptors between the isolated *in silico* cell pavement cell and the mean of the population (excluding the circular cells) summarizes the effect of interactions of two cell types and the shape divergence between the specified and resultant geometries. In a similar way to showed in Figure 2.19, different peaks to the specified main protrusion can appear in the  $L_n$  (D,K) and Marginal difference profiles (F,M), and the contribution of different modes acquire more importance. Finally, the cumulative difference decreases whereas the entropy tends to increase in the populations (G,N). The specified density of the second type was 20% in all the cases. The error bars show the standard error. Pavement cell populations were: ssp1 N=56/74,58/71,59/72; ssp2 N=41/54,41/50,45/53 ; ssp3 N=37/50, 44/54, 43/52. When the second cell type (“stomata”) was allowed to vary in size the Pavement cells taken from spp1: N=56/74, 57/74, 64/77; spp2 N=41/52, 46/57, 46/54 and spp3, N=40/54,43/55,45/55.

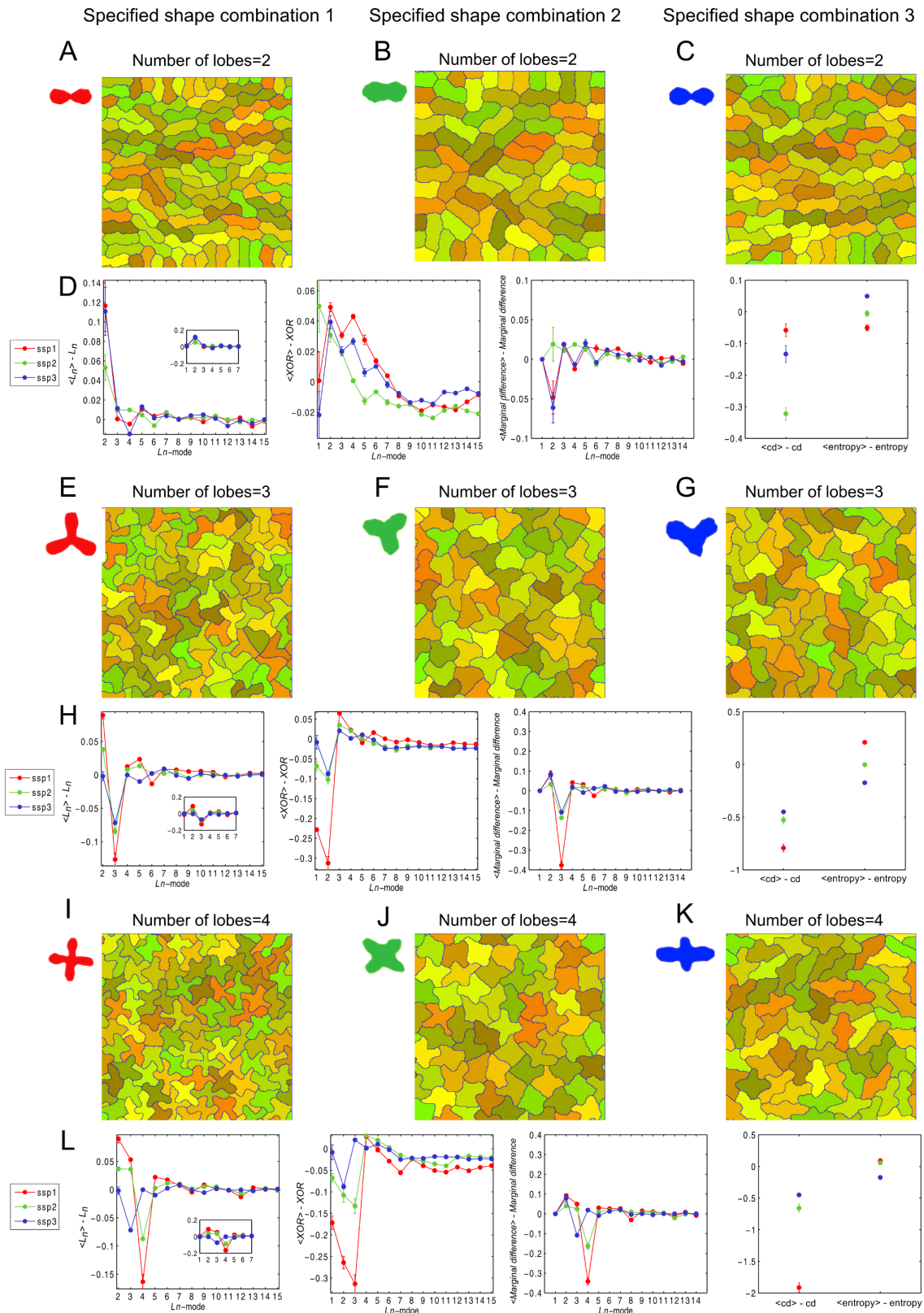


**Figure 2.23: The divergence between single specified cell and their populations do not depend on the specific number of lobes specified (Lobe 2-4). Single and examples of their population for three specified shapes (spp) together with the LOCO-EFA quantifiers are shown for lobe number 2-4.**

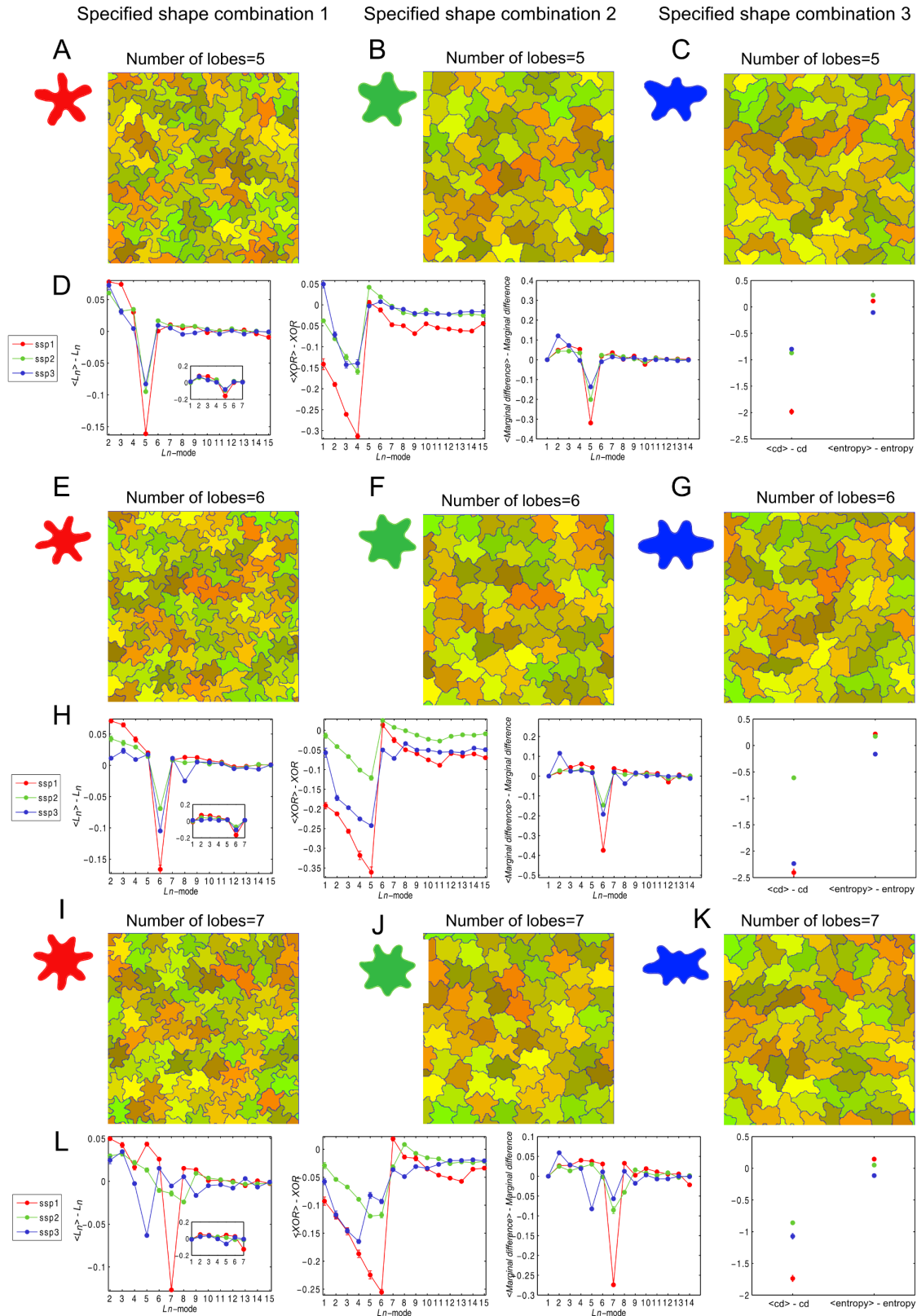


**Figure 2.24: The divergence between single specified cell and their populations do not depend on the specific number of lobes specified (Lobe 5-7). Single and examples of their population for three specified shapes (spp) together with the LOCO-EFA quantifiers are shown for lobe number 5-7.**

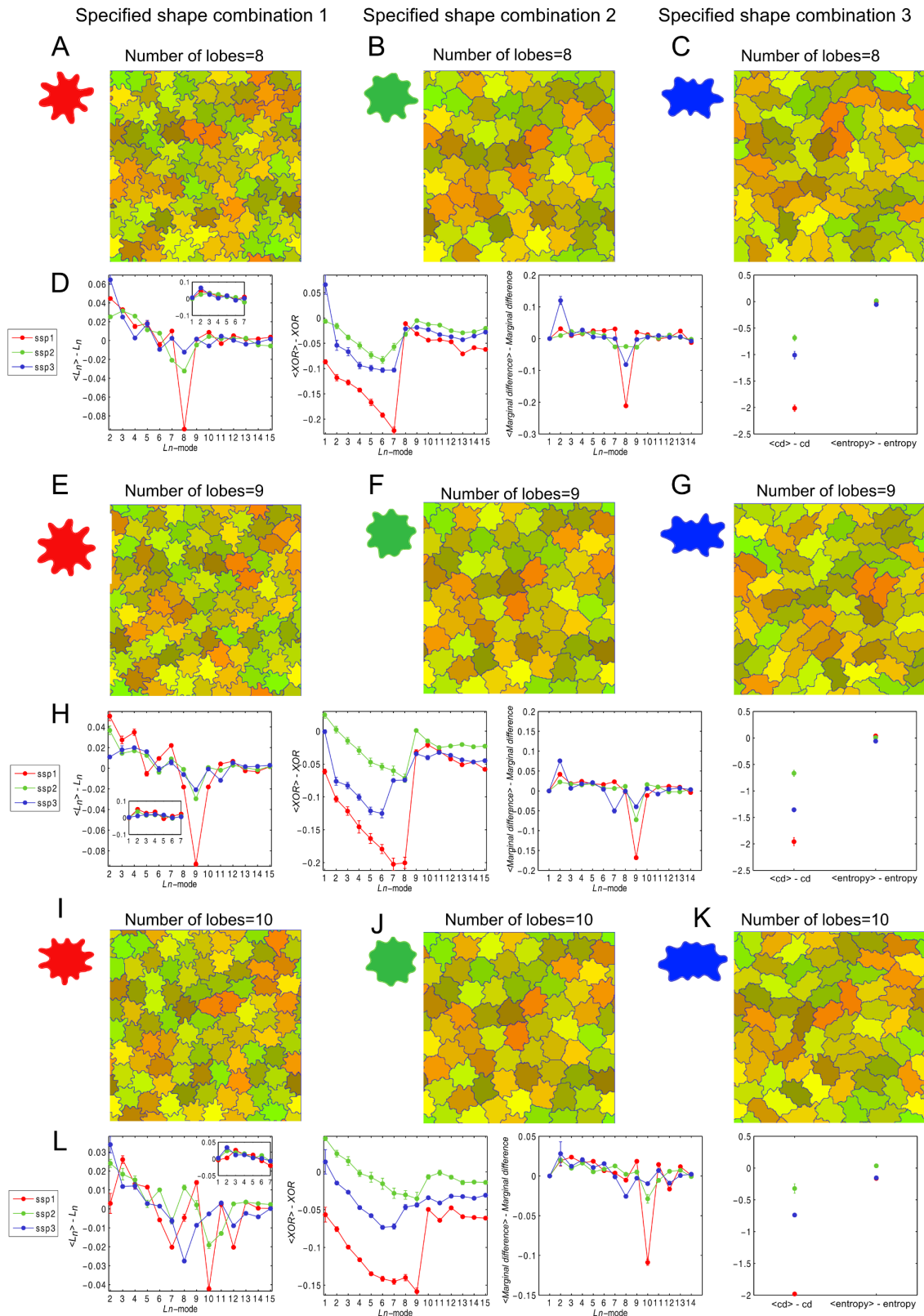


**Figure 2.25: The divergence between single specified cell and their populations do not depend on the specific number of lobes specified (Lobe 8-10). Single and examples of their population for three specified shapes (spp) together with the LOCO-EFA quantifiers are shown for lobe number 8-10.**



## Chapter 3

# Long time lapse and image analysis on *in vivo* leaf development at the cellular scale

### Abstract

Monitoring the changes in the tissue at the cell scale as growth progresses through live imaging provides us with an unprecedented resource to gain insights into the dynamic nature of development. *In vivo* imaging, however, needs to be combined with appropriate computational tools that enable extraction of meaningful quantitative data from the images. To capture cell growth, cell shape and cell divisions in relevant spatial and temporal scales during leaf development required development of new tools and protocols in both confocal imaging and imaging processing. In this chapter, I describe the pipeline that allowed the analysis of long time-lapse images at the cellular scale, highlighting the powerful combination of live imaging and computational image analysis techniques.

### 3.1 Introduction

Plant morphogenesis is a dynamic process during which cells divide, grow, and acquire a specific shape. Although static images of plant development have been very valuable as a first approximation to untangle the spatio-temporal dynamics of these processes, the dynamic information that is possible to extract from a static analysis is limited (Reddy *et al.*, 2007; Cunha *et al.*, 2012; Sappl & Heisler, 2013).

In contrast, recent developments of mesoscopic live-imaging at tissue and organ level allow direct observation of division and expansion at cellular resolution over time. This represents an invaluable resource to capture dynamic and quantitative data at single cell level, offering insights that cannot be achieved with any static analysis (Megason & Fraser, 2007; Cunha *et al.*, 2012; Sappl & Heisler, 2013).

In plants, recent examples of time-lapse imaging combined with computational algorithms have proved to be essential to gain insights into the dynamic nature of plant development (Roeder *et al.*, 2012a; Robinson *et al.*, 2011; Kuchen *et al.*, 2012; Uyttewaal *et al.*, 2012; Schiessl *et al.*, 2012). However, when the study involved cellular resolution, individual cells were identified manually in different time frames, limiting the extension of this approach to tens of cells. Another major problem is that live-imaging is limited to a couple of days because of photobleaching, phototoxicity or just because the tissue reaches a critical size to be imaged. Altogether, this makes it impossible to capture the tissue dynamics at cellular scale with appropriate temporal and spatial resolution. Thus, during the course of this project, in order for me to study events of plant morphogenesis that occur in the time scale of several days, such as the dynamics of cell growth, cell morphogenesis and cell division along the leaf, it was necessary to adjust existing methodologies and develop new ones.

In this chapter, I present a pipeline that allows us to overcome the limitations mentioned above and provides us with an automatic way to identify cells over long periods of time. The development of such a tracking algorithm required the synergy of live-imaging and the development of diverse computational algorithms. On one hand, the bright and uniform expression of a fluorescent membrane marker in the *speechless* background combined with optimized confocal microscope parameters enabled long time-lapse experiments and the acquisition of very good quality images. On the other hand, image analysis combined with the possibility to segment automatically complex cell shapes (Segmentation Potts Model) together with a parametrized way to capture cell shape (LOCO-EFA chapter 2) allowed the development of an automatic tracking algorithm. In this chapter, I detail the procedure of live imaging, image processing, and automatic tracking in the leaf. This procedure was used to analyse the dynamics of cell growth, cell division and cell morphogenesis during leaf development. Importantly, although this pipeline was designed for cells in the epidermis of the leaf, in principle, it can be applied to other tissues.

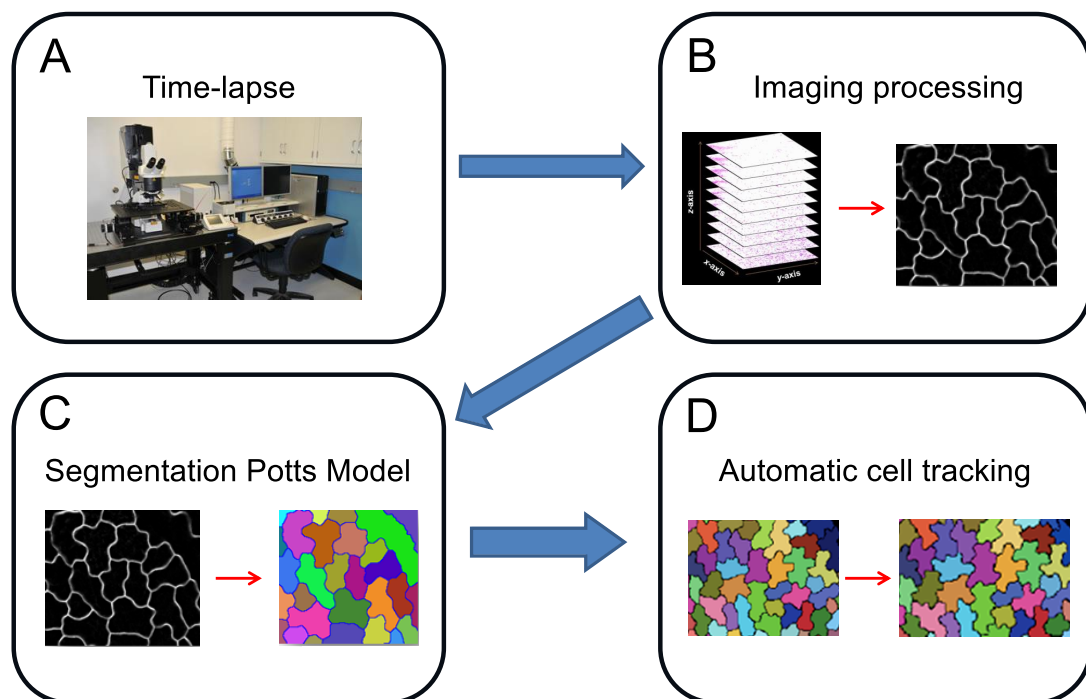


**Figure 3.1: General pipeline to capture dynamic shape and size changes during leaf development at cellular level.** A) Time-lapse imaging using confocal microscopy and a custom-made perfusion chamber. B) Imaging processing includes the 2D projections of the Z-stack and denoising activity. C) Cells are automatically identified from the confocal images using the Segmentation Potts Model algorithm. Finally, D) cell lineages are automatically recognized using an algorithm for cell tracking.

## 3.2 Time-lapse Imaging

As mentioned above, capturing cell dynamics during leaf development *in vivo* for long periods of time is a powerful approach to gain understanding of how the combined action of cell growth and cell morphogenesis contributes to the overall organ shape. Live-imaging required the synergy of appropriate confocal microscope settings, a custom-made perfusion chamber, long-lasting membrane markers and a simplification of imaging. In this section, I describe the protocol I followed for imaging the cell dynamics. I start with the plant preparation prior to imaging, and follow up with a general description and considerations for confocal imaging acquisition during a time-lapse experiment.

### 3.2.1 Plant preparation prior to imaging

Confocal image acquisition requires a careful selection of transgenic lines expressing a fluorescent plasma membrane marker that 1) provides a good signal, 2) is resistant to photobleaching and 3) is expressed over long periods of time during the leaf development (Cunha *et al.*, 2012). After an initial screening of different fluorescent markers, a wild type

ecotype Columbia line containing aquaporin-pmCherry as a membrane marker (Nelson *et al.*, 2007) was selected for the analysis.

To capture growth and shape dynamics of pavement cells' development from the starting point of their morphogenesis at the tip of the leaf to the point when they are first recognized at the bottom of the leaf requires approximately 7 days (from 5 days after stratification to 12 days after stratification, although cell shape saturation occurs later, see Chapter 4). During this period, the width of the first leaf ranges from 300  $\mu\text{m}$  to 3  $\text{mm}$ , the leaf acquires 3D curvature and multiple stomata divisions still occur, altogether making it impossible to continue imaging with cellular resolution at the tissue-scale in feasible time periods without irreversible damage to the tissue. In order to overcome these difficulties, a "simplified" leaf of the *speechless* mutant (MacAlister *et al.*, 2007) was chosen for the analysis.

The plasma membrane mCherry line was crossed with *speechless* (T-DNA SALK\_078595 or *spch4* in MacAlister *et al.*, 2007) to generate a heterozygous line containing the membrane marker suitable for confocal imaging (referred to hereafter as *spch4-pmCherry*). The SPEECHLESS (SPCH) protein is a basic helix-loop-helix (bHLH) transcription factor involved in the asymmetrical cell divisions that produce the stomata lineage in *Arabidopsis thaliana* (MacAlister *et al.*, 2007). Thus, the homozygous *speechless* mutants plants do not contain stomata or any other intermediate members of the stomatal lineage.

Notably, the *spch4-pmCherry* line grows with a similar speed as wild type plants in the tracking chamber (Figure 3.3 and Robinson *et al.*, 2011) and the overall organ shape of their leaves is very well conserved. Thus, the use of *spch4-pmCherry* provides a system to simplify the problem of whole-tissue imaging over long time periods and allows acquisition of quantitative morphogenesis data at cellular resolution representing leaf development. Importantly, it provides a system to study the dynamics of cell growth, cell shape and cell divisions that are independent of the stomatal lineage, thus simplifying the elucidation of the cell behaviour that is relevant for the correct leaf morphogenesis (further discussed in Chapter 4). Thus, the analysis of *speechless* morphogenesis simplifies the complexity of imaging and the characterization of cell dynamics. Of course, it will complement the analysis of wild type development when the technical difficulties are overcome.

Heterozygous *spch4-pmCherry* plants were genotyped by PCR (details of primers used and PCR conditions in the appendix section) and selected for further analysis. Seeds were sterilized using 0.05% sodium dodecyl sulphate and 70% ethanol for 10 minutes. Then, seeds were rinsed twice with 100% ethanol and sown in plates containing 25 ml of MS agar (0.8% (w/v) agar, 1x Murashige and Skoog salt mixture, 1% (w/v) sucrose, 100  $\mu\text{g/ml}$  inositol, 1  $\mu\text{g/ml}$  thiamine, 0.5  $\mu\text{g/ml}$  pyridoxine, 0.5  $\mu\text{g/ml}$  nicotinic acid, 0.5  $\mu\text{g/ml}$  MES, pH 5.7).

After sterilization, seeds were stratified in the dark at 4°C for 4 days. Next, they were transferred to the growth room under long-day conditions (20°C and 16 hours light) in

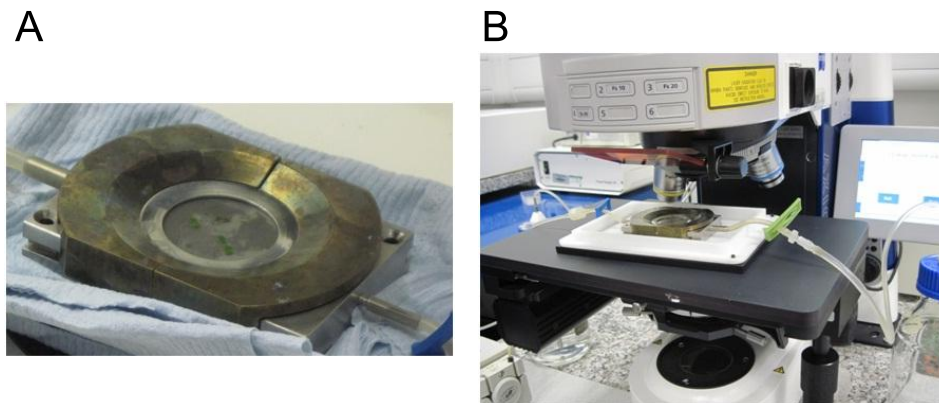


**Figure 3.2: Custom-made perfusion chamber allows live-imaging of leaf development for long time periods.** A) Inner chamber, where seedlings are placed over a mesh and then covered by a cover-slip under sterile conditions. B) The inner chamber and the outer base are set up under the confocal microscope for imaging. At the same time, the medium is fluxing through the chamber.

the Controlled Environment Conditions (CEC) facility.

Homozygous plants *spch4* (i.e containing no stomata) showing good expression of the membrane marker were placed inside the perfusion growth chamber (Figure 3.2) when they were 6-7 days after stratification (DAS) corresponding to 140-170 hours after stratification (HAS, indicated for each experiment in the appendix section). The typical width of these plants at this developmental stage is 0.125-0.179 mm, as quantified from the Z-stack in 3D (because the leaf acquires 3D curvature, see section below) by independent measurements using VolViewer (developed by Jerome Avondo, details in: <http://cmpdartsvr1.cmp.uea.ac.uk/wiki/BanghamLab/index.php/VolViewer>) and an algorithm created by Matthew Hartley, described below.

The perfusion tracking chamber is a custom-made device used for time lapse imaging at the John Innes Centre. In this case, it was adjusted to a confocal microscope (details on confocal microscopy below). The chamber has two main parts: an outer containment tray used to attach the chamber to the microscope and an inner imaging chamber (Figure 3.2). The imaging chamber is made of stainless steel so that it is possible to sterilize it. It allows the flux of liquid medium that enters at one extreme and exits at the other, using an electrical pump (Sauret-Gueto *et al.* 2012 and Calder *et al.*, *in preparation*). Inside the imaging chamber, the seedling is placed on a mesh that positions the tissue close to the cover glass.

Plants were grown in the perfusion tracking chamber under constant flow of liquid medium (1/4 strength Murashige and Skoog, 0.75% sucrose, 1.1  $\mu\text{g/ml}$  MES, pH 5.8) at 1  $\mu\text{l/s}$ . The details and considerations of confocal time-lapse imaging are discussed next.

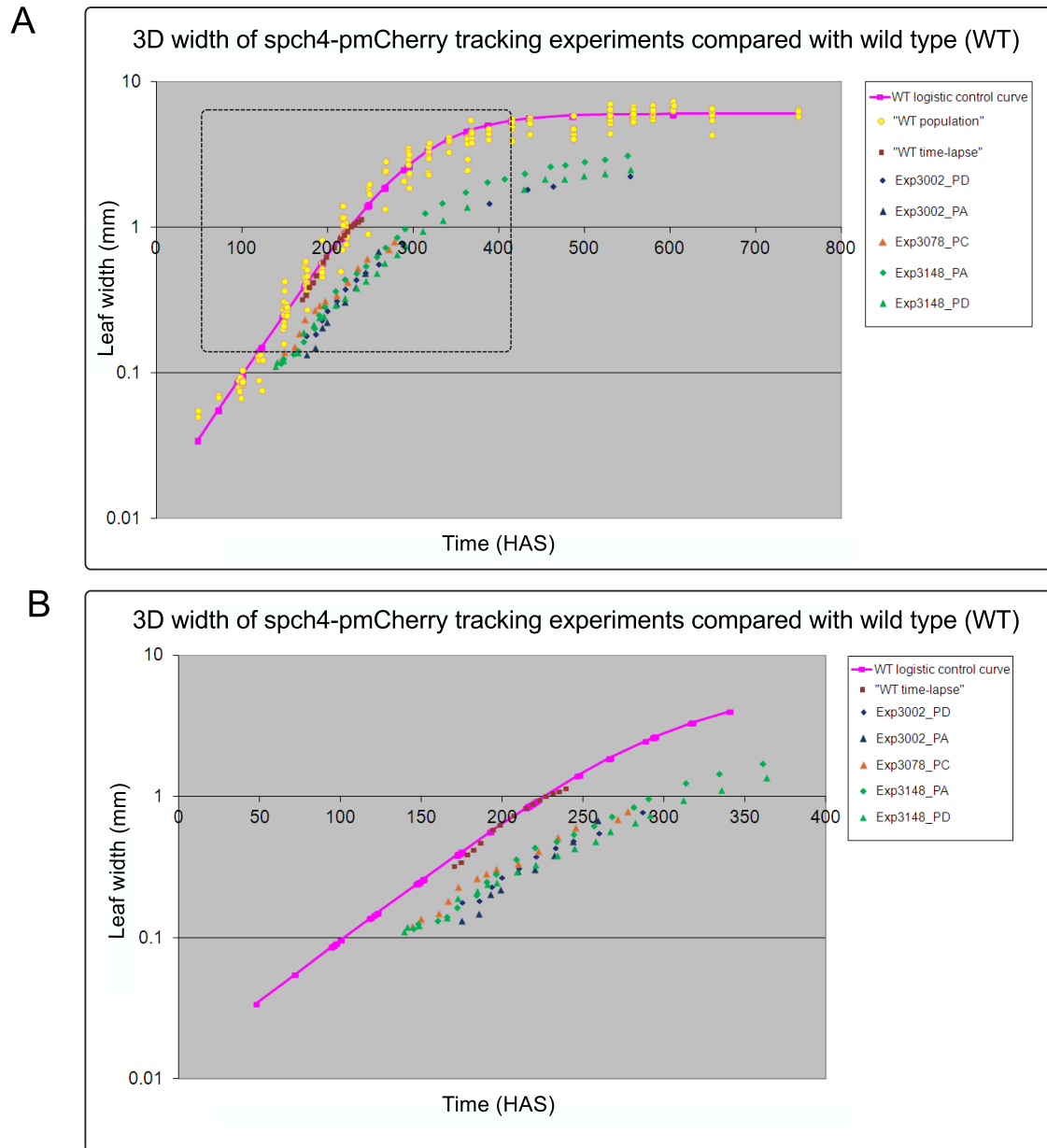


**Figure 3.3: 3D width over time of wild type and spch4-pmCherry is similar.** A) To rule out an effect on leaf growth due to the experimental conditions, the width of dissected wild type leaves growing outside the chamber (yellow circles and a logistic fit curve, in pink; provided by Samantha Fox, see details in Kuchen *et al.*, 2012) was compared with the width of wild type leaves growing inside the chamber (dark red) and with the width of leaves of spch4-pmCherry growing inside the chamber as well. Time-lapse experiments are identified by a number (ExpID3002, ExpID3078 and ExpID3148) and different plants within the experiment are identified with a letter (for example, PA refers to plant A, etc.). Wild type 3D width and spch4-pmCherry 3D width during time-lapse experiments show a similar slope, that is better appreciated in B) showing a zoom of the rectangular area of the plot in A. As the leaf curves during its development, the 3D width (see main text) was compared. It was measured using VolViewer and a custom algorithm developed by Matthew Hartley, giving similar results.

### 3.2.2 Confocal microscope live-imaging

Confocal microscopy has proved to be a very good tool for live-imaging of leaf development (Robinson *et al.*, 2011; Kuchen *et al.*, 2012). *In vivo* imaging, however, requires a

**Table 3.1:** Strategy for live-imaging intervals.

Time (DAS)	Imaging interval
6-8	Every 5-6 h (three times during the day)
9-11	Every 10-12 hours (twice per day)
12-13	Once per day
14-23	Once every two days.

careful balance of parameters that allows a good spatio-temporal resolution without compromising normal development. In this section, I present the combination of parameters that I found works the best for *spch4*-pmCherry, such as image interval, as well as some considerations during imaging.

The abaxial epidermis of the first true leaf was imaged using a Leica TCS SP5 II confocal microscope. Specifically, the 561 nm Diode laser and pinhole size of 1 airy unit were used. Emitted light of pmCherry was set to 570-630nm, and a hybrid detector was used to provide increased sensitivity under the 20X multi-immersion objective using water. Time-lapse experiments were identified by a number (ExpID3002, ExpID3078 and ExpID3148) and different plants within the experiment were identified with a letter (for example, PA refers to plant A, etc.).

The temporal spacing between time points was chosen to optimize the time of imaging with the spatial resolution of cellular events so that cell divisions and changes in morphology could still be detected using the automatic tracking algorithm described below (Table 3.1). Moreover, the resolution of all the images was kept to no less than 1.321 pixels per micron (a comparable resolution is important for calculating growth and shape parameters). The exact interval between time points for individual experiments is detailed in the appendix.

The total time of scanning per time point needs to be optimized because tissue grows and pushes the desired region of interest outside the specified imaging distance in the z-plane or xy-plane. When the overall size of the leaf is impossible to fit in one image (keeping the resolution), it is important to subdivide the field in tiles that need to overlap (so, they can be stitched together without problems afterwards). However, more tiles also imply that the time of scanning will increase. At the same time, a slow scanning results in a good image quality that will minimize manual intervention in the subsequent steps of image analysis. In general, a distance of 1 micron between the sections in the Z-plane is a good compromise between the time of scan and the quality of the image (the maximum is 1.5 microns). The acquisition of a 172  $\mu\text{m}$  image stack using bidirectional scanning with a frame size of 1024 and 2 line averages, will take approximately 15 minutes at the beginning of the time lapse. Later on, when it is needed to subdivide the tissue into tiles in order to have a complete image in its full spatial context, the scanning can take up to 3 hours. These parameters provided excellent image quality for the downstream image

processing applications.

The mounted chamber was moved to the CEC growth room when no imaging was performed.

## 3.3 Image processing

The confocal microscope imaging process produces a set of optical sections of the leaf (a Z-stack). This raw data needs to be transformed into meaningful representations to allow extracting quantitative data from the Z-stacks. The heterogeneous image quality during a time-lapse and the intrinsic properties of the leaf epidermis (curvature) and cells (complex shapes), make the image analysis face as many challenges as the image capture. In this section, I describe the protocol for image analysis that was used during the course of this work.

### 3.3.1 2D projection

The analysis of cell dynamics in the epidermis of the *Arabidopsis thaliana* leaf can be further simplified if a 2D projection is considered. Although a 3D reconstruction is possible, epidermal cells are very flat and the resolution of top and bottom membranes will require a very fine Z-stack that compromises the exposure of live tissue to phototoxicity and increase enormously the time required for scanning. Besides overcoming technical difficulties, 2D projections are also favoured given that pavement cell morphogenesis involves preferential extension in the xy direction (Figure 3.4A). Indeed, the thickness in the z-axis during leaf development is almost constant even under water stress (Wuyts *et al.*, 2012) and during time-lapse experiments performed in this work (Figure 3.4B average thickness is 13.2 +/- 3.6 microns).

The imaging processing starts by converting the microscope optical sections (Z-stack) into individual images in Portable Network Graphics (PNG) format using *Bioformats converter* (<http://www.bioimage.ucsb.edu>).

The simplest approach for creating a 2D-projection from the Z-stacks is to take the maximum projection (implemented into the software of many confocal microscopes). In this projection, each pixel at position  $(x', y')$  is given by the highest value of all pixels at position  $(x_n, y_n)$  for  $n$  optical slices at different Z positions. This approach works very well when the surface to project is in a single plane. However, the leaf is curved and some optical sections contain parts of the epidermis and subepidermis tissue (Figure 3.4A-B); so, a maximum projection image contains cell outlines of both tissues overlapped. Thus, to create a 2D-projection that correspond just to the epidermis, the leaf curvature needs to be taken into account.

The 2D-projections of a convex surface such as the leaf epidermis were achieved using an in-house script written by Matthew Hartley (epidermis) and Jop van Rooij (subepidermis).

The first step in the algorithm is to find the curved surface. This is achieved by applying a strong Gaussian filter in 3D (Z-stack). In simple terms, a Gaussian filter acts on each pixel, setting its value to the weighted-average of all pixel values for a given radius. Typically, the setting 8 6 6 10, corresponding to a Gaussian filter of kernel size of 8 in the x and y directions and 6 in the z direction followed by a blur of the whole surface of radius 10 gives very good results (usually using settings between 6 6 5 8 and 9 9 6 10 works with the confocal data of the leaf). Next, a vector normal to the plane of projection at each point in the plane is calculated and the coordinates of the point of maximum intensity along that vector (these points describe a 2D surface embedded in the 3D space of the image) is used to create the final 2D-projection.

The algorithm has the advantage of recovering both the projection (Figure 3.4D) and the surface of the top layer of the epidermis (Figure 3.4E), which represent a height map that can then be used to measure the dimensions of the leaf (width or length) accurately. Indeed, the width of the leaf was calculated using the surface and projection. This was done by manually setting two points that correspond to the transversal plane using a script and interface provided by Mathew Hartley. The width of the leaf, chosen as approximation of leaf dimension, follows a very similar trend to that of the leaf length (Kuchen *et al.*, 2012).

An extra feature of the algorithm is that by adjusting the distance between the detected surface and projection, it permits to take a projection of the next layer below the epidermis by stripping off the upper most layer (Figure 3.4F, although the resolution is lower than the projection of the epidermis).

In situations when the confocal imaging required tiling (for example, to capture the whole tissue, when the leaf size is too big, required to divide the scanning field in several parts), the individual 2D-images (PNG format) were later stitched. All the images were rotated so that the midvein of the leaf is perpendicular to the x-axis, and then the image was cropped to cover only the area of the leaf. Finally, to reduce noise, the background was extracted and brightness and contrast were adjusted when needed. All the above was done using the functions implemented in *Fiji* (<http://fiji.sc/Fiji>).

The next step in the pipeline is to find individual cells in the images, a process referred to as segmentation.

## 3.4 Segmentation

In a 2D projection, cells are represented by pixels within a confocal image. Segmentation is the process of going from a pixel-based representation of data to an object-based repre-

sentation, such that quantitative properties and characteristics of the objects, for example cell shape and cell area, can be extracted from the images (Roeder *et al.*, 2012a). Because of the complexity of pavement cell shape, it has been very challenging to automatically segment these cells, leading to an intensive manual intervention (see for example Andriankaja *et al.*, 2012). This is, of course, time consuming and limits the amount of cell data (and images) that can be analysed.

In this work, collaboration with Jop van Rooij (Marée's group) made it possible to extend a computer algorithm to automatically segment pavement cells that overcomes such difficulties. The algorithm, called Segmentation Potts Model, is detailed in van Rooij *et al.*, 2013a and is briefly described in the next section.

#### 3.4.1 Segmentation Potts Model (SPM)

The SPM is based on the Cellular Potts Model (CPM), an energy-based modelling formalism, in which cells are represented within a lattice and their dynamics are governed by an energy function (Graner & Glazier, 1992; Glazier & Graner, 1993, also see Chapter 2, where the CPM was used to create *in silico* cells to test the LOCO-EFA method). Briefly, cell dynamics in the CPM come about by considering a random change within the neighbouring lattice points each time step (small retraction or contraction, also called “copy event”). The changes are accepted or rejected with a certain probability depending on the total energy contribution (Hamiltonian). Copy events that are energetically expensive are accepted with a probability that drops exponentially with the change in energy (i.e. a very expensive copy event has very low probability to occur).

The SPM uses the same principles as the CPM but it includes two important modifications in the energy function that make it possible to use it as a segmentation tool. The first added term allows interaction with the image by adding an energy cost according to the normalized signal intensity of a pixel (given by the fluorescence of the membrane marker in this case). Thus, the copy events that extend into a high intensity pixel are less favoured; as a consequence the SPM-cells are “trapped” by the contouring plasma membrane signal. The second term, the total target area (rather than a single target area), controls the fraction of the image that will be occupied by cells. This term avoids the need to assume *a priori* the area and number of real cells.

In very simple terms, the algorithm takes as an input the 2D projection of the leaf (Figure 3.5A) and starts by normalizing the intensity of the plasma membrane marker (rescaling it between -1 and 1, with a defined threshold; shown in Figure 3.5B); then, it proceeds by allocating SPM-cells within the confocal image automatically (manual seeding or nucleous staining is not required). Over time, those SPM-cells expand and interact between each other and with the image, giving as a result a match of one SPM-cell to one epidermal cell (Figure 3.5C). Finally, the cell outline is smoothed recursively by assigning each unsegmented (unoccupied) pixel to the SPM-cell that is within its neighbourhood

(see details in van Rooij *et al.*, 2013a).

Although the SPM algorithm gives very good results for epidermal cells at early stages of development (when cells are rectangular or hexagonal), the segmentation of pavement cells with complex shapes introduces an extra complication. Because of the puzzle-like shape, with lobes and narrow necks, the extensions of SPM-cells located inside real cells are less favourable (because in order to extend, they need to overcome a large local energy barrier). This results in that a single biological cell is often represented by multiple SPM-cells (Figure 3.5D). The solution to this problem was to introduce persistence in the SPM dynamics when two neighbouring SPM-cells interact. This simply implies that when there are two SPM-cells separated by a normalized signal the intensity of which is below zero (for example, indicating that the interface is not a high intensity membrane marker signal), the likelihood of extension in a certain direction (i.e. accepting copy events) increases. In this way, SPM-cells will continue expanding with a persistence strength that depends on the signal value of the interface between SPM-cells, the persistence vector of each SPM-cell and the vector of the place that is being copied to. In other words, when two SPM-cells are in contact in a region of low intensity, the incorporation of persistence makes the boundary between two cells more likely to continue moving into the direction it has been recently following making it easier to overcome the energy maxima caused by a jigsaw puzzle-like shape. Of course, persistence levels need to be optimal to avoid the risk of causing SPM-cells to occupy the space of two real biological cells. Thus, the incorporation of balanced levels of persistence improves the segmentation of complex pavement cells (Figure 3.5E).

Rather than test all the possible combinations of relevant SPM parameters (at least 6), all the confocal images were segmented using the same settings for the algorithm (appendix section).

However, the complexity of cell shapes, variation within the image and big size (up to 4900 x 4000 pixels) of the time-lapse images required manual verification of the segmentation (approximately, 5% to 30% of false positives or false negatives depending on the image). In this way, cells that were over-segmented (one SPM-cell for two or more real cells) and SPM-cells that do not represent any real cell (for example, the edges of the image) were eliminated manually. In addition, SPM-cells that represent one single biological cell were fused. Manual correction was performed using a custom-made program with a user interface that was provided by Jop van Rooij.

The final segmented image permits extraction of cell area, cell perimeter, cell contour (used for shape quantification as described in Chapter 2), and was used as an input for the tracking algorithm described in the following section. Moreover, using the SPM it is possible to extract features about the topology such as number of neighbours and their characteristics.

### 3.5 Automatic cell tracking

Cell growth rates and cell shape change can be calculated only when the same cell (and its properties) is identified in consecutive time points. Cell tracking or the identification of single cells in different time frames can be done manually (Robinson *et al.*, 2011). However, this approach limits the scope of spatio-temporal analysis. To overcome these difficulties and take advantage of other methods developed to analyse images and cell morphogenesis (SPM and LOCO-EFA), we developed an automatic tracking algorithm that permits cell lineage identification in time series of images.

Automatic cell tracking requires both establishing a common coordinate system between two successive images (also called image registration) and identification of the same cells between images. Although, there is no cell movement, no cell fusion and no cell death in epidermal plant tissue, the coordinate system is changing constantly due to overall growth and local anisotropy during leaf development (Kuchen *et al.*, 2012). In addition, at the cellular level, cells are dividing, expanding and increasing their shape complexity (Chapter 4). Moreover, during imaging, the tiling, movement of the leaf inside the chamber due to grow, or variance in the position between imaging moments could modify the coordinate system. Thus, these global and local changes needed to be taken into consideration to develop the tracking algorithm.

In brief, as a starting point for estimating both the common coordinate system and the tissue growth, some cells are matched in successive images using the quantitative measures of the cell shape described previously (Figure 3.6A-B and LOCO-EFA, described in Chapter 2). The rationale is similar to comparing unique “finger prints” between individual cells at consecutive moments, on the assumption that at a subsequent time point, the same cell should still show the most similar profile to itself. Initially, tissue growth and the change in the common coordinate system are modelled as a purely affine transformation (that is the same as assuming that growth is uniform or that successive images are just an translation, uniform expansion or contraction). Then, the centroids of the matched cells are used to calculate local growth deviations from the global growth estimation, refining the growth vector. Next, cells with similar shape and within the same neighbourhood (displaced just by the local growth) in different time points are recognized as the same cell. Iteration of this simple algorithm performs very well to track pavement cells (Figure 3.6E, in general about 80-92% of cells present in consecutive time frames).

The steps of the algorithm are as follows:

1. Calculate shape parameters (LOCO-EFA), real areas (rather than in pixel/voxel unit) and centroid positions for all cells. Cell area was corrected automatically using the resolution of the confocal image included in the raw confocal data.
2. Select cells with a distinctive shape, based on their shape parameters (we can re-

fer to these cells as landmark cells). The selection of these cells can be specified algorithmically ( $L_n$ -mode profile) or manually. Between 4-8 landmark cells selected gave good results (Figure 3.6B).

3. Compare shape parameters between successive images, using a weighted sum of squares to find the closest matches for the selected cells. As the  $L_n$ -mode and XOR profile (Chapter 2) of one cell is very similar over time (Figure 3.6A), we compare the  $L_n$ -mode profile of the landmark cells against the profile of the rest of the cells and find the candidate cells in the next time point which profile is the most similar.
4. Given the list of suggested matches, estimate global growth parameters between successive images. The global growth parameters scale together with the displacements of the image. Only an affine transformation is considered at this stage.
5. Use these parameters to attempt to match cells, searching for centroids in a region around the point predicted by applying the expected growth and determining suitability of the match using real areas and shape parameters (Figure 3.6C).
6. Given the selected matches, refine the growth parameters, also including estimations of local growth that deviate from global growth.
7. Repeat steps 5) and 6), refining parameters and matching a greater proportion of cells, until the proportion matched stops increasing with further iterations (Figure 3.6D-E).
8. Look for cell divisions by determining whether pairs of cells in the later time point together give a suitable real area and centroid to be considered a match for cells in the previous time point.
9. Finally, there are two possible kinds of match: one to one and one to two corresponding to the same cell expanding and cell division. There is also mismatches because of error in the image, leading to one cell to none (for example, it happens that some cells are absent in a particular image because of an error during image acquisition or segmentation). Incorrect matches also can happen when cells have a very similar shape and they are very close to each other (i.e. base of the leaf).

Because of the variations in the quality and size of images, a final human inspection of the matches and manual correction of the errors ensured that cell lineages obtained using the cell tracking algorithm were correct.

The output of the cell tracking algorithm (Figure 3.7) includes information that permits the study of the spatio-temporal dynamics at the cellular level such as cell division, cell position, cell growth, cell shape as well as tissue information such as local growth displacements (growth anisotropy) and topological characteristics over time. The boundaries of the leaf (tip, starting of petiole and left and right border) were set manually.

The algorithm was implemented, refined and integrated into the previous image processing analysis by Matthew Hartley in the Python programming language, using Numpy and Scipy libraries ([dsnr.jpl.nasa.gov/software/Python/numpydoc/](http://dsnr.jpl.nasa.gov/software/Python/numpydoc/) and [www.scipy.org/](http://www.scipy.org/)), with Pygame ([pygame.org/](http://pygame.org/)) for display purposes.

## 3.6 Discussion and concluding remarks

Diverse studies of leaf development have aimed to capture cell dynamics over time (see for example, Andriankaja *et al.*, 2012). However, static images are not as powerful as time-lapse imaging, where cell data is captured in its full and intact spatial context. *In toto* imaging, or the imaging and tracking of every single cell that forms a tissue or organ is a powerful approach to understand how cell growth, cell morphogenesis and cell division occur in a developing tissue or organ (Megason & Fraser, 2007). In this chapter, I described the pipeline that involved the synergy between confocal imaging optimization and new image analysis techniques that allowed *in toto* imaging of leaf development.

The motivation to develop such an integrative pipeline was that current imaging protocols aimed at the extraction of quantitative cell information from time-lapse imaging were inconvenient for the analysis of epidermal cell dynamics during leaf development. For example, De Reuille *et al.* (2005) reported a pipeline that creates 2D projections of the dome-like meristem and proposed a tracking algorithm that was adapted to analyse leaf development (Kuchen *et al.*, 2012). However, this approach requires extensive manual intervention (marking cell vertices in consecutive images). Another related method for cell tracking was proposed by Liu *et al.* (2010) with focus on meristematic cells in the shoot apex. This method is based on graph matching and local geometry (i.e the vertices of cell neighbours), a feature that is fairly conserved over time for cells in the meristem. In case of pavement cells, a graph matching algorithm will be complicated because the cell shape experiences a very dramatic transition from a geometrical simple shape to a jigsaw-like shape (Chapter 4 and 5). The tracking method presented in this chapter does not rely on the conservation of the vertices of a cell, but uses the shape as a feature for finding cells in the tracking procedure. Moreover, other proposed methods for segmenting cells with complex shape rely on very high resolution images, perhaps only achieved with fixed material (Federici *et al.*, 2012).

Improvement of current imaging techniques and development of new tools made it possible to capture the dynamics of cell growth and cell shape change until it is very close to saturation in different parts of the leaf, and cell divisions finish (Chapter 4). First, the use of bright and long-lasting membrane markers, combined with the simplified leaf of the *spch* mutant and an optimal imaging strategy during time-lapse to minimize the exposure of the leaf, made it possible to track cell dynamics over long periods of time. In addition, the complexity of the time-lapse data required the development of new tech-

niques for imaging processing that allowed us to extract relevant information from the raw confocal images. These imaging processing tools included 2D projections of curved surfaces, segmentation of complex shapes and a cell tracking algorithm.

Therefore, to exploit the full potential of live-imaging and microscopy methods, they must be combined with computational approaches and models that help to convert the resulting, highly complex image data sets into biological insights. Indeed, a robust pipeline for analysing *in toto* leaf development is able to quantify the behaviour of a system at the cellular level because it permits a detailed description of morphogenetic and developmental processes at cellular resolution, such as spatio-temporal dynamics of cell division, cell position, cell growth and cell shape dynamics throughout development (Chapter 4).

Currently, the output of the SPM is used as an input for the cell tracking algorithm. In the future, the pipeline can be improved by allowing the SPM and the cell tracking algorithm to feedback into each other: conflicts in the segmentation (one biological cell to two SPM-cells or vice versa) could be resolved by looking at the future and/or the past time-points of the cell tracking (for instance, cell division happen in only one direction; hence, once a cell division is detected, it is expected that the future time points show two different cells). This possible extension is likely to decrease the manual intervention.

**Table 3.2: DNA extraction buffers**

<b>Extraction Solution*</b>	Stock	100 ml
Water		63 ml
100 mM (1.57%) Tris-HCl pH=8	1M	10 ml
250 mM (1.86%) KCl	1M	25 ml
10 mM (0.37%) EDTA	0.5 M	2 ml

(a)

<b>Dilution Solution<sup>+</sup></b>	stock	100 ml
Water		100 ml
3% BSA	powder	3 g

(b)

\*Adjust to pH 9.3 with 1N KOH.

+ Adjust pH to 7.6 with 1 N KOH

## 3.A Appendix

### 3.A.1 DNA extraction protocol\*\*

1. Cut a young piece of leaf with a pair of tweezers and place in a PCR tube.
2. Add 50 $\mu$ l of **Extraction Solution** to the collection tube. Close the tube, vortex and spin briefly to make sure the tissue is covered by the solution (Table 3.2a).
3. Incubate at 95 °C for 10 minutes (the leaf tissue usually do not appear to be degraded after this treatment).
4. Add 50 $\mu$ l of **Dilution Solution**, mix with the pipette and transfer 50 $\mu$ l genomic DNA solution to a new tube (Table 3.2b).
5. Store the diluted leaf extract at 2-8 °C.

\*\*This protocol was provided by Vladimir Nekrasov.

**Table 3.3: Genotyping of the spch4-pmCherry line**

Line	Left primer	Right primer	Expected size	PCR amplification conditions
spch4 (SALK_078595)	TATGAGGGACTCGCATTATC	AAAACAAATTCGTTTGCTCCC	Wild type:1047; Mutant: BP+RP: ~700bp	94 C for 2 min; (94 C for 20s; 54 C for 1min; 72 C for 1min) for 35 cycles; 72 C for 5 min;

**Table 3.4: Parameters used for the segmentation using the SPM.**

Parameter	Value	Brief description
<i>hamiltonianneigh</i>	0	Neighbourhood over which surface tension is calculated
<i>imageinteraction</i>	350	Constant that is multiplied with the normalized signal at each pixel in the Hamiltonian function.
<i>estimationoffset</i>	-2	Offset for target coverage estimation algorithm
<i>temperaturescale</i>	350	Percentage of the highest possible contribution of the interfacial tension with the medium.
<i>persistencestrength</i>	3	Percentage of persistence.
<i>persistenceclength</i>	100	Number of Monte Carlo steps (mcs) between updating persistence vectors
<i>runtime</i>	10000	Mcs used for segmentation

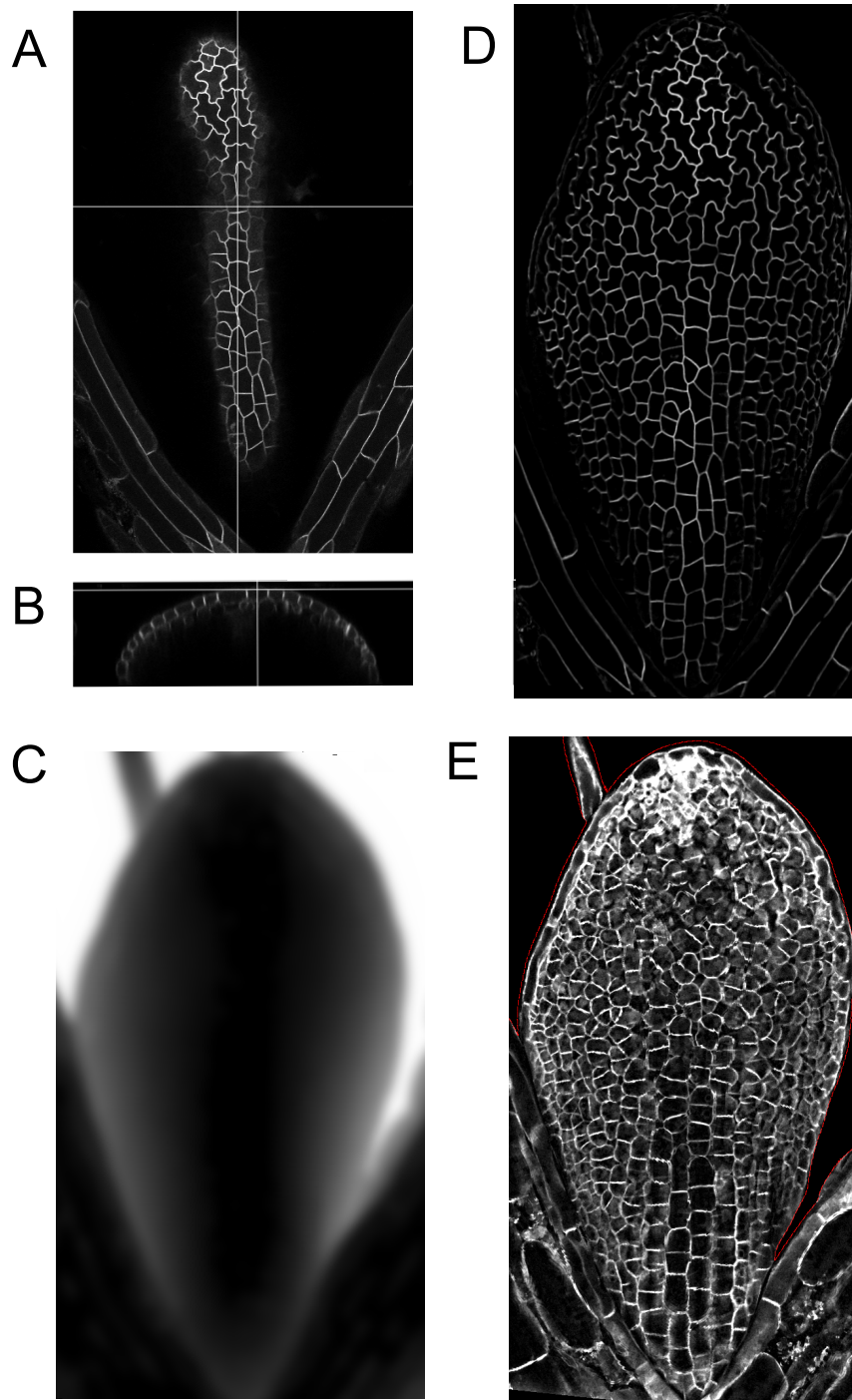


**Figure 3.4: Projections of the leaf epidermis using confocal optical sections require a special algorithm because the surface is curved.** A) Optical slice obtained using a confocal microscope. Although, the maximum resolution is achieved in the xy direction, the slices are not in the same plane. B) Optical transversal section through the horizontal line denoted in A in the z plane. Note the curvature of the surface and the constant thickness of the epidermal layer (average thickness in this example is  $10.2 \pm 1.2 \mu\text{m}$ ). C) The algorithm to create 2D-projections of a curved surface involves a strong 3D Gaussian filter and maximum intensity approach that is used to create a smoothed height map of the surface. D) The final projection takes the maximum intensity along the normal to the surface (similar to a top view of the leaf). E) By changing the distance between the detected surface and projection, it is possible to project inner surfaces. In this example, the planes of the Z-stack are spaced each  $1 \mu\text{m}$  and overall thickness of the Z-stack is  $150 \mu\text{m}$ .

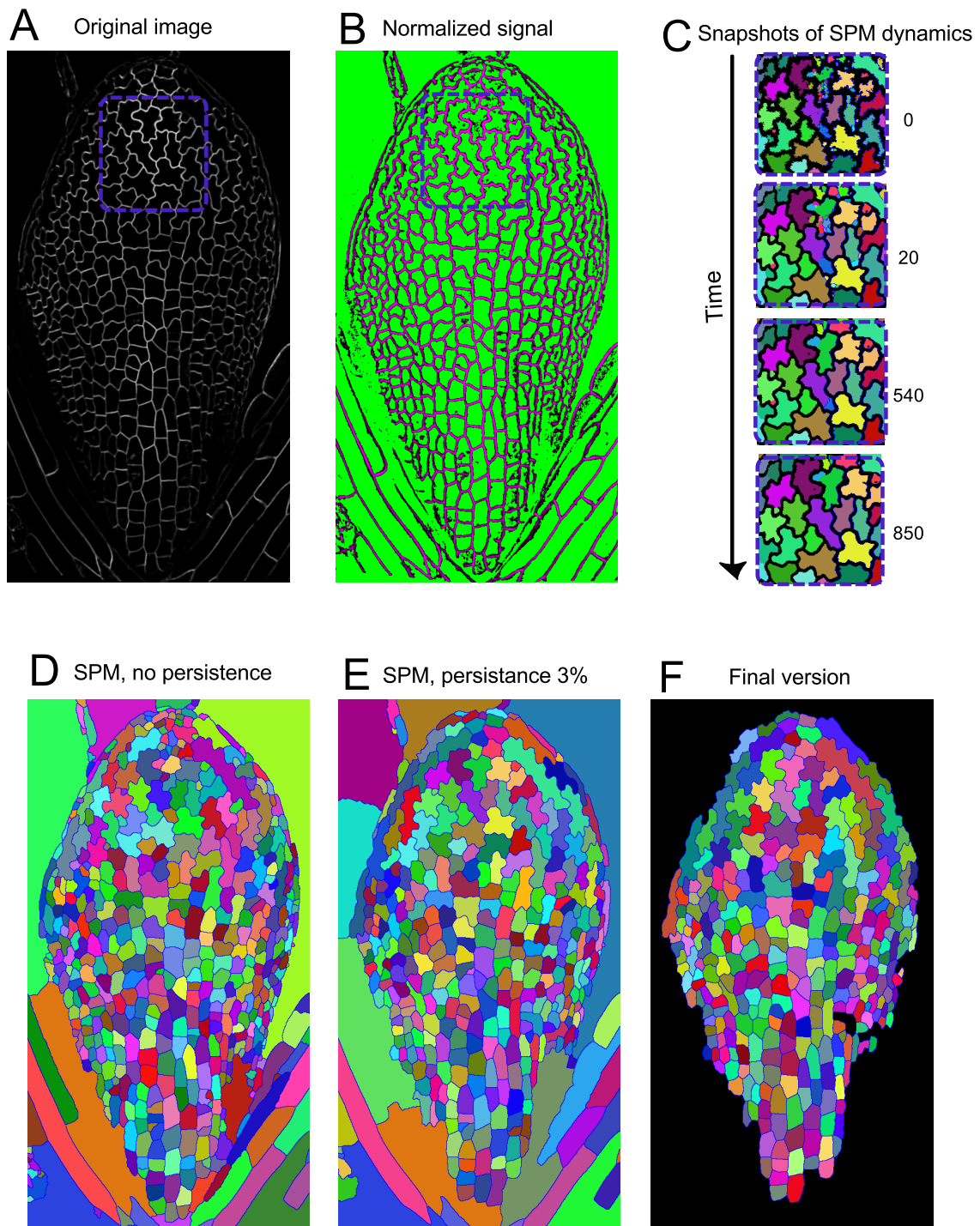


**Figure 3.5: Segmentation Potts Model is used to find cells in the confocal image.**

A) Original image after image processing (ie. 2D projection). B) The SPM algorithm normalizes the signal given by the pmCherry marker. SPM-cell extension is unfavoured if it implies crossing a high level of intensity given by the membrane marker (pink). C) Snapshots of SPM dynamics in a section of the leaf (denoted by the square in A-B). A single SPM-cell is identified with a colour. Over time, the SPM-cells compete and exclude each other, giving as a result that each biological cell is represented by a single SPM-cell. The number on the right of each inset is the simulation time (see details in van Rooij *et al.*, 2013a). D) Final result of the SPM simulation without persistence. E) By incorporating reasonable amounts of persistence, more pavement cells are correctly resolved. F) Manual correction ensures that each real cell is correctly identified.

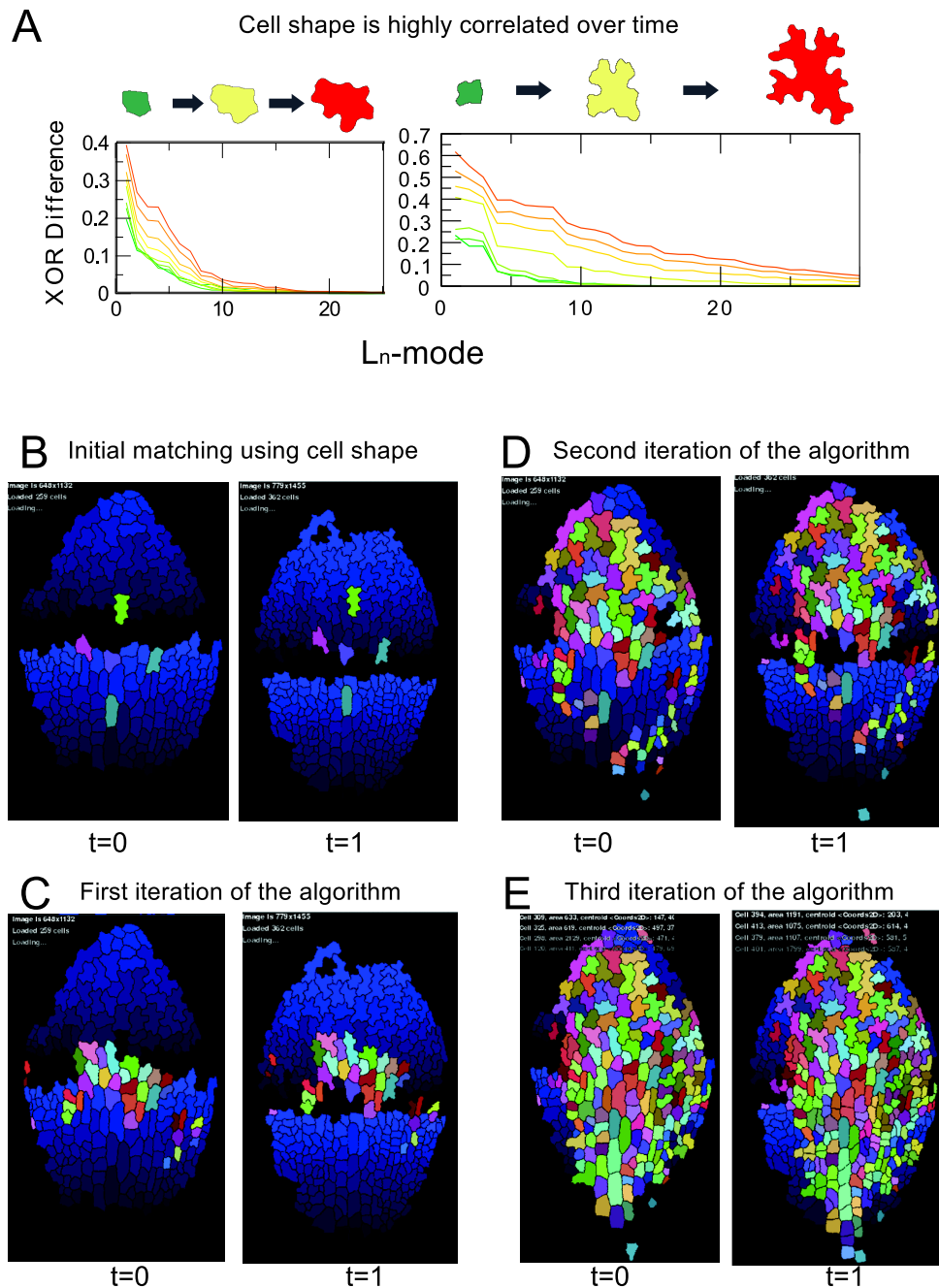


**Figure 3.6: Cell tracking algorithm.** A) The cell shape over time is characterized using LOCO-EFA parameters (XOR, or the difference between the original and reconstructed shape using  $N$  number of  $L_n$  modes is shown for two cells changing over time, see also Chapter 2). Note that the cell shape profile is changing in a very similar fashion over time (each colour is a time point, green colours are early time points and red colours correspond to late time points). This property is used to locate some initial cells based on the change on their shape. B) The cell tracking algorithm takes as input the segmented image (each cell is identified with a unique RGB number) and uses the information of the shape to locate some initial matches (landmarks) among two time points (in this case, four landmarks initiate the algorithm). C) Assuming homogeneous growth, the algorithm continues finding matched cells taking the cell shape and relative displacement into account. D-E) Iteration of this process refines the growth parameters and locates more cells automatically.

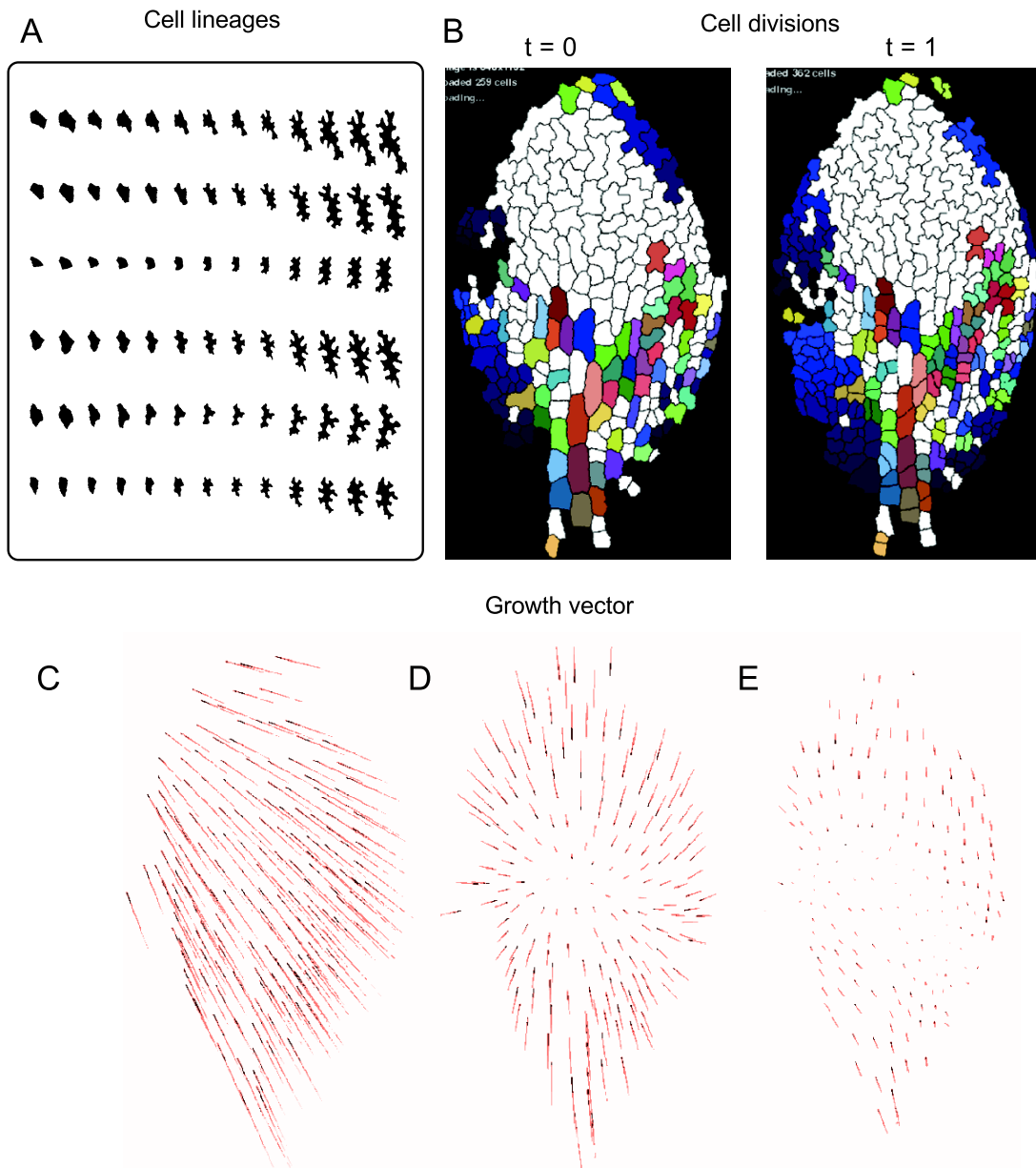


**Figure 3.7: Cell tracking algorithm enables the extraction of quantitative and dynamic data at the cell and tissue level.** A) The output of the tracking algorithm includes cell lineages (not to scale), B) cell divisions and C-E) growth vector and anisotropy within a tissue. The growth vector is calculated using the displacements of centre of mass in two consecutive time-points. C) The overall displacement of the centroids of two cells. D) After removing the average of all the vectors results in a map of overall displacements. E) Finally, the anisotropic growth is calculated by subtracting a proportion of the displacement relative to the vectors in the centre (or relative to any other point of reference). This corresponds to removing the proportion of isotropic growth, leaving just the component that correspond to the anisotropic growth.

### 3 Long time lapse and image analysis on in vivo leaf development at cellular scale

ExpID3002_PA							
Series Name	Date Moved to CER	Time moved to CER	Date Imaged	Time imaged	age at imaging (DAS)	Age (HAS)	3D Leaf Width PA (mm)
TL01_plantA	6/26/2012	4:30:00 PM	7/3/2012	11:18:00 PM	7	174.80	0.132
TL02_plantA	6/26/2012	4:30:00 PM	7/4/2012	10:02:00 AM	8	185.53	0.148
TL03_plantA	6/26/2012	4:30:00 PM	7/4/2012	5:32:00 PM	8	193.03	0.202
TL04_plantA	6/26/2012	4:30:00 PM	7/4/2012	11:38:00 PM	8	199.13	0.22
TL05_plantA	6/26/2012	4:30:00 PM	7/5/2012	10:12:00 AM	9	209.70	0.298
TL06_plantA	6/26/2012	4:30:00 PM	7/5/2012	8:39:00 PM	9	220.15	0.306
TL07_plantA	6/26/2012	4:30:00 PM	7/6/2012	8:48:00 AM	10	232.30	0.385
TL08_plantA	6/26/2012	4:30:00 PM	7/6/2012	8:24:00 PM	10	243.90	0.48
TL09_plantA	6/26/2012	4:30:00 PM	7/7/2012	11:32:00 AM	11	259.03	0.682
TL010_plantA	6/26/2012	4:30:00 PM	7/8/2012	13:52 PM	12	285.37	no

ExpID3002_PD							
Series Name	Date Moved to CER	Time moved to CER	Date Imaged	Time imaged	age at imaging (DAS)	Age (HAS)	3D Leaf Width PD (mm)
TL01_plantD	6/26/2012	4:30:00 PM	7/3/2012	11:40:00 PM	7	175.17	0.179
TL02_plantD	6/26/2012	4:30:00 PM	7/4/2012	10:02:00 AM	8	185.53	0.185
TL03_plantD	6/26/2012	4:30:00 PM	7/4/2012	5:45:00 PM	8	193.25	0.23
TL04_plantD	6/26/2012	4:30:00 PM	7/4/2012	11:53:00 PM	8	199.38	0.268
TL05_plantD	6/26/2012	4:30:00 PM	7/5/2012	10:27:00 AM	9	209.95	0.315
TL06_plantD	6/26/2012	4:30:00 PM	7/5/2012	8:55:00 PM	9	220.42	0.377
TL07_plantD	6/26/2012	4:30:00 PM	7/6/2012	9:07:00 AM	10	232.62	0.438
TL08_plantD	6/26/2012	4:30:00 PM	7/6/2012	8:05:00 PM	10	243.58	0.487
TL09_plantD	6/26/2012	4:30:00 PM	7/7/2012	11:52:00 AM	11	259.37	0.557
TL010_plantD	6/26/2012	4:30:00 PM	7/8/2012	15:00	12	286.50	0.781
TL011_plantD	6/26/2012	4:30:00 PM	7/9/2012	10:40	13	306.17	no
TL012_plantD	6/26/2012	4:30:00 PM	7/10/2012	11:00:00 AM	14	330.50	no
TL013_plantD	6/26/2012	4:30:00 PM	7/11/2012	11:26:00 AM	15	354.93	no
TL014_plantD	6/26/2012	4:30:00 PM	7/12/2012	8:37:00 PM	16	388.12	1.464043
TL015_plantD	6/26/2012	4:30:00 PM	7/13/2012	20:35	17	412.08	no
TL016_plantD	6/26/2012	4:30:00 PM	7/14/2012	17:32	18	433.03	1.81
TL017_plantD	6/26/2012	4:30:00 PM	7/15/2012	23:38	19	463.13	1.903
TL018_plantD	6/26/2012	4:30:00 PM	7/17/2012	19:56	21	507.43	no
TL019_plantD	6/26/2012	4:30:00 PM	7/19/2012	17:18	23	562.80	2.258

EXPID3078_PA							
Series Name	Date Moved to CER	Time moved to CER	Date Imaged	Time imaged	age at imaging (DAS)	Age (HAS)	3D Leaf Width PA (mm)
TL00_plantA	9/27/2012	6:30:00 PM	10/3/2012	13:38:00	6	139.13	no accurate
TL01_plantA	9/27/2012	6:30:00 PM	10/3/2012	18:06:00	6	143.60	0.125
TL02_plantA	9/27/2012	6:30:00 PM	10/3/2012	23:36:00	6	149.10	0.14
TL03_plantA	9/27/2012	6:30:00 PM	10/4/2012	10:43	7	160.22	0.153
TL04_plantA	9/27/2012	6:30:00 PM	10/4/2012	16:33:00	7	166.05	0.166
TL05_plantA	9/27/2012	6:30:00 PM	10/4/2012	23:03:00	7	172.55	0.197
TL06_plantA	9/27/2012	6:30:00 PM	10/5/2012	10:36	8	184.10	0.277
TL07_plantA	9/27/2012	6:30:00 PM	10/5/2012	16:23	8	189.88	0.305
TL08_plantA	9/27/2012	6:30:00 PM	10/5/2012	22:34:00	8	196.07	0.365
TL09_plantA	9/27/2012	6:30:00 PM	10/6/2012	12:29:00	9	209.98	0.47
TL010_plantA	9/27/2012	6:30:00 PM	10/7/2012	0:36:00	10	222.10	0.523
TL011_plantA	9/27/2012	6:30:00 PM	10/7/2012	13:27:00	10	234.95	0.592
TL012_plantA	9/27/2012	6:30:00 PM	10/8/2012	0:30	11	246.00	0.709
TL013_plantA	9/27/2012	6:30:00 PM	10/8/2012	14:07	11	259.62	0.752
TL014_plantA	9/27/2012	6:30:00 PM	10/8/2012	19:04:00	11	264.57	no accurate
TL015_plantA	9/27/2012	6:30:00 PM	10/9/2012	10:59:00	12	280.48	no accurate
TL016_plantA	9/27/2012	6:30:00 PM	10/9/2012	20:30:00	12	290.00	1.096896291
TL017_plantA	9/27/2012	6:30:00 PM	10/10/2012	23:57	13	317.45	1.310370931
TL018_plantA	9/27/2012	6:30:00 PM	10/11/2012	19:50	14	337.33	no accurate
TL019_plantA	9/27/2012	6:30:00 PM	10/12/2012	20:58	15	362.47	no accurate
TL020_plantA	9/27/2012	6:30:00 PM	10/13/2012	21:51	16	387.35	no accurate
TL021_plantA	9/27/2012	6:30:00 PM	10/14/2012	19:49	17	409.32	no accurate

EXPID3078_PC								
Series Name	Date Moved to CER	Time moved to CER	Date Imaged	Time imaged	age at imaging (DAS)	Age (HAS)	3D Leaf Width PC (mm)	elapsed time (h)
TL00_plantC	9/27/2012	6:30:00 PM	10/3/2012	14:02:00	6	139.53	no accurate	0.00
TL01_plantC	9/27/2012	6:30:00 PM	10/3/2012	18:45:00	6	144.25	0.121	4:43:00
TL02_plantC	9/27/2012	6:30:00 PM	10/4/2012	0:04:00	7	149.57	0.138	10:02:00
TL03_plantC	9/27/2012	6:30:00 PM	10/4/2012	11:12	7	160.70	0.151	11:08:00
TL04_plantC	9/27/2012	6:30:00 PM	10/4/2012	16:56:00	7	166.43	0.186	16:52:00
TL05_plantC	9/27/2012	6:30:00 PM	10/4/2012	23:27:00	7	172.95	0.233	6:31:00
TL06_plantC	9/27/2012	6:30:00 PM	10/5/2012	11:04	8	184.57	0.268	18:08:00
TL07_plantC	9/27/2012	6:30:00 PM	10/5/2012	16:39	8	190.15	0.288	5:35:00
TL08_plantC	9/27/2012	6:30:00 PM	10/5/2012	22:51:00	8	196.35	0.311	11:47:00
TL09_plantC	9/27/2012	6:30:00 PM	10/6/2012	12:29:00	9	209.98	0.3405	13:38:00
TL010_plantC	9/27/2012	6:30:00 PM	10/7/2012	1:00:00	10	222.50	0.419	26:09:00
TL011_plantC	9/27/2012	6:30:00 PM	10/7/2012	12:53:00	10	234.38	0.52	11:53:00
TL012_plantC	9/27/2012	6:30:00 PM	10/7/2012	23:42	10	245.20	0.607	22:42:00
TL013_plantC	9/27/2012	6:30:00 PM	10/8/2012	1:41	11	271.18	0.7	25:59:00
TL014_plantC	9/27/2012	6:30:00 PM	10/8/2012	7:52:00	11	277.37	0.79	32:10:00
TL015_plantC	9/27/2012	6:30:00 PM	10/9/2012	no taken	no	no taken	no taken	no taken
TL016_plantC	9/27/2012	6:30:00 PM	10/9/2012	22:06:00	12	291.60	1.064345193	14:14:00
TL017_plantC	9/27/2012	6:30:00 PM	10/10/2012	1:27	13	294.95	no accurate	3:21:00
TL018_plantC	9/27/2012	6:30:00 PM	10/11/2012	21:22	14	338.87	no accurate	47:16:00
TL019_plantC	9/27/2012	6:30:00 PM	10/12/2012	no taken	no	no taken	no taken	no taken
TL020_plantC	9/27/2012	6:30:00 PM	10/13/2012	19:39	16	385.15	no accurate	46:17:00

Figure 3.8: Details of the tracking experiments.

EXPID3148_PA								
Series Name	Date Moved to CER	Time moved to CER	Date Imaged	Time imaged	age at imaging (DAS)	Age (HAS)	3D Leaf Width PA (mm)	elapsed time (h)
TL00_plantA	1/10/2013	6:00:00 PM	1/16/2013	15:06:00	6	141.10	no accurate	0:00
TL01_plantA	1/10/2013	6:00:00 PM	1/16/2013	19:10:00	6	145.17	0.116	4:04:00
TL02_plantA	1/10/2013	6:00:00 PM	1/16/2013	22:24:00	6	148.40	0.125	7:18:00
TL03_plantA	1/10/2013	6:00:00 PM	1/17/2013	10:32	7	160.53	0.133	12:08:00
TL04_plantA	1/10/2013	6:00:00 PM	1/17/2013	15:51:00	7	166.85	0.14	17:27:00
TL05_plantA	1/10/2013	6:00:00 PM	1/17/2013	22:09:00	7	172.15	0.163	6:18:00
TL06_plantA	1/10/2013	6:00:00 PM	1/18/2013	10:18	8	184.30	0.202	18:27:00
TL07_plantA	1/10/2013	6:00:00 PM	1/18/2013	16:32	8	190.53	0.248	6:14:00
TL08_plantA	1/10/2013	6:00:00 PM	1/18/2013	22:08:00	8	196.13	0.284	11:50:00
TL09_plantA	1/10/2013	6:00:00 PM	1/19/2013	10:57:00	9	208.95	0.362	12:49:00
TL010_plantA	1/10/2013	6:00:00 PM	1/19/2013	22:33:00	9	220.55	0.435	24:25:00
TL011_plantA	1/10/2013	6:00:00 PM	1/20/2013	11:54:00	10	233.90	0.48	13:21:00
TL012_plantA	1/10/2013	6:00:00 PM	1/20/2013	22:21	10	244.35	0.54	23:48:00
TL013_plantA	1/10/2013	6:00:00 PM	1/21/2013	11:04	11	257.07	0.62	1:00
TL014_plantA	1/10/2013	6:00:00 PM	1/21/2013	21:51:00	11	267.85	0.723	10:47:00
TL015_plantA	1/10/2013	6:00:00 PM	1/22/2013	11:17:00	12	281.28	0.847	24:13:00
TL016_plantA	1/10/2013	6:00:00 PM	1/22/2013	20:35:00	12	290.58	0.973	9:18:00
TL017_plantA	1/10/2013	6:00:00 PM	1/23/2013	19:42	13	313.70	1.242	32:25:00
TL018_plantA	1/10/2013	6:00:00 PM	1/24/2013	16:06	14	334.10	1.455	20:24:00
TL019_plantA	1/10/2013	6:00:00 PM	1/25/2013	19:11	15	361.18	1.723694171	47:29:00
TL020_plantA	1/10/2013	6:00:00 PM	1/26/2013	20:40	16	386.67	2.025738077	25:29:00
TL021_plantA	1/10/2013	6:00:00 PM	1/27/2013	16:09	17	406.15	2.143830431	44:58:00
TL022_plantA	1/10/2013	6:00:00 PM	1/28/2013	15:54	18	429.90	2.312	23:45:00
TL023_plantA	1/10/2013	6:00:00 PM	1/29/2013	22:01	19	460.02	2.587	53:52:00
TL024_plantA	1/10/2013	6:00:00 PM	1/30/2013	15:57	20	477.95	2.656	17:56:00
TL025_plantA	1/10/2013	6:00:00 PM	1/31/2013	13:47	21	499.78	2.8	39:46:00
TL026_plantA	1/10/2013	6:00:00 PM	2/1/2013	14:16	22	524.27	2.917	2:00
TL027_plantA	1/10/2013	6:00:00 PM	2/2/2013	16:34	23	550.57	3.106	26:18:00

EXPID3148_PD								
Series Name	Date Moved to CER	Time moved to CER	Date Imaged	Time imaged	age at imaging (DAS)	Age (HAS)	3D Leaf Width PD(mm)	elapsed time (h)
TL0-1_plantD	1/10/2013	6:00:00 PM	1/16/2013	1:10:00 PM	6	139.17	0.11	0:00
TL00_plantD	1/10/2013	6:00:00 PM	1/16/2013	3:33:00 PM	6	141.55	0.119	2:23:00
TL01_plantD	1/10/2013	6:00:00 PM	1/16/2013	7:27:00 PM	6	145.45	no accurate	6:17:00
TL02_plantD	1/10/2013	6:00:00 PM	1/16/2013	10:38:00 PM	6	148.63	0.122	9:28:00
TL03_plantD	1/10/2013	6:00:00 PM	1/17/2013	10:47:00 AM	7	160.78	no accurate	21:37:00
TL04_plantD	1/10/2013	6:00:00 PM	1/17/2013	4:04:00 PM	7	166.07	0.138	26:54:00
TL05_plantD	1/10/2013	6:00:00 PM	1/17/2013	10:26:00 PM	7	172.43	0.19	33:16:00
TL06_plantD	1/10/2013	6:00:00 PM	1/18/2013	10:33:00 AM	8	184.55	0.214	45:23:00
TL07_plantD	1/10/2013	6:00:00 PM	1/18/2013	4:51:00 PM	8	190.85	0.24	51:41:00
TL08_plantD	1/10/2013	6:00:00 PM	1/18/2013	22:22	8	196.37	0.245	57:12:00
TL09_plantD	1/10/2013	6:00:00 PM	1/19/2013	11:15	9	209.25	0.292	1:00
TL010_plantD	1/10/2013	6:00:00 PM	1/19/2013	22:45	9	220.75	0.326829268	11:30:00
TL011_plantD	1/10/2013	6:00:00 PM	1/20/2013	12:09	10	234.15	0.38001514	24:54:00
TL012_plantD	1/10/2013	6:00:00 PM	1/20/2013	22:41	10	244.68	0.426949281	35:26:00
TL013_plantD	1/10/2013	6:00:00 PM	1/21/2013	11:26	11	257.43	0.479409538	48:11:00
TL014_plantD	1/10/2013	6:00:00 PM	1/21/2013	20:56	11	266.93	0.565480696	57:41:00
TL015_plantD	1/10/2013	6:00:00 PM	1/22/2013	11:53	12	281.88	0.647993944	72:38:00
TL016_plantD	1/10/2013	6:00:00 PM	1/22/2013	21:11	12	291.18	0.74337623	81:56:00
TL017_plantD	1/10/2013	6:00:00 PM	1/23/2013	17:52	13	311.87	0.935654807	102:37:00
TL018_plantD	1/10/2013	6:00:00 PM	1/24/2013	17:31	14	335.52	1.108251325	126:16:00
TL019_plantD	1/10/2013	6:00:00 PM	1/25/2013	21:09	15	363.15	1.367146101	2:00
TL020_plantD	1/10/2013	6:00:00 PM	1/26/2013	20:40	16	386.67	to process	23:31:00
TL021_plantD	1/10/2013	6:00:00 PM	1/27/2013	16:09	17	406.15	to process	43:00:00
TL022_plantD	1/10/2013	6:00:00 PM	1/28/2013	15:45	18	429.75	1.8143	66:36:00
TL023_plantD	1/10/2013	6:00:00 PM	1/29/2013	15:51	19	453.85	2.131	90:42:00
TL024_plantD	1/10/2013	6:00:00 PM	1/30/2013	14:41	20	476.68	2.146	113:32:00
TL025_plantD	1/10/2013	6:00:00 PM	1/31/2013	13:54	21	499.90	2.233	136:45:00
TL026_plantD	1/10/2013	6:00:00 PM	2/1/2013	14:22	22	524.37	2.339	161:13:00
TL027_plantD	1/10/2013	6:00:00 PM	2/2/2013	19:57	23	553.95	2.491	190:48:00

Figure 3.9: Details of the tracking experiments.



## Chapter 4

# Dissecting spatial and temporal scales during leaf development at the cellular level

### Abstract

Position-dependant cellular outcomes are considered very important during morphogenesis. However, the role of position in the dynamics of the cell's behaviour during development has not been explored in plants. This is in part because the study of positional-dependant outcomes in plants presents several major problems: 1) the cell's relative position is also changing during organ growth, 2) often, the spatial and the temporal patterns overlap (i.e. cells at one extreme of the organ are also the oldest) and 3) it is technically challenging to capture cell dynamics at relevant spatial and temporal scales. Using a combined pipeline of long time-lapse imaging and computer algorithms to extract cellular dynamics it is possible to overcome the last difficulties. Here, I present the analysis of the cell's dynamics (growth, cell shape and division) at different spatial and temporal scales of leaf growth. Interestingly, the dynamics of the cell growth and the cell shape change are highly influenced by the developmental time of the cell and in minor extend, by their position. However, the position is important in the dynamics of cell divisions, that are restricted towards the base of the leaf. Importantly, direct measurement of cell division, shows that the division zone is not constant in length and that the frequency of divisions is decreasing over time in a rather gradual-fashion. The results presented in this chapter permit re-evaluate the role of position and developmental cell age and highlights the importance of separating different spatial and temporal scales during the analysis of plant development.

## 4.1 Introduction

How the dynamics of cellular behaviour (i.e, cell growth, cell morphogenesis) is regulated in time and space to produce organs with a defined shape and size remains poorly understood. One hypothesis is that the cell response depends on the cell's position with respect to the organ boundaries conferred by "morphogens", diffusible molecules that distribute in a graded fashion (Wolpert, 1969, 1994; note, however, that gradient formation is not limited to pure diffusion, see Muller & Schier, 2011; Grieneisen *et al.*, 2012). In fact, it has been extensively proposed in diverse contexts that "morphogen gradients" regulate and coordinate the growth, change in shape and fate acquisition in a position-depend manner during development (Wolpert, 2002; Anastasiou *et al.*, 2007; Grieneisen *et al.*, 2007; Jaeger *et al.*, 2008; Kazama *et al.*, 2010; Schwank & Basler, 2010; Wartlick *et al.*, 2011; Kennaway *et al.*, 2011; Kuchen *et al.*, 2012).

The positional information conferred by a gradient is presumably very important for cell types that, like plant cells, cannot move freely to adjust their position to a specific cellular environment. Indeed, in plants these mobile signals have been proposed (for example see a discussion for auxin in Grieneisen *et al.*, 2012 or more general diffusible substances in Kennaway *et al.*, 2011). However, in contrast to animals where some morphogen gradients have been identified, measured and successfully characterized (Gregor *et al.*, 2007a; Wartlick *et al.*, 2011), in plants there are scarce examples of gradients that have been directly measured and characterized (perhaps the only example is the auxin gradient in roots, see Grieneisen *et al.*, 2007; Petersson *et al.*, 2009).

A prototypical system to study the role of position on the dynamics of cellular behaviour during plant morphogenesis is the leaf. Strikingly, during leaf development there is a strong longitudinal spatial gradient in the cell size and cell shape: small polygonal cells are at the leaf base and enlarged jigsaw puzzle-like pavement cells are at the tip (Donnelly *et al.*, 1999; Andriankaja *et al.*, 2012). At the same time, cell divisions are restricted mainly at the base of the leaf until they disappear (Donnelly *et al.*, 1999; Kazama *et al.*, 2010; Andriankaja *et al.*, 2012). Besides showing this characteristic cellular behaviour, the nature of leaves as organs that reach a final predetermined size, allow us to use them as a model to understand the long-standing question of how an organ determines its final size by regulating behaviour at the the cellular level.

However, evaluating the role of the position in the cellular dynamics in plants presents several difficulties. First, the cell's relative position within the leaf is changing. Even though plant cells are restricted to move in relation to their neighbours, cells are constantly being displaced from the base of the leaf towards the tip. Therefore, the notion of position acquire different meanings, depending on the frame of reference (i.e. position from a fixed location such as the tip of the leaf *versus* the position of the cells with respect to other cells).

Another complication in addressing the influence of the position in a tissue-context is that often spatial patterns overlap with temporal patterns, making it cumbersome to

identify causal relationships; for instance, bigger and more “jigsaw puzzle-like” cells at one extreme in the organ (i.e pavement cells at the tip of the leaf) are also the oldest cells. Then, it is not easy to differentiate if the cellular behaviour is due to position or due to a specific developmental stage (i.e cell age).

A third problem is that quantify a particular cellular outcome in relation with its position or differentiation status in an organ requires quantitative criteria, which is often lacking (for example see discussion regarding the cell shape in Chapter 2). Moreover, such quantification also requires overcoming the constraints of accessing the dynamic cellular behaviour at relevant temporal and spatial scales without destroying the plant.

To overcome these obstacles, I use a combination of live imaging, automatic segmentation, automatic cell tracking algorithm (Chapter 3) and quantitative analysis of cell shape (Chapter 2) to follow the dynamics on cell growth and cell morphogenesis of populations of cells from early stages until the overall organ begins to reach its growth limit (Figure 3.3 in Chapter 3). This framework permitted me to correlate cell position with cellular behaviour extracted from the *in vivo* context of plant development. These correlations led to several hypothesis of the underlying mechanism regulating the cellular response that can be explored in the future.

I begin by presenting the analysis of the cell growth and the cell shape at different spatial and temporal scales. These two aspects have been reported as strongly correlated (Donnelly *et al.*, 1999). Thus, it is easy to compare and appreciate the subtle differences on their behaviour when one looks at them together. Interestingly, the dynamics of growth and shape is highly influenced by the age of the cell (taking as  $t = 0$ , the time after cell division).

These results, led to the analysis of how cell divisions are organized within the leaf and are discussed in the second part of the chapter. The results presented here supports that cell divisions happen in a restricted spatial domain at the base of the leaf, but contrary to previous reports (Kazama *et al.*, 2010; Andriankaja *et al.*, 2012; Lenhard, 2012), it does not remain constant in length. Temporal analysis of cell divisions also reveals that at the same time they are progressively restricted in space, the proportion of dividing cells is also decreasing over time.

Once correlations between spatial and temporal scales and cellular dynamics have been established, it is important to probe the system through perturbations in order to gain further insights about the underlying mechanism controlling these correlations. An obvious candidate to test is the plant hormone auxin involved (directly or indirectly) in gradient formation that could confer positional information (Galinha *et al.*, 2007; Grieneisen *et al.*, 2007, 2012). In the context of the leaf, auxin is distributed non-homogeneously, and a peak of activity is present at the tip of the leaf from early leaf developmental stages, according to the auxin marker DR5 expression pattern (Aloni *et al.*, 2003). In addition, auxin has been suggested to promote the development of pavement cells by increasing their shape complexity in a concentration-dependent manner (Xu *et al.*, 2010; Li *et al.*,

2011), in the modulation of cell division (Lincoln *et al.*, 1990; Hu *et al.*, 2003; Guo *et al.*, 2013) and in the transient arrest of leaf growth during shade avoidance (Carabelli *et al.*, 2007). Surprisingly, I found that under the experimental conditions used and the concentration of auxin previously reported as optimum (20nM of NAA), cell shape complexity is lower than the counterpart control experiment. Rather, auxin experiments increased the length of the cell cycle, without affecting the zone where division takes place.

Finally, I discuss the importance of the results obtained from the analysis of cellular dynamics for the overall organ size regulation. Although the identification of the specific “morphogens” underlying differential cellular behaviour (depending or not on the position) are beyond the scope of this work, the analysis of the dynamics of cell growth, cell shape and cell divisions extracted from time lapse experiments discard previous hypothesis and open new ones about the regulation of cellular dynamics during leaf morphogenesis.

## 4.2 Are cells growing and changing shape according to their position?

Cell size and shape show a strong proximo-distal gradient within the leaf (Donnelly *et al.*, 1999; Andriankaja *et al.*, 2012). Pavement cells with a bigger area and showing a jigsaw-like shape are first identified at the tip of the leaf. Over time, they are also located at the base of the leaf. However, there is scarce dynamic information at the cellular level on how cells are growing and acquiring their shape to account for this pattern. The few reports published (Asl *et al.*, 2011; Zhang *et al.*, 2011; Elsner *et al.*, 2012) do not provide enough spatial and temporal resolution to separate the effects due to position from the effects due to developmental stage.

In this section, the cell growth and the cell shape change are evaluated at different spatial and temporal scales. However, before to pursue the analysis of the cell growth and the cell shape dynamics, I would like to introduce different notions of position and the motivation to analyse different spatial scales (Figure 4.1).

### 4.2.1 Different spatial scales

Under the assumption that a morphogen gradient underlies the regulation of the cellular behaviour, the analysis of the cell dynamics taking different spatial scales into account could help to infer some characteristics of such hypothetical gradient (diffusion rate, production, degradation, etc.) and how those relate to the specific developmental context (such as organ growth, effect of the boundaries, etc. See Box1). Therefore, the analysis of different spatial scales is important because of the different implications regarding the

characteristics of the morphogen and its relation with the overall organ growth and shape (see below). There are reports of two kinds of scales where the position is relevant:

1. *Absolute position* (Figure 4.1A),
2. *Relative position* (Figure 4.1B).

The first refers to a fixed distance from a reference point (i.e. tip of the root, petiole of the leaf, etc.). This scale was suggested to be important for specifying the region where cell proliferation takes place within the leaf (Kazama *et al.*, 2010; Andriankaja *et al.*, 2012; Lenhard, 2012). It was proposed that regardless of the overall leaf growth, the position at which cell division takes place (also called cell cycle arrest front) stays at a constant distance from the leaf base for several days (Figure 4.1A), until it suddenly disappears (I will come back to this affirmation later). This behaviour was attributed to a morphogen produced at the base of the leaf that diffuses through the leaf blade and decays in each position. Then, the precise position of the boundary of cells that divide and cells that just expand was given by a concentration threshold  $C_{th}(t)$  of this putative morphogen (Kazama *et al.*, 2010). This implies that in order to keep the division zone within a fixed distance (100  $\mu m$ ), the morphogen needs to diffuse and renew itself faster than the overall organ growth (for example, to avoid dilution of the morphogen because of growth; see a discussion of the effect of growth in Wartlick *et al.*, 2011). Therefore, under this scenario the absolute position is important.

In contrast, a relative position is important when the concentration of the underlying morphogen “scales” with the tissue size during development. The scaling gradient of Decapentaplegic (Dpp), important during *Drosophila* wing disc growth is one of the best characterized gradients that scales (Wartlick *et al.*, 2011 and references therein). The scaling phenomenon refers to the fact that although the gradient amplitude  $C_0$  and the decay length  $\lambda$  increase over time (see Box1), the ratio  $C(r, t)/C_0(t)$  (where  $r = x/L$  is the relative distance to the source) is invariant during development. Then, when the proportion of Dpp concentration is plotted according to the relative position, all the curves will coincide regardless of the specific time point measured. Moreover, in this case the decay length  $\lambda$  is proportional to the tissue length  $L$  (and the ratio  $\lambda/L$  is constant). This phenomenon of gradient scaling has also reported in the gradient of bicoid in *Drosophila* embryo (Gregor *et al.*, 2005, 2007a) and other closely related dipteran species (Gregor *et al.*, 2005). To evaluate the hypothesis of a scaling gradient within the leaf, requires the analysis of the cell dynamics according to the relative position (Figure 4.1B). The scaling is interpreted as an adaptation of variations on the patterning due to growth and there are several hypothesis about how the scaling could operate (see for example Ben-Zvi *et al.*, 2008, 2011; Wartlick *et al.*, 2011), but the discussion of these are beyond the scope of this chapter.

The importance of the absolute and the relative position in the examples discussed above assumes that the position relevant for the cell dynamics is fixed. This is the case of

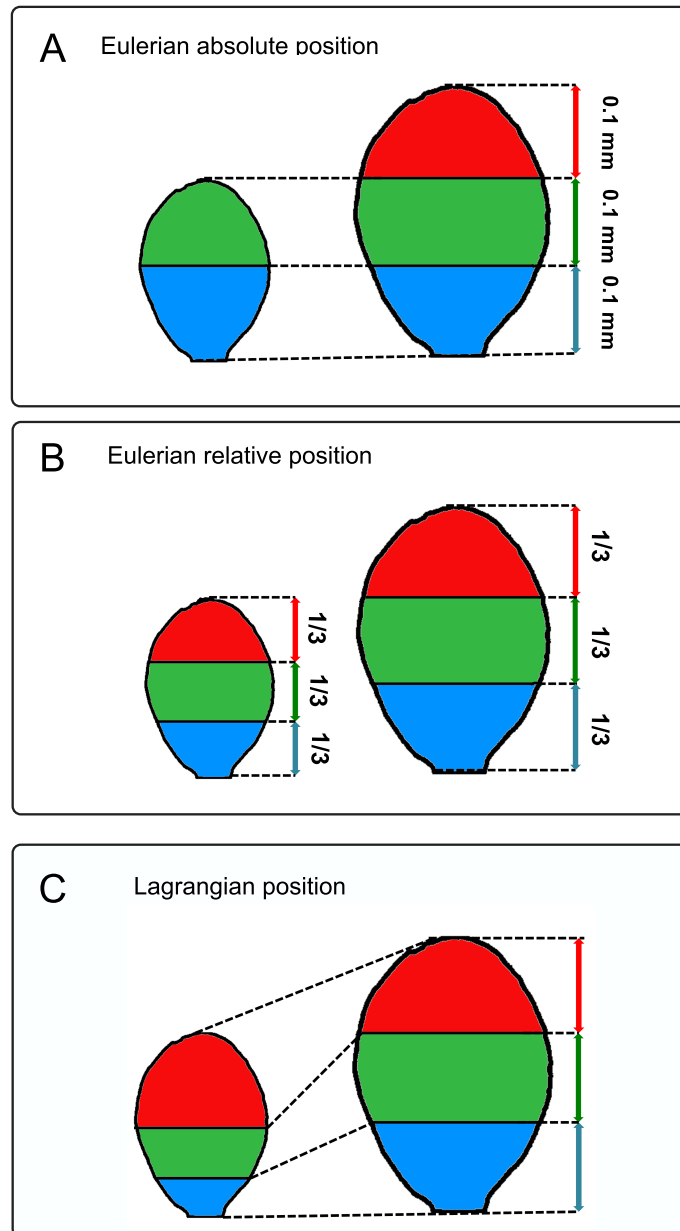


**Figure 4.1: Schematic representation of different spatial scales.** A) An absolute position was reported to be important for the specification of the zone where cell division takes place within the leaf. Taking as a reference the base of the leaf, some regions (red) will be available just at later stages of development (right). B) A relative position is important when the concentration of the morphogen scales, as suggested for Dpp signalling in *Drosophila* (see main text and Box1). In this case, there is always a region corresponding to a proportion of the tissue, regardless the time point considered. C) A Lagrangian position accounts for the fact that a cell is transiting through the tissue over time. In this case, because division is mainly localized at the base of the leaf, cells are being “pushed” forwards towards the tip. Then, the region in blue (left) will expand over time (right).

*Drosophila* wing disc, where the position of the cell is almost constant because the cell division and organ growth is homogeneous (Wartlick *et al.*, 2011), and in the case of *Drosophila* embryo where there is no growth (Gregor *et al.*, 2005). However, within the leaf, cell division happens within a restricted space (base of the leaf) that causes cells being “pushed”

forwards (new cells occupy the relative space of the others causing an overall displacement). This introduces an extra complication to analyse the effect of position because the position of a cell (absolute or relative) is also changing. Therefore, to evaluate if a fixed position of the tissue or the moving position of the cell is important, it is useful to introduce different frames of reference (Silk & Erickson, 1979):

1. *Eulerian position* is a fixed position within the leaf, such as the absolute and relative position, discussed previously (Figure 4.1A-B). The analysis of this scale answers the question on how a tissue fragment changes behaviour over time irrespective to the cells that transit it.
2. *Lagrangian position* is the position followed by the cells over time (Figure 4.1C). The analysis of this scale answers the question on how cells change behaviour over time possible because the influence of their “moving” position through the tissue.

A useful analogy to explain the difference between these two frames of reference is that cells can be considered fluxing through the leaf (from the base towards the tip, for instance) such as droplets of water are fluxing in a river. If one considers a fixed position in the river and measures the water flow at that position (for example, the water that a static rock “sees”), it will correspond to an Eulerian frame of reference. In contrast, if one could follow the droplets of water (for example, as a fish could do), then it will correspond to a Lagrangian frame of reference.

Importantly, the Lagrangian frame of reference takes into account the displacement due to local growth of the tissue. A Lagrangian frame of reference is relevant, for example, if the important aspect influencing cell dynamics is the fact that cells are changing position or under the assumption that cells are “carrying” information with them.

Therefore, there are diverse ways of analysing the data taking into account different spatial scales and frames of reference, each with different biological implications. As the putative diffusible signals underlying differences in cell behaviour are unknown in the leaf, the analysis of the cell dynamics in different spatial scales is very important and is discussed in the following section.

**Box1. Morphogen Gradients using diffusion and linear degradation**

In this box, I briefly summarize some aspects of gradient formation using diffusion (non-directional movement) and linear degradation. The gradients of Decapentaplegic (Dpp) and Wingless (Wg) in *Drosophila* imaginal discs, and Bicoid in the embryo have been analysed considering this kind of mechanism (Kicheva *et al.*, 2007; Gregor *et al.*, 2007a; Wartlick *et al.*, 2011).

Considering a single line of cells (one dimensional case), the spatial and temporal changes in morphogen concentration  $C$  due to production, spreading, and degradation can be formally expressed using the diffusion equation with linear degradation:

$$\frac{\delta C}{\delta t} = D \frac{\delta^2 C}{\delta x^2} - kC \quad (4.1)$$

where  $C$  is the concentration of the diffusible signal,  $D$  is the diffusion coefficient (with units [ $\mu m^2/s$ ]),  $x$  is the distance from the source (in  $\mu m$ ) and  $k$  is the degradation rate constant (units [ $1/s$ ]). The distance,  $x$ , is considered from the source boundary at  $x = 0$  (where the morphogen is produced) to the boundary that corresponds to the total length of the tissue  $x = L$ . Because the molecules of morphogen are constantly produced at the source at  $x = 0$ , there is a constant flux ( $j_0$  [molecules/ $\mu m^2 \cdot s$ ]) of molecules coming from the source. The spatial difference in concentration will cause the molecules of the morphogen to spread.

Over sufficient time, when the gradient does not change anymore, it is said to have reached a steady state. Assuming that  $C(L) \approx C(\infty) = 0$ , the steady state solution for gradients formed by diffusion and linear degradation (Eq. 4.1) is:

$$C(x) = C_0 e^{-\sqrt{\frac{k}{D}}x} = C_0 e^{-\frac{x}{\lambda}} \quad (4.2)$$

where  $\lambda$  is the the *decay length* (or characteristic length) defined as the distance from the source at which the gradient decays to a fraction of  $1/e$  of  $C_0$ . The concentration at the source boundary  $C_0$ , is also known as the gradient *amplitude* and depends on the flux of molecules across the source boundary  $j_0$ , the diffusion  $D$  and the degradation  $k$  over the tissue:

$$C_0 = \frac{j_0}{\sqrt{Dk}}; \quad (4.3)$$

in turn, the decay length  $\lambda$  is related to the morphogen diffusion and degradation as follows:

$$\lambda = \sqrt{\frac{D}{k}}. \quad (4.4)$$

In some cases, the ratio  $C(r,t)/C_o(t)$  (where  $r = x/L$  is the relative distance to the source) is invariant during development and the  $\lambda$  is proportional to the tissue length  $L$ ; then, it is said that the gradients scales. The scaling phenomenon is said to occur as an adaptation of patterning to changes in organ size and there are different hypothesis on how this might operate (Ben-Zvi *et al.*, 2011; Wartlick *et al.*, 2011)

Other gradient formation mechanisms for example, not including degradation, non-linear degradation, and cell lineage transport are very comprehensively discussed in Wartlick *et al.*, 2009.

In plants, active transport has been reported as very important aspect in the formation of gradients due to time scales and spatial distances involved (Grieneisen *et al.*, 2012).

**Box 2. Calculating the growth rate and shape change**

This box explains how growth rates and shape change were calculated as a function of time. I will refer to growth rates, but the same principles were applied to the analysis of shape complexity.

Growth is simply the change in area over time:

$$\frac{dA}{dt}; \tag{4.5}$$

while growth rate is defined as the proportion of growth over time:

$$\frac{1}{A} \cdot \frac{dA}{dt} \tag{4.6}$$

Within sufficiently short time intervals growth can be estimated as linear or exponential, or by any other function regardless of the underlying complexity of the real growth function (Tzur *et al.*, 2009).

As the real model of growth or change in shape is unknown, two general possibilities were tested: area-dependent (exponential) and area-independent (linear) cellular growth, given by the following equations:

1) Exponential growth:

$$A_{i+1}(t) = A_i e^{\alpha \Delta t} \tag{4.7}$$

2) Linear growth:

$$A_{i+1}(t) = A_i + \beta \Delta t \tag{4.8}$$

where  $\beta$  and  $\alpha$  are the linear or exponential growth constants respectively,  $A_i$  is the cell area at  $t_i$  and  $\Delta t = t_{i+1} - t_i$  is the time interval between two consecutive time-points. Different growth constants,  $\alpha_n$  or  $\beta_n$ , are assumed for every time interval (for example,  $\alpha_0$  or  $\beta_0$  for  $(t_0, t_1)$  and  $\alpha_1$  or  $\beta_1$  for  $(t_1, t_2)$ , etc).

**Area-dependent growth**

The change in area over time or growth can be expressed using the following differential equation:

$$\frac{dA}{dt} = \alpha A \tag{4.9}$$

From the solution of such equation (Eq. 4.7), the growth constant assuming an area-dependent model (Eq. 4.9) is:

$$\alpha = \frac{\ln\left(\frac{A_{i+1}}{A_i}\right)}{\Delta t}. \tag{4.10}$$

To get the proportion of growth, one can divide the growth in Eq. 4.9 by  $A$ . Thus, in this case, the growth constant  $\alpha$  coincides with the growth rate.

**Area-independent growth**

Under this model, the change in area over time is simply given by a constant:

$$\frac{dA}{dt} = \beta \tag{4.11}$$

Note that the growth constant  $\beta$  carries units  $[\frac{\mu m^2}{h}]$ ; so, strictly speaking is not a rate  $[\frac{1}{h}]$ . Similarly, from the solution of such equation shown in Eq. 4.8, the growth constant is calculated as:

$$\beta = \frac{A_{i+1} - A_i}{\Delta t} \tag{4.12}$$

The results obtained were independent on the model assumed.

### 4.2.2 Cells grow and change shape differently according to their position

The rate of growth and cell shape were calculated along the leaf taking into account different spatial locations (absolute and relative) to assess if cells are changing size and shape in a position-dependant manner. Because of the specific mode of cell growth and cell shape change are unknown, two models (exponential and linear, see Box 2) were used to calculate the growth rate and cell shape change, without qualitative differences.

The results are shown in Figure 4.3 and Figure 4.4 for the cell growth and the cell shape, respectively (the number of cells considered are shown in Figure 4.5). The mean of the growth rate and the cell shape change are shown colour-coded according to their absolute (Figure 4.3A-C and Figure 4.4A-C) and relative position (Figure 4.3D-F and Figure 4.4D-F). Note that when an absolute position is considered, the upper regions of the leaf are present only at later stages of development (for example, the tip region corresponding to 949 - 1422  $\mu\text{m}$  is present only after 300 - 350 Hours After Stratification or HAS).

The cell area and the cell shape are higher at the tip than at the base of the leaf (Figure 4.2, Figure 4.3A,D and Figure 4.4A,D) regardless of the spatial scale taken into consideration, in accordance with the observation that cells are bigger and “more puzzle-like shaped” at the tip of the leaf (Donnelly *et al.*, 1999).

The growth and the shape change in early stages (up to 230 hours) taking a relative position were very similar along the leaf (Figure 4.3B,E and Figure 4.4B,E). Later in development, the cell growth and the cell shape change showed a clear separation of tip, middle and bottom regions regardless of the spatial scale (absolute or relative) taken into consideration. Interestingly, Figure 4.3 and Figure 4.4 show that the change happens in a graded-fashion within the leaf, with cells at the tip growing and changing shape faster than cells at the base of the leaf.

However, when the growth rate or the relative shape change is considered, it is evident that in proportion cells at the tip are growing and changing shape slower than cells at the bottom (Figure 4.2, Figure 4.3C-F and Figure 4.4C-F). This graded behaviour of cell growth and shape taking the proportion of change is more evident but not dependant on the relative position and this tendency is stronger for the cell growth than for the cell shape change (see for example, Figure 4.3F and Figure 4.4F).

In the analysis of cell shape similar results were obtained using the cumulative difference (see Chapter 2) and entropy (see appendix Figure 4.25).

Importantly, the graded behaviour in growth and growth rates (and shape and relative shape change) is independent of the specific length of the region taken into account (regions from 100, 200, 300 and 400  $\mu\text{m}$  and different proportions of the leaf were evaluated giving the same result, not shown), suggesting that the graded behaviour is not dependent of a gradient that has a specific range of action in absolute or relative scales (i.e 100  $\mu\text{m}$  was suggested for the division zone).

Altogether, the results presented in this section suggest that cells are changing dif-

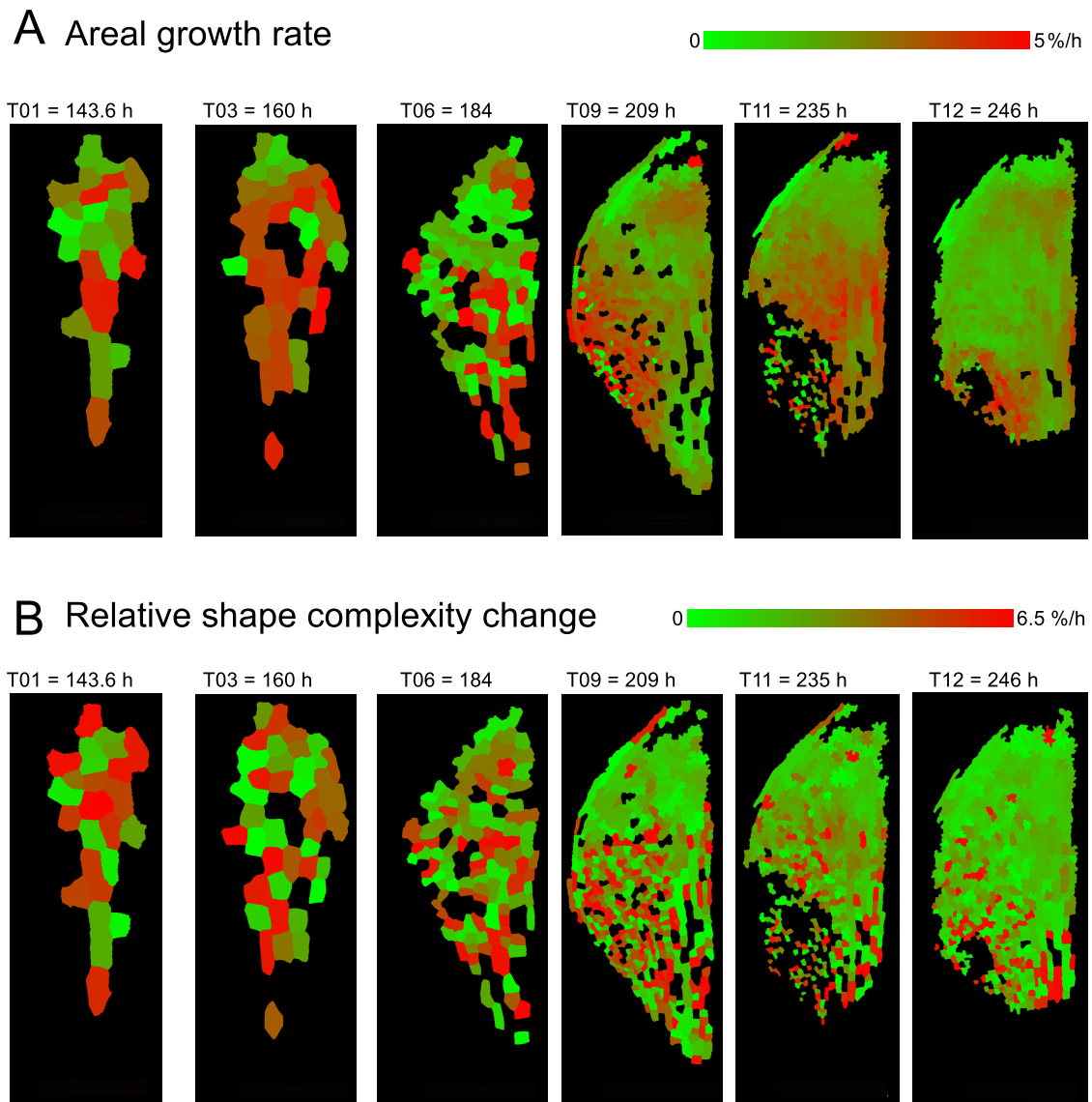


**Figure 4.2: Cell growth rate and relative cell shape complexity.** A) Growth rate is similar across the leaf at early time points. Over time, however, cells at the tip of the leaf are growing slower than cells at the base of the leaf. B) The change in cell shape complexity (cumulative difference) is also similar across the leaf. Over time cells at the base of the leaf show higher rates of cell shape change. The tip and base of each leaf are aligned with one another. The colour gradient is the percentage of change in cell area (A) and cumulative difference (B). Not to scale.

ferently according to their position: cells at the tip are growing and changing shape in proportion slower than cells at bottom. However, to discard the possibility that cells behave differentially not *because* of their position (absolute or relative) but because the position they are transiting is different or because an intrinsic property of the cells (such as their developmental age), a Lagrangian frame of reference was also evaluated and it is presented next.

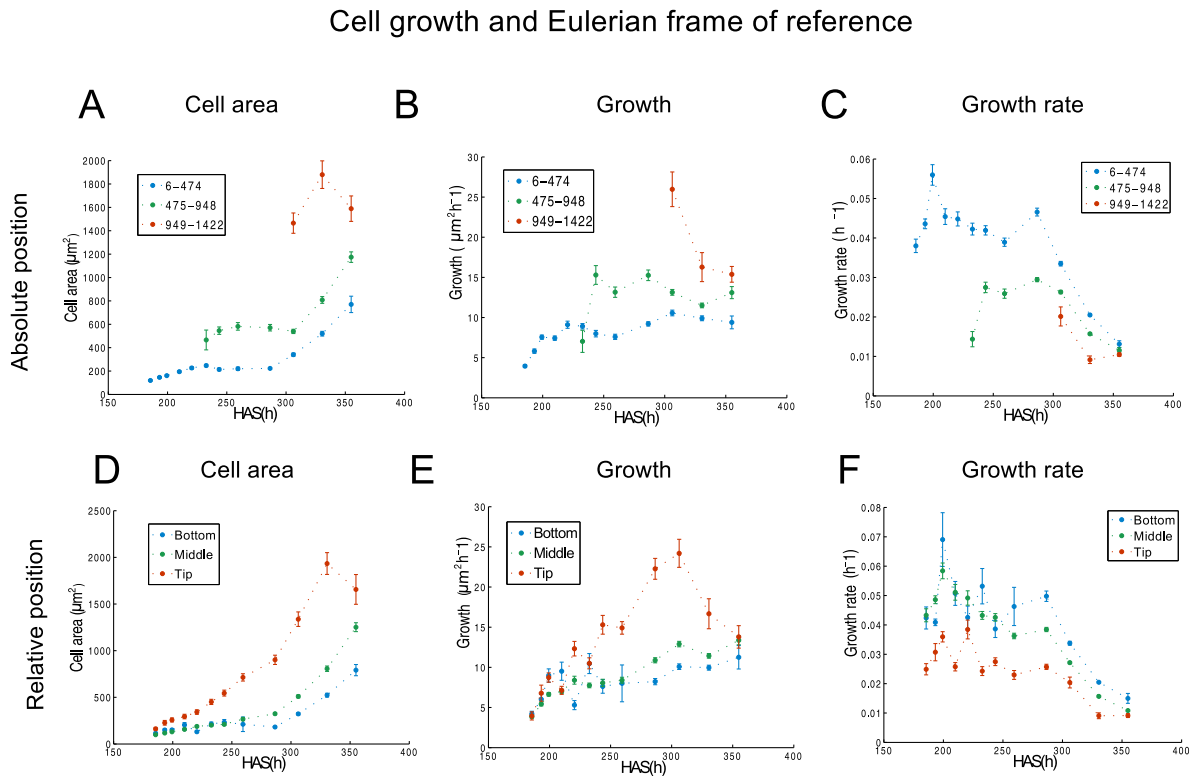


**Figure 4.3: Cell area varies in a graded-fashion from the base to the tip of the leaf.**

A, D) Average cell area in absolute and relative scales, respectively. Taking the base of the leaf as a reference, the cell area is on average larger at the tip of the leaf than at the bottom. B) The change in area taking an absolute position is also larger at the tip and decreases towards the base of the leaf. E) Considering a relative scale, the growth is very similar at early stages of development but, over time it is possible to distinguish a similar tendency as before: cells at the tip have higher areal growth. C, F) The growth rate, however, shows that in proportion cells are growing slower at the tip of the leaf than at the base. The cell growth and growth rate showed in B-C and E-F, were calculated using using Eq. 4.12 and Eq. 4.10 (see Box2), respectively. Error bars represent 1+/- standard error. The time in the x-axis is measured in hours after stratification (HAS).

### 4.2.3 Cell growth and cell shape taking a Lagrangian frame of reference: following groups of cells.

Since growth within the leaf is spatially inhomogeneous, the absolute and relative position of cells changes during development (Figure 4.6). Indeed, if the position of a cell is followed over time keeping the region of the petiole fixed (at absolute or relative distance of  $x = 0$  or  $r = 0$ , respectively), it can be appreciated that cells are being displaced (Figure 4.6B,C). This implies that a cell located nearby the base of the leaf, over time will be localized further away from the base. For instance, a cell which centroid was located at  $x = 95 \mu\text{m}$  or  $r = 0.45$  (starting position) will have a final position at  $x = 1044.7 \mu\text{m}$  and  $r = 0.67$ , after 155 hours of time lapse.

Because the position of cells is changing, perhaps the “information” that cells experience (or are exposed to) is also different. Then, to evaluate if the gradient of cell dynamics

## Cell shape and Eulerian position

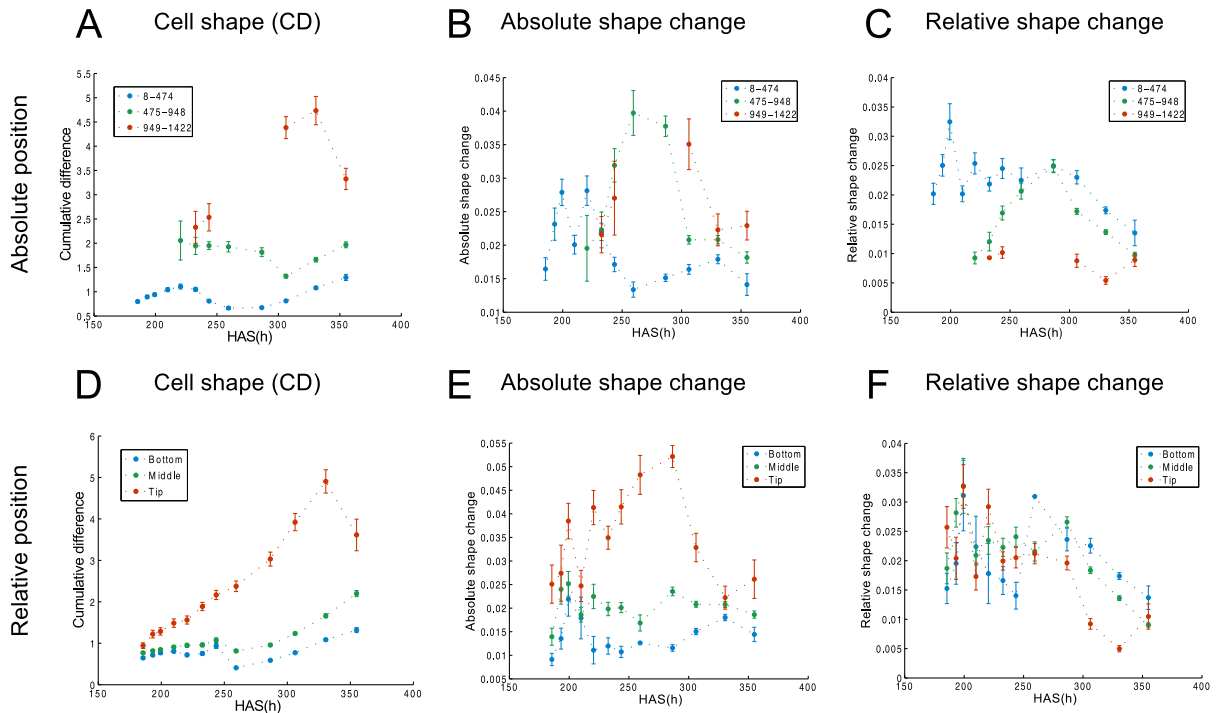


**Figure 4.4: Cell shape is changing in a graded-fashion from the base to the tip of the leaf.** A, D) Cell shape complexity measured using the cumulative difference (see Chapter 2), show a graded increase from the base to the tip of the leaf, in a very similar fashion than cell area (compare Figure 4.3A,D). B, E) The absolute shape change is higher towards the tip of the leaf than at the bottom. Cells located in the relative tip and in the region [475-1422  $\mu\text{m}$ ] changed shape rapidly compared with other regions. C-F) The relative shape change shows that in proportion, cells are changing shape faster at the bottom of the leaf. F) When the relative position is considered, there is not visible difference in the relative shape change before 250 hours. Error bars represent 1 +/- standard errors. The time in the x-axis is measured in hours after stratification (HAS).

is preserved when cells are changing their position, groups of cells (Lagrangian approach) were followed and their cell growth and cell shape change were calculated.

To track groups of cells over time, one can assume that the final position of a group of cells will also reflect its initial position. This is a reasonable assumption considering that cells are displaced as a whole in only one direction (cells are “moving” away from the base of the leaf) and they cannot change their neighbours. Thus, groups of cells were followed taking as a reference their position at the last image of the time lapse and then, they were tracked backwards in time. A fixed position along the leaf of 300  $\mu\text{m}$  will contain about 8-10 cells in length (total number of cells analysed are shown in Figure 4.8). This accounts for the fact that cells are displaced differentially within the tissue due to inhomogeneous divisions and internal tissue deformation.

The results of this approach can be seen in Figure 4.7. Strikingly, when groups of cells are followed, they are still changing in a graded-fashion conforming to their position.

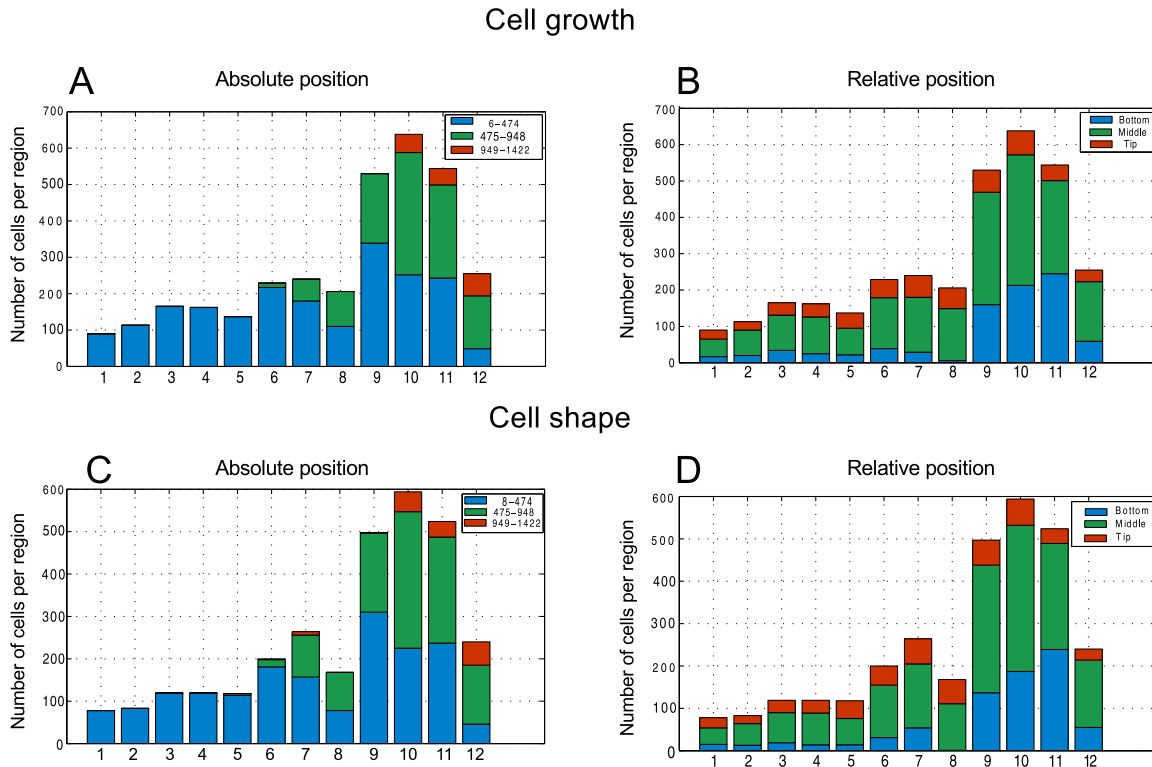


**Figure 4.5: Number of cells analysed taking an Eulerian frame of reference in absolute and relative position.** A-B) Number of cells used to analyse the cell area and dynamics of cell growth (relate with Figure 4.3). C-D) Number of cells used to analyse the dynamics of cell shape change (relate with Figure 4.4). In the x-axis, the time points (from 1-12) correspond to intervals between 185.53 to 354.9 HAS (details are showed in appendix of Chapter 3).

This tendency is more strongly apparent when the growth rate or relative shape change is considered (Figure 4.7C-F) and it is more evident for the cell growth than for the cell shape.

However, these results can still be interpreted in two ways: 1) cells are changing according to their (also changing) position or, 2) cells are changing differently due to differences in their developmental stage. The last possibility is plausible because the spatial gradient of cell dynamics overlaps with the spatial gradient of cell age (i.e differentiate cells are at the tip whereas cells that just divided are at the base of the leaf). An additional temporal scale, the cell age, was evaluated to distinguish between these options, and it will be described in the next subsection.

#### 4.2.4 Different temporal scales

To address the influence of the cell's developmental stage on the dynamics of cell behaviour, it is also very important to separate the different temporal scales involved in the dynamics of the cell growth and the cell shape. These different temporal scales can be distinguished as:

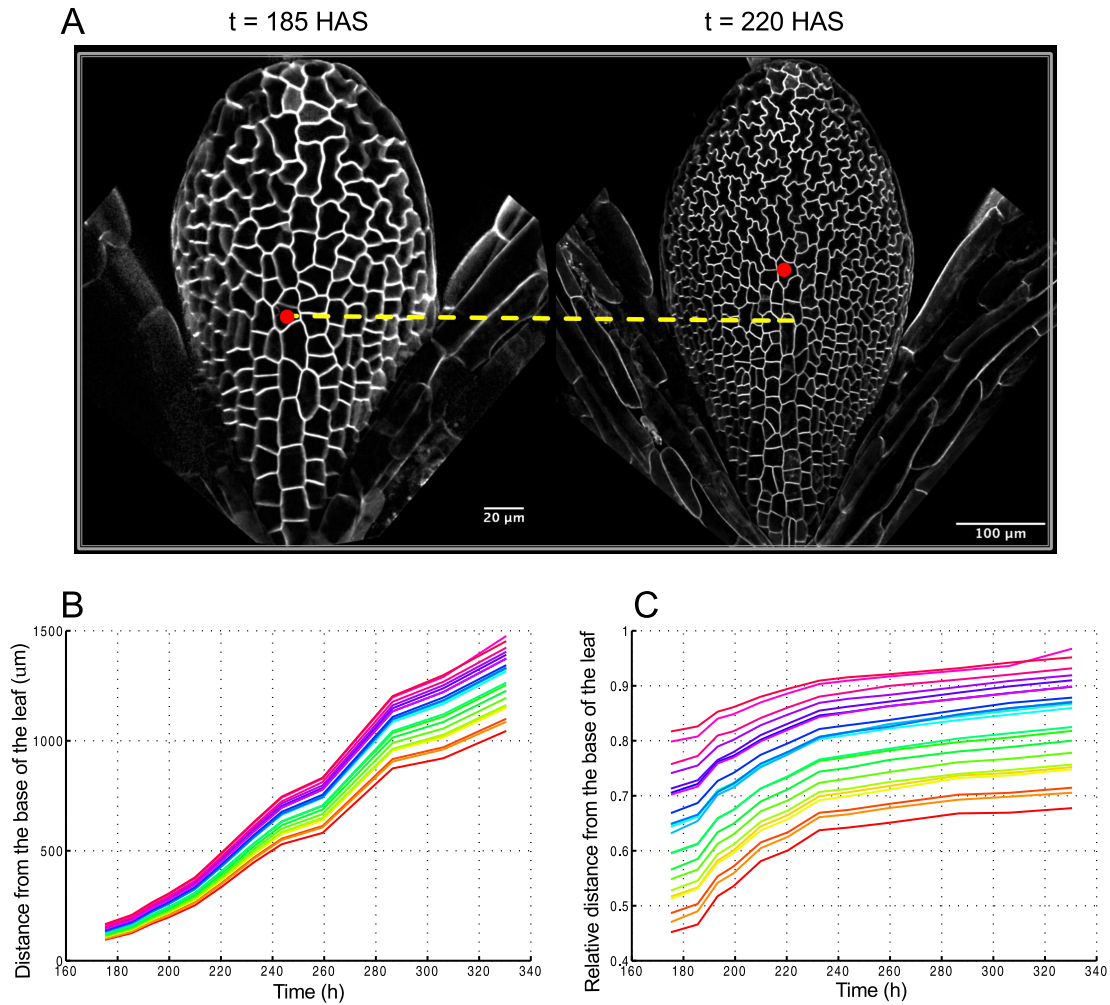


**Figure 4.6: Cells in the leaf are changing position during development.** A) The cell marked with a red dot on the right will change its relative position (shifting upwards) at later time points (left). B-C) Taking the position of the petiole as a reference (set to 0) and tracking groups of cells (each indicated with a different colour) is possible to observe how the position of a cell is changing in absolute (B) and relative scales (C).

1. *Time of the plant.* This is the time in which the plant has been developing from its approximate germination ( $t_p = 0$ , Figure 4.9A) to the moment of imaging. It is measured in hours after stratification (HAS, see Chapter 3).
2. *Time of the cell.* This refers to the time taking as a reference the cell division (i.e. time at division is  $t_c = 0$ , see Figure 4.9B). It is also measured in hours and will be referred to as the cell age hereafter.

Once a cell division is identified (this is, when two cells in a given time point are recognized as a single cell in the previous time point), the time of the daughters cells is set to 0 hours (Figure 4.9B, and corresponds to the “birth” time of the cell). Then, the cell age over time is calculated as the difference between the subsequent time-points (in HAS) and the time of birth of the cell. In this sense, aligning cells according to the time after division

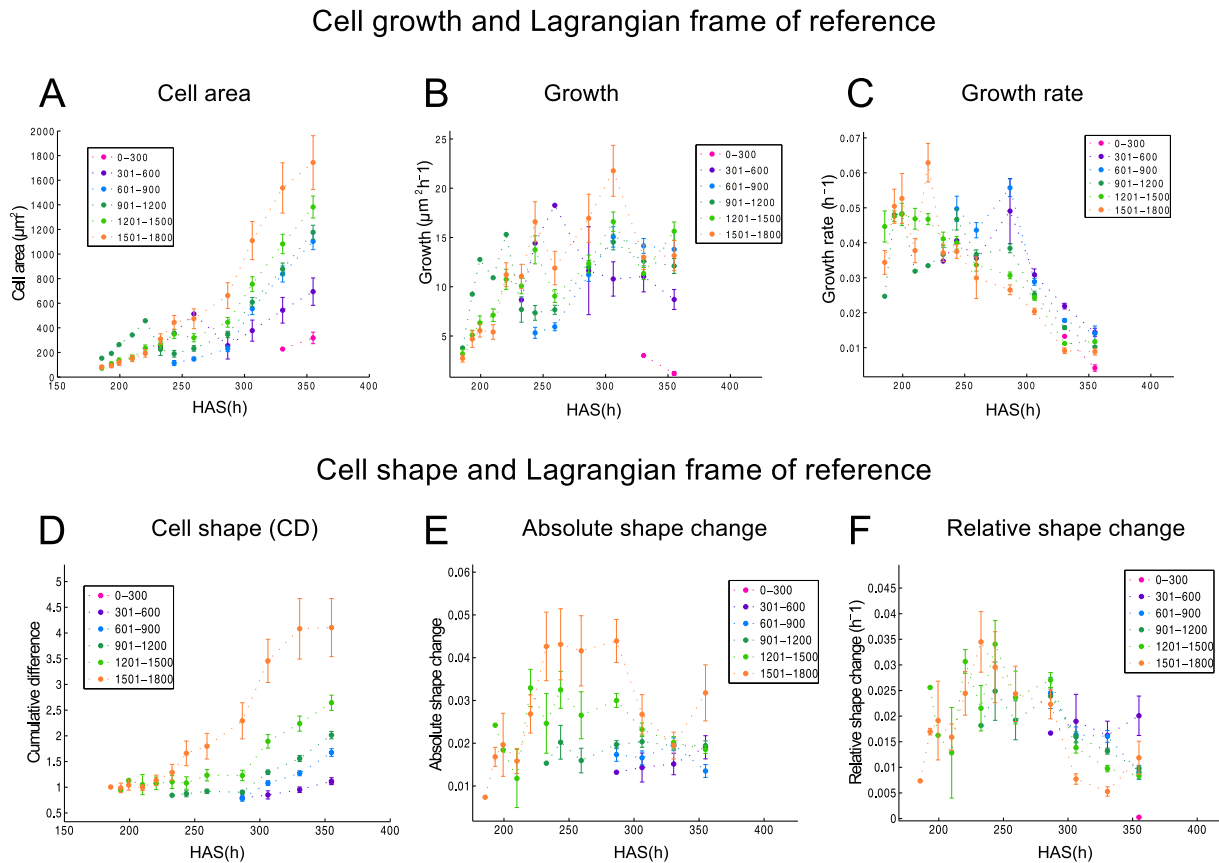


**Figure 4.7: Cell growth and cell shape dynamics taking Lagrangian frame of reference still show a gradient according to the position.** The colour code indicates groups of cells that shared the last position (at  $t=354.9$  hours). A,D) The cell area and cell shape showed a strong proximodistal gradient, where cells at the tip are bigger and more complex than cells at the base of the leaf. B) The growth shows some small differences among cells coming from different regions. E) The absolute change in shape, however, shows that cells at the tip changed shape faster than cells that ended at the base of the leaf. C,F) The growth rate and relative shape change shows that cells that were located at the base of the leaf were growing and changing shape faster than cells that ended up closer to the tip. Regions of  $300\ \mu\text{m}$  in length contain 8-10 cells; the actual number of cells is shown in Figure 4.8. Averages with  $1\ \pm$  standard error are shown. The time in the x-axis is measured in hours after stratification (HAS).

is comparable to analysing a “synchronized population” that otherwise is impossible to analyse in plant development.

Next, to evaluate if cells are behaving in a position-dependant manner independently of their cell age, I colour-coded the synchronized population (aligned by the time of cell division) according to their cell position. Two extreme scenarios arise, depicted in Figure 4.10. First, after aligning cells with their time, the position is not playing an important role and therefore, the cell growth rates (colour-coded) are well-mixed (Figure 4.10A). The other possibility is when considering the cell age, cells still behave differently depending on their position (Figure 4.10B).

The results are shown in Figure 4.11, Figure 4.12 and Figure 4.14 (and the number of cells analysed are shown in Figure 4.13 and Figure 4.15). The absolute cell area and cell

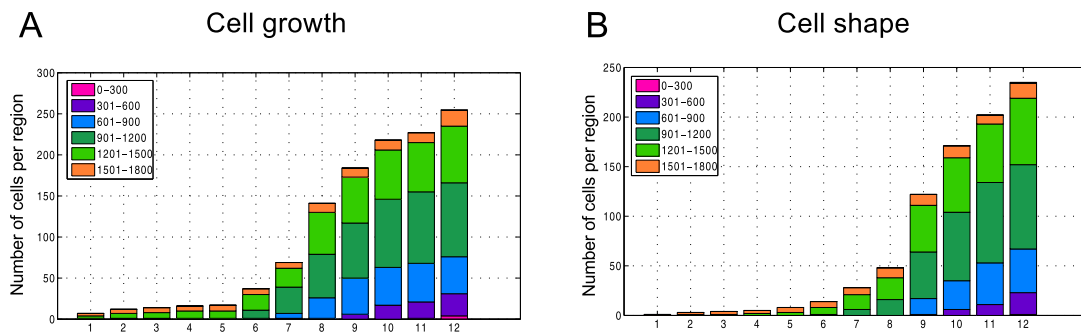


**Figure 4.8: Number of cells considering a Lagrangian frame of reference.** The colour code indicates groups of cells that shared their last position (every  $300\mu\text{m}$ ). A fixed position of  $300\mu\text{m}$  along the leaf will contain about 8-10 cells in length. In the x-axis, the time points (from 1-12) corresponding to 185.53 to 354.9 HAS and are showed.

growth rates do not show any obvious separation depending on the position in Eulerian coordinates (Figure 4.11). In contrast, the absolute value of cumulative difference (as an approximation for shape complexity) revealed a subtle separation depending on the position (Figure 4.12A,D), meaning that cells located at the tip (absolute or relative) are wavier and more complex than cells at the base of the leaf of the same age. However, when the rates of shape change were evaluated, there was not an visible separation according with the position (Figure 4.12B-C, E-F).

When a Lagrangian frame of reference is considered, cells do not present difference in neither the absolute values nor rates of change of cell growth and cell shape, meaning that the cohort of cells followed over time behave similarly when their age is taken into account (Figure 4.14).

These results suggest that the developmental stage of the cell is strongly influencing the dynamics of the cell growth and the cell shape, regardless of the position. Moreover, the absolute values and rates of change in cell area and cell shape follow a very similar tendency when cells are aligned considering its time after cell division. This can be appreciated better in Figure 4.16, showing the dynamics in cell area and cell shape for several experiments (without considering the position). Interestingly, cell area and the relative growth rate follow a very clear trend, the first increasing and the latter decreasing over time (Figure 4.16A,C).

Although cell shape complexity is also increasing over time in a similar manner to cell area (Figure 4.16A,D), the absolute and relative change in shape showed a different tendency compared to the growth and the growth rate. This is in agreement with the fact that, although cell area and cell shape complexity showed a strong correlation (Figure 4.17A), the absolute change and relative change were not strongly correlated (Figure 4.17B-C).

Despite of the strong tendency of cells to change depending on their age, some experiments showed bigger variation than others (for example see ExpID3078-PA in Figure 4.16).

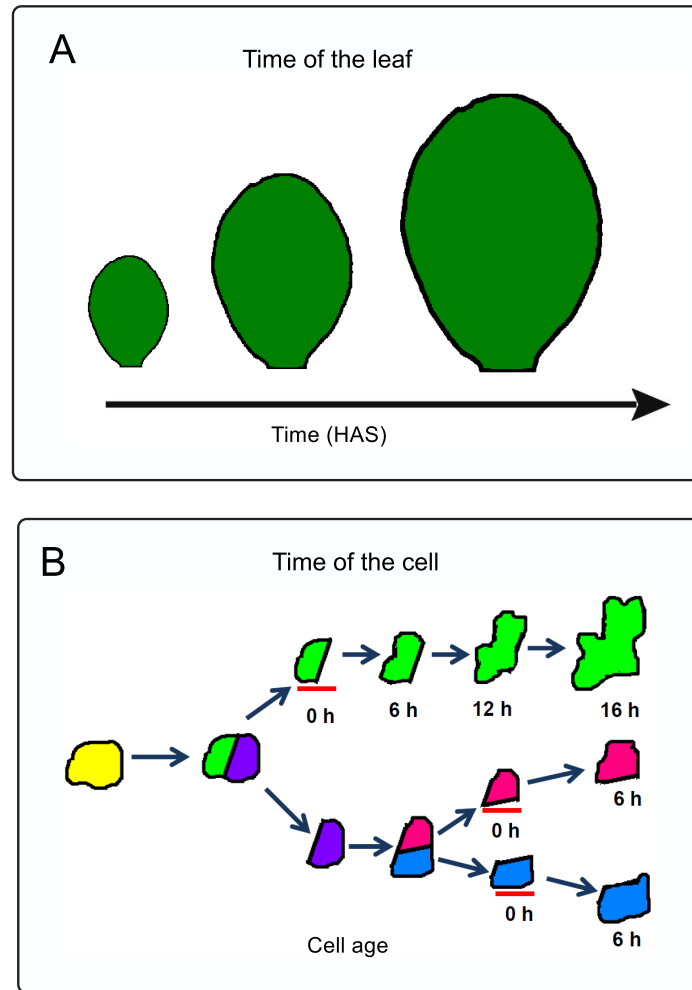


**Figure 4.9: Schematic representation of different temporal scales.** Distinction of different temporal scales allows to explore further the role of position and the predominant factor influencing the dynamics of the cells during leaf development. A) Schematic representation of the time of the leaf, measured in hours after stratification (HAS). B) The time of the cell or cell age, starting after its division ( $t_c = 0$ , highlighted in red).

To discard the possibility that this variation is explained because the synchronized population is formed by sub-populations of cells dividing once, twice, or  $n$  more times until they commit to differentiation, cells were further separated according to the number of divisions that were detected during the time lapse. The results are shown in Figure 4.18, suggesting that there is not an obvious difference of cells after their first, second, third or fourth division (see appendix Figure 4.26 and Figure 4.27 for other experiments).

Altogether, the results presented until now suggest that cells grow and change shape strongly depending on their cell age, despite their position and regardless of the number of divisions that they have pursued. Thus, the next question to gain insights in how cell dynamics is regulated in a growing organ is to find out what determines the spatio-temporal dynamics of cell division in a determinate organ. This topic will be briefly discussed in the next section.

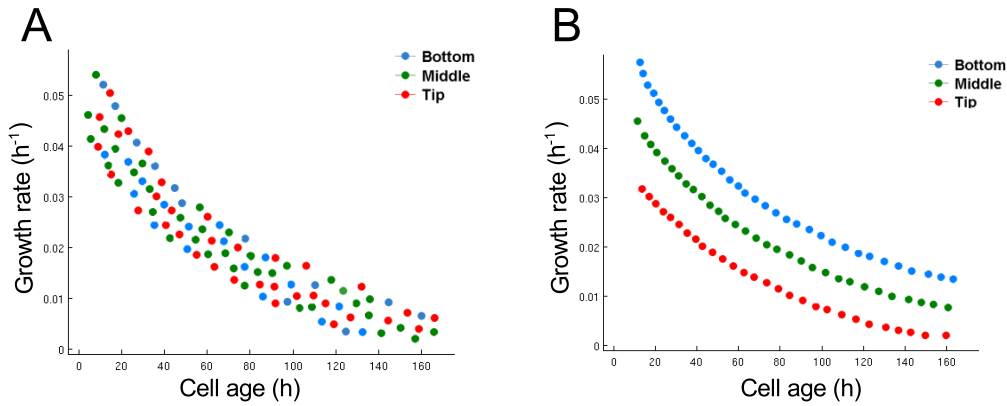


**Figure 4.10: Alternative hypothesis of the effect of the cell age in cell dynamics when the position is taken into account.** When cells are aligned with their time after division and colour-coded according to their position, there are two extreme possibilities: A) there is no effect on the position (the colours representing position are well-mixed) and B) the position is still influencing the rate of change (the colour-code is clearly different).

Cell growth and Eulerian frame of reference

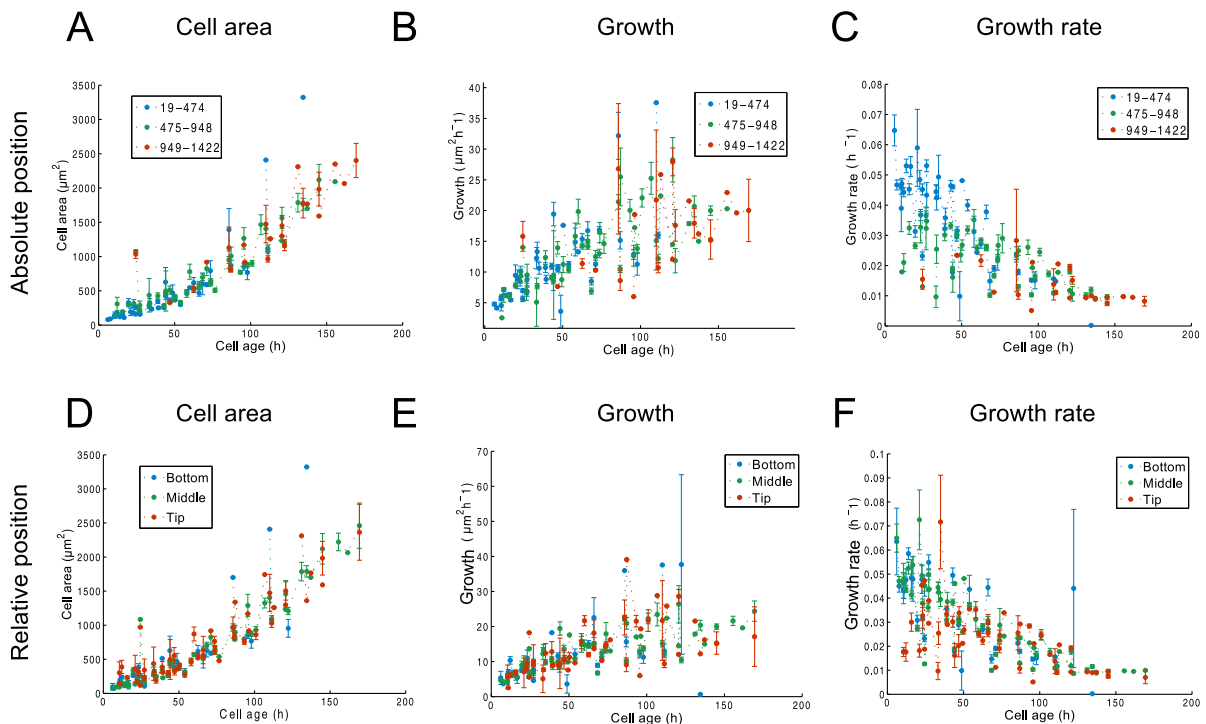


**Figure 4.11: Cell growth and Eulerian frame of reference when cells are aligned by their age does not show strong differences depending on the position.** A,D) Regardless of the absolute or relative scales considered, cell area is independent of cell's position and follows a strong trend to increase over time. B,E) The cell growth also shows that there are not visible differences depending on the position (absolute or relative). C, F) This is further suggested when the growth rate is considered. Averages with  $1 \pm$  standard error are shown. Number of cells are shown in Figure 4.13.

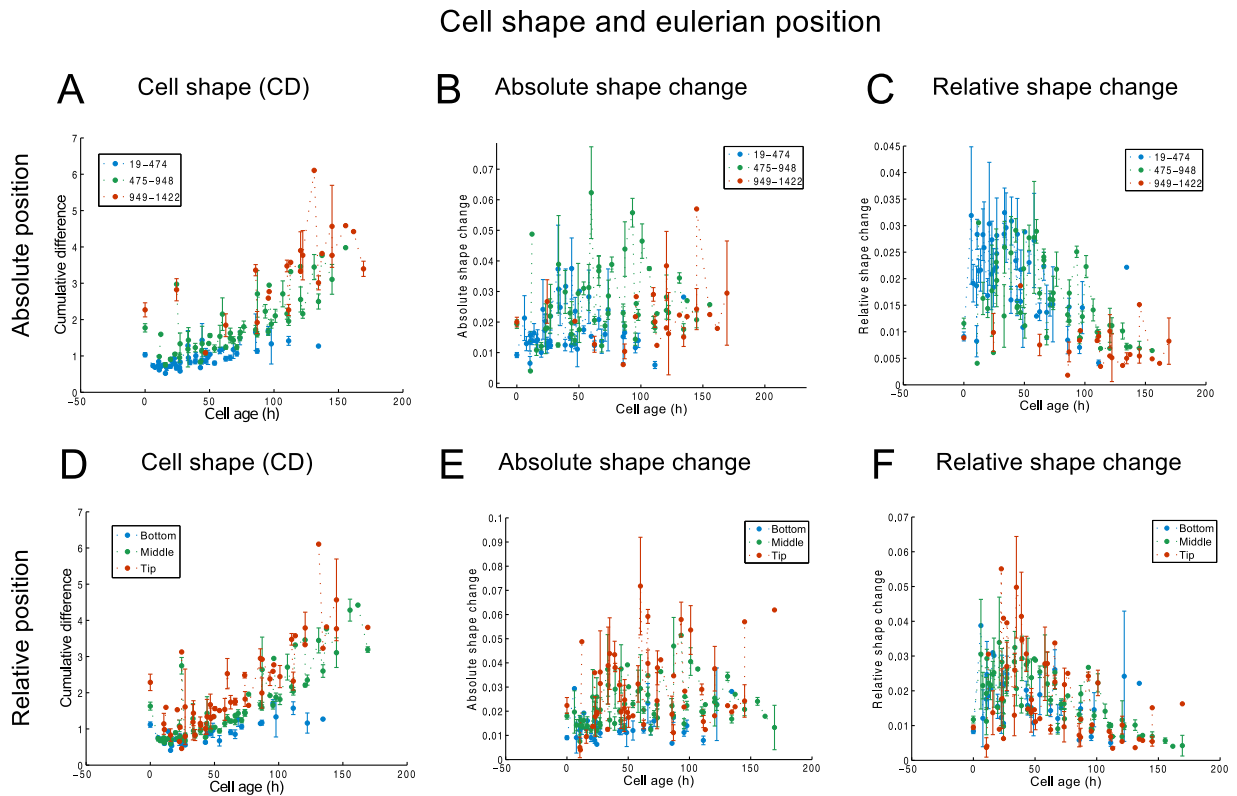


**Figure 4.12: Cell shape dynamics and Eulerian frame of reference when cells are aligned by age does not show strong differences depending on the position. A-D)** Cell shape complexity shows a slight difference depending on the position. Cells are on average more complex towards the tip region taking an absolute and relative positions. B,E) However, when the absolute change of shape is evaluated, there is not visible differences. C,F) The relative shape change also show that the differences depending on the position are minimal. Averages with standard errors are shown. Number of cells are shown in Figure 4.13.

### 4.3 Dynamics of cell divisions within the leaf

Cell division occurs in a restricted spatial pattern, mainly localized at the base of the leaf (Donnelly *et al.*, 1999; Kazama *et al.*, 2010; Andriankaja *et al.*, 2012). In contrast with other plant organs (i.e roots), the divisions disappear over time. Recently, it was reported that cell divisions within the leaf are contained within a fix-domain of about  $100 \mu\text{m}$  from the base of the leaf for several days until it abruptly disappears (Kazama *et al.*, 2010; Andriankaja *et al.*, 2012; Lenhard, 2012).

Using *in vivo* time lapse data, I revisit this spatial and temporal pattern. In addition, I explore some other characteristics of dividing cells such as the rate of division over time and the length of the cell cycle.

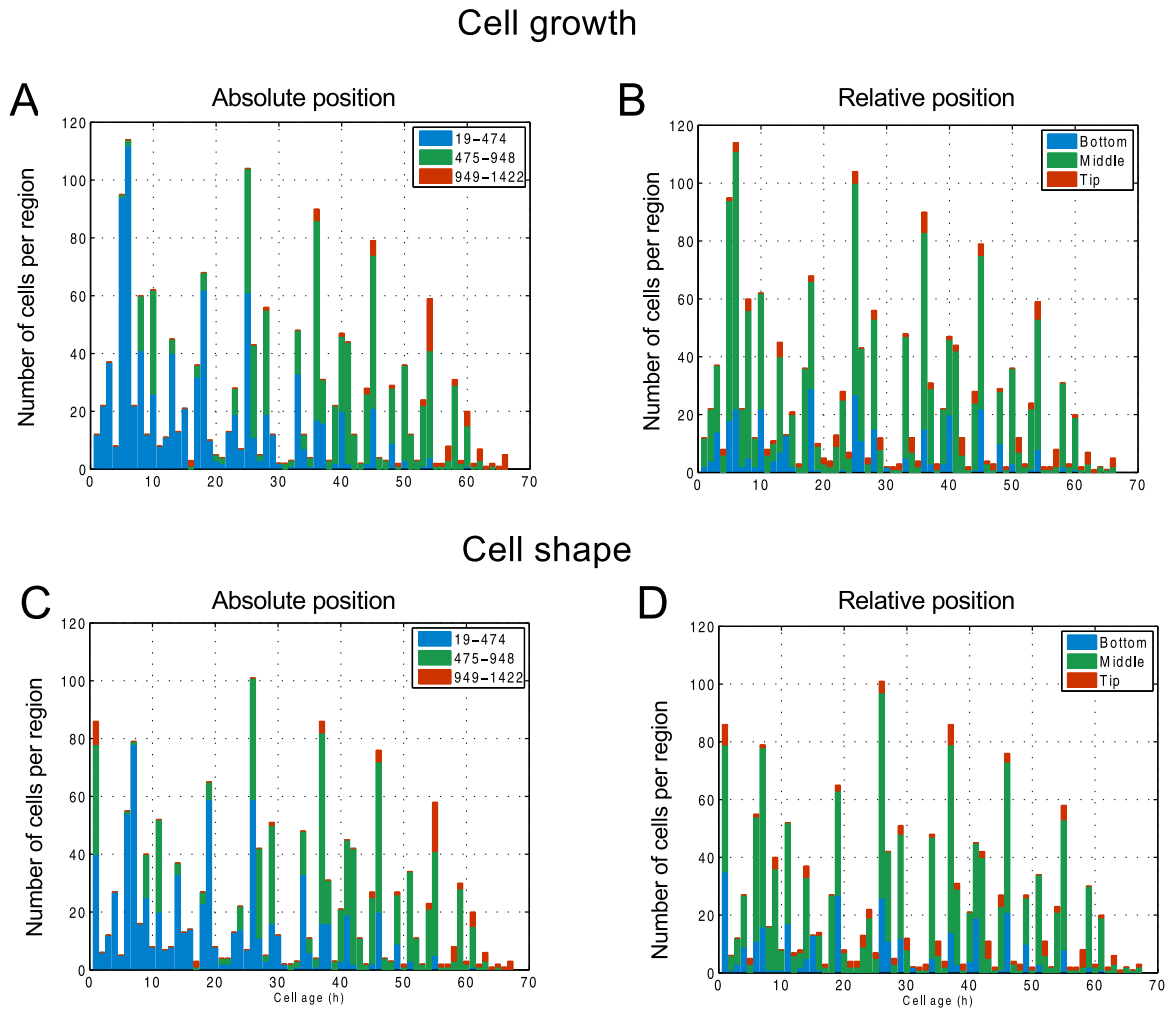


**Figure 4.13: Number of cells considering a Eulerian frame of reference when cells are aligned by age.** A-B) Number of cells taken into account for the analysis of cell area dynamics. C-D) Number of cells taken into account for the analysis of cell shape dynamics. In the x-axis, the age categories (from 1-66) are showed. See also the Methods section in this chapter.

### 4.3.1 Spatial and temporal dynamics of cell division: revisiting the cell cycle arrest front

The cell cycle arrest front (or, division zone) was identified as the length from the base of the leaf where the majority of cell divisions were detected (Kazama *et al.*, 2010). Figure 4.19 shows the spatio-temporal dynamics of the division zone, taking 80% of the detected divisions for three independent experiments (taking 90% showed a similar tendency). Although these leaves correspond to different experimental conditions (see next section), the behaviour of the overall leaf length and the division zone is very similar (Figure 4.19A).

Throughout leaf development, the proportion of the leaf that contains dividing cells gradually decreases (Figure 4.19C). However, the absolute size of the division zone first increased until approximately  $350 \mu\text{m}$  at about 220 hours and then, it decreases until cell divisions were not detected by 330 hours (this was corroborated by manual inspection

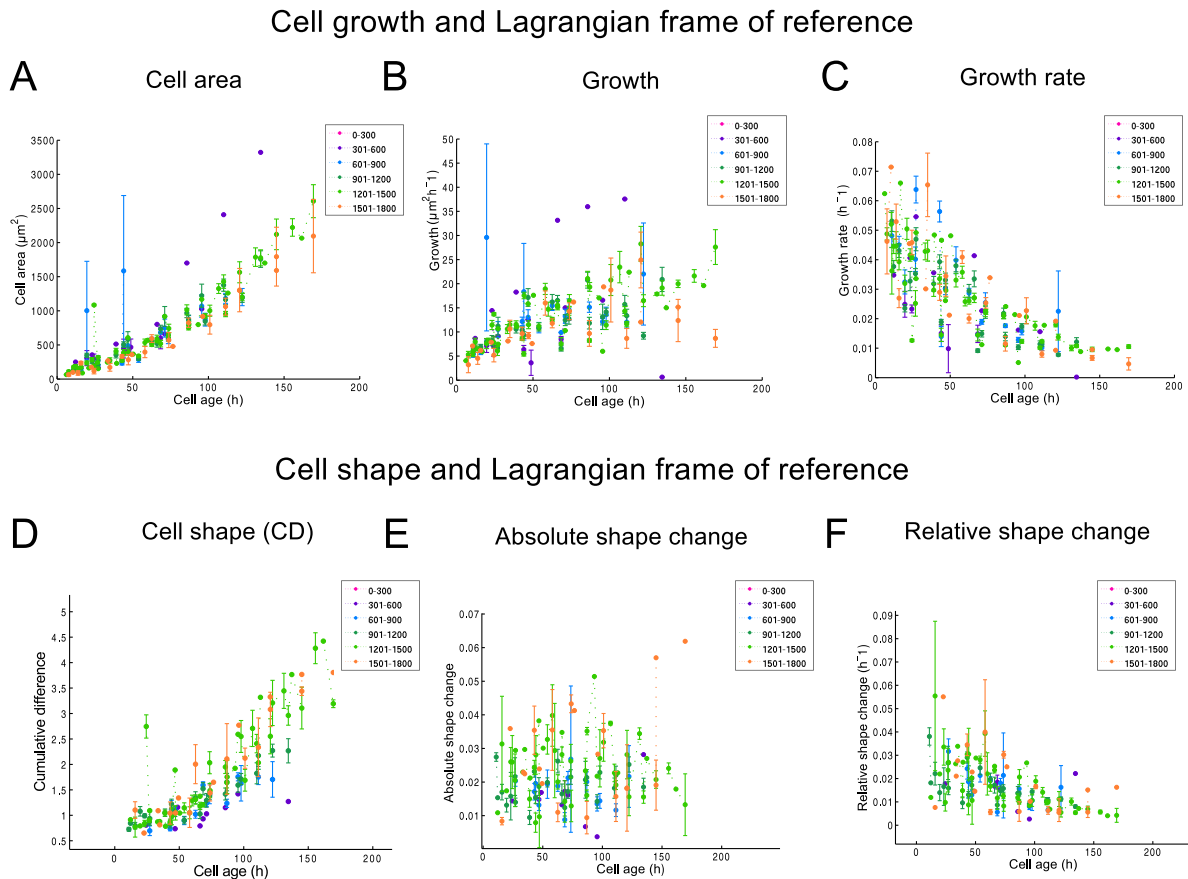


**Figure 4.14: Cell area and cell shape dynamics taking a Lagrangian frame of reference when cells are aligned by their age does not show strong differences depending on the position.** The colour-code indicates the end position of groups of cells (in this case 340 HAS). A,D) Cell area and cell shape are increasing over time without a visible effect depending on the cell's position. B,E) The absolute growth and absolute shape change does not show any difference depending on the position. C,F) Similarly, the relative growth and relative shape change does not show separation when position was considered. Averages with  $1 \pm$  standard errors are shown (dots without error bar represent single values data points). The number of cells considered are shown in Figure 4.15.

of individual images for ExpID3002-PD and ExpID3078-PA). This behaviour was very consistent among layers of the leaf, as is shown in Figure 4.19D, where the divisions in the mesophyll were tracked manually (see also Figure 4.28 in the appendix). This is in agreement with the uniform expression throughout all cell layers of the B-type cyclin gene *CYCB1:1*, and further supports the use of the epidermis as a marker for tracking cell proliferation in the leaf (Andriankaja *et al.*, 2012).

Together with the spatial restriction of the region where divisions are detected, the division rate (proportion of dividing cells per hour) is decreasing (Figure 4.20). There are at least two possible explanations to account for the observed decrease in the division rate: 1) cells are increasing the duration of their cell cycle or 2) cells are leaving the cell cycle. The results showed here support the second option (an exception is the leaf ExpID3148-

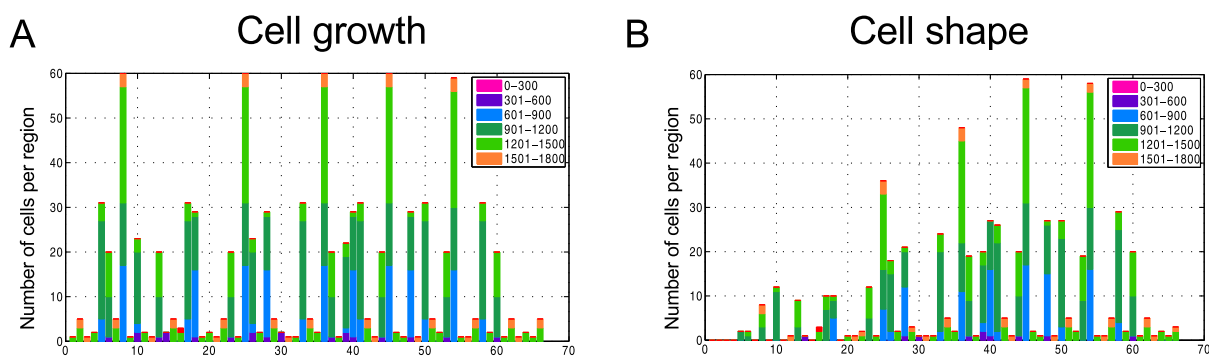


**Figure 4.15: Number of cells considering a Lagrangian frame of reference when cells are aligned by age.** A) Number of cells taken into account for the analysis of cell area dynamics. B) Number of cells taken into account for the analysis of cell shape dynamics. In the x-axis, the age categories (from 1-66) are showed. See also the Methods section.

PA that was treated with auxin). Therefore, over time cells are dividing less frequently and in a more restricted spatial domain.

These results support that the cell divisions are contained in a spatially restricted domain. However, in contrast of what was previously reported, the length of cell cycle arrest front does not stay constant. Moreover, according to high spatio-temporal resolution *in vivo* data, it does not decrease drastically either.

An outstanding question is how this spatio-temporal dynamics of cell division is regulated. Although the answer to this question is beyond the scope of this work, in the final Chapter, I speculate about some possibilities.

## 4.4 Perturbation of the system: auxin treatments

In order to gain further insights into the regulation of the cell dynamics during leaf development, additional time-lapse experiments adding auxin and its control were performed.

The motivation to test auxin as a first candidate is that it has been involved in the transient arrest of growth during shade-avoidance syndrome (Carabelli *et al.*, 2007), development of the puzzle-like cell shape (Xu *et al.*, 2010, 2011; Li *et al.*, 2011) and regulation of the cell divisions within the leaf (Lincoln *et al.*, 1990; Hu *et al.*, 2003; Guo *et al.*, 2013). When plants are exposed to shade, for example because neighbouring plants have overgrown them, they arrest transiently leaf growth and redirect the growing machinery to the stem in an attempt to overcome the shade. Interestingly, this temporal arrest of growth depends on auxin-induced cytokinin breakdown (Carabelli *et al.*, 2007). Auxin has also been involved in the development of pavement cell shape during leaf development (Xu *et al.*, 2010, 2011; Li *et al.*, 2011) and in the regulation of cell divisions within the leaf (Lin-

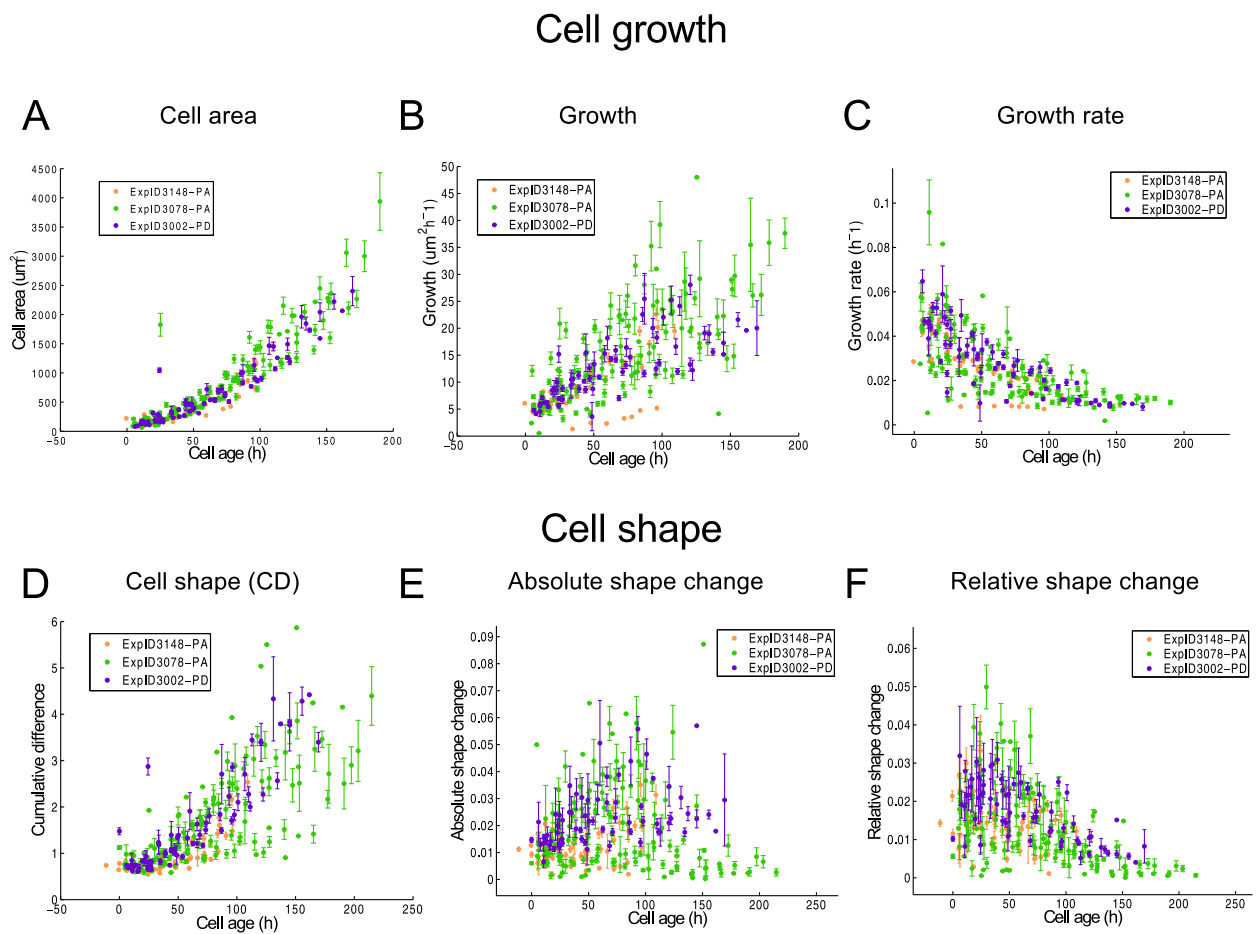


**Figure 4.16: The overall growth and shape dynamics follows a very similar trend when the cell age is taken into account.** A) Cell area increases over time in a very similar manner. B) Growth has also the tendency to increase over time but the variability is higher. C) The growth rate also shows a strong tendency, but it is decreasing over time. D) Cell shape complexity is also increasing over time, but it shows higher variation than cell area (A, specially ExpID3078-PA). E) Absolute shape change increases very slowly and shows high variability in the three experiments analysed. F) The relative shape change increases until approximately 50 h, and then decreases. Averages with standard errors are shown. Each colour indicates an independent experiment. The three leaves analysed correspond to ExpID3002-PD (no treatment), ExpID3078-PA (DMSO added) and ExpID3148-PA (NAA added, see section 4.4) and are plotted separately to appreciate the variation within experiments.

coln *et al.*, 1990; Hu *et al.*, 2003; Guo *et al.*, 2013). In addition, auxin response (quantified by DR5) is not distributed homogeneously in the leaf during development (Figure 4.21, Aloni *et al.*, 2003), but it presents a maximum towards the tip of the leaf, possibly leading to different auxin concentration exposures. Then, the logic behind the experiment was that if auxin is indeed involved in the mechanism that regulates the dynamics of the cell growth, cell shape and/or cell division, these (or some of them) will be altered when the plants are exposed to exogenous sources of auxin or in mutants where hormone signalling or transport is impaired.

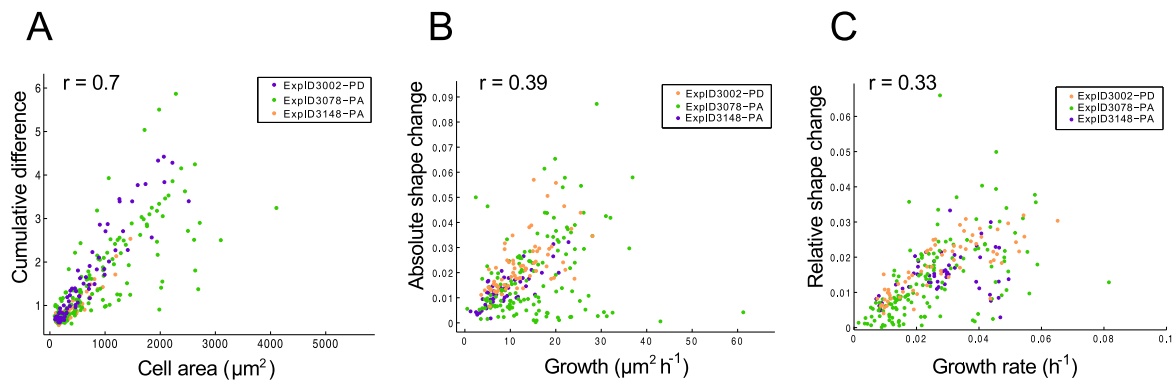


**Figure 4.17: Cell growth and cell shape are correlated.** A) The overall cell area and cell shape are highly correlated but not their B) absolute rate of change or the C) relative rate of change. The mean of each variable per time interval corresponding to three experiments were used to calculate coefficient of correlation ( $r$ ).

Mutants in auxin production and auxin transport (segregating triple *yucca* mutants and *pin1* mutants, see appendix Figure 4.35) were prepared with a membrane marker. However, these mutants show a significant alteration in the overall plant development (*yucca*, *pin1*) and in leaf morphology (*pin1*), that the analysis of those could obscure the results obtained and were not further analysed.

An analysis of different spatio-temporal scales of the auxin treatment (ExpID3148-PA) and its control (ExpID3078-PA) was performed in the same way as described before. The results are shown in the appendix Figure 4.29-Figure 4.34. Similarly to previously discussed results, the rates of cell growth and shape change under auxin treatments showed a gradient-like behaviour taking an Eulerian (Figure 4.29-Figure 4.30) and Lagrangian coordinates (Figure 4.33) that disappears after alignment by cell age (Figure 4.31, Figure 4.32, Figure 4.34). Thus, there were no qualitative differences in the cell behaviour under auxin treatment and its control. However, when the overall values and rates of change are compared with other experiments, it is evident that the exogenous auxin treatment (20 nM) decreases on average the cell complexity (Figure 4.22, see discussion).

Moreover, there was no a dramatic difference in the overall leaf length, the length of the division zone or the relative division rate (Figure 4.19A-C and Figure 4.20A). The only alteration observed is that the average length of the cell cycle was increased under auxin treatments (Figure 4.20B). However, this behaviour is observed just in one of the two leaves analysed and repetition of this experiment and different auxin concentrations will be needed to draw a conclusion.

## 4.5 Discussion and concluding remarks

The aim of this chapter was to gain understanding on the regulation of cellular dynamics during leaf morphogenesis through the dissection of different spatial and temporal scales

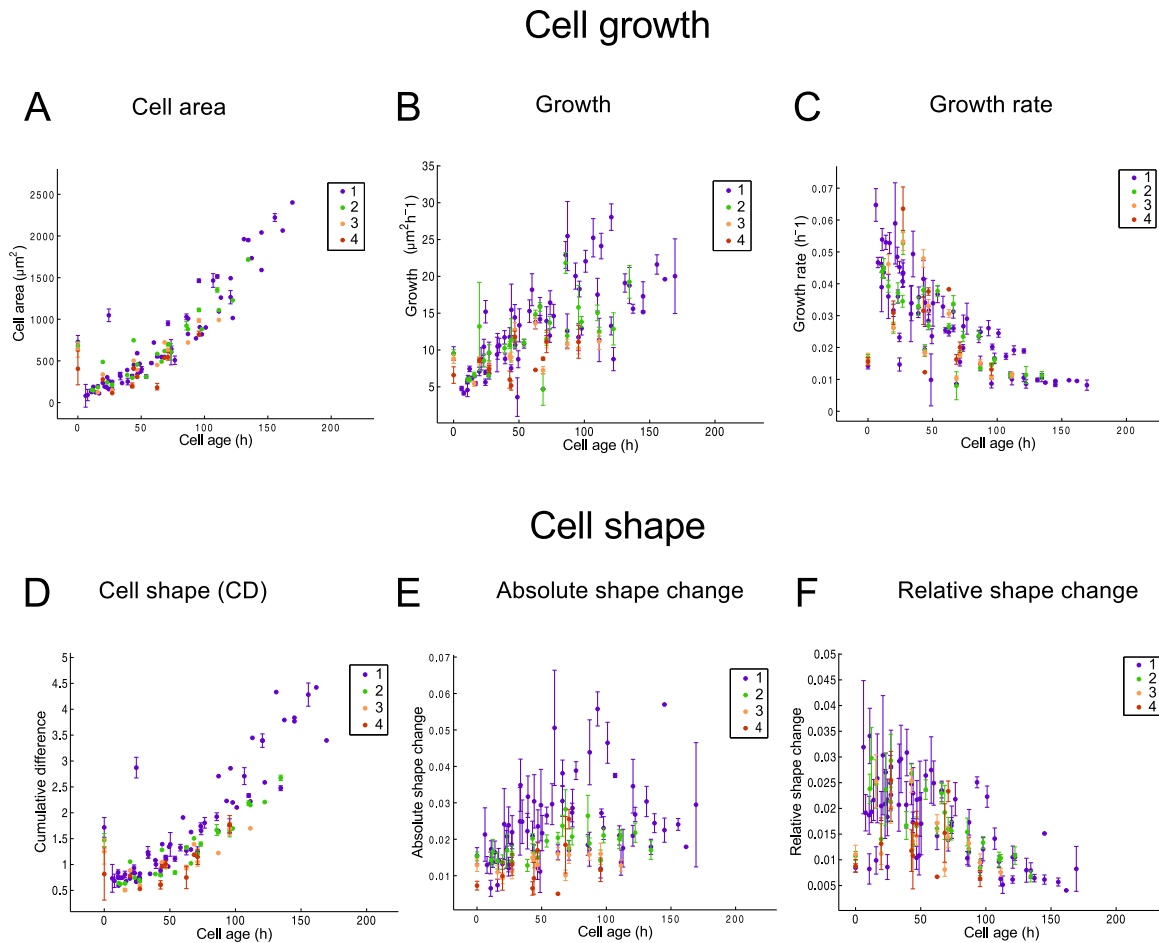


**Figure 4.18: Cell area and cell shape dynamics change independently of the number of cell divisions pursued.** The number in the legend indicates the number of divisions detected within the time-lapse (the fourth division is likely to correspond to the last division). A-C) In general, the overall tendency in cell area does not depend on the number of divisions that a cell will perform. D) Cell shape shows a slight separation, that should be analysed statistically. E-F) The absolute and relative shape change does not show differences. Averages with standard errors for ExpID3002-PD are shown. Other experiments are shown in the appendix Figure 4.26 and Figure 4.27.

involved in leaf development. This was achieved using a combined pipeline of long time-lapse imaging and computer algorithms to extract cellular dynamics (described in Chapters 2 and 3). This analysis allowed separating the role of position and developmental cell age in the dynamics of cell growth and cell shape to re-evaluate the spatio-temporal pattern of cell divisions during leaf development.

In addition to the overall gradient in cell area and cell shape complexity, the analysis of their dynamics showed that there are also gradients of growth and shape rates at the cellular level. This is consistent with previous studies that tracked growth focused on regions of the leaf of *Arabidopsis thaliana* (Kuchen *et al.*, 2012; Remmler & Rolland-Lagan, 2012) or focused on late stages of development in other leaf species (Avery, 1933; Schmundt *et al.*, 1998; Granier & Tardieu, 1998).

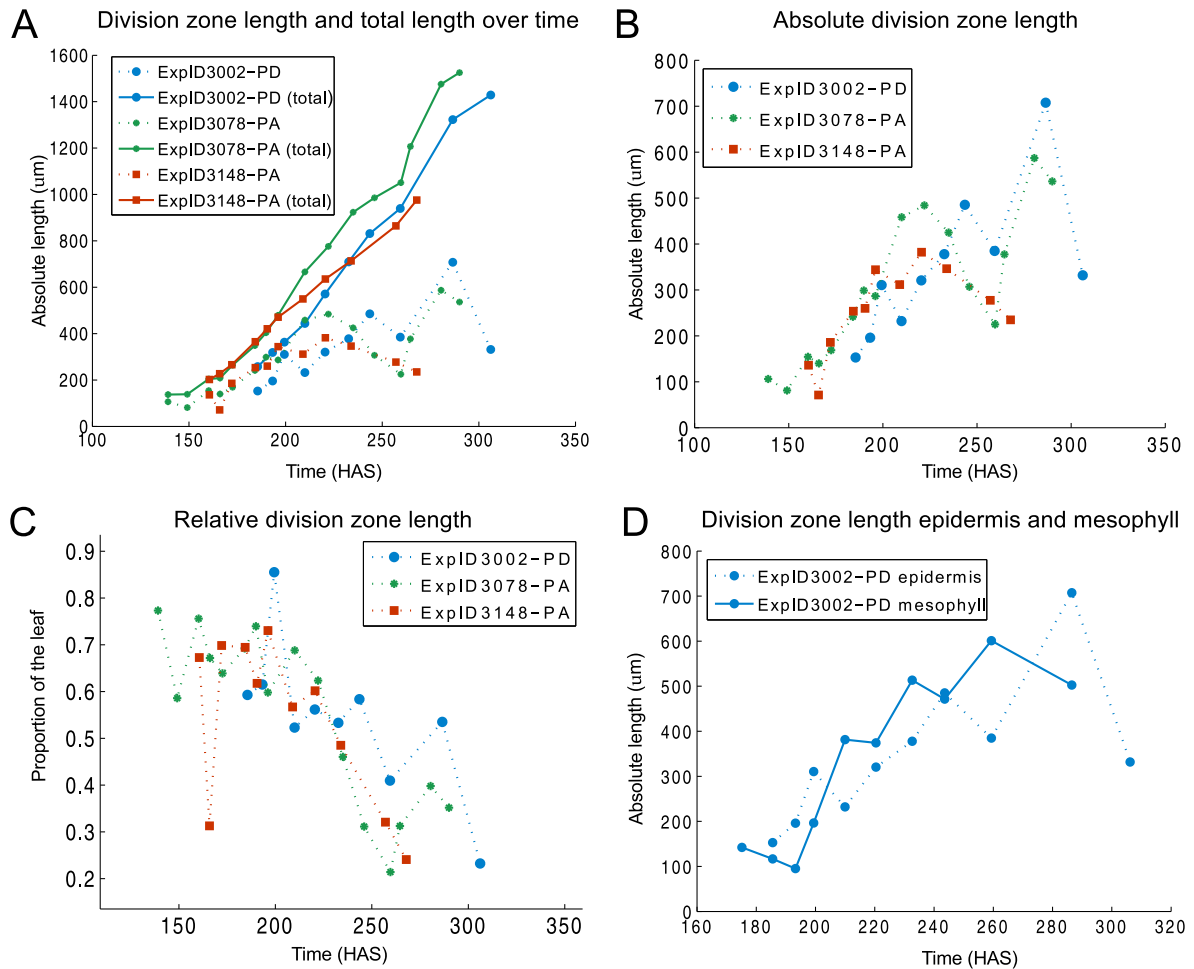


**Figure 4.19: The zone where division takes place is not within a fixed distance.** A) Length of the cell cycle arrest front and total leaf length for different leaves (three independent experiments) show a very similar tendency. B) Absolute length of the division zone shows that the place where divisions occurs increases over time up to approximately 220 HAS, and then decreases. C) The proportion of the leaf where cells are dividing is decreasing over time. D) The dynamics of the division zone follows a very similar trend in internal layers (mesophyll). Importantly, neither of the relative nor the absolute distance is constant as suggested in Kazama *et al.*, 2010. The length of the cell cycle arrest front showed here, considers the place from the base of the leaf where the 80% of the cell divisions took place (similar results were found when the 90% of divisions were considered, no shown). The three leaves analysed correspond to ExpID3002-PD (no treatment), ExpID3078-PA (DMSO added) and ExpID3148-PA (NAA added) and are plotted separately to appreciate the variation within experiments.

Indeed, the growth rate and the relative shape change are smaller at the tip than at the bottom of the leaf. This pattern reflects the fact that, when cell division arrests, cells are saturating and slowing down their cell growth and shape change towards the tip region. These gradients prevailed when an absolute and relative Eulerian coordinates were analysed, independently of the size of the region. Moreover, this graded behaviour also persisted when groups of cells were followed taking into account their displacement due to inhomogeneous division (and growth) and internal tissue deformation (Lagrangian approach). Then, to distinguish between the possibility that the graded cell behaviour

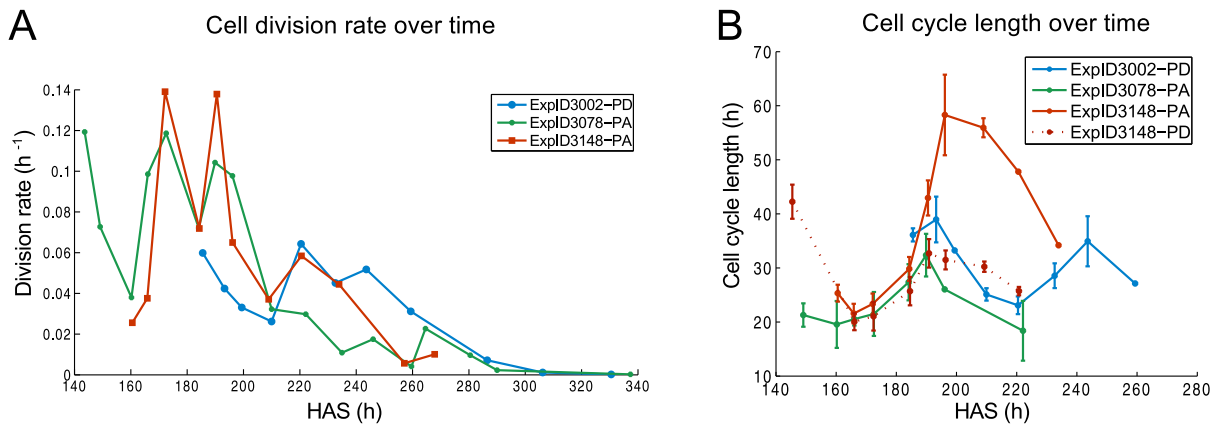


**Figure 4.20: Division rate decreases over time.** A) The division rate is decreasing over time. This indicates that at the same time as the division zone is becoming spatially restricted, there is also a decrease in the frequency of cell division over time. The division rate was calculate as the ratio between the number of cells that divide to the total number of cells, divided by the time interval between time points (see methods section). B) Length of cell cycle over time (time interval between two consecutive divisions) shows increasing and decreasing phases. Averages and standard errors are shown. ExpID3148-PA (treatment with 20 nM of NAA) shows an increase in the cell cycle length. However, this increase was not detected in the other leaf from the same experiment (ExpID3148-PD)

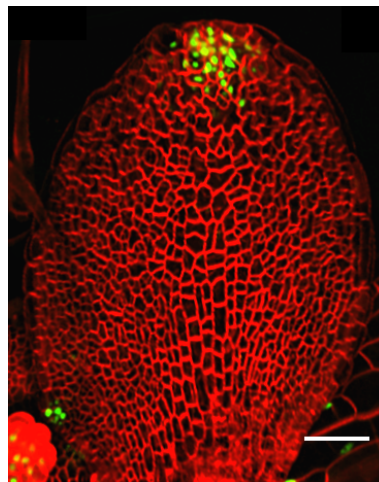


**Figure 4.21: Auxin response is localized at the tip of the leaf.** Wild type Columbia plant 7 days after stratification (DAS) expressing pmCherry membrane marker (red) and DR5-Venus expressed in the nucleolus (green signal) shows that there is strong auxin-response towards the tip of the leaf. Scale bar correspond to 30  $\mu m$ .

was due to a “changing” position or, due to differences in developmental stage, an extra temporal scale (the time of the cell) was included in the analysis. This was achieved by aligning cells with respect to the time at their cell division, that is easily performed once cell lineages have been identified (see Chapter 3).

Importantly, when the cell age is considered, the gradients of growth and shape rates depending on the cell’s position disappear. This suggests that cells behave differently because of their age and not because the position and highlights the importance of dissect-

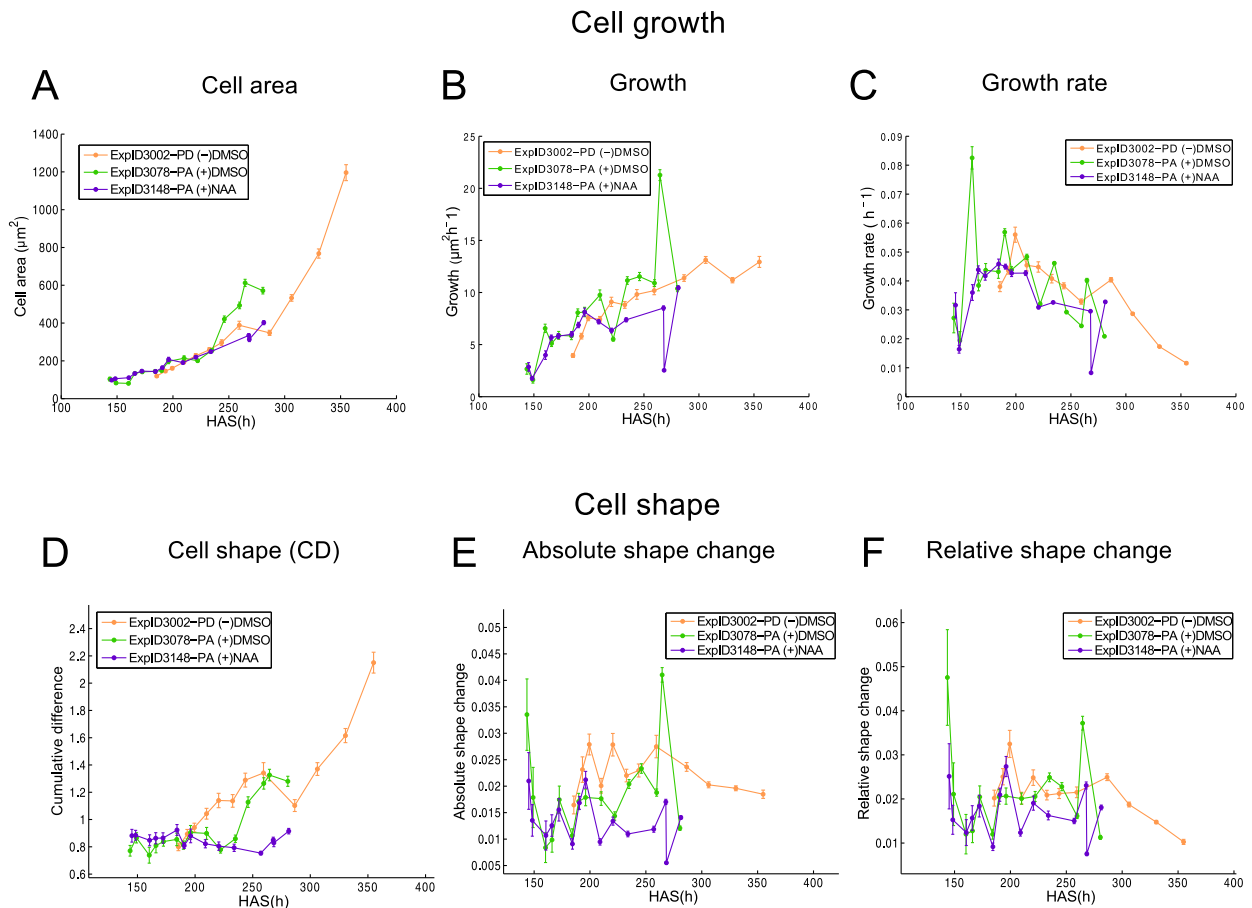


**Figure 4.22: Cell growth and cell shape under auxin treatments.** A-C) Cell growth shows a very similar trend among experiments. D) Cell shape complexity, in contrast, decreased under auxin treatments. E-F) The absolute and relative shape is slightly decrease under auxin experiments and follows a very similar trend than the growth rate.

ing not only the spatial but also the temporal scales in the analysis of the cell dynamics.

An important remark is that cells are behaving differently according to the position, but not *because* of the position. On the contrary, the results presented here strongly suggest that cell position is playing a minor role in determined the dynamics of cell growth and shape. This is a challenging affirmation because cells at the tip of the leaf are rarely dividing, so it is always a very limited sample size (number of cells considered are shown in Figure 4.13 and Figure 4.15) and a statistical approach will be required to evaluate if this difference is significant. However, if there is still an influence of the position, this is minimal.

Thus, differences in developmental cell age provide an explanation for the long-standing observed gradients of growth rates within the leaf and shows that it is not necessary to attribute this behaviour to gradients in concentration of growth regulating substances, as proposed before (Remmler & Rolland-Lagan, 2012).

Surprisingly, once the cell age is taken into account and a “synchronized population” is evaluated, it is possible to distinguish a strong tendency of the growth rate and relative shape change to decrease over time in all the experiments evaluated. This observation im-

plies that the dynamics of cell growth and cell shape follow a very similar trend after cell division, suggesting that division “resets” the dynamics of cell growth and shape. This is a plausible possibility because during the cell cycle many proteins undergo synthesis and degradation, that might reset the state of the cell. For instance, recently it was shown that protein degradation during division “resets” the concentration of the members of the network involved in the asymmetric cell division in the root stem region (Cruz-Ramirez *et al.*, 2012).

The strikingly similar trend on the growth rate and the relative shape change followed by cells aligned with their cell age leads to the question on how cell growth and cell shape dynamics are regulated after cell division. I could argue that cell shape complexity is increasing because the combined action of an internal patterning mechanism (i.e Turing instability) in a growing domain, which I will discuss briefly in the next chapter.

There are different proposals about what regulates the cell growth. One hypothesis is that cells change their cell growth dynamics as they progress towards commitment to differentiation. Under this scenario, cell growth rate could be modified by the number of divisions performed (or, only by the last division before differentiation). However, there was no noticeable different behaviour when cells were further separated depending on the number of cell divisions they underwent during the experiment (Figure 4.18; the fourth division is likely to correspond to the last division because the tracking experiments extended until divisions disappeared from the leaf).

Other possibility is that cell growth regulation occurs by means of a size-sensing mechanism. This implies that cells are growing depending on their size, topic that has been widely discussed in unicellular organisms and in culture of animal cells (Jorgensen & Tyers, 2004; Tzur *et al.*, 2009; Turner *et al.*, 2012).

A size control mechanism could be inferred by plotting the growth rate after cell division versus the area at the time of cell division and analysing their correlation (Turner *et al.*, 2012; Kafri *et al.*, 2013). In the hypothetical situation in which there is a mechanism that measure size (“sizer”), smaller cells grow faster in proportion than bigger cells and the correlation is -1. On the contrary, no correlation (i.e the slope is zero) could suggest that there is no size-dependence. In the case of the leaf, Figure 4.23 shows that the correlation for the cell growth is the intermediate value of -0.51 (compare with the relative change in cell shape of -0.2). Note, however, that this approach is merely about assessing a correlation, that not necessarily reflects causality. Thus, further analysis need to be done to determine if cell growth is size-dependent in the leaf.

Another possibility is that instead of a “sizer”, the cell growth could be controlled by means of a “timer” (Turner *et al.*, 2012). Thus, cells slow down their growth over time. Time averaging has been suggested in different contexts (Gregor *et al.*, 2007b; Tostevin *et al.*, 2007; Wartlick *et al.*, 2011; Saunders *et al.*, 2012), but how cells could measure time remains unknown.

Perhaps, as pointed out by Tzur *et al.*, 2009, the underlying regulation of cell growth

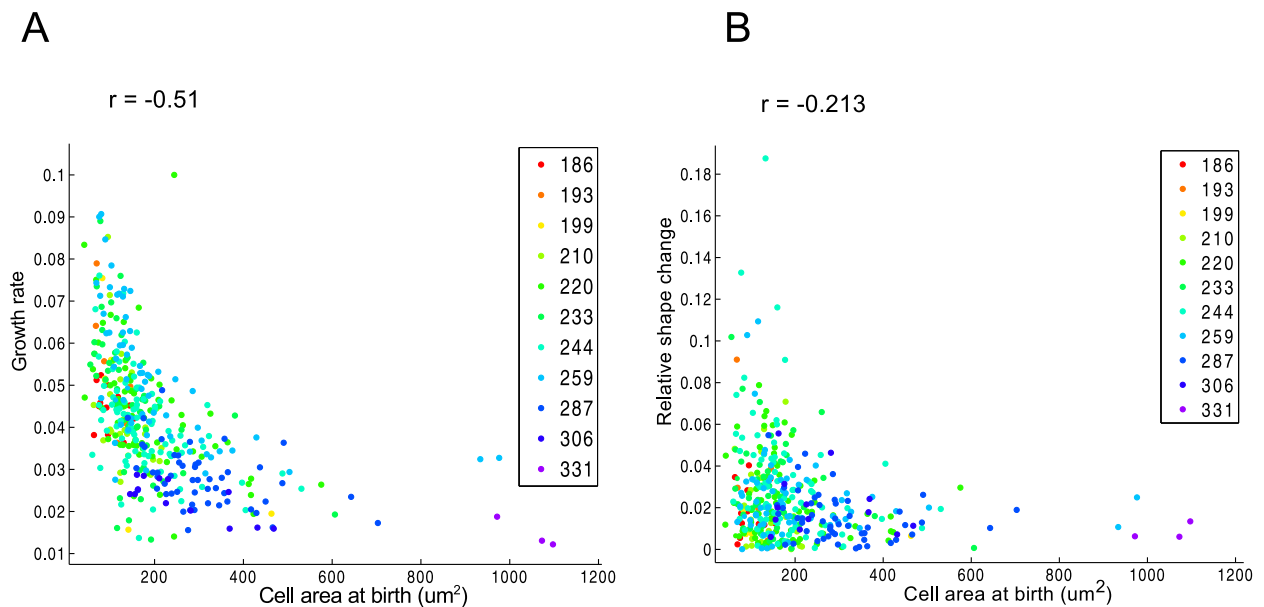


**Figure 4.23: Cell growth and cell shape after cell division.** In the hypothetical case in which the growth regulation depends on the cell size, smaller cells grow proportionally more than larger cells and the coefficient of correlation is -1. On the contrary, if the cell growth is independent of the cell area, the correlation is zero. A) In the leaf, the growth rate and the cell area at birth show a correlation of -0.51, indicating that the cell growth might be influenced by the cell area at birth time (see main text). B) The proportion of shape change is poorly correlated with the cell area ( $r = -0.213$ ). The time (in HAS) where the divisions were detected is colour-coded. Further statistical analysis will be required to test if the putative area-dependence is also modulated over time.

could be more complex than just a “sizer” or a “timer” and might involve both components. For instance, it could be that cell growth is regulated by the cell size but this regulation is different over time (early and late stages during leaf development, see Figure 4.23), or different during the cell cycle (variation depending on the cell cycle phase, see Turner *et al.*, 2012; Tzur *et al.*, 2009; Kafri *et al.*, 2013) or in different moments during development (as in the shoot apical meristem and sepal, reported in Schiessl *et al.*, 2012).

Another important implication after the analysis of the cell growth and the cell shape in a synchronized population is that cell division goes from being just a subdivision of the space (Su & O’Farrell, 1998), to have a role in influencing the dynamics of cell growth and shape in a tissue. Therefore, the analysis of the spatial and the temporal patterns of cell divisions within the leaf is also very important for understanding organ morphogenesis.

With this in mind, I revisited the previously published dynamics of the region where cell divisions take place, also called “the cell cycle arrest front”. In my opinion, the name “cell cycle arrest front” is misleading because cells could continue “cycling”, through endoreduplication, so I refer to it as division zone or proliferation zone. Importantly, using *speechless* simplifies the analysis of the cell divisions that are independent of the stomatal lineage and that potentially follow a different dynamics (White, 2006).

The results presented here supports the existence of a region within the leaf where the cell division occurs more frequently (Donnelly *et al.*, 1999; Nath *et al.*, 2003; White, 2006); however, there were important differences regarding the spatial and temporal dynamics previously suggested.

First, it was proposed that the division zone is contained within a constant distance region of  $100 \mu\text{m} \pm 14 \mu\text{m}$  (mean and standard deviation) from the base of the leaf (Kazama *et al.*, 2010; Lenhard, 2012; Tsukaya, 2013). However, tracking of cell divisions obtained through *in vivo* imaging showed that the division zone is not staying at fixed distance. Rather, it is increasing approximately  $350 \mu\text{m}$  at 220 HAS and then, it decreases until disappears (at around 330 HAS, see Figure 4.19). This discrepancy in the results could be explained because in previous studies, cell divisions were indirectly inferred rather than directly tracked. Indeed, Kazama *et al.*, 2010 based the measurement of the position of the division zone on the PCYB1,1::CYB1,1::GUS expression pattern. While Andriankaja *et al.* (2012) defined the proliferation zone very indirectly using as a criteria the relation between cell circularity (score greater than 0.389, see Chapter 2 for a discussion on the shortcomings of this measure) and small cell area (smaller than  $261 \mu\text{m}^2$ ).

Secondly, it was proposed that the cell division did not disappear gradually down the leaf, but rather, was established and abolished abruptly within a day (Kazama *et al.*, 2010; Andriankaja *et al.*, 2012). Nevertheless, the data presented here shows that the decrease on cell division is rather gradual. This discrepancy in the results obtained could be explained because using solely the criteria of cell circularity and cell size to define the proliferative zone make impossible to detect low frequency cell divisions. For instance, sometimes cells with high cell shape complexity could still divide (although less frequently), leading to miscalculations when cell shape is taken strictly as cell differentiation. In addition, the interval between the time of imaging of previous reports is more coarse than the achieved in this study. Thus, measuring the cell division zone indirectly or without enough spatial and temporal resolution, could give the false impression that cell division “abruptly” disappears.

Importantly, over time the relative frequency of cell division is also decreasing. Thus, cell division is more confined in space at the same time as fewer cells divide. A decrease in the relative frequency of cell division could be attributed to a prolongation of the cell cycle. However, this is not supported by the experimental data (Figure 4.20B) and it is more likely that an increasing proportion of cells are leaving the cell cycle, in agreement to previous proposals (Asl *et al.*, 2011).

An outstanding question is what regulates the dynamics of the division zone until it disappears. The analysis of the spatial pattern of cell division shows that the possibility of a gradient determining its spatial dynamics could be considered and some speculative options will be discussed in the general discussion at the end of this work (Chapter 6, section 6.3).

As a first attempt to gain further insights into the regulation of cell dynamics (cell

growth, cell shape and cell division), I performed some tracking experiments under auxin treatments. This hormone has been involved in the transient arrest of growth during shade-avoidance (Carabelli *et al.*, 2007), in the development of pavement cell shape (Xu *et al.*, 2010, 2011; Li *et al.*, 2011) and in the regulation of cell divisions within the leaf (Lincoln *et al.*, 1990; Hu *et al.*, 2003; Guo *et al.*, 2013). Therefore, it was expected that the dynamics of the cell growth, the cell shape and/or the cell division (or some of them) would be modified when the plants are exposed to exogenous sources of auxin.

As mentioned before, the auxin treatment (using 20 nM NAA) decreased the cell shape complexity of pavement cells without altering the overall length/width of the leaf. This is consistent with the previous reports (Xu *et al.*, 2010, Grieneisen *et al.*, 2013a), that suggested that the influence of auxin in cell shape morphogenesis is a concentration-dependent feature acting on the patterning that underlies the jigsaw puzzle-like cell shape and that higher concentrations of auxin could inhibit the formation of new lobes (and therefore, decrease the shape complexity). However, some other shorter time-lapse experiments showed increased cell shape complexity using the same concentration of 20 nM NAA (not shown here).

Besides the cell shape complexity, the only variable that showed alteration under auxin treatment was the length of the cell cycle. However, analysis of other leaf within the same experiment (ExpID3148-PD) did not show this increase (Figure 4.24). Therefore, further tracking experiments under different auxin concentration and the analysis of mutants altered specifically in cell division through the influence of auxin (such as ARGOS and AXR1) will be needed to corroborate this effect.

Thus, the results of auxin treatments suggest that the influence of auxin in the intracellular patterning that underlies complex shapes could be separated from the effect of the hormone in cell divisions and/or leaf growth (see also Chapter 6, section 6.6).

Importantly, the pipeline presented here and the dissection of spatial and temporal scales at the cellular level will facilitate the analysis of the regulation of the cell dynamics. Although the distinctions between Eulerian and Lagrangian frames of references is important for the evaluation of cell dynamics, an analysis taking these two coordinate system into account has scarcely been addressed in plant morphogenesis (Silk & Erickson, 1979).

Remarkably, this is the first time that the dynamics of cell shape is evaluated in such a quantitative way. Although the cell shape and the cell area follow a very similar trend and the overall qualitative behaviour was similar (i.e. both showed a graded behaviour over space), the rates of change in these two aspects differ slightly. Further work will focus on the analysis of the specific shape of the curves quantitatively (for example, fitting curves under different models and statistical analysis) and will be very important to further characterize the cell behaviour.

Although the precise regulation of the cell dynamics that underlie the leaf morphogenesis is beyond the scope of this work, the analysis of cell growth, cell shape and cell

division in relevant spatio-temporal scales enables the re-evaluation of previous conceptions and opens new hypothesis (see Chapter 6).

### 4.6 Materials and Methods

Cell growth was calculated using the real cell area extracted from 2D projections (see details in Chapter 3). Similarly, the change on cell shape complexity was calculated using the cumulative difference and entropy (Chapter 2). Cumulative difference was calculated using 2-50  $L_n$  modes. Entropy followed a similar trend (for example, Figure 4.25 in the appendix)

Negative values in the rate of cell growth and cell shape change were eliminated because they are considered errors of the image, segmentation or tracking procedure. Moreover, pavement cells on the leaf margins were excluded from the analysis because it is not possible to take a complete representation of these cells in the 2D projections.

The rate of change in cell area and cell shape showed in the main text, were calculated using Eq. 4.12 and Eq. 4.10 (see Box2, see Figure 4.24 in the appendix).

Mesophyll division zone was set manually, looking at two consecutive images of the time lapse and assigning a blue dot to cells that will not divide in the next time point and green dot to cells that will divide (see appendix Figure 4.28).

For auxin treatments, the medium was supplemented with the synthetic auxin NAA (1-naphthaleneacetic acid) from an stock solution of 20 *mM* to produce a final concentration of 20 *nM* NAA while the control experiment was supplemented with the same volume of DMSO (dimethyl sulfoxide), the solvent of NAA.

The age of the cells was calculated as:

```
birth_time = cell.snapshots[cell.born_at].has
has = cell.snapshots[k[i+1]].has
cell_age = has - birth_time
```

where `cell.snapshots` is the  $k$  number of time points within the time-lapse experiment and  $1 < i < k$ . `has` is the time in hours after stratification (see details in appendix of Chapter 3). The age categories correspond to the number of each element of the “cell age” array.

The relative division rate was calculated as:

```
relative_division= (Number of dividing cells/ Total number of cells)/ time_interval
```

Plots were generated using python and MATLAB scripts. Correlation coefficients were calculated using MATLAB.

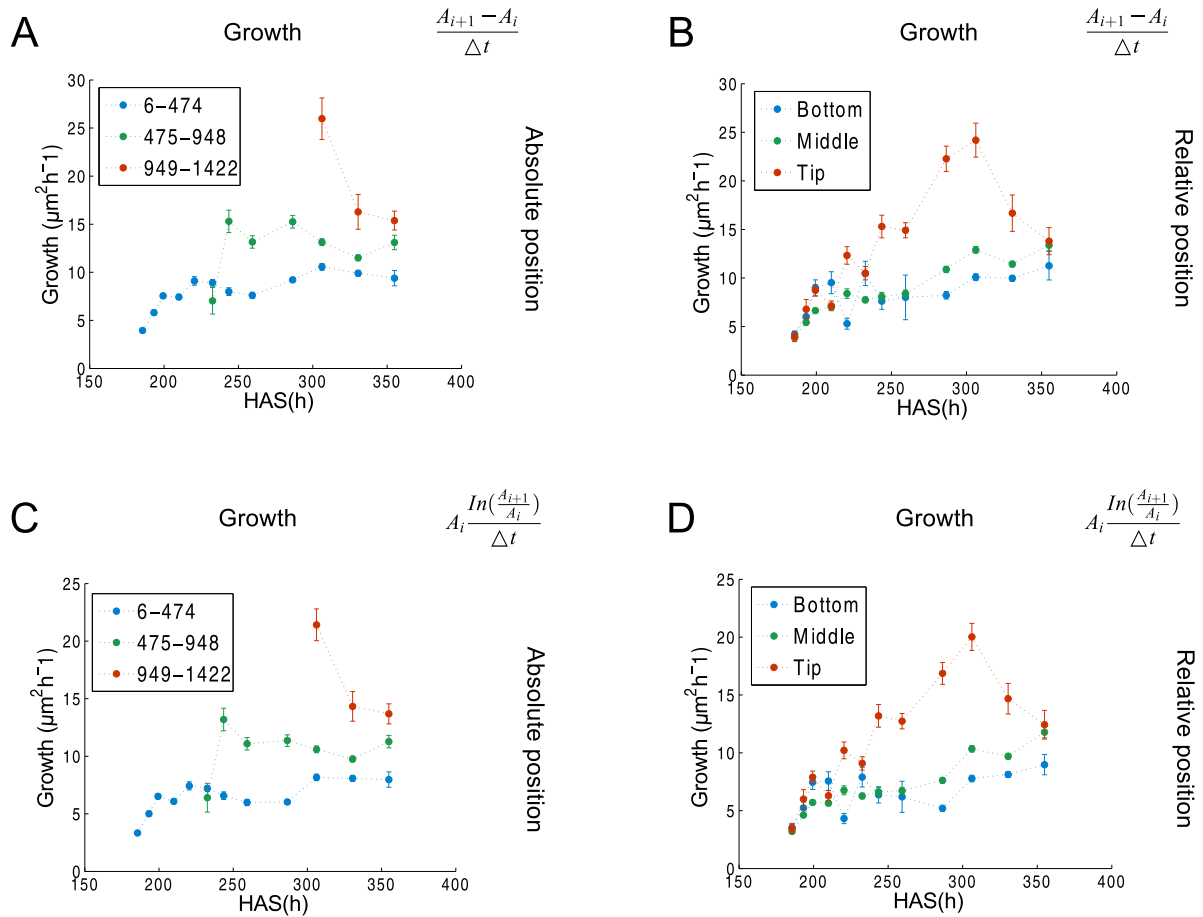


**Figure 4.24: Gradients in cell growth are independent on the underlying model assumed.** A,C) Cell growth assuming a linear model and taking and absolute position (A) strongly resemble the cell growth assuming an exponential mode of growth (C). In the same way, when considering the relative position, B) the cell growth under a linear model shows a very similar behaviour than D) the cell growth assuming an exponential model. The same behaviour occur when the cell shape is analysed (not shown). See also Box2.

## 4.A Appendix:

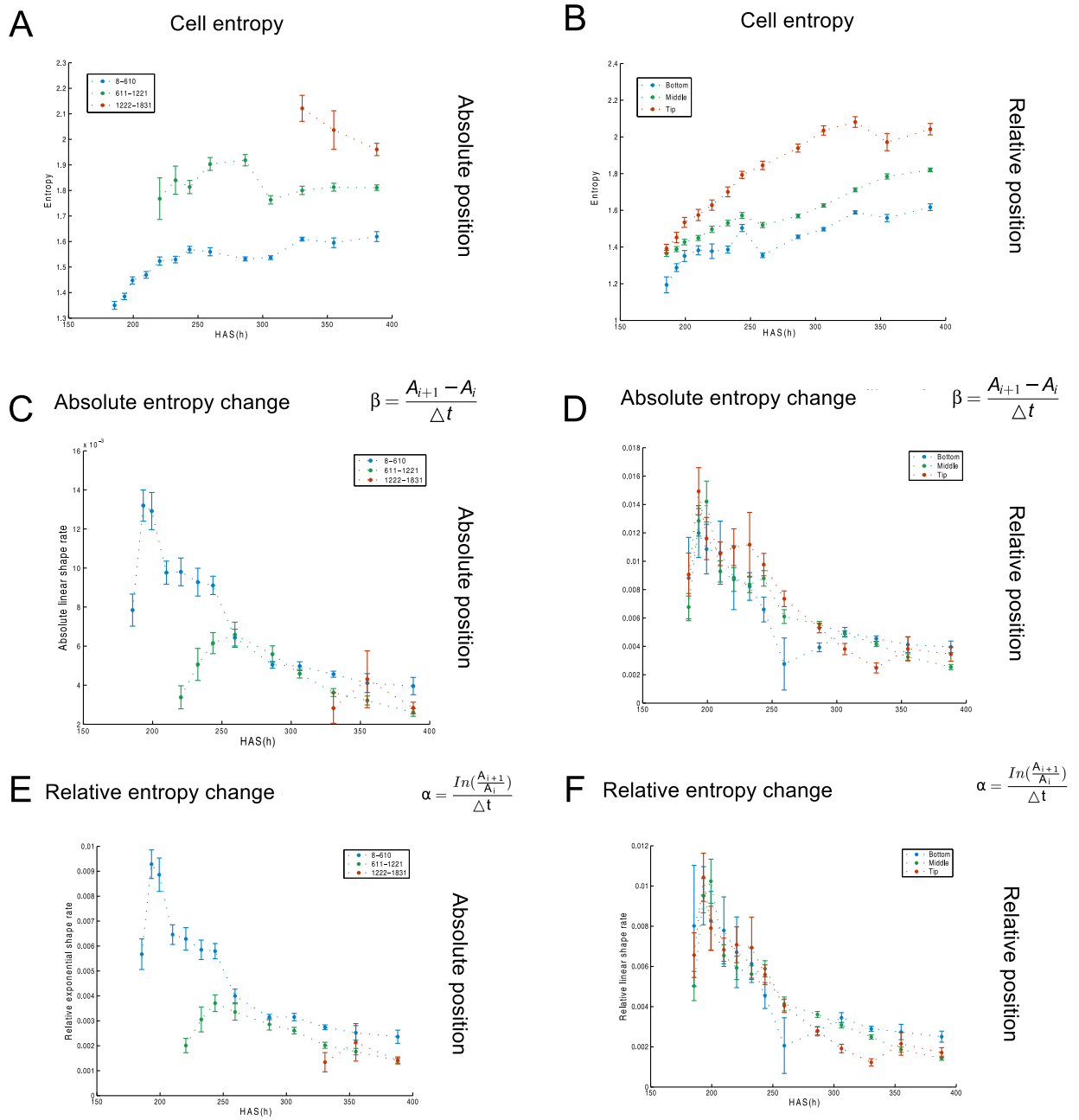


**Figure 4.25: Entropy follows a similar trend than cumulative difference.** The time of the leaf and Eulerian frame of reference are considered. Compare with Figure 4.4.

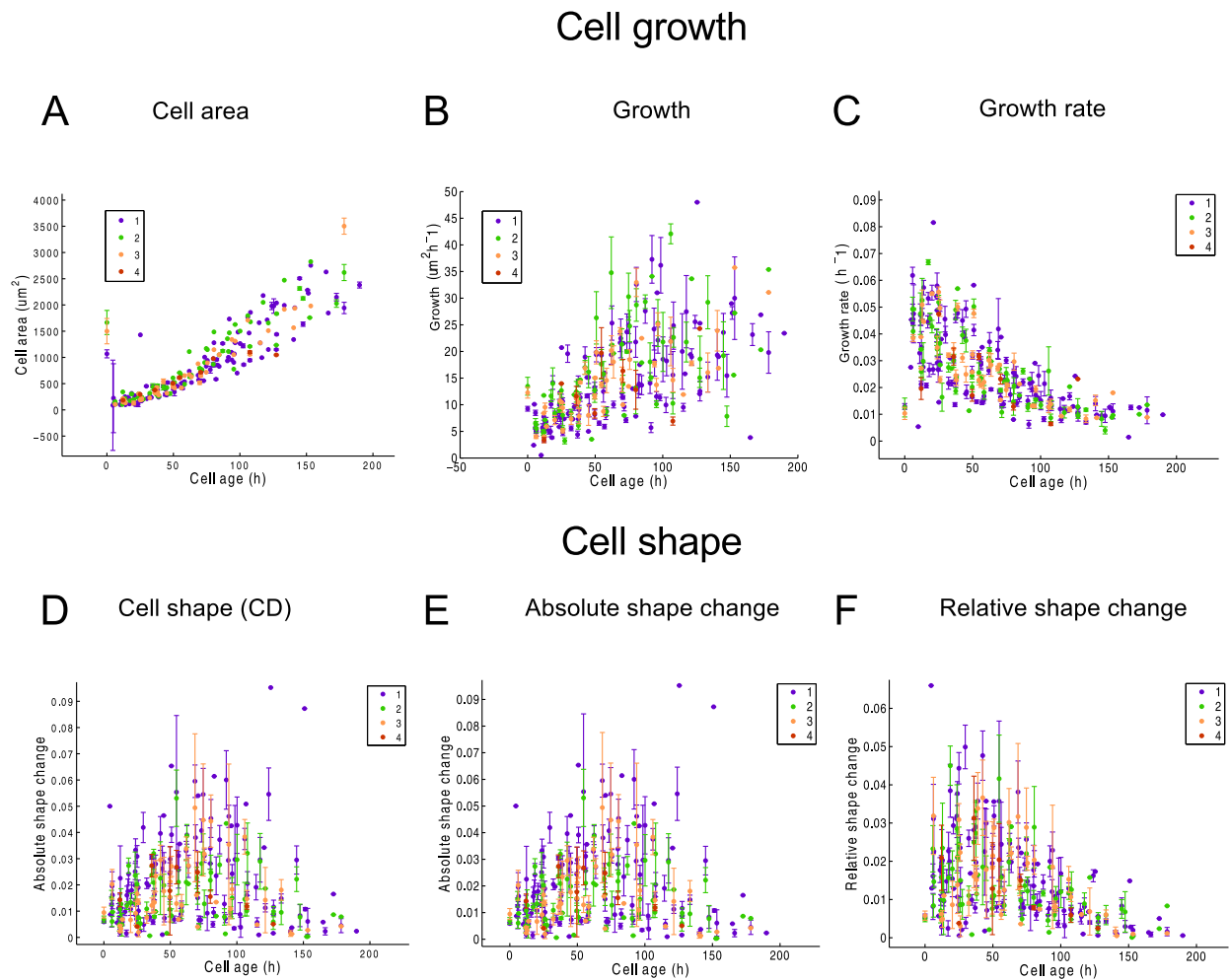


**Figure 4.26: Cell area and cell shape dynamics change independently of the number of cell divisions pursued (ExpID3078-PA).** Related to Figure 4.18 and Figure 4.27. A-F) No differences are detected when the number of divisions performed are taken into consideration.

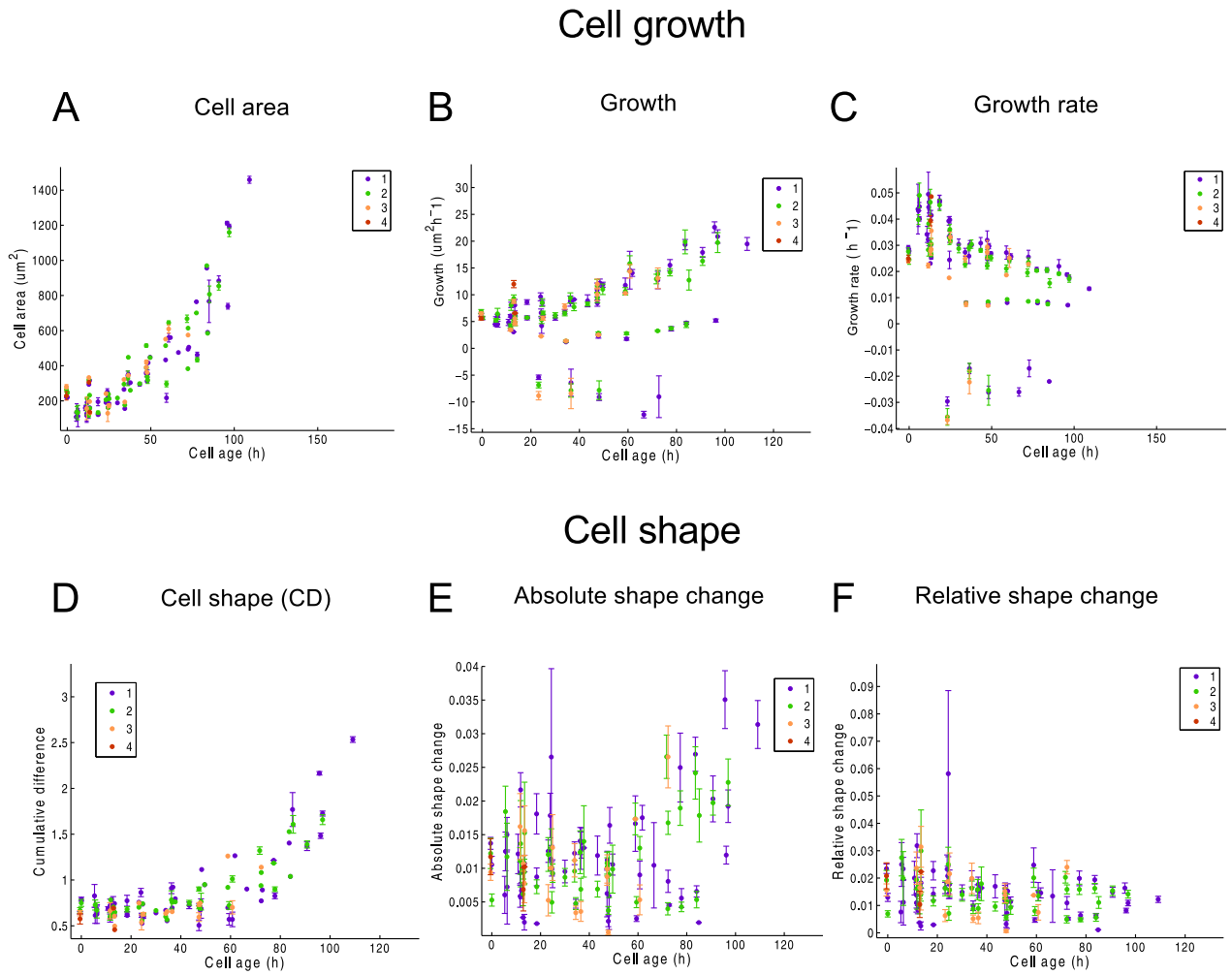


**Figure 4.27: Cell area and cell shape dynamics change independently of the number of cell divisions pursued (ExpID3148-PA).** Related to Figure 4.18 and Figure 4.26. A-F) No differences are detected when the number of divisions performed are taken into consideration.

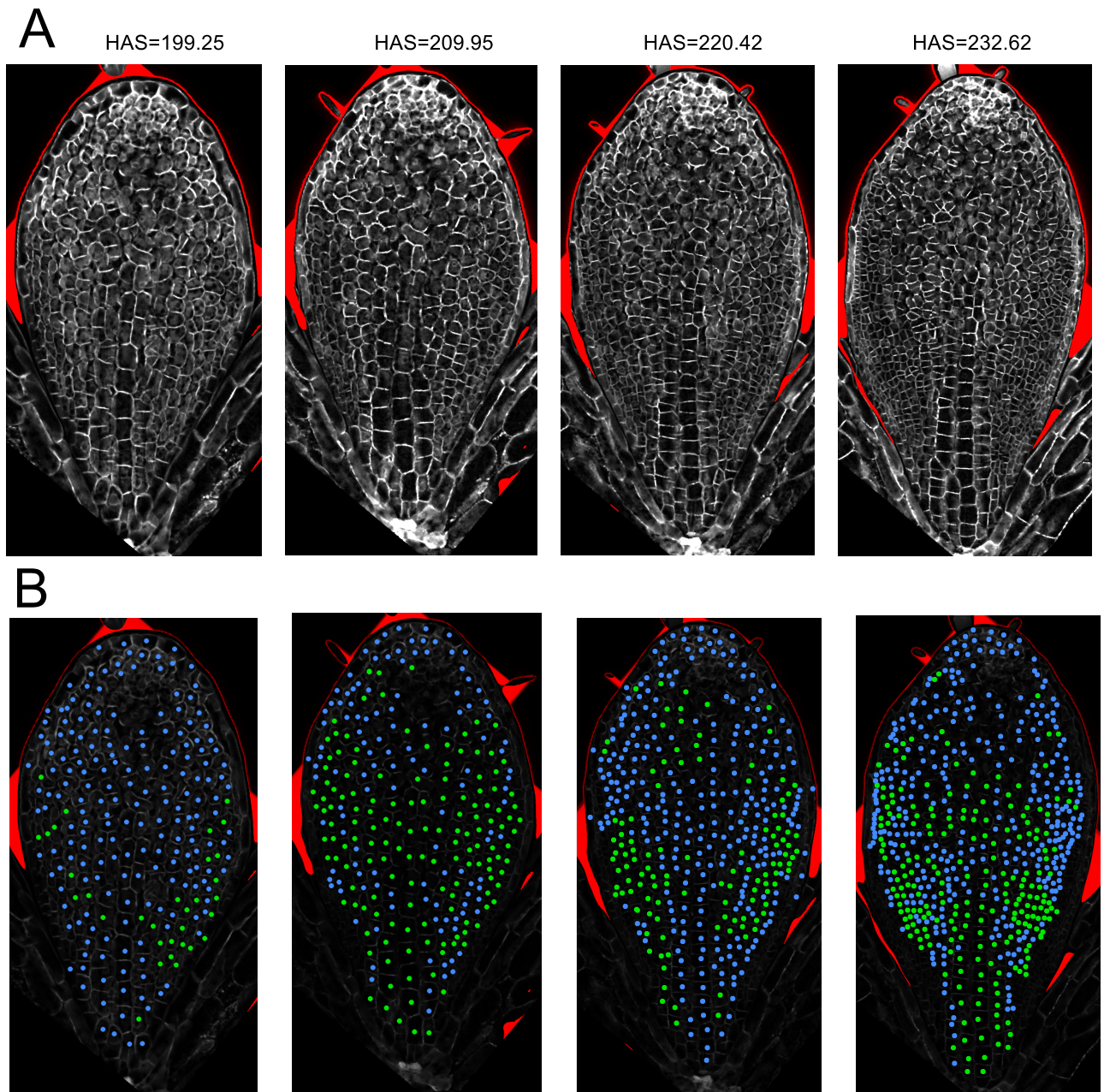


**Figure 4.28: Mesophyll divisions were tracked manually.** A) 2D-projections varying the threshold between surface (see Chapter 3), make possible to visualize internal layers (mesophyll). B) Cells that will divide in a consecutive time point (towards the right) were identified visually and marked with a green dot. The rest of the cells were marked with a blue dot.

## 4 Cell dynamics during leaf development

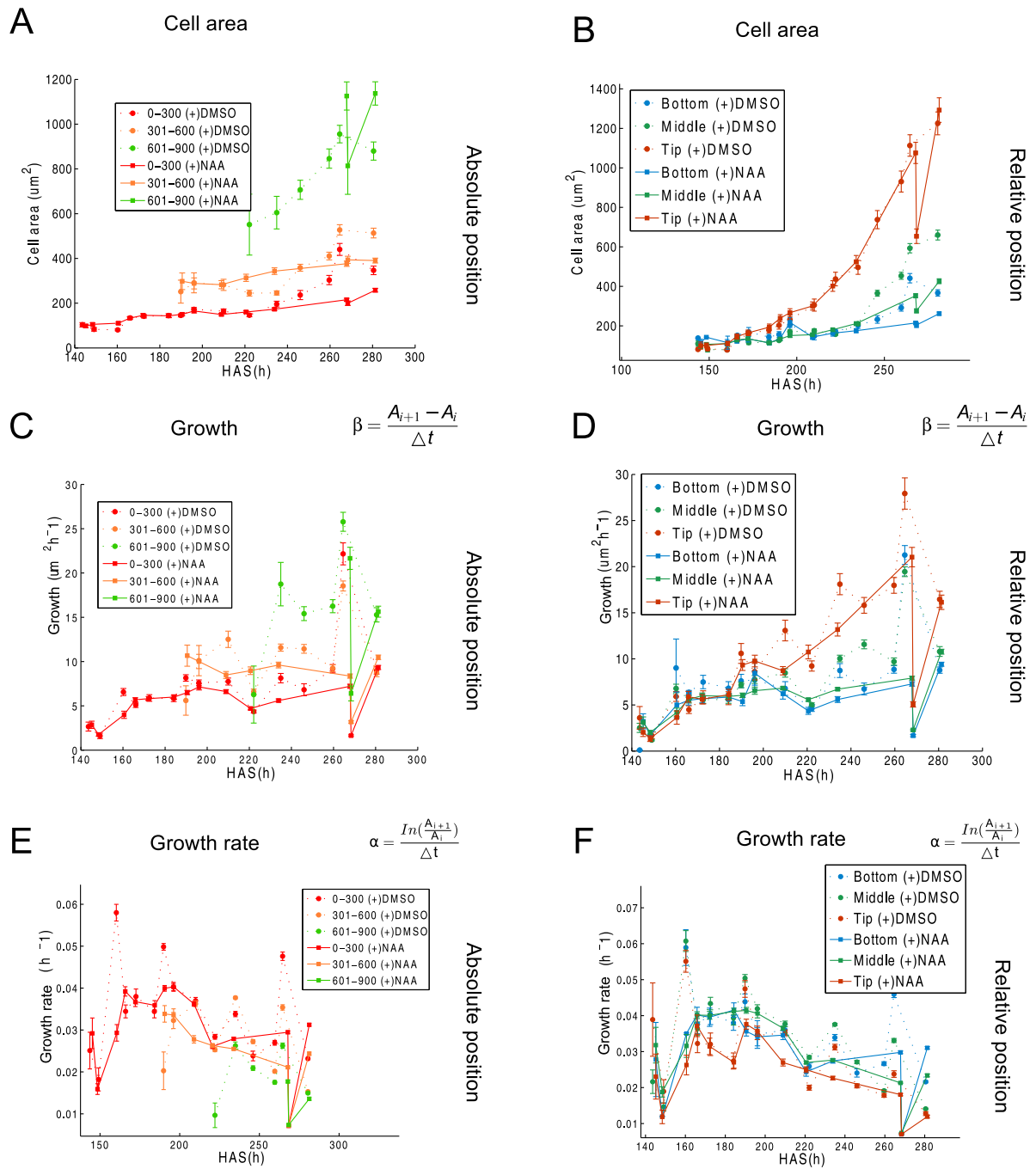


**Figure 4.29: Time of the leaf (HAS) and Eulerian frame of reference showing the growth for auxin and its control (+DMSO).** No obvious difference is found when comparing the cell area, growth and growth rate in the control and auxin treatment.

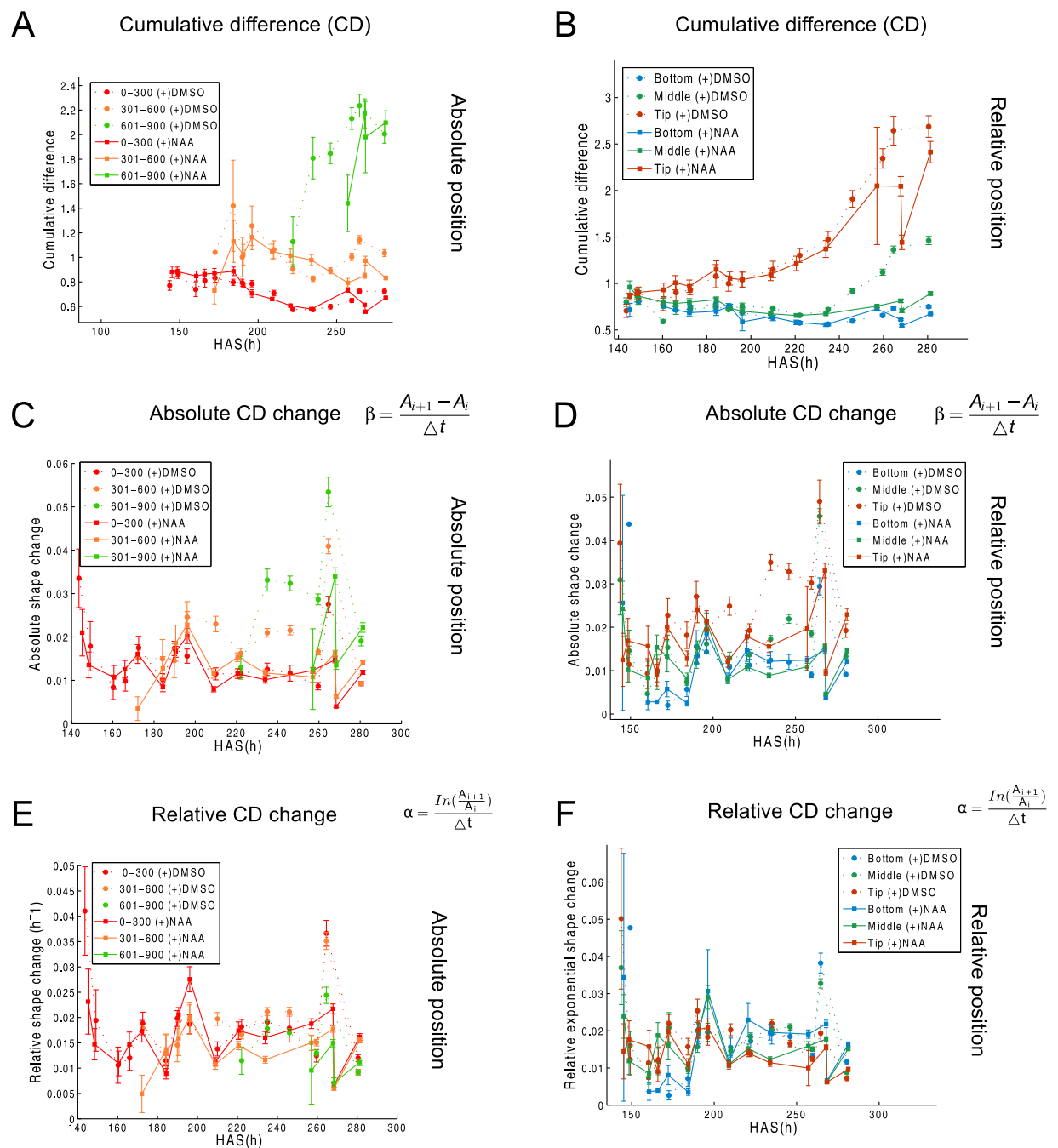


**Figure 4.30: Time of the leaf (HAS) and Eulerian frame of reference showing the cell shape for auxin and its control (+DMSO). There is not obvious difference between the auxin and the control treatment.**

## 4 Cell dynamics during leaf development

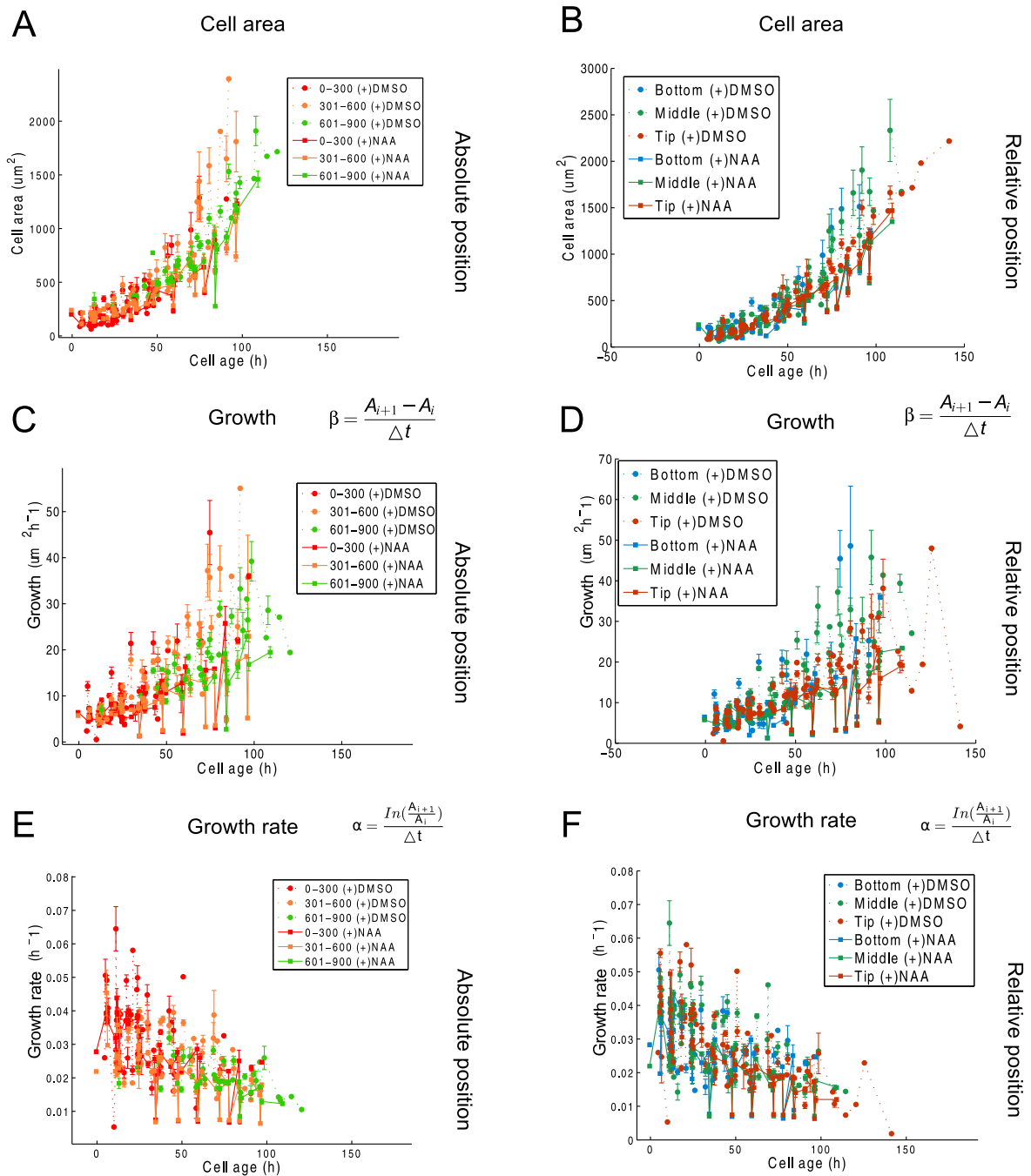


**Figure 4.31: Time of the cell (cell age) and Eulerian coordinates of reference analysing the cell growth under auxin and its control (+DMSO). No differences are appreciated between these two experiments.**

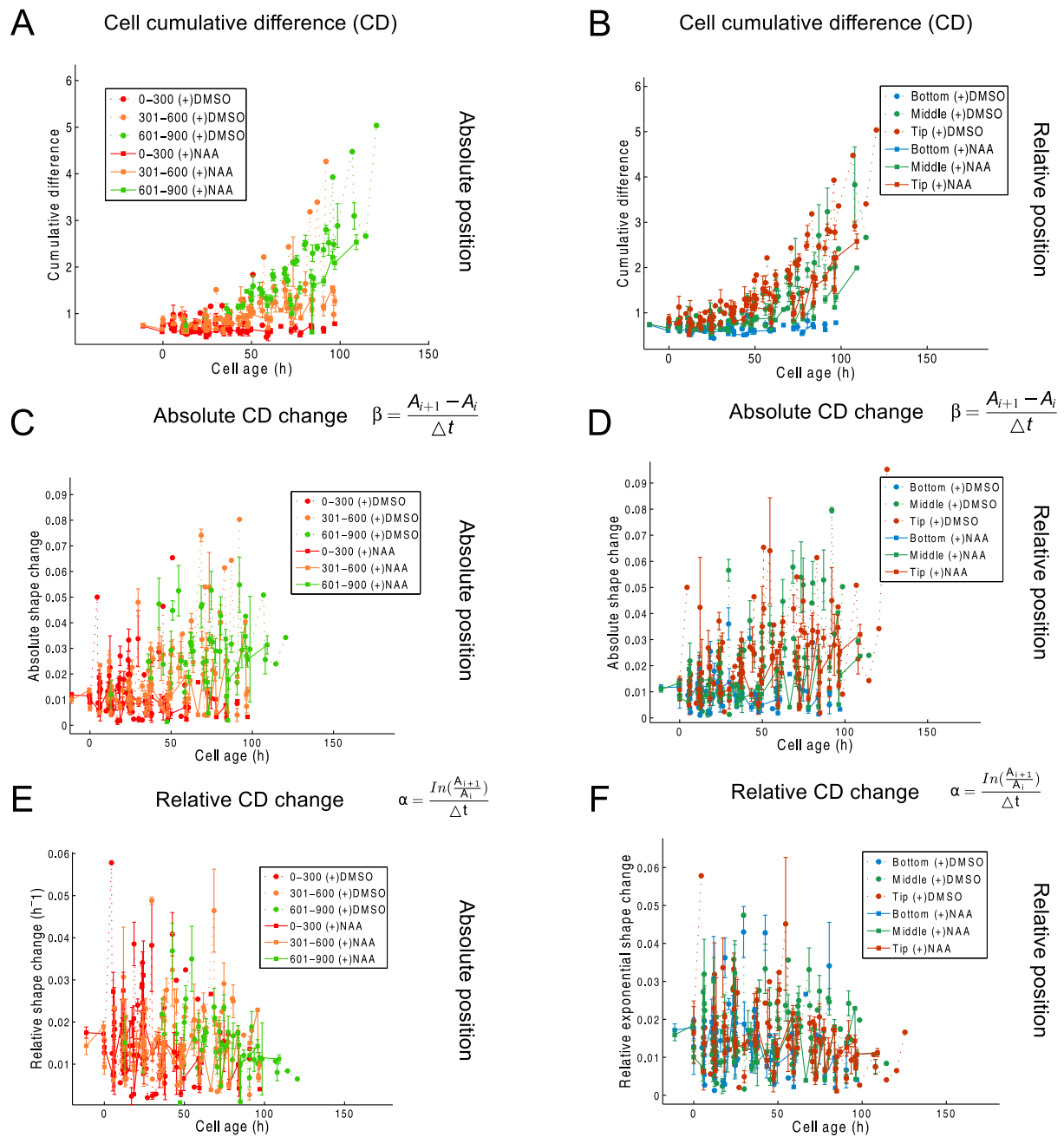
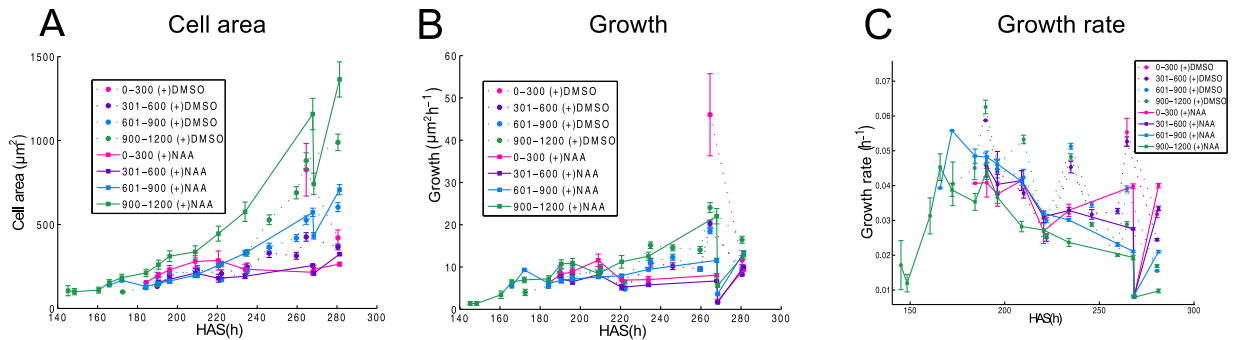


**Figure 4.32: Time of the cell (cell age) and Eulerian coordinates of reference analysing the cell shape for auxin and its control (+DMSO). No differences are appreciated in the experiment with auxin and the control experiment.**

Cell growth and Lagrangian frame of reference



Cell shape and Lagrangian frame of reference

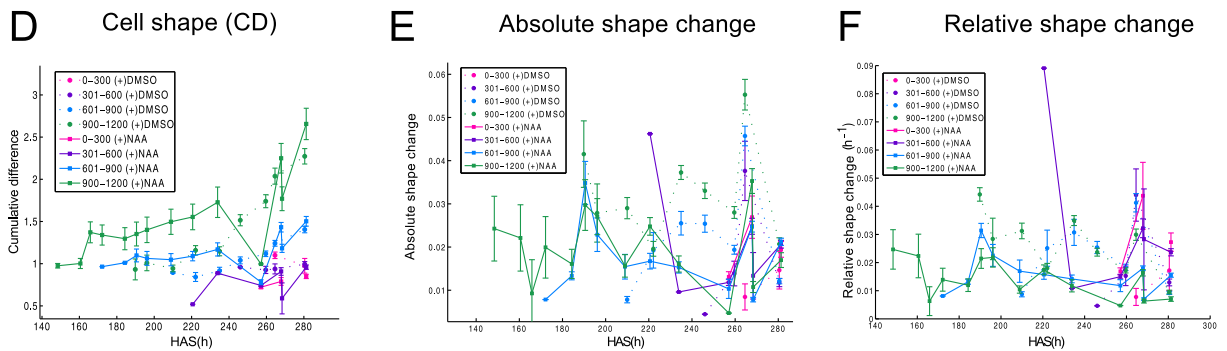
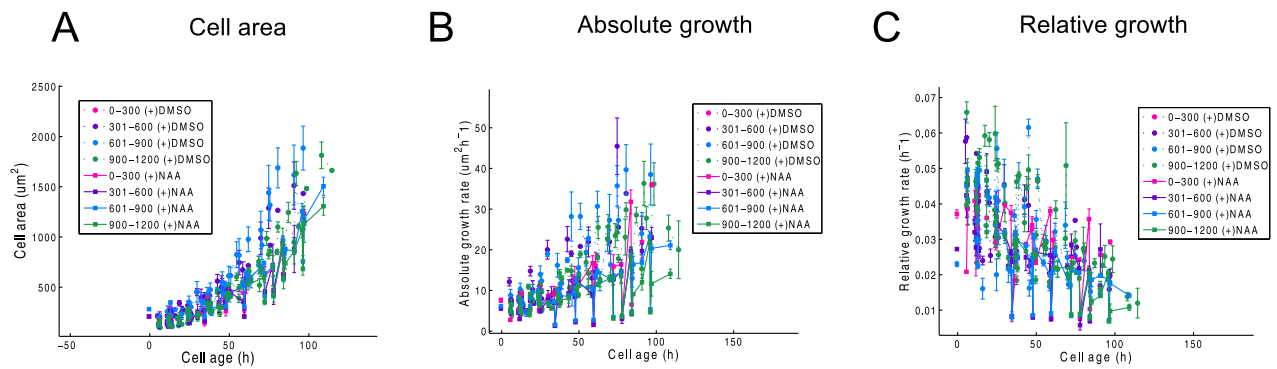


**Figure 4.33: Time of the leaf (HAS) and Lagrangian frame of reference for the analysis of the cell growth and the cell shape for auxin and its control (+DMSO).** The last time point in the analysis of cell growth corresponds to  $t=15$  for both experiments, corresponding to 280 HAS (DMSO) and 281 HAS (+NAA). The last position for the analysis of cell shape was the time point 13 and 14 corresponding to 264.57 HAS (DMSO) and 267.85 HAS (NAA), respectively. No differences are obviously appreciated.

## Cell growth and lagrangian position



## Cell shape and lagrangian position

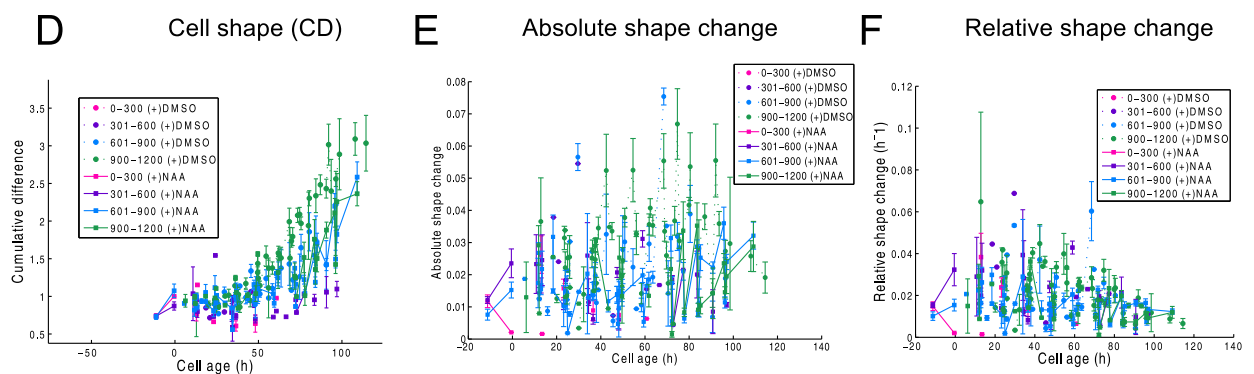


**Figure 4.34: Time of the cell (cell age) and Lagrangian frame of reference for the analysis of the cell growth and the cell shape for auxin and its control (+DMSO).** The time point that was taken as a reference to group cells correspond to 280 HAS (DMSO) and 281 HAS (+NAA). No difference is appreciated between the experiment under auxin and its control.

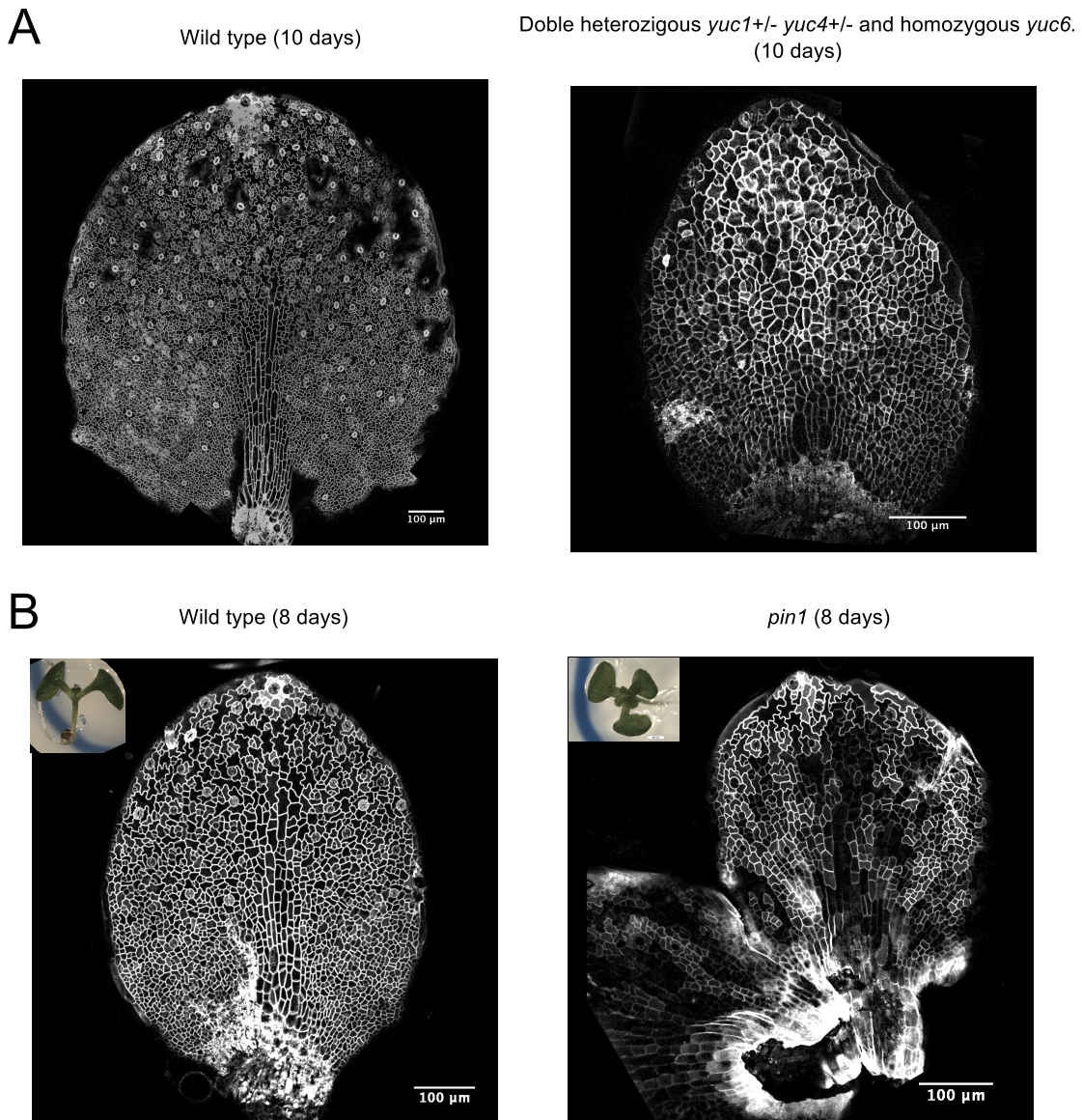


**Figure 4.35: Mutants involved in auxin biosynthesis and auxin transport present strong developmental defects.** A) Wild type (right) and *yucca* mutant (left) on the same stage and growing in the same conditions showed dramatic differences in organ size. B) Wild type (right) and *pin1* mutant (left) on the same stage. The mutant show fusion of leaves, defects in phyllotaxis and were smaller that the counterpart wild type control. The days refers to days after stratification.

## Chapter 5

# Cell shape influence on intracellular dynamics

### Abstract

One of the most characteristic features of pavement cells is their geometry. Although the molecular and genetic basis of cell morphogenesis is invaluable for the understanding of cell morphogenesis, a less explored topic is the effect that cell shape could impose in the intracellular dynamics that underlies cell shape acquisition. In this chapter, I review some relevant literature suggesting that cell shape is not just the result of molecular interactions but, at the same time, it could have an active role for intracellular patterning. I also discuss some hypothesis on how the cell shape could influence the intracellular dynamics. Finally, I speculate about the role of pavement cell geometry in the polarity that underlies the lobe-indentation patterning, emphasizing the potential role of the dynamics of growth and shape obtained through long time-lapse experiments and image processing tools.

## 5.1 Introduction

Cells are shaped in accordance with their developmental context and their final shape is highly correlated with their function. A lot of effort has been invested in dissecting the molecular basis of cell morphogenesis, identifying small GTPases and the cytoskeleton as very important players in plant and animal cell morphogenesis (Etienne-Manneville & Hall, 2002; Yang, 2008). Strikingly, these conserved proteins regulate a multitude of cellular functions including cell adhesion, cytoskeletal remodelling (hence, mechanical stresses), spreading, motility, cell morphogenesis and polarization (Etienne-Manneville & Hall, 2002).

Although the molecular basis of cell morphogenesis is by no means complete, another aspect that has been less discussed is the potential influence of cell geometry in diverse intracellular processes. Consider, for example, that the cell shape represents the space in which all intracellular reactions take place; thus it imposes certain constraints in the molecular dynamics within the cell. Specially interesting is the possible feedback on the molecular players involved in cell morphogenesis as well, a feedback of cell shape that has not been considered before.

In this chapter I discuss the possible effect of cell shape in intracellular dynamics. I start by providing some experimental examples where cell shape has been suggested to play an active role in the dynamics that underlie some key developmental processes at the cellular level. Then, I discuss some theoretical hypothesis on how cell geometry could influence intracellular dynamics during development, pointing out some of the key assumptions. Finally, in light of the shape and growth dynamics of pavement cells obtained using long time-lapse experiments and image processing tools (Chapter 3), I discuss the potential role of the cell geometry during pavement cell morphogenesis.

## 5.2 Influence of cell shape changes during development

In this section I review some examples that suggest that cell shape is an important factor influencing development. The best documented examples can be classified into two groups: 1) cell differentiation and 2) cell division. In these studies, cell shape has been physically or genetically manipulated to adopt a particular geometry (round, star, branched etc.) from which, the effects of such distortion are measured. In other studies when shape manipulations were not possible, the importance of cell geometry was suggested through the use of multilevel computational models.

### 5.2.1 Role of cell shape in cell differentiation

While differentiation may cause changes in the cell shape, several studies have suggested that changes in the cell shape themselves can alter cell differentiation. Experiments where the cell shape was manipulated from round to spread, by changing the area of contact with the substratum in tissue culture (Figure 5.1), showed that cell spreading was often a prerequisite for proliferation while cell rounding was associated with maintenance of a differentiated state in animal epithelial cells (Chen *et al.*, 1997; Watt *et al.*, 1988; Roskelley *et al.*, 1994; Ingber, 1993a). Keratinocytes that were manipulated to be round, expressed higher levels of proteins related with cell differentiation (for example, involucrin) compared with spread cells (Watt *et al.*, 1988). Similarly, in mammary epithelial cells, rounding was necessary for the expression of proteins such as casein, characteristic of these cells when they differentiate (Roskelley *et al.*, 1994).

Cell shape changes from round to spread were also related with cell survival. When capillary endothelial cells were manipulated to be flattened and spread, cell survival was significantly favoured compared with cells that were restricted to be round, regardless of the area of contact with the substrate (that will control how spread the cell is) or the specific combination of adhesion receptors in the substratum (Chen *et al.*, 1997). These examples suggest that cell shape changes themselves (i.e rounding) could influence certain cell types to undergo differentiation or entry to apoptosis (Figure 5.1).

Cell shape can also influence the commitment towards a specific cell fate, as suggested in the case of human Mesenchymal Stem Cells (MSC). Those multipotent cells are derived from bone marrow and can differentiate into bone cells (osteoblast), cartilage cells (chondrocytes) and fat cells (adipocytes). Manipulation of MSC shape using patterned substratum (Figure 5.1A,B) showed that changes on their shape from round to spread were enough to favour a specific cell fate pathway: flattened and spread cells became osteocytes whereas round cells underwent adipogenesis (McBeath *et al.*, 2004). Differential commitment dependant on cell shape was also suggested by experiments using microcontact printing techniques to manipulate the cell shape to acquire diverse geometries with different curvatures and aspect ratios (rectangles, star, etc.). Osteogenesis was favoured when the imposed shape had high aspect ratio (such as rectangular shapes) and shapes with high curvature; conversely, adipogenesis was preferred in circular shapes, and shapes with convex sides (Kilian *et al.*, 2010).

The effect of cell shape in fate acquisition was also shown by culturing MSC cells on top of nanotubular structures with different diameters; cells were forced to elongate and protrude lamellipodium according to the diameter of the nanotube. Interestingly, osteogenesis was favoured just by modifying the dimensions of the nanotubes (that in turn, modified the elongation of MSC cells) without the influence of any osteogenesis inducing media (Oh *et al.*, 2009). This reinforces the hypothesis that the change on the cell shape itself is important for the cell fate specification on these cells.

The molecular basis of the influence of cell shape in differentiation of MSC cells has

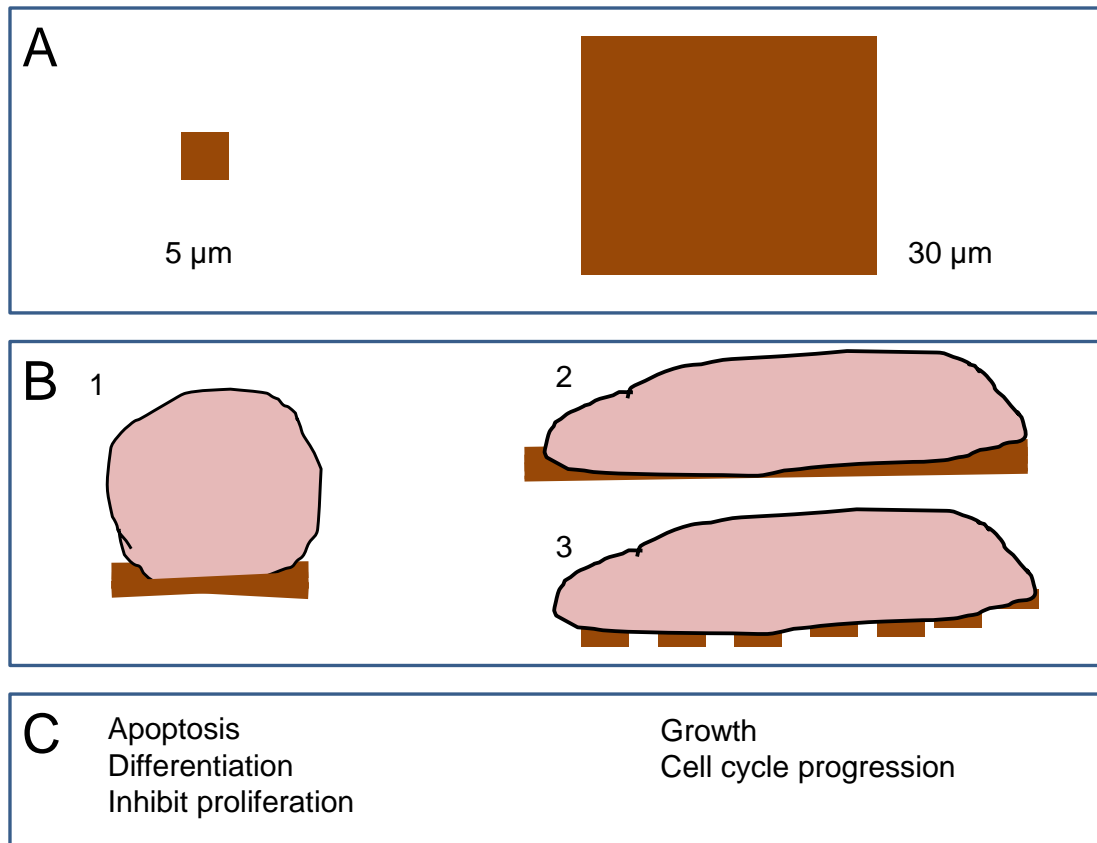


**Figure 5.1: Cell shape manipulation by changing the size of the substratum.** A, B) Cell shape in culture can be manipulated by changing the size of the micropatterned substratum because cells can spread differently depending on the available adhesive area. B1) If the substratum is small, the contact area of the cell and substratum is also small and cells tend to round up. B2) Conversely, if the substratum area is big, cells are allowed to spread and as a consequence, cells become flat. B3) However, if the area of substratum is small but distributed in a spaced pattern, cells can still spread and acquire a flattened shape. C) When cells were forced to be round, they tended to differentiate or entry into apoptosis while cells that could spread, continued growing and progressed through cell cycle. These shape effects do not depend on the area of contact or the specific composition of substratum, suggesting that cell shape itself is actively involved in regulating these processes.

been correlated with small GTPases and cytoskeleton (Figure 5.2). Spread cells showed enhanced activity of RhoA GTPase compared with round cells. Interestingly, increasing RhoA activity by itself could switch MSC commitment to osteoblast and, conversely, inhibition of RhoA results in adipogenic differentiation. However, when the shape was fixed to be round or spread, neither constitutive active nor dominant negative RhoA could drive osteogenesis or adypogenesis, respectively. Only overexpression of a RhoA effector, Rho kinase (ROCK) lead to osteogenesis independently of the shape (McBeath *et al.*, 2004). This molecule, ROCK kinase, mediates actin cytoskeletal tension and stress fiber formation by activation of the myosin light chain kinase, which in turn, activates the motor protein myosin II.

Independent experiments reaffirmed the importance of the cytoskeleton for differential commitment upon MSC shape manipulation. Cell shapes with high curvature (i.e. pointy star) that favoured an osteogenic fate showed higher expression of myosin II and vinculin compared with shapes with concave sides (like a flower-shape) that favoured an adipocyte commitment. Furthermore, disruptions of cytoskeleton using cytochalasin D (inhibits F-actin polymerization), blebbistatin (inhibits myosin II) and Y-27632 (which inhibits ROCK kinase, involved in actin-myosin tension) caused a decrease in osteogenesis with the corresponding increase of cells adopting an adipogenic fate regardless of the imposed shape (Kilian *et al.*, 2010). In addition, cells manipulated to become highly elongated also induced high cytoskeletal stresses that led to osteoblast differentiation (Oh *et al.*, 2009). Then, a contractile cytoskeleton promoted an osteogenic fate whereas disruptions of contractility (by certain shapes or chemical treatments) favoured an adipogenic outcome, suggesting a requirement for cytoskeletal contractility in the shape-dependent influence of differentiation (McBeath *et al.*, 2004; Oh *et al.*, 2009; Arnsdorf *et al.*, 2009; Kilian *et al.*, 2010 and Figure 5.2). This correlation of high stresses conferred by cytoskeleton and osteogenic fate acquisition may be related with the native environment of bone cells, namely, bone tissue is stiff (then, cells elongate) and the fluid flows inside the voids (where bone cells develop) might confer an extrinsic source of stress within the bone (Arnsdorf *et al.*, 2009; Kilian *et al.*, 2010).

### 5.2.2 Role of cell shape in cell division

The role of the cell geometry in cell division is perhaps one of the most studied cases where the cell shape influences the position of the plane of division.

For example, the division plane specification of the rod-shaped bacterium *E. coli* is determined by the complex MinCDE that is influenced by the cell shape. The MinCDE complex is a well characterized system that oscillate at the extremes of the bacterium and inhibits the formation of tubulin-like FtsZ, ensuring the formation of the division plane at the centre of the cell (Moseley & Nurse, 2010). When the shape was genetically manipulated to be round or branched, the oscillations still occurred along the longest axis, with the subsequent change on the plane of division. When there was not a clear long axis (in round cells), the direction of the MinD oscillations were modified randomly, as well as the plane of division (Corbin *et al.*, 2002; Varma *et al.*, 2008). These experiments suggested that cell shape *per se*, and not the extremes of a rod-shape, influences MinCDE movement. Recently, this observation was confirmed by the analysis of the dynamics of this complex when the purified proteins were allowed to interact in chambers of diverse shapes, corroborating that the geometry imposes constraints on where MinCDE assembles and moves (Schweizer *et al.*, 2012).

In eucariotes, the short axis rule, namely the plane of division lies in the shortest axis of the cells, is a shape-dependent feature of cell division that has been reported in am-

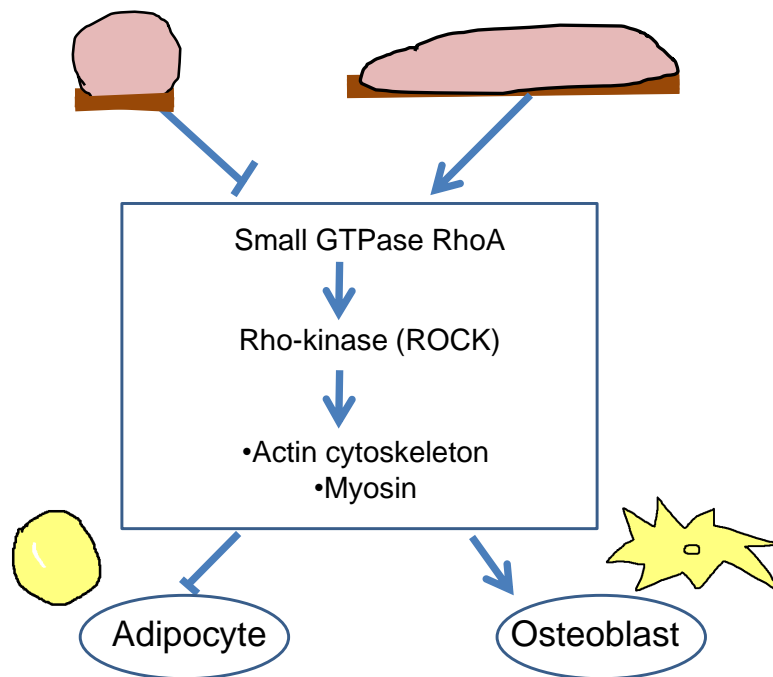


**Figure 5.2: Cell fate acquisition in human mesenchymal stem cells (MSC) is influenced by the cell shape and mediated by Small GTPases and cytoskeleton.** Spread cells showed enhanced activity of RhoA GTPase compared with round cells. Furthermore, increasing of RhoA activity by itself could switch MSC commitment to osteoblast and, conversely, inhibition of RhoA results in adipogenic differentiation. RhoA, in turn, activates the Rho-kinase (ROCK) that is involved in regulation of actin-myosin contractility.

phibian, sea urchin eggs, mammals and plants (Gray *et al.*, 2004; They & Bornens, 2006; O'Connell & Wang, 2000; Minc *et al.*, 2011; Besson & Dumais, 2011). Shape manipulations of mouse eggs showed that their spindle and cleavage plane can be redirected such that their division plane lay along the experimentally imposed short axis (Gray *et al.*, 2004; O'Connell & Wang, 2000). This observation was confirmed by an elegant experimental setting where the shape of sea urchin zygotes is systematically manipulated to adopt certain shapes by placing those cells inside microfabricated chambers of diverse geometries (Minc *et al.*, 2011). These results suggest that cell shape could override other signals when changes in shape are externally imposed.

Furthermore, recent experiments also showed that cell rounding at the onset of mitosis is a normal and necessary event for the correct formation of the spindle, and subsequent cell division. For example, an abnormal chromosome segregation occurs when HeLa cells were mechanically prevented to change shape (Matthews *et al.*, 2012; Lancaster *et al.*, 2013). Strikingly, this behaviour depends on Ect2 localization, a Rho guanine exchange factor (RhoGEF) protein, that participates in the activation of RhoA (Matthews *et al.*, 2012; Lancaster *et al.*, 2013), similarly to the players involved in cell fate decision discussed in the previous section.

How cell shape could influence spindle orientation has been discussed recently. Correct division in experimentally manipulated shapes was dependant on microtubule (MT) integrity (Minc *et al.*, 2011; Lancaster *et al.*, 2013). This observation led to the suggestion that cell shape could be sensed by MT, which exert pulling forces that centre the nucleus and spindle underlying the site of cell division (Minc *et al.*, 2011). In addition, cell shape changes (i.e. rounding) could be important for keeping the chromosomes in the range of MT and thus, a critical length of microtubules that 'reaches' chromosomes is needed; this was supported by the rescue of the defects on chromosome segregation in manipulated cell shapes by allowing the increase on MT length (Lancaster *et al.*, 2013).

Other possible mechanism by which MT could be regulating the division plane is that MT could transport and deliver regulatory signals. For example a complex of microtubule-binding motor protein MKLP1 and a Rho GTPase activating protein (RhoGAP) binds to a Rho guanine nucleotide exchange factor (RhoGEF) to activate Rho protein at the site of furrow formation. Then, stable microtubules could deliver the activator RhoGEF at the places of furrow formation (Howard, 2009).

Another possibility is that there is something else regulating MT dynamics, and thus the effect of cell shape through MT is an indirect consequence of an upstream process such as forces (mentioned later in this chapter) or intracellular gradients. In the context of cell division, it was proposed that intracellular gradients involved in mitotic spindle localization could feedback on MT nucleation and stabilization. The Ran-GTP shows a nucleo-cytoplasm gradient during interphase (Kalab *et al.*, 2002). This protein, alternates from a guanosine triphosphate GTP-bound active form (Ran-GTP) close to chromosomes to a guanosine diphosphate (GDP)-bound inactive form (Ran-GDP) in the cytoplasm, and participates in the delivery of cargoes during the assembly of the mitotic spindle and nuclear envelope. It has suggested that this intracellular gradient could provide a positional marker for spindle formation by liberating cargoes required for MT polymerization and organization, in a gradient-dependent manner (Kalab *et al.*, 2002; Caudron *et al.*, 2005). Thus, an intracellular gradient could modulate MT assembly and stability (Howard, 2009; Kalab *et al.*, 2002; Niethammer *et al.*, 2004). Cell geometry, however, could also influence such a putative intracellular gradient as will be discussed in the next section.

Finally, another suggested possibility in which cell shape influences cell division, that does not depend directly on MT, is that geometric cues act together with polarity determinants. The second cell division in *C. elegans* requires the correct expression of PAR proteins. The spindle failed to locate in the correct place just when both the distortions on cell shape (to be round instead of elongate) and the mutation *par3* were present but not when they were separate (Tsou *et al.*, 2003). This suggests that geometrical constraints imposed by the cell shape could provide a default guiding cue in the absence of cell polarity (Thery & Bornens, 2006). An unexplored question is the influence of the cell shape in the mechanism involved in the localization of the polarity cues (i.e PAR proteins) in the appropriate place.

### 5.2.3 Examples of the influence of cell shape in intracellular patterning in plants

Cell shape acting as an active rather than a passive player on plant development has rarely been discussed. The only example of the influence of cell shape changes in cell patterning was proposed in lateral root initiation using computational modelling. Laskowski and collaborators showed that the cell shape changes (elongation) due to root curvature in the differentiation zone influences auxin accumulation on the outside of that curve. This local auxin accumulation caused by cell elongation also enhances AUX1 (auxin importer) localization, that in turn, positively feeds back to increase the auxin concentration even more. They suggested that the feedback between the influence of cell shape, auxin and its transporters lead to stable patterning underlying lateral root initiation (Laskowski *et al.*, 2008).

Until now, I have discussed some experimental examples where the cell geometry, rather than being just the resultant of molecular interactions could play an active role in different aspects of development. This leads to the question on how the cell shape could by itself influence intracellular dynamics. Some hypothesis will be discussed in the next section.

## 5.3 How the cell shape could influence intracellular patterning?

Experimental settings where the cell is forced to acquire a particular shape and modelling experiments have suggested that cell shape could influence actively the intracellular dynamics that lead to differentiation, position of the plane of division, or lateral root initiation, to mention just some examples. The mechanistic ground in which cell geometry could influence those aspects has scarcely been discussed. Broadly, there are two alternatives on how cell shape could affect the intracellular dynamics: mechanical influence and biochemical influence. The former involves the role of forces and stresses and the second refers to role of biochemical interactions in signalling pathways.

### 5.3.1 Mechanical influence

Cell shape affects the pattern of stresses that a cell experiences; in turn, a change in cell shape could induce a specific cellular response according to the mechanical stimuli. Mechanotransduction or the ability of a cell to respond to mechanical stimuli has been reported in some animal cells. In this section, I will mention briefly some examples and some suggested possibilities on how mechanical cues could be transduced by the cell.

Perhaps the most studied examples of molecules that respond to mechanical perturba-

tion are stress-sensitive ion channels (reviewed in Sukharev & Sachs, 2012). In plants there are several putative mechanosensitive channels (Monshausen & Gilroy, 2009; Hamant *et al.*, 2010). An example of mechanical-induced channels are the plant proteins homologous to bacteria mechanosensitive channels, whose mutant affect  $Cl^-$  changes in root cells (Haswell *et al.*, 2008). However, to my knowledge, none of these have been confirmed.

Recently, an increase amount of examples of transcription factors able to transduce a mechanical input have been reported (see a review in Mendez & Janmey, 2012). An interesting example is the transcriptional regulators YAP/TAZ that have suggested as part of the signal transduction pathway of mechanical cues exerted by the extracellular matrix (ECM) rigidity and the cell shape. Upon shape manipulation, spread cells showed nuclear expression of these proteins while small and round cells showed cytoplasmic expression. Interestingly, YAP/TAZ nuclear localization upon mechanical stimulation is dependant on Rho-GTPase and actomyosin, that are also required for the cell differentiation triggered by changes in the ECM stiffness and cell shape manipulation (Dupont *et al.*, 2011).

The molecular basis of how mechanical cues could be transduced by a cell does not have a definite answer and there are several suggested hypothesis. For example, mechanotransduction could rely on protein conformation changes in response to force, that could trigger changes in the kinetics of mechanosensitive proteins or, it could simply lead to the exposition of binding sites on molecules (Sukharev & Sachs, 2012; Asnacios & Hamant, 2012 and references herein). Other possibility is that the change of pattern of stresses after cell manipulation (using micropatterned substratum, Figure 5.1) may induce condensation of chromatin that, in turn, influences gene expression (Versaevel *et al.*, 2012). Another suggested possibility is that forces could reorient microtubules and, as a consequence, reorient molecular motors and the delivery of vesicles towards a specific places of the cell (Ingber, 1993b,a). Lastly, it was proposed that upon cell shape change, mechanical instabilities may generate spontaneous symmetry breaking events that may lead to polarity (asymmetries within a cell, see review in Asnacios & Hamant, 2012).

In plants, mechanical stimuli were able to modify auxin transporters (PIN1) localization in the shoot apical meristem (Heisler *et al.*, 2010; Nakayama *et al.*, 2012) and align microtubules (Hamant *et al.*, 2008). However, to my knowledge, there is not yet information of how a mechanical signal is sensed or transduced in plant cells .

In the next section, I discuss the effect of cell geometry in intracellular dynamics through its effect on reaction-diffusion systems.

### 5.3.2 Biochemical influence

The effect of cell shape on biochemical systems discussed in this section involves the interaction of chemicals and their diffusion inside the cell (also referred broadly as reaction-

diffusion systems). For simplicity, these effects are grouped into two categories: 1) shape effect on isoclines and 2) shape effect on intracellular dynamics through surface/volume ratio.

### 5.3.2.1 Effects of the cell geometry on the isocline of a reaction-diffusion system

The cell shape influence on the isocline or interface between two (or more) stable states within a reaction-diffusion system was recently discussed in the context of polarization and motility of keratocytes (Marée *et al.*, 2012). This effect refers to the length minimization of the interface or chemical isocline within a system that involves biochemical reactions coupled with diffusion in two dimensions (Figure 5.3A). As mentioned in Marée *et al.*, 2012, reaction diffusion systems can be represented as gradient flow problems where the stable states are given by the minima of “energy”. As a consequence, the transition region between steady states or isocline also occupies the minimum of interface. Taking the assumption that the boundaries of a cell are impermeable to the players (there is not leakage of proteins, also referred as no-flux boundary condition), the isoclines are always perpendicular to the cell edge (Figure 5.3A,B). Given that they also tend to minimize their interface, the contour of the cell thus influences the location and form of the isoclines. Because a detailed mathematical description is beyond the scope of this chapter, I will focus on the possible implications of this phenomenon in biological systems.

The characteristic ‘front-back’ polarity of keratocytes arise from interactions of small GTPases (Cdc42, Rac and Rho), phosphoinositides and cytoskeleton, as showed by experimental evidence and modelling work (see Marée *et al.*, 2012 and references herein). In this case, the steady states correspond to 1) high concentration of the active forms of Rac and Cdc42 and low concentration of active form of Rho (or “front”) and 2) low concentration of the active form of Rac and Cdc42 and high concentration of Rho (or “back”). Simulations of these interactions allow studying the dynamics of this system and their feedbacks that are perhaps impossible or very difficult to disentangle *in vivo*.

The most interesting observation is that, because of the minimization of the interface of a isocline, cell curvature speeds up the dynamics of the system towards a new equilibrium (for example, the polarization of front and back or repolarization in the keratocyte). In a hypothetical static cell shape, regions of high curvature within the cell result in transient curved isoclines, that over time will change to preserve the perpendicular-relationship with the outline (Figure 5.3C, red arrow). Thus, high curvature regions in the cell caused curved isoclines to straighten over time, such as the overall length and curvature of the interface decreases. As a result of this phenomenon, the overall dynamics is accelerated and the simulated cell responds rapidly and repolarizes upon environmental changes. This effect of the cell curvature on the isoclines of a reaction-diffusion model and the dynamics to reach the steady state in a motile cell was also discussed by Vanderlei *et al.* (2011), using a different modelling approach.

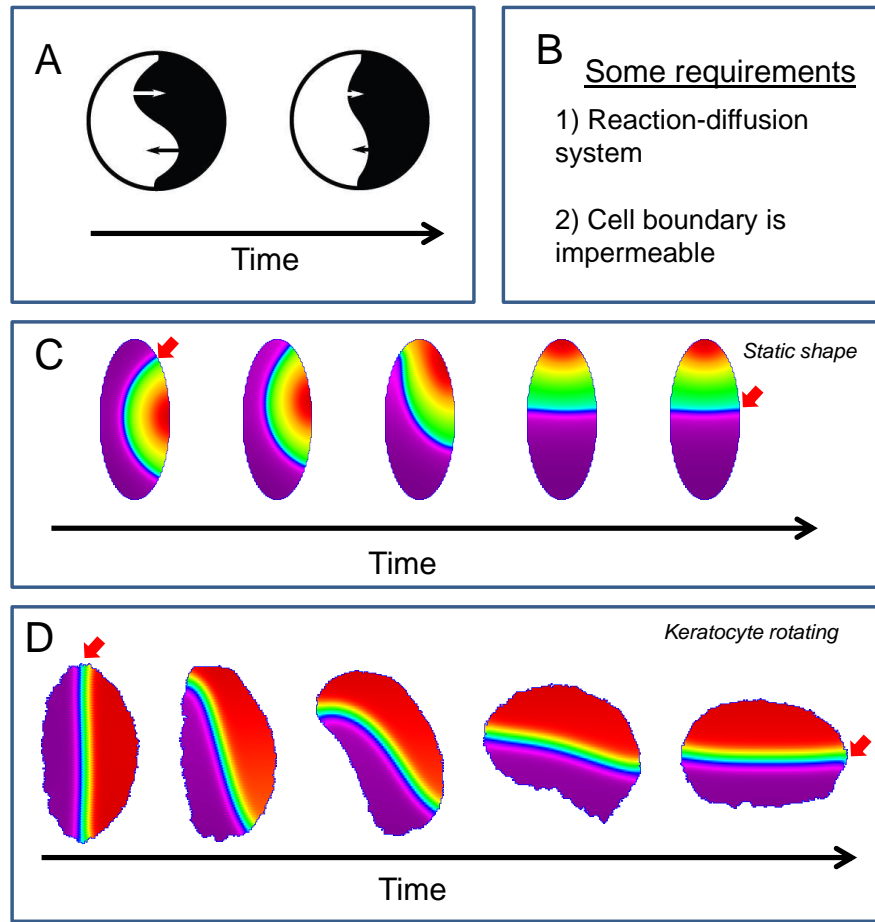


**Figure 5.3: Effects of the cell shape in the interface or isocline of steady states in a reaction diffusion system.** A) The isocline is the interface between two steady states (white and black). Over time, the local curvature will speed up the dynamics of the reaction-diffusion system in such a way that the isocline conserves the minimal interface and an orthogonal relationship with the outline. B) Some requirements are that the system couples biochemical reactions with their diffusion and that the system has no-flux boundary conditions. C) When the shape is static and the initial condition locates the front-back polarity along its longest axis, the interface (and the overall dynamics) reorients to occupy the minimum length. D) Realistic keratocyte-shape and reaction-diffusion simulation, where the shape is allowed to interact with the patterning. In this case, the simulated keratocyte rotates and translates to adapt to new stimuli in realistic time scales (contrasting with the case when the cell shape is fixed, not shown here). Colour-code in C and D refer to high concentration of Rac. Figure showed in A was adapted from Grieneisen *et al.*, 2013a and C-D were adapted from Marée *et al.*, 2012.

An important consideration is that cell shape is not static. On the contrary, shape during cell morphogenesis and cell motility is very dynamic. An implication of cell shape changes (for example, after changing the direction of movement, Figure 5.3D) is that they will transiently modify their internal isoclines. Interestingly, when the biochemical players that are modified can influence the cell shape, a potential feedback loop between the biochemistry and geometry is established: changes in cell shape will alter the isoclines, speeding the dynamics towards an equilibrium and, in turn, the biochemical players will modify the cell shape. Indeed, Marée *et al.*, 2012 showed that when the cell shape is al-

lowed to interact with the patterning mechanism of front-back polarity, the keratocyte cell is able to respond and integrate stimulus faster (within realistic time scales).

The shape effect on the isoclines in a reaction-diffusion system could influence many other cell types as it is the result of general features. However, this kind of effect of cell shape curvature in intracellular dynamics has been addressed only theoretically to date. Further questions to explore are how this phenomenon behaves in three dimensions and how it is affected with changes on cell size that often accompanies cell morphogenesis (see Chapter 4 and section 5.4). However, in my opinion, the most challenging aspect will be to test experimentally the existence of the “isocline effect” in a real biological context (see discussion in this Chapter).

### 5.3.2.2 Effects of the cell shape through its influence in the surface/volume ratio in intracellular gradients.

Intracellular gradients and its importance in cell division and motility has been documented in animals (Kalab *et al.*, 2002; Niethammer *et al.*, 2004) and suggested in plants (for example in the context of the transport of the hormone auxin, see Grieneisen *et al.*, 2007; Laskowski *et al.*, 2008; Kramer, 2009; Van Berkel *et al.*, 2013). Interestingly, an intracellular gradient will vary within a cell depending on the cell geometry and size. In this section, I discuss some theoretical considerations and give an intuitive explanation on how cell shape could influence intracellular gradients that involve chemicals that react and diffuse within the confined space of the cell.

Take the scenario of two substances with opposite activities (i.e active and inactive form of small GTPases or a kinase and phosphatase) and spatial segregation (for example, one bounded to the membrane and other diffusing in the cytoplasm, see Figure 5.4A). Given the spatial segregation and antagonistic activities, they will establish a steady-state gradient of their substrate in one or other state (Brown & Kholodenko, 1999; Meyers *et al.*, 2006). For example, if the substratum is phosphorylated at the membrane and it diffuses into the cytoplasm where it is dephosphorylated, there might be a spatial gradient of the phosphorylated form: high concentration close to the membrane that progressively decreases towards the centre of the cell (Brown & Kholodenko, 1999 and Figure 5.4C).

In general terms, the size of such a gradient is a function of the relationship between the rate of interconversion, diffusion coefficients and cell diameter (Brown & Kholodenko, 1999). The distance over which the spatial gradient decays or decay length (in this case, the concentration of the phosphorylated form of the substrate) is given by:

$$\lambda = \sqrt{\frac{D}{k_p}} \quad (5.1)$$

where  $k_p$  is the degradation rate or conversion to a dephosphorylated form and  $D$  is the diffusion coefficient of the substratum. In other words, the decay length is the average

distance that the phosphorylated form of the substrate diffuses before it is dephosphorylated (gradient decays to a fraction of  $1/e$  of the concentration at the membrane, see also Chapter 4, Box 2). Taking a  $k_p$  of  $0.1\text{--}100\text{ s}^{-1}$  and a  $D$  of  $1\text{--}10\text{ }\mu\text{m}^2/\text{s}$ , the decay length corresponds to  $0.1\text{ }\mu\text{m}$  to  $10\text{ }\mu\text{m}$ , that is within the typical size of a cell (Meyers *et al.*, 2006). The opposite reaction (kinase reaction with a  $k_{ki}$ ) will determine the amount of phosphorylated form of the substrate at the plasma membrane (for a detailed explanation see Brown & Kholodenko, 1999). Importantly, these considerations imply that the effect of a gradient (i.e. its decay length) produced by this kind of reaction-diffusion system is dependent on the size of the compartment in which the reactions take place.

It is also important to consider that the intracellular space can change 1) globally, because of cell growth or when the cell spreads and flattens and 2) locally, because of cell protrusions (like lobes, neurites, etc.). Cell growth will have a net effect of decreasing the proximity at which these substances can interact. Thus, the average concentration of the activated or phosphorylated form decreases as the cell increases in size because this makes the substratum diffuse out of the kinase “scope” (given by  $\lambda$ ). Conversely, if the cell is small (about the length  $\lambda$ ), the substratum will be highly phosphorylated, because the majority of the cytoplasm will be within the decay length of the gradient.

Changes in cell shape that increase the surface-to-volume ratio, such as when a cell spreads and flattens or cytoplasmic extensions (lamellipodia, lobes, etc.) and any other local cell curvature, will increase the proximity of the interactors and thus, its reaction. Note that the effect of local cell curvature is quite different to the discussed in the previous section. In this case, curvature allows the plasma membrane to fold back onto itself so that two regions of the plasma membrane (and the proteins attached to it) become close to each other and activate the substratum in the cytoplasm (always that the space between it and the membrane is within a distance  $\lambda$ ). Thus, the greater the surface-to-volume ratio, the greater the fraction of the activation (phosphorylation, GTP-bound, etc.) within this domain (Meyers *et al.*, 2006).

Consistent with this argumentation, there is experimental evidence suggesting that regions of high surface-to-volume ratio contains a distinct biochemistry compared with the rest of the cytoplasm. The periphery of fibroblast cells is thinner than the centre of the cell (because of the nucleus) and it showed higher activation of the small GTPase Cdc42 than the central region, as reported by a fluorescent probe MeroCBD (Nalbant *et al.*, 2004; Meyers *et al.*, 2006). Modelling of a signal transduction from a receptor to a cascade of kinases and phosphatase (i.e B-adrenergic receptor to MAPK1,2 through a cAMP-PKA-B-Raf-MAPK1-2) in neurons with realistic shape predicted the existence of a preferential cAMP accumulation in thin dendrites compared to cell body because an increase of the receptor density per unit of area. This relation was confirmed by experiments (Meyers *et al.*, 2006; Neves *et al.*, 2008).

Therefore, for a reaction-diffusion system involving antagonistic activities and spatially restricted, cell geometry through surface-to-volume ratio could play a role in the

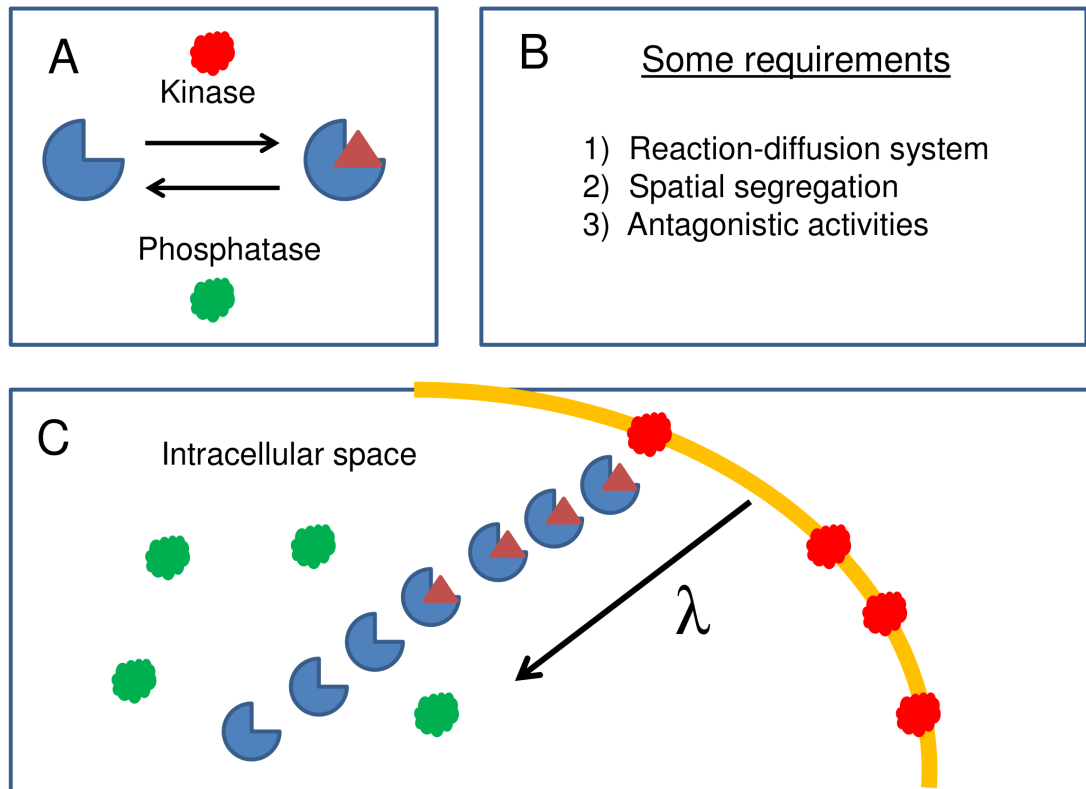


**Figure 5.4: Effect of cell geometry in the formation of intracellular gradients.** A) Two antagonistic reactions like kinase (red) and phosphatase (green) will “compete” for the substratum (blue). B) Some other requirements are that those enzymes act in spatially distinct domains and that the substratum diffuses freely in the cytoplasm. C) Then, the activate-form of the substratum will form intracellular gradients showing higher concentration closer to the membrane (yellow) and lower concentration in the centre of the cell. The gradient of the phosphorilated substratum will depend on the kinetics of reaction, size and shape of the domain and diffusion constant. The “scope” of the gradient is given by  $\lambda$ , where  $D$  correspond to the diffusion constant and  $k_p$  is the degradation rate or conversion to a dephosphorilate form.

formation of micro domains. Importantly, local variation of cell geometry could be sufficient to create a distinct biochemical profile.

## 5.4 Potential of the pavement cell shape to influence intracellular dynamics

As discussed so far, there are experimental and theoretical considerations that support the hypothesis that cell shape could actively influence the intracellular dynamics in diverse ways.

A very interesting, but poorly explored aspect is the effect of the cell geometry on the molecules that also contribute to cell morphogenesis. The development of new methods to study cell shape dynamics (see Chapters 2 and 3) together with the identified key

molecular players involved in their morphogenesis, make the intricate jigsaw puzzle-like shape of pavement cells an excellent system to address the role of the cell shape in intracellular patterning responsible for its own morphogenesis.

### 5.4.1 Curvature effects during pavement cell morphogenesis

The shape of pavement cells changes from a very symmetrical shape to a very asymmetrical jigsaw puzzle-like shape with protruding lobes alternating with indentations, that altogether create a highly wavy shape (Figure 5.5).

Interestingly, cell morphogenesis in these cells involves similar molecular players underlying cell polarity as those in the keratocyte and in other cell shape effects discussed before. Briefly, the small GTPase ROP2 (and ROP4) located in the lobe region recruits filaments of actin through RIC4 and represses the activity of ROP6 (also a small GTPase). Conversely, ROP6 is located at the indentation regions and organizes microtubules through RIC1 (Figure 5.6, Fu *et al.*, 2002, 2005, 2009). Recently, it was shown that PIN1 is located also in the lobe regions and that auxin influences the active forms of ROP2 and ROP6 with distinct affinities (Xu *et al.*, 2010). Importantly, ROPs can alternate between an active form attached to the membrane and an inactive slow-diffusing form in the cytoplasm, characteristics that make them candidates for the patterning mechanism underlying lobe-indentation polarity (similarly to the front-back polarity in keratocytes discussed before). In fact, these interactions have been modelled in Grieneisen *et al.*, 2013a studying pavement cell polarity and interdigitation, and in Payne & Grierson, 2009 in the context of root hair polarity.

The highly asymmetrical and curved outlines of pavement cells could influence the intracellular dynamics in several ways. As discussed before, the geometry of a cell influences the isoclines of the steady states in a reaction-diffusion system. In fact, two dimensional simulations of the ROP-PIN1-auxin network using a realistic pavement cell shape showed that the steady state of the reaction-diffusion system is reached faster than the same network modelled in a circular domain. Because of the curvature in pavement cells with a fully developed shape, the peaks of the active form of ROP2 are “attracted” to the lobe regions by minimizing the interface of the isoclines, that keep an orthogonal relationship with the outline (Grieneisen *et al.*, 2013a).

Furthermore, the spatial segregation of ROPs (namely that the active form of the ROPs is in the membrane and the inactive form in the cytosol) will potentially influence their gradients and the downstream signalling, specially in regions with high curvature and high surface-to-volume ratio like lobes. This effect has not been explored in pavement cells, mainly because there is very limited information about the spatial segregation of active and inactive form of ROPs and, the regulators ROP-GEF and ROP-GAP (that convert the active to inactive and vice versa). Thus, in different but not exclusive manners, the puzzle-like pavement cells could influence its own intracellular dynamics.



**Figure 5.5: Pavement cell morphogenesis.** Examples of pavement cell development obtained through long time-lapse experiments and image processing tools (discussed in detail in Chapter 3). These cells change from a very symmetrical shape to a very asymmetrical shape with alternating lobes and indentations. Importantly, lobe events can happen at different times (some new lobe events are marked with a red arrow head) and new lobes also arise from bifurcations of the pre-existing ones (some bifurcation events are showed with a green arrow head). The scale bar in the first and last image in each row correspond to  $10 \mu\text{m}$ . The  $t=0$  is the time when the cell division is detected. Time is indicated in hours.

An important remark is that previous considerations studying the effects of shape in these cells have assumed a static geometry. Following the results of the long time-lapse experiments, it is outstanding that cell shape changes very dynamically over time (Figure 5.5 and Chapter 4) and therefore, future simulations need to take into account realistic dynamics of cell growth and shape immersed inside a tissue. Ideally, once the reaction-diffusion model is placed within the constraints of a realistic cell morphology and this is allowed to changing shape (Figure 5.5), the predicted micro-domains could be

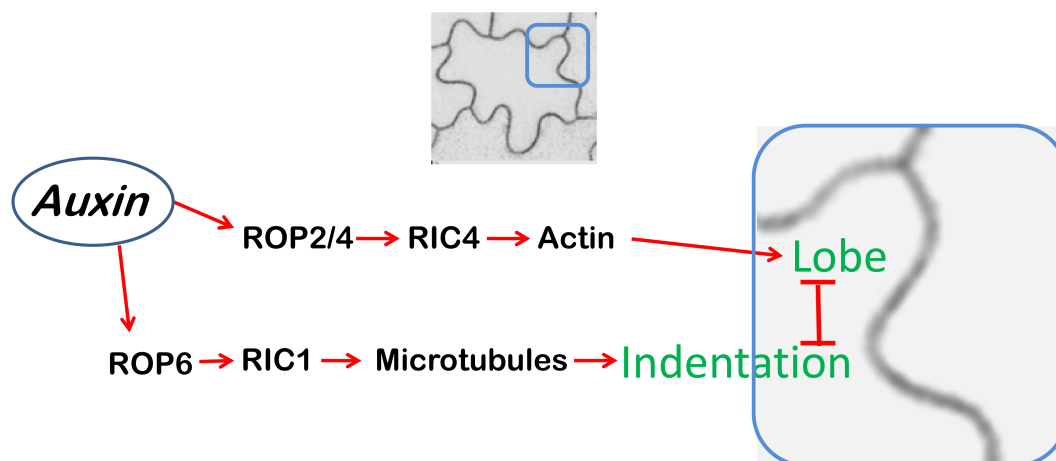


**Figure 5.6: Schematic representation of the molecular basis of pavement cell morphogenesis.** Small GTPases, cytoskeleton and the phytohormone auxin have been reported as key molecular players for the correct shape acquisition in these cells. Two antagonistic pathways specifying lobe and indentation regions are regulated by ROPs, cytoskeleton and auxin. Importantly, auxin was reported to influence both pathways (through ROP2 and ROP6 with different affinities). Other important players that were not included in this schematic representation for simplicity are PIN1 proteins localized at the lobe regions, SPIKE (a GEF protein), and other MT-related proteins (see a detailed review in Craddock *et al.*, 2012).

directly compared to experimental data (i.e. using biosensors able to distinguish between the active and inactive form of small GTPases, as suggested in Holmes & Loew, 2008).

Thus, the dynamics of ROPs, important for the correct cell geometry, could also be influenced by the cell shape. This implies an interesting feedback loop between the biochemistry and geometry, that has not been explored before in cell morphogenesis studies. It will be very interesting to further explore this feedback in dynamical simulations enabling the cell shape to interact directly with the biochemistry and using as templates realistic cell shapes (Figure 5.5).

#### 5.4.1.1 Secondary lobe formation: dynamical intracellular patterning

Long time-lapse experiments allowed a fine scale resolution of temporal and spatial scales involved in pavement cell morphogenesis. This uncovered novel aspects of cell shape acquisition in these cells: 1) after the formation of the primary lobes, it is possible to identify the formation of new lobes bifurcating from the pre-existing ones (Figure 5.5 green arrows and Figure 5.7), 2) lobes can be formed at different moments during cell morphogenesis (new lobe formation events are detected, see Figure 5.5, red arrows). This observation contradicts a previous study that proposed an isotropic growth after the formation of lobes (Zhang *et al.*, 2011). This study reached such conclusion because their time lapse experiments started when the cell shape was already wavy and finished before secondary lobe formation was detected (Zhang *et al.*, 2011). Another existing hypothesis concerning

the mechanism that leads to the complex pavement cell shape was that differential growth rates between stomata and pavement cells would lead to pavement cells to “buckle”, giving rise to their shapes (Asl *et al.*, 2011). However, the pavement cells’ shapes were normal in the *speechless* mutant, indicating that the cell morphogenesis does not depend on stomata as proposed previously (Asl *et al.*, 2011; Staff *et al.*, 2012).

As lobe bifurcations in pavement cells were identified using long time-lapse and imaging tools discussed in this thesis (Chapter 3), there is a lack of previous reports about the mechanistic basis of lobe bifurcation in the context of plant cells. However, bifurcating morphogenesis occurs recurrently in the development of several organisms and there are different suggested hypothesis on how this may operate (Lu & Werb, 2008; Iber & Mersha, 2013). In animals, for example, lung development involves bifurcations of the lung epithelium into the surrounding mesenchyme in a very stereotyped manner (Metzger *et al.*, 2008). Experimental evidence points out the role of the Fibroblast Growth Factor 10 (FGF10) that diffuses in the mesenchyme and promotes cell proliferation and local growth (for details and other important molecular players, see Lu & Werb, 2008; Hirashima *et al.*, 2009 and references herein). It has been suggested that lung bifurcation is a self-organizing phenomenon caused by the interaction between FGF10 and its regulators in a growing domain. Briefly, the proposed mechanisms include: 1) geometrical effect on the FGF10 gradient coupled with growth and 2) a Turing patterning in a growing domain. Some similarities and differences can be extracted with respect to the case of pavement cell morphogenesis.

The first possibility is that bifurcations arise because the chemicals specifying local growth are governed by gradients and their derived fluxes, that are deformed by the geometry of the external lung boundary (mesenchyme) and the internal epithelia (Clement *et al.*, 2012a,b; Hirashima *et al.*, 2009). The curved geometry of the lung mesenchyme (where FGF10 is produced and from where it diffuses to the internal epithelia) as well as the geometry of the epithelia (which carries the receptors) will cause the deformation of the FGF10 gradient. This, in turn, creates differential fluxes of FGF10 in regions with high curvature that could affect the downstream processes, including growth (see Clement *et al.*, 2012a for a detailed explanation and assumptions of the model). Indeed, modelling the influence of the deformed FGF10 gradient (and fluxes), coupled with its local induction of growth, led to growth instabilities of the bronchial epithelia causing spontaneous branching. This feedback re-enhances the instabilities and derives further shape changes. Interestingly, different modes of branching (such as bifurcations and lateral branching) were recapitulated just by changing the growth response of FGF10 (i.e linear or sigmoidal). A similar conclusion on the role of the overall geometry was drawn when a different model was analysed (including FGF10, TGF-beta and SHH in Hirashima *et al.*, 2009). Thus, under these assumptions lung branching morphogenesis emerges spontaneously from the dynamic interactions between gradients and shape (Clement *et al.*, 2012a,b; Hirashima *et al.*, 2009).

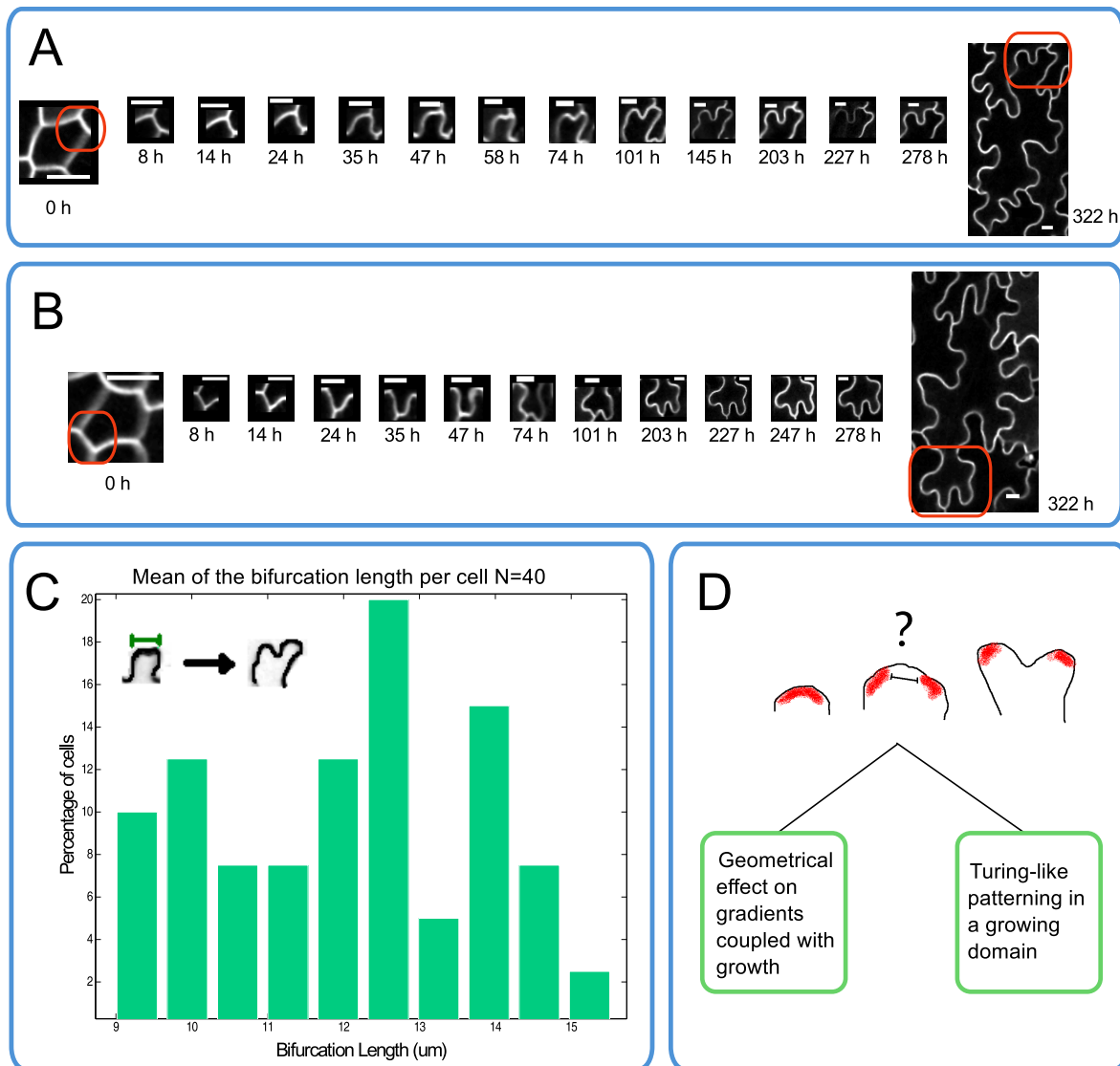


**Figure 5.7: Pavement cell lobe bifurcations.** Long time lapse experiments have enabled a fine-scale resolution of pavement cell morphogenesis. A-B) The dynamics of a single lobe (red inset in the first and last picture) is shown for two pavement cells. Lobes elongate and, over time, they split into two (bifurcations). Scale bar in all the images is  $10 \mu\text{m}$ . The time in hours is indicated below each caption, where 0 h corresponds to the time-point right after the cell has divided. There is a range from  $8.94 \mu\text{m}$  to  $15.5 \mu\text{m}$  of length (with mean of  $12.01 \mu\text{m}$ ) in which bifurcations take place. C) The mean of the length of the lobe before bifurcation (per cell) was quantified for a time lapse interval of 13.4 days. D) Different hypothesis could account for pavement cell bifurcation, including the influence of the cell shape, for example by deforming a gradient that is coupled with growth and the possibility of a Turing patterning in a growing domain.

The second suggested possibility is that lung bifurcations emerge from a Turing patterning mechanism (Menshykau *et al.*, 2012). In this scenario, interactions of FGF10 and its regulators are responsible for a self-organized emergence of new branches and bifurcations from homogeneous initial conditions. In this case, new bifurcations appear with certain periodicity and there is also a typical length. Interestingly, simulations of a

Turing-based model including growth showed that different branching modes can be the result of different growth rates: fast growth triggers lateral branching while slow growth favours bifurcations (Menshykau *et al.*, 2012; Iber & Menshykau, 2013).

Bifurcations of pavement cells could be the result of any or a combination of these possibilities. Notably, there is a minimum lobe length before a lobe splitting event (from  $9.5\mu\text{m}$  to  $15\mu\text{m}$ , see Figure 5.7C) which could be compatible with any of the discussed models. Under the assumption of a bifurcation induced by a growth instability mediated by a gradient (and flux), the minimal length is related with the surface tension of the lung epithelia (Clement *et al.*, 2012a). In a Turing mechanism, the spacing between high concentration peaks (i.e ROP2/4) could conserve a frequency that could also lead to a minimum length of splitting (Menshykau *et al.*, 2012).

Although there is no experimental evidence of gradients at the cellular scale, the influence of the cell shape by means of the modification of the gradients inside the cell or those formed between neighbouring cells cannot be ruled out, in light of recent studies that suggest that some molecules involved in pavement cell morphogenesis (i.e. small GTPases and auxin, see Figure 5.6) form such gradients.

On the other hand, a mechanism driven by a Turing instability could also be plausible. Modelling of the interactions responsible for pavement cell morphogenesis showed that cell polarity (assumed to underlie lobe formation) can arise from Turing-like instabilities that give rise to a lobe-indentation pattern (Grieneisen *et al.*, 2013a). Although typically a Turing mechanism accounts for equally spaced structures and pavement cells bifurcations do not look periodic (Figure 5.5), the possibility that the initial polarity is periodic but it is deformed due to growth and interactions with neighbouring cells, cannot be discarded (see *in silico* tissues simulations in Chapter 2).

Importantly, cell shape coupled with cell growth could play an important role in deforming a given gradient or in the dynamics of a Turing mechanism (Figure 5.7), implying that the cell shape could have an important role in its own morphogenesis. Thus, there are different hypothesis that could explain the genesis of the bifurcation phenomenon in these cells, and simulations incorporating realistic growth dynamics and allowing different feedbacks will shed light towards one possibility or the other (or even some other mechanisms not included in this discussion).

In my opinion, the most important aspect of secondary lobe formation is that it implies that the intracellular patterning that accounts for the multi-polar fashion cell shape is very dynamic and lobes are newly formed rather than being specified at one moment alone.

## 5.5 Discussion and concluding remarks

Instead of provide an exhaustive list of examples of the influence of cell shape in intracellular dynamics or possible hypothesis, the aim of this chapter was to stand out the

importance of cell geometry in the study of morphogenesis, topic that has been rarely taken into consideration.

Although the precise mechanism(s) by which the effects of cell geometry are translated to changes in dynamics are unknown, there are different theoretical possibilities that can be considered. For simplicity, I grouped these possibilities into two general categories: the effect of the shape through mechanics and the effect through biochemical reaction-diffusion systems. However, this division could be very artificial. For example, it is remarkable that the same molecular elements (small GTPases and cytoskeleton) are recurrent elements in both scenarios. Indeed, small GTPases link these hypothesis because 1) they are able to form gradients and Turing instabilities (Payne & Grierson, 2009 and Grieneisen *et al.*, 2013a) and, 2) these proteins influence the cytoskeleton and hence, the mechanical status of a cell. Perhaps, a common basis for the effect of the cell shape includes a combination of the influence in the dynamics of reaction-diffusion systems together with the mechanical influence, mediated by the cytoskeleton.

A very interesting possibility is that the mechanotransduction induced by shape could operate through the effects on the biochemical influence. For instance, changes in the cell shape (i.e. when it is flattening, rounding or forming local protrusions) would also cause an increase or decrease in the phosphorylation status of the cell (and any other spatially separated antagonistic activities, as discussed in section 5.3.1), that could regulate the cytoskeletal activity or any other molecules (Meyers *et al.*, 2006) and hence, influence the mechanics of the cell.

Furthermore, the principles that underlie the self-organizing properties of a reaction-diffusion system of biochemical elements (for example, self-amplifying feedback and long-range inhibition in some Turing systems) are very general and they are not restricted to chemical substances, on the contrary, they could be involved in the mechanical basis of pattern generation as well (Asnacios & Hamant, 2012; Goehring & Grill, 2013). Thus, mechanotransduction induced by shape deformation could activate or inactivate signalling pathways using the same basis that were discussed in the context of biochemical influence.

Nonetheless, the challenge to evaluate the biochemical hypothesis is that the predicted dynamics must be visualized and tracked at the molecular level. In animal systems the use of biosensors provided robust measurements on intracellular gradients (Kalab *et al.*, 2002) and spatial dynamics of active and inactive forms of small GTPases (Nalbant *et al.*, 2004). Unfortunately, these tools are limited in plants.

In animal systems, the effects of the cell shape have been evaluated using single cells. This is difficult in plants because culture of single cells (protoplasts) are believed to behave very different from the real tissue. Nevertheless, a recent report provided encouraging results using single xylem cells cultured *in vitro*. The role of ROP11 and their regulators in the cell wall patterning was analysed using fluorescent tags of ROPs and their regulators. Noteworthy, it was possible to visualize active domains of ROP11 and the spa-

tial segregation of GAP and GEF (Oda & Fukuda, 2012). These results suggest that these plant cells could be an excellent system to analyze the effect of the cell shape in intracellular dynamics and confirm or refute some hypothesis (i.e. isoclines, surface-to-volume ratio, etc.).

Another important remark to take into account in the study of the effects of cell shape is that the cell geometry is not static but it is dynamically changing. In the case of pavement cells morphogenesis, the use of confocal time-lapse and imaging tools (Chapters 2 and 3) enabled to extract cell shape and growth dynamics involved in cell morphogenesis (Chapter 4 and section 5.4 in this Chapter). Importantly, as suggested for the work on lung morphogenesis, cell growth is fundamental for the patterning that underlie bifurcations, regardless of the specific mechanism involved (i.e. a deforming gradient, surface-volume ratio effect, a Turing instability, etc.). Thus, mathematical models that incorporate realistic growth dynamics will be essential to discern hypothesis of secondary lobe formation (Figure 5.7). Moreover, growth dynamics should be incorporated into current models studying the establishment and maintenance of the patterning that underlies cell polarity (and that precedes the formation of lobe-indentation shape) to test their scope and limitations.

Finally, in my opinion the most important implication of the effect of cell shape is that the molecular players involved in cell morphology are in turn, influenced by the cell geometry, establishing a feedback between them. In the context of pavement cell development, such a feedback between the cell shape and the polarity determinants, could reinforce the patterning that leads to the generation of new lobes.

In conclusion, since the role of cell geometry is potentially important, future studies should take it into consideration to build an integrative understanding of cell morphogenesis.

# Chapter 6

## General Discussion

### 6.1 Introduction

The analysis of the cellular dynamics in relevant temporal and spatial scales combined with quantitative tools to extract cellular behaviour allows studying the problem of morphogenesis at unique cellular resolution. In this final chapter, I present an overview of the outstanding questions that remain unanswered and give my opinion about how the findings and methods presented in this work could be combined with other approaches to address these problems.

First, a quantitative assessment of cell dynamics permitted to re-evaluate previous hypothesis related with the dynamics of cell behaviour during leaf morphogenesis. For instance, despite the graded behaviour of the rate of growth and shape change across the tissue, their dynamics showed minor influence of the position once cells were aligned according to their developmental stage (taking as a reference the time at cell division). This finding questions the proposal that the graded growth rate is explained by a proximodistal gradient in a position-dependent manner. In the same way, the notion of a cycling arrest front positioned at constant distance from the base of the leaf and that suddenly disappears needs to be revisited. Using a direct way to identify cell divisions from early periods until they disappear, provides us with an invaluable resource that opens the possibility to propose new hypothesis about its regulation. Here I speculate about some hypothesis that can be tested using the pipeline described in Chapter 2 and 3.

Another interesting aspect of leaf morphogenesis at the cellular scale is the phenomenon of compensation. This effect refers to the cell elongation beyond wild type limits that compensates for the decrease in the number of cells, such that the overall leaf maintains approximately a wild type size. Using the information of the dynamics of cell growth analysed in previous chapters, the compensation phenomenon is briefly revisited here.

When discussing compensation, we are confronted by the fact that we have scarce understanding on how the limits of cell growth are achieved and modulated during development. This is in part because the difficulty to access the dynamics of late stages of

leaf development at the cellular level. In my opinion, this problem can be overcome using the same pipeline as described previously.

Although cell divisions and cell growth are important during leaf development, these events by themselves are not enough to account for the leaf morphogenesis, but it is also necessary to include the direction and anisotropy of growth (Coen *et al.*, 2004), related to the concept of polarity. Here, I analysed the polarity at cellular level through analysis of the cell shape dynamics. Interestingly, new lobes are formed as bifurcations of pre-existing, pointing out the dynamical nature of the patterning that underlies complex cell geometries. Moreover, I speculate about the existence of different notions of cell polarity. On one hand, the polarity that is important for the specification of complex cell shapes and generates the characteristic jigsaw puzzle-like shape of pavement cells. On the other hand, the possible polarity that underlies axiality and provides directionality (an angle in which the main directions are oriented) and contributes to the overall shape of the leaf.

Altogether, the possibility to access to the dynamics of cellular behaviour in high spatial and temporal resolution combined with other approaches (i.e physical and genetic perturbations, and mathematical modelling) will allow to revisit some fundamental questions in developmental biology.

## **6.2 From a “static” to a “dynamic” view of development: new methods and importance of quantitative descriptions**

The combination of *in vivo* imaging at the level of tissue or organs and computational tools to extract dynamic information from images creates a powerful approach to address developmental mechanisms (Megason & Fraser, 2007).

The long time scales (in the order of days) and the diverse spatial range (in the order of microns to centimetres) at which leaf development occurs make time-lapse imaging at cellular resolution a very challenging task. Indeed, the analysis of cellular dynamics at high spatial and temporal resolution required the synergy of previous imaging tools (for example, the perfusion chamber and membrane markers as used in Robinson *et al.*, 2011; Kuchen *et al.*, 2012; Sauret-Gueto *et al.*, 2012) and new quantitative tools for image processing such as the Segmentation Potts Model (van Rooij *et al.*, 2013a), LOCO-EFA (Chapter 2) and the automatic tracking algorithm (Chapter 3).

On the experimental side, the use of mutants or inducible mutants has recurrently facilitated the study of plant development (Torii *et al.*, 1996; Wellmer *et al.*, 2006). A very important aspect of this work was the use of *speechless* plants for tracking experiments. This system simplifies the interpretation of the dynamics of cellular behaviour because all the cell types belonging to the stomata lineage are absent, making it straightforward

to study the dynamics of formative cell divisions and analysis of the cell shape dynamics of complex geometries without the influence of stomata-derived cells. Moreover, *speechless* plants grow in a very similar fashion as the wild type within the perfusion chamber and the experimental conditions used (Chapter 3). Although there are still several technical difficulties in extending this pipeline to the analysis of wild type leaves for long time periods, the comparison of the data presented here and the wild type will be very valuable.

As more advanced microscopy techniques and image analysis tools become available, it is necessary to develop quantitative tools to extract information from the images. During the second chapter of this work, I presented the LOCO-EFA method. This method offers a manner to quantitatively assess and characterize the cell geometry of complex shapes and, importantly, to evaluate the rates at which cell shape is progressing over time along the leaf (Chapter 4). It also allows populations to be characterized and contrasted (see Section 6.6). Other metrics including the angle of direction with reference to a particular axis of the leaf (for instance along the midvein), the cell anisotropy and the  $L_n$  distribution within a packed tissue will be very important in the analysis of the dynamics of anisotropy and direction at the cellular level (see Section 6.6) and tissue properties that could not be included in this work.

The LOCO-EFA method combined with the Segmentation Potts model (SPM) was used to develop the algorithm to track individual cells over time and to automatically identify cell lineages. Altogether, the combination of imaging and computational techniques permitted to access leaf development with a cellular detail that was not achieved before.

In fact, the traditional approach of dissecting leaves throughout development created a fair picture of *where* cellular events take place (for example, cell division at the base of the leaf and cell shape complexity starting at the tip of the leaf). Although very valuable, this approach represented just a static picture of development. With the implementation of time lapse and computational tools, we are in the possibility to address also *how* cellular patterns are established. Hopefully, this work will open possibilities to analyse the dynamics of leaf development and help in the transition from a “static” view towards a “dynamic” view of development.

Importantly, this pipeline can be combined with novel techniques to visualize the spatio-temporal dynamics of gene regulatory networks (GRN), including fluorescent marker proteins and inducible systems (Reddy *et al.*, 2007; Wachsman *et al.*, 2011), and will be a very important resource for the analysis of the molecular basis of cellular behaviour at the tissue-level.

Besides providing direct insights, imaging and quantitative analysis of development also provide information that can be used to compare new hypothesis to quantitative mathematical models of development (Sharpe, 2011).

Next, I present an overview of outstanding questions that are very relevant for mor-

phogenesis but have thus far remained unanswered. I speculate about possible hypothesis and comment on how the pipeline and results obtained in this thesis could be extended to address these questions.

### 6.3 How is the division zone in the leaf regulated?

The leaf, as a determinate organ, reaches particular dimensions that are constrained by the genetic and the environmental conditions. The size of the leaf is bounded in part because the cell divisions are not constantly maintained as occurs in the shoot and root meristems, but they disappear over time. As discussed in Chapter 4, the place where cell division occurs within the leaf is not fixed and its disappearance is rather gradual.

The precise spatial regulation of this dynamics is important for the overall leaf growth and shape. For instance, when the division happens in ectopic regions, such as in TCP mutants or miRNA (Nath *et al.*, 2003; Palatnik *et al.*, 2003; Rodriguez *et al.*, 2010) and over-expression of CYCD3 (Dewitte *et al.*, 2003), the leaf loses its flat shape and becomes wrinkled. In addition, differences in the timing of the disappearance of cell division or in the frequency of cell divisions might affect the number of cells formed and potentially also leaf size (not always, sometimes there is 'compensation', see below). Therefore, the correct suppression of cell division is important for the overall leaf shape.

Despite its importance, the question of what regulates the dynamics of the division zone until it disappears remains unknown. It has been proposed that differentiation of the photosynthetic machinery is very important for regulating the exit from proliferation (Andriankaja *et al.*, 2012). Upon chemical treatments that disrupt chloroplast signalling (norflurazon treatments), leaves arrested their growth and their cells were smaller and showed low shape complexity (measured using circularity). This led the authors to propose that the proliferation zone had expanded and that the overall arrest in the leaf was due to inhibition of cell expansion caused by the disruption of chloroplast signalling. However, as chloroplast are directly related with metabolism, plants with altered chloroplast maturation will have a deficit of energy; thus, it is not clear if chloroplast differentiation is the fundamental mechanism that regulates the arrest of cell division or if alteration of chloroplast signalling cause a general delay of development that indirectly affects leaf growth (i.e it is well known that the availability of resources will alter the size of individuals, in yeast, plants and even in humans).

Despite the fact that many genes have been involved in restricting and promoting cell division and cell differentiation (see more information in these recent reviews: Breuninger & Lenhard, 2010; Johnson & Lenhard, 2011; Powell & Lenhard, 2012), at the moment we have just a scattered picture of the underlying mechanism.

Although the dissection of the basic principles behind the dynamics of cell division is beyond the scope of this work, using the data presented in Chapter 4 and recalling the

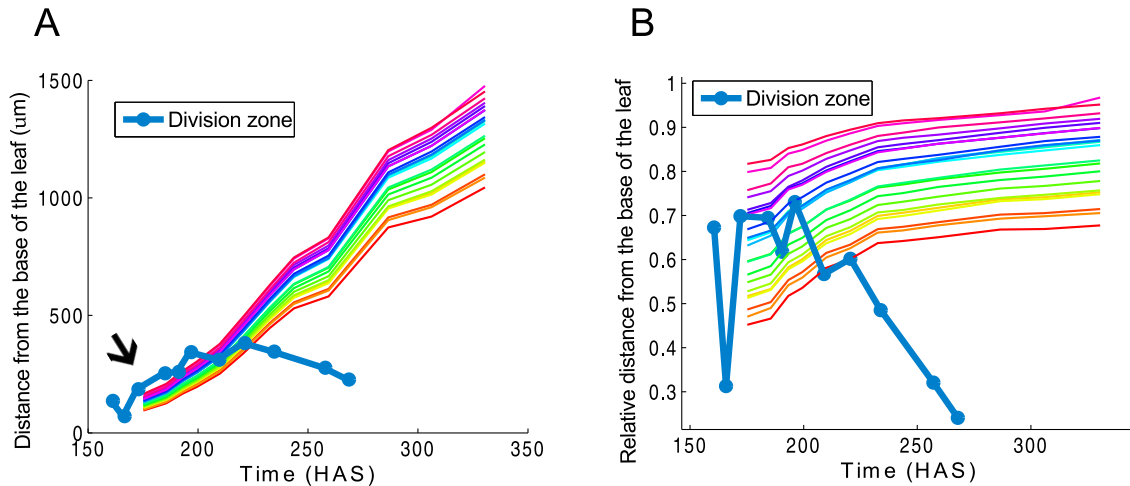


**Figure 6.1: Cell division zone and displacement of cells during leaf growth.** Due to higher growth rates at the base of the leaf, cells are “pushed” towards the tip of the leaf (each color represent the displacement of the centroid of a cell). A) Absolute division zone (bold blue line) overlaps with the absolute displacement of cells due to inhomogeneous cell divisions and internal tissue deformation (Lagrangian frame of reference). Then, cells exposed to the hypothetical signal that induce cell division at early stages of development (indicated by the arrow) could continue dividing at the same time as they are transiting through the leaf. B) The relative position of the division zone plotted together with the relative displacements of cells shows also an overlap but it is not as strong as the absolute position. The division zone and displacement correspond to the same leaf (ExpID3002-PD). The base of the leaf is fixed and correspond to 0.

analysis of the different spatial scales, I can speculate about different possible explanations. Assuming that there is a mobile signal influencing cell division, in my view, there are two main modes of behaviour:

1. The observed profile of cell division *directly* reflects the profile of the gradient of the mobile signal (position taking an Eulerian frame of reference). Thus, the dynamics of the gradient mirror the dynamics of cell division observed.
2. The observed profile of cell division *indirectly* reflects the profile of the gradient. For example, if cells are exposed to the mobile signal that induce divisions in just a specific spatial or temporal window, and they are displaced within the tissue before the actual division is detected. Under this assumption, it is very important to take into account the changes in cell position during the growing tissue (Lagrangian frame of reference).

In both scenarios, it is necessary to take into account the effect of tissue growth. In fact, growth itself could change the concentration and/or distribution of the mobile signal. Assuming an exponential gradient, the effect of growth in a gradient depends on the ratio of the degradation rate to the growth rate (see Wartlick *et al.*, 2011 for details). Then, if the

degradation rate is much bigger than the growth rate, the gradient “renews” itself faster and it will not be “stretched” (or “diluted”) by growth. Thus, under the first assumption, the dynamics of the putative mobile signal (i.e degradation, production, etc.) must be adjusted with the growth of the leaf to account for the observed pattern of division.

In the second scenario, the mobile signal has a more restricted spatial or temporal distribution, and the observed profile of cell division is produced after the exposure to the morphogen. Under this assumption, the displacement of cells due to growth is very important (see Figure 6.1). There are different ways by which this possibility could operate. For instance, if there is a limited temporal or spatial window of morphogen exposure (indicated by the arrow in Figure 6.1A) and the division is detected just after. This mechanism was proposed to account for limb digit formation (Wolpert, 2002), making the difficult assumption that cells are able to somehow measure the time of exposure of a gradient. Another alternative is that, as cells divide and move out of the morphogen expression domain (perhaps also indicated by the arrow in Figure 6.1A), they transport their molecular content and the divisions are detected after. This mechanism is also called cell lineage transport and it has been proposed to function in some animal systems (Ibanes *et al.*, 2006; Wartlick *et al.*, 2009).

Moreover, it is very important to take into account that it is not a decision of “all or nothing” because the relative division rate is also decreasing perhaps because more cells are leaving the cell cycle (the alternative option is that cells are increasing their cell cycle length; but this was not supported by the data, see Chapter 4). Then, it is also necessary to account for this temporal gradient (perhaps assuming that the mobile signal is decreasing or that the sensitivity of the cells to the morphogen is decreasing).

A possible way to distinguish between a fixed position gradient and a gradient that is moved by cells, would be to locate mutants or treatments that causes leaves with an increase or decrease of cell numbers, then the division zone must keep the same dynamics if the putative mobile signal acts at an absolute distance (Eulerian frame of reference) or change if the cells are carrying information with them. However, these mutants should fulfill two requirements: 1) they must not be involved in setting the division zone, a difficult *a priori* assumption given that the nature of the mobile signal is unknown and, 2) they should not change the overall growth rate. The selection of such a mutants is difficult because, nevertheless there are many reported mutants involved in cell proliferation and cell expansion (reviewed in Breuninger & Lenhard, 2010; Johnson & Lenhard, 2011; Powell & Lenhard, 2012), no one has yet analysed quantitatively and dynamically in relevant spatial and temporal scales during leaf growth.

Another possibility that I cannot rule out with the available data is that instead or in addition to the putative morphogen signal promoting division, there is a repressive signal (an “an arrest” signal) emanating from the tip of the leaf (Nath *et al.*, 2003).

Most likely, the regulation of the cell division is given by the balance between different pathways (see Chapter 1). The quantitative analysis of cell dynamics in mutants using

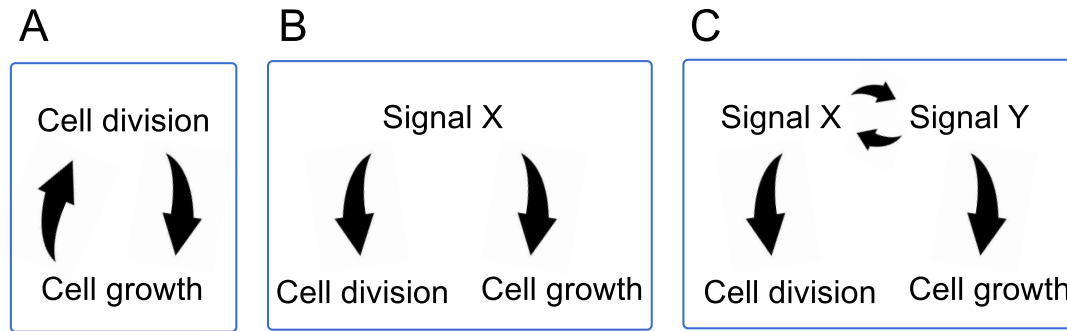


**Figure 6.2: Cell growth and cell division might be related in different manners to ensure a coordination during morphogenesis.** Simplified version of different hypothesis on how cell division and cell growth might be coupled. A) There is a direct link. B) There is a common upstream regulator that coordinate both processes. C) Cellular growth is regulated in parallel with the cell division and the coordination happens indirectly. These possibilities could lead to coordination of cell division and cell growth during morphogenesis. However, in the options B and C, these events can be separated. Multiple layers of regulation are possible and are not included in this simplified scheme. Furthermore, different manners of coupling cell division and cell growth might be operating at different moments during development.

a pipeline similar to the one presented here combined with the gene regulatory network dynamics (for example Pullen *et al.*, 2013; Alvarez-Buylla *et al.*, 2010) will help to elucidate the underlying mechanism. Moreover, modelling work that allows for representation of cells (for example adapting the CPM simulations showed in Chapter 2 or introducing a cellular framework in a previous leaf model, described in Kuchen *et al.*, 2012) and including realistic growth parameters extracted from time-lapse data, will be very helpful to explore different hypothesis.

## 6.4 Coordination of cell growth and cell division: compensation

Cell division and cell growth must be coordinated in order to produce organs with proper sizes and shapes (Neufeld & Edgar, 1998; Tzur *et al.*, 2009; Wartlick & Gonzalez-Gaitan, 2011). Nevertheless, how this coordination takes place remains unknown. In principle, there are different possibilities by which cell division and cell growth may be coupled (Neufeld & Edgar, 1998; Rupes, 2002; Jorgensen & Tyers, 2004; Wartlick & Gonzalez-Gaitan, 2011). These include: 1) direct coupling of cell division and cell growth, 2) an indirect coupling by a common upstream regulator and 3) independent regulation of cell growth and cell division (Figure 6.2).

All these scenarios could result in coordination between cell proliferation and cell growth; but in the second and the third case, cell growth and cell division are separa-

ble processes. In my opinion, it is important to distinguish all these different options when this problem is addressed in plants, because considering different scenarios could help to disentangle how these processes are coordinated during development. However, it is clear that more than one option can operate during leaf development because eventually cell division and cell expansion are separated in time and post-mitotic cells continue growing. In this sense, growth and cell cycle can be coupled in different ways within an organism, reflecting perhaps the context. For instance, recently it was reported that a cell size dependence to enter to the cell cycle is present for cells in the shoot apical meristem but not for cells in the sepal primordium (Schiessl *et al.*, 2012).

Under the first scenario (Figure 6.2A), if the cell division and cell growth were directly coupled, alteration in one would lead to effects on the other. Indeed, when the cell cycle is perturbed (for example, by over-expression of negative regulators), cells grow more than in wild type conditions to compensate for the changes in cell division (see more about compensation below). However, to my knowledge, there are no reported cases of changes in division due to altered cell elongation. Favouring the second and third options (Figure 6.2B,C) there is a long-list of genes and molecules that have been implied in one or both processes (see General Introduction and a recent review in Powell & Lenhard, 2012) but the detailed discussion of those is beyond the scope of this work.

An important observation is that plants and animals can maintain their overall organ growth and shape despite alteration to cell numbers (review in Day & Lawrence, 2000; Marshall *et al.*, 2012). Indeed, alterations in cell proliferation produce normally sized structures with either small or large cells (Su & O'Farrell, 1998).

In leaves, there are many reports of an abnormal cell volume increase when there is defective cell proliferation, such that leaves are almost normal in size and shape but contain fewer and bigger cells (Figure 6.3). This is often referred as the compensation phenomenon (Tsukaya, 2002; Beemster *et al.*, 2006; Tsukaya, 2013). The compensation has been proposed as an evidence towards the presence of an unknown, organ-wide system that couples cell proliferation to cell expansion in leaves (Beemster *et al.*, 2006). This possibility cannot be ruled out as many of the genetic components act non-cell autonomously (Serralbo *et al.*, 2006; Savaldi-Goldstein & Chory, 2008; Fujikura *et al.*, 2009; Eriksson *et al.*, 2010; Bai *et al.*, 2010; Kawade *et al.*, 2010, 2013).

However, one straightforward interpretation of compensation is that it results from independent regulation or uncoupling of cell division from cell growth. Despite of cell division disruption, the tissue could continue growing and reach comparable size than the wild type. In this case, the presence of bigger or smaller cells than in the wild type becomes a side-effect of more or fewer divisions in the same time interval. Thus, compensation is not produced by any new mechanism but it is just the outcome of changes in the frequency of cell division.

In plants, however, it has been argued that the processes of cell growth cannot be independent of cell proliferation (Beemster *et al.*, 2006; Tsukaya, 2013). In my opinion, there

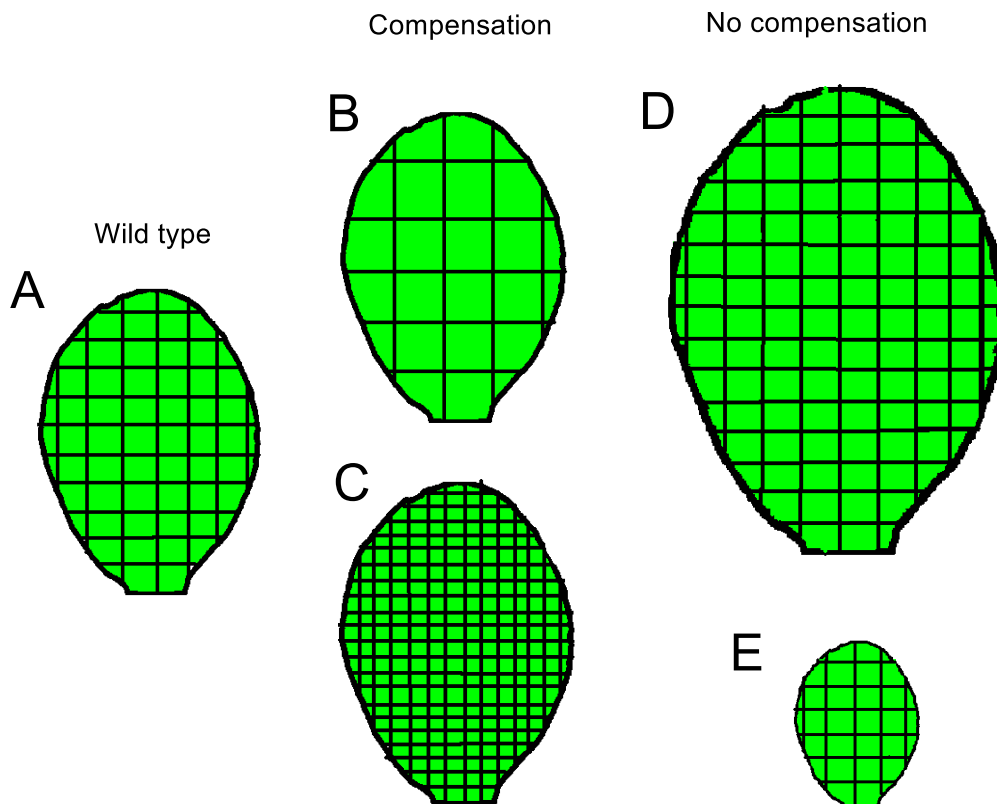


**Figure 6.3: Cell size and overall leaf size when cell division is disrupted.** A) schematic representation of cell size and leaf size in the wild type leaf. B) When cell divisions are perturbed, it can occur that cells grow more to compensate for the fewer number of cells (see a recent review in Horiguchi & Tsukaya, 2011). C) It is also possible that cells are smaller but the number of cells increase and the organ retains its overall size (such as in the *erecta* mutation, see Tisne *et al.*, 2011). However, this compensatory behaviour does not happen always. D) There are also cases when bigger leaves result from the increase in cell number, keeping the cell size unaltered (as in the overexpression of AN reported in Mizukami & Fischer, 2000). E) Also, the overall leaf is smaller when there are fewer cells with normal cell size (as in *short root* mutant, see Dhondt *et al.*, 2010).

is no evidence on why cell proliferation and growth could not be separated (regulated by common signals or regulated in parallel, Figure 6.2B-C), and all the possibilities should be considered, at least because the effects could be evaluated separately.

The observation that changes on the frequency of cell divisions do not affect the overall size of the leaf apparently contradicts the results obtained in Chapter 4. There, I stated that the cell growth follows a very similar trend after cell division and that cell division perhaps “resets” the overall growth. An interesting future experiment is to evaluate if this characteristic trend prevails in the mutants that compensate (and the exceptions, see Figure 6.3D-E). One possible outcome is that the trend of growth at the cellular level is conserved in these mutants and the only difference is that cells stop to grow at different times. In this case, it is very relevant to evaluate together the dynamics of the overall leaf

growth, because even if the final leaf size is approximately the same, the time and/or the speed in which the final size is reached could be different. The other possibility is that after alignment by their cell age, the cell growth in these mutants is distinct. This different hypothesis could be addressed in straightforward manner applying the pipeline described in Chapter 3 to mutants that show compensation and the exceptions (Figure 6.3).

Whatever is the explanation for the compensation, this phenomenon points out that the number of cells present in the leaf is flexible. Indeed, in nature, the coordination between cell growth and cell division can also be regulated by environmental conditions. Short-day conditions cause a decrease in the epidermal cell number in the leaf and, delaying flowering by removing floral buds caused an increase in cell area (Cookson *et al.*, 2007). These observations just highlight that the coordination of cell growth and cell division may have further layers of regulation.

Independently of the details of the coordination between cell growth and cell division, the examples discussed here suggest that the cell growth can be modulated during development and that its control is robust (and may be separable) from the cell cycle. Then, perhaps the most important aspect for understanding the mechanism that regulate the overall size of the leaf is what stops cell growth.

### 6.5 Limits of cell growth

A very important question in development is how cells stop growing and how this decision is coordinated such that organs within the individuals and among members of the same specie maintain a similar size and shape. As discussed in the previous section, it is outstanding that the final size of the cells can be modulated, meaning that the limits of cell growth within the leaf are flexible. How this modulation occurs and what limits the cell's size are very exciting questions that remain, in my opinion, poorly explored.

Cell growth is, of course, bounded by physical constraints. The ratio between surface and volume needs to be within limits to allow the exchange of signals with other cells or with the medium (Marshall *et al.*, 2012). Nevertheless, in plants there are examples of cells that can achieve up to 1/3 in length with respect the overall organ, for example giant cells in sepals (Roeder *et al.*, 2010) and cells at the edge of the leaf (data not shown). Notably, these giant cells seem to have a different identity than the rest of cells (Roeder *et al.*, 2012b), suggesting that perhaps they have a different fate.

A size limit specific to the cell type is also supported by stomata and guard cells. These cells show remarkable similar cell size. In fact, some studies have used cell size as a criteria to select populations of stomata (Andriankaja *et al.*, 2012). Another example in which the limits of cell size happens according to the cellular identity is the stem cells in meristems. Their cell size, despite of undergoing through constant divisions, remains stable (they need to growth back to their "rest" size, though). Altogether, these examples suggest that the bounds of cell size may be related with the specific cell fate and/or cell context within the plant. However, the question of what maintains the cell's size within

limits once it has reached a specific value, remains unanswered.

Interestingly, cell size strongly correlates with ploidy and nucleus size (Su & O'Farrell, 1998; Sugimoto-Shirasu & Roberts, 2003; Marshall *et al.*, 2012). Moreover, the endoreduplication coincides with cell expansion in the leaf epidermis (Beemster *et al.*, 2005). This is an interesting correlation but a causal relationship has been difficult to draw because cell growth is not always associated with endoreduplication. For instance, when extra cell expansion occurs due to impairment of cell division, there is not always an increase of endoreduplication (review in Sugimoto-Shirasu & Roberts, 2003). Conversely, cells can also grow dramatically without increasing the amount of nuclear DNA (De Veylder *et al.*, 2001). Moreover, some plants such as rice and lettuce do not endoreduplicate (Tsukaya, 2013). Therefore, cell size and endoreduplication is for now just a correlation. Besides, if one assumes that endoreduplication is important for achieving the cell's size limits, the question on how cells stop growing is just restated as how cells stop entering into cycles!

An interesting hypothesis that I cannot rule out is that endoreduplication somehow modifies the dynamics of cell growth (for instance, reducing the speed of growth). This is a testable prediction that could be addressed using the methods presented in this thesis with a quantitative measure of DNA to monitor endoreduplication (for example, using the nucleotide analog 5-ethynyl-2'-deoxyuridine, EdU as in Schiessl *et al.*, 2012).

There are some theoretical suggestions on how cells could stop growing in a multicellular context. The majority include the capacity of cells to measure the accumulation of intracellular signals over time (temporal integration) or measure a gradient over a tissue scale (spatial integration; see a review in Lander, 2013). Nevertheless, such hypothetical substances have not been identified in plants and there is a scarce number of known gradients within the leaf. Gradient forming substances include KLUH (Anastasiou *et al.*, 2007; Kazama *et al.*, 2010), SHORT ROOT (Dhondt *et al.*, 2010) and ERECTA (Shpak *et al.*, 2004), but none has been analysed in detail as some gradients in animal field (such as Bicoid in Gregor *et al.*, 2007a and Dpp in Kicheva *et al.*, 2007).

A problem in the study of the limits of cell growth is that it is very difficult to get information on how cells reached their final size once the overall leaf growth is saturated. Using the methods described in this work, and starting the time-lapse later (so, that cells are followed until the late phases), I foresee not a complication to capture the dynamics of cell growth when it is very close to its limits. Hopefully, a dynamical analysis using long time-lapse imaging combined with molecular fluorescent tools will shed light on how cells stop to growth.

## 6.6 Cell polarity and growth

Although spatial and temporal regulation of cell division is important for leaf development (see for example Nath *et al.*, 2003; Dewitte *et al.*, 2003), there are also many cases where despite the disruptions to cell division, leaf morphogenesis continues normally. For instance, leaf shape was unaffected when cell division was inhibited or decreased,

(i.e. compensation, see Section 6.4) or when cell divisions were misorientated (see a review in Meyerowitz, 1996). Using time-lapse and finite element modelling to account for limb extension, Boehm *et al.*, 2010 showed that the gradient in proliferation rates is also not sufficient to explain the limb morphogenesis. These observations suggest that cell division *per se* cannot be considered as the driving force for morphogenesis.

Indeed, isotropic cell growth and cell division by themselves cannot create an organ with an anisotropic shape (Su & O'Farrell, 1998), but it is necessary to include the notion of polarity (Coen *et al.*, 2004; Green *et al.*, 2010; Kuchen *et al.*, 2012). An important question is whether at the cellular level it is also necessary to include polarity to account for the anisotropy and direction at the tissue level.

Mathematical analysis has suggested that cell polarity can arise spontaneously through a simple mechanism including antagonistic activities of small GTPases and their differences in diffusion rates, that might be shared in plants and animals (Abley *et al.*, 2013). Also, the proposed network could account for coordination of polarity between and across cell files. A missing link is whether this intrinsic polarity could be coupled with a process that simultaneously 1) creates asymmetries in the cell shape and 2) provides directionality and anisotropy to build up an organ with the right size and shape.

Notably, the proposed genetic regulatory network that gives rise to the intracellular partitioning and that could also account for coordination (see Abley *et al.*, 2013, and a recent review Grieneisen *et al.*, 2013b) share the same elements as the the proposed network that accounts for the characteristic jigsaw puzzle-like shape of pavement cells. This raises the hypothesis that a similar mechanism to that creating complex cell geometries could also account for the cell polarity that gives direction and contributes to the organ shape. With this hypothesis in mind, methods to quantify the complex shape of the pavement cells were developed (LOCO-EFA and SPM) and their dynamics were assessed over time (Chapter 4). Interestingly, cell shape complexity as a whole (measured using cumulative difference and entropy) showed a proximodistal gradient that was dependant on the developmental stage of the cell. Surprisingly, long time-lapse also revealed that new lobes were formed as bifurcations of the pre-existing lobes, expected behaviour from an Turing instability system in a growing domain (under the right parameters) and perhaps the effect of the cell growth and cell geometry, as discussed in Chapter 5.

Besides the time lapse in the simplified background of *speechless*, I prepared some mutants important for the cell shape and the cell polarity (review in Grieneisen *et al.*, 2013b), under a membrane marker. Due to the redundancy in the ROP family (i.e. a double mutant of ROP2 and ROP4 is needed to obtain changes in the lobe regions), the choice of the mutants was done on basis of the effects that would change the dynamics of multiple ROPs. Among the first candidates are the guanine exchange factors (GEFs), guanine disassociation inhibitors (GDIs) and GTPase-activating proteins (GAPs) proteins that potentially modulate the behaviour of several ROPs (reviewed in Etienne-Manneville & Hall, 2002). SPIKE1 is the only GEF protein whose reported loss of function had a dramatic alteration

in cell shape (Qiu *et al.*, 2002) and is able to interact with several ROPs *in vitro* (Uhrig *et al.*, 2007). These proteins switch ROPs between inactive and active forms (Berken *et al.*, 2005); recently, the upstream activity of SPIKE1 was involved in the maintenance of PIN2 polar distribution in the plasma membrane of epidermal cells of Arabidopsis's roots (Lin *et al.*, 2012). Another candidate that could interfere with multiple ROPs is the ROP-interactive CRIB motif-containing protein 1 (RIC1), involved in both microtubule organization and suppression of ROP2 activation in the indentation zones of pavement cells in *Arabidopsis thaliana* (Fu *et al.*, 2009).

Figure 6.4B shows that *spike1* (loss of function as reported in Qiu *et al.*, 2002) has dramatic cell shape defects. This phenotype is expected if the two pathways for creating a lobe and an indentation are compromised. Interestingly, the leaf shape is also dramatically altered and elongated in the proximodistal axis in comparison with the wild type (Figure 6.4D-E). Noteworthy, this mutant present holes inside the tissue, indicating a lack of coordination between cells, alterations in the cell wall, fragile leaves, or a combination of these. The effect on the overall leaf shape is likely to be independent of the holes in the tissue because other mutants with defective cell shape (but without holes) such as *angustifolia* have been reported to have an elongate leaf shape in the proximodistal axis as well (Bai *et al.*, 2010).

In contrast to the dramatic leaf shape alteration on *spike1*, the leaf shape of RIC-OX (overexpression of RIC1 as reported in Fu *et al.*, 2009) does not show any major defects (Figure 6.4F), despite of the defective cell shapes (Figure 6.4C). Thus, an impaired cell geometry (compare shape complexity in Figure 6.4J) not always implies a defective overall organ shape.

To account for the change on the whole leaf shape, an intriguing possibility is that the overall organ differences stem from differences in cellular behaviour at these mutants in respect to the direction of cell elongation (i.e angle at which the principal direction of cell growth occurred). A quick inspection can be done using the “spatial angle” discussed in Chapter 2 that corresponds to the angle that the semi-major axis of the first elliptic harmonic (i.e the longest axis of a cell) needs to rotate to be parallel to the x-axis (in this case, the x -axis coincides with the midvein). Note, however, that this is just an approximation that is valid assuming that the preferred direction of elongation coincides with the longest axis of a cell (alternatively, this angle could reflect rotations within the leaf, that although rare as reported in Remmler & Rolland-Lagan, 2012; Kuchen *et al.*, 2012, cannot be ruled out). Interestingly, in *spike1* mutants, the cell direction is mainly oriented along the proximodistal axis and there is not much variation (Figure 6.4H) while in RIC-OX, the main axis of elongation is variable as in the case of the wild type (Figure 6.4G, I).

Remarkably, cells in both mutants still show a very similar anisotropy (preferred elongation in one axis, calculated as the ratio of semi-major axis to the semi-minor axis of the first harmonic, see Figure 6.4J right and Chapter 2). Altogether, this suggests that the polarity mechanism that accounts for a jigsaw puzzle-like shape might be decoupled (or

different) from the mechanism that gives directionality at the cellular level and that accounts for the overall shape (Figure 6.4K). A detailed study of the dynamics of the cell growth parameters (Coen *et al.*, 2004) in these and other mutants can be addressed in a straightforward manner in the future using the tools reported in this work.

Assuming a similar network of polarity determinants (ROPs, auxin and downstream interactors), an outstanding question to explore in the future is how these two levels of polarity specification (at the level of cell shape and at the level of cell orientation) are related. Although there has been a lot of progress in understanding the theoretical cellular basis that underlies tissue polarity that might account for PIN polarity coordination (Abley *et al.*, 2013; Grieneisen *et al.*, 2013b), it is still unknown if a similar mechanism could control the orientations of specified growth at the cellular level.

In one scenario, the direction of cell elongation and cell anisotropy is also given by an intracellular partitioning mechanism and it is coordinated among neighbours and over the tissue (as proposed in Abley *et al.*, 2013, see Figure 6.5). Another possibility is that cell anisotropy and cell direction are just the indirect resultant properties of a gradient at tissue scale and/or derive from the mechanical properties of a connected tissue (Figure 6.5, i.e. polarity-based axiality that operates at tissue level as proposed in Kennaway *et al.*, 2011; Kuchen *et al.*, 2012 or resultant *in silico* pavement cells shapes in Chapter 2; or, stress along the tissue that *per se* do not have directionality).

A difficulty to address these questions is the scarcity of polarity markers in plants cells that renders it very difficult to differentiate a simple axiality from a polarity at the cellular level (Figure 6.4K, Figure 6.5) during the development of the leaf shape.

In the same way, an interesting hypothesis is whereas the planar cell polarity of PIN1 at early stages of leaf development is important for the mechanism that confers directionality in cell elongation (for instance, acting directly by setting an early pattern as proposed in Kuchen *et al.*, 2012). Alternatively, PIN1 localization could be involved in setting the auxin transport important for vascular development and just indirectly affecting cell directionality and anisotropy.

Once again, the pipeline discussed in Chapter 2-3 together with analysis of the growth vectors, anisotropy and orientation at the cellular level of the time-lapse data already collected and mutants affecting leaf shape in different manners could provide with a quantitative description at the cellular level that could be incorporated into existing (Kuchen *et al.*, 2012) or cell-based models of leaf shape morphogenesis. Importantly, this approach could be combined with local perturbations (the interface of wild type and polarity mutants by clonal analysis or leaf cuttings), to test different hypothesis on how the local coordination of polarity at cellular level can affect the global leaf shape.

Moreover, the complex geometry of pavement cells and the possibility to extract their shape and growth dynamics will be very important for testing how a similar molecular network could or could not specify the polarity that underlies complex shapes and the polarity or axiality that drives cell elongation in a preferred direction. This would imply

that a similar patterning mechanism is acting in parallel within the same cell! This is not a completely unfavourable option, given that recently, Oda & Fukuda, 2012 showed that patches of ROP11 can be formed upon its ectopic expression in these cells.

Importantly, the complex shape of pavement cells make them an ideal system to study fundamental principles of patterning inside a cell, a field that remains unexplored in the plants. I reported here the recurrent formation of lobes in *Arabidopsis thaliana*. However, not all plants show this feature, some others do not develop a jigsaw puzzle-like shape at all (see some examples Figure 6.6). This opens also the possibility that the polarity that underlies complex cell geometries has been modulated over evolutionary time scales. The study of the shape and growth dynamics in non-model plants will also be important for unravelling the basic principles leading to different or shared polarity regulatory networks.

## 6.7 Final remarks

The motivation of this thesis was to explore the patterns and dynamics at the cellular level during leaf development aiming towards the understanding of the cellular basis of morphogenesis. A long time-lapse combined with computational tools allowed to study the patterns of cellular behaviour with high spatial and temporal resolution. In my opinion, the analysis of *in vivo* dynamics is very important to build and constrain hypothesis, that without real data would be unbounded.

Many aspects of cellular behaviour are proposed as the result of morphogens acting at the tissue-scale. The graded behaviour of absolute values and that of growth rates along the leaf is not an exception, and it was proposed that a graded growth factor could account for this pattern (Remmler & Rolland-Lagan, 2012). Under this scenario, cells of a similar stage but in different locations within the leaf, would behave depending on its position. Surprisingly, this was not the case when cells were aligned according to the time of their cell division. Therefore, the quantitative analysis of cell growth and cell shape dynamics revealed that the developmental stage of the cell is primordial for determining cellular dynamics and highlights the importance of considering the cellular scale in the formulation of hypothesis about the morphogenesis at the organ scale. Interestingly, the relative rates of cell growth and cell shape follow a very similar trend after the cell division and this tendency was independent on the number of divisions pursued. What regulates cell growth dynamics and how cell growth is arrested are exciting open questions to explore in the future.

Even though the cell growth rate and cell shape rate were influenced in very small proportion by the position (if any influence), there is the possibility that a morphogen could influence the place where division takes place. Moreover, I cannot rule out that

other aspects of cell dynamics such as the arrest of cell growth and the direction of cell growth is determined by an external gradient.

Hormones, of course, are the first candidates to test. Surprisingly, the only way to assess the behaviour of the two major plant hormones, auxin and cytokinin, is through indirect measure of some reporters. Moreover, other signalling pathways at the plasma membrane by receptor-like kinases or small peptides may also play a role in the coordination of cell behaviour during tissue morphogenesis but remain very poorly explored. In the future, quantitative tools to analyse the dynamics of hormones and other gradient-forming molecules will be very important to characterize the effect and influence of gradients in plants.

Many cellular alterations (i.e frequency of division, cell shape) could still lead to a normal looking leaf shape. This could be taken as evidence that the cellular scale is not important and that the mechanisms that account for a correct shape occurs at the tissue-level. However, the interpretation of gradients inevitably happens at the cellular level and in some cases, the dynamics of the gradient formation could be importantly influenced by the cells themselves (Ibanes *et al.*, 2006). The fact that, for example, final cell size can be modulated for the a correct organ shape and size, in my opinion, just highlights that our understanding on how the cell growth is regulated and coordinated with the growth of the overall tissue is very poor.

Another cellular pattern emerging as an essential feature during morphogenesis is polarity. A very interesting hypothesis is that, despite similar molecular components and principles, the cell polarity that accounts for the formation of complex cell geometries is separable from the polarity that gives anisotropies and direction to cell growth. It will be very interesting to study in detail how the direction and orientation at the cellular level occurs during development combined with local-perturbations (i.e clonal analysis, leaf cuttings, etc.) and mathematical modelling.

Finally, there are still many unanswered questions on how different cellular behaviours are translated into a shape and I provided here with a survey of the ones that in my opinion are the most interesting. Importantly, these outstanding questions are not exclusive to plants but represent general problems in morphogenesis. Nevertheless, I believe the approach and pipeline presented here provide us with a useful quantitative and testable framework for beginning to assess the interplay between cellular dynamics and morphogenesis. Hopefully, as phrased by Su & O'Farrell, 1998: "scientific progress is often marked by the realization that we are ready to address an old question that has become accessible."

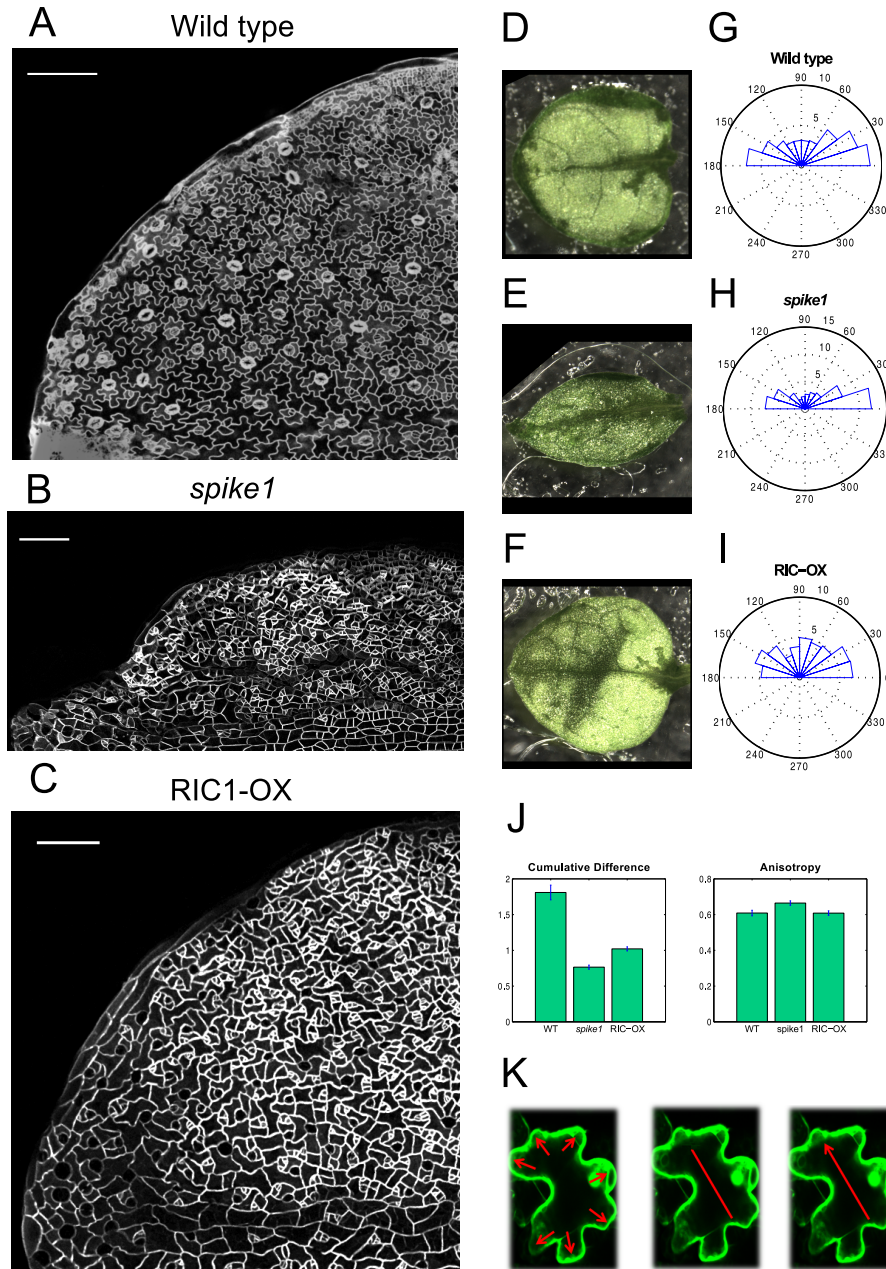


**Figure 6.4: Different notions of cell polarity.** A) Pavement cells in a wild type leaf showed their characteristic jigsaw puzzle-like shape. B) Cells in *spike1* mutant and C) RIC1 over-expression (RIC1-OX) fail to develop jigsaw-like geometries. D-F) Overall leaf organ is altered in *spike1* (E) mutant but not in RIC1-OX (F) compared with the wild type leaf (D). G-I) Angle histogram plots (the proportion of cells is shown in the radius). The angle showed here, is the angle that the first semi-major EFA mode needs to rotate in counter clockwise direction to be parallel to the x-axis. It can be interpreted as the angle of preferred cell elongation taking as a reference the midvein. The majority of *spike1* cells (H) are aligned in parallel to the midvein. In contrast, cells in wild type RIC1-OX (I) are more distributed as in wild type (G). The shape complexity, quantified using the cumulative difference, is dramatically decreased in the mutants (J, left). However, the anisotropy (J, right) is very similar in the wild type and mutants. Anisotropy was measured as the ratio of the semi-major to semi-minor axis of the first EFA harmonic. K) The cell polarity that underlies complex geometrical cell shapes might be separated from the cell axially and/or cell polarity that give directional cell changes important for leaf morphogenesis (arrow is pointing towards an arbitrary location). Scale bar represent  $100\mu m$  in A-C.

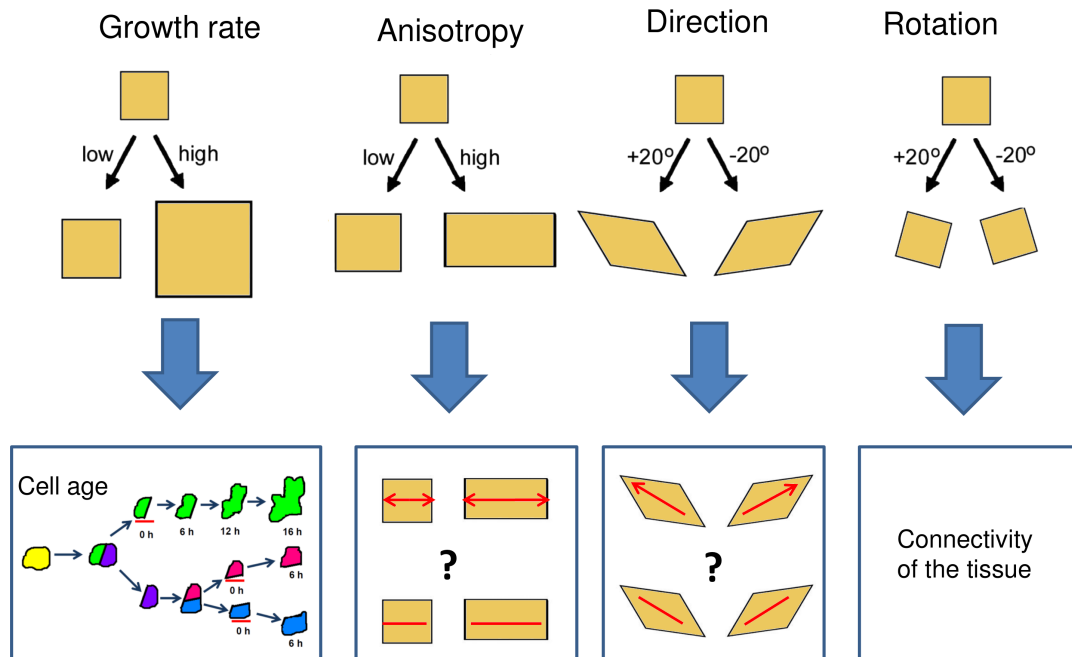


**Figure 6.5: Growth parameters at the cellular level.** How growth features are specified at the cellular level remains unknown. The growth rate at the cellular level is highly influenced (correlated) with the cell age (Chapter 4). How exactly the cell growth rate is regulated is an exciting question to explore in the future. Under the hypothesis that the polarity that gives rise to jigsaw puzzle-like shapes can be separated from the polarity that gives a normal leaf shape, a future question is if the anisotropy and direction at the cellular level are explained by (1) an intracellular polarity system (so, each cell has its own compass) or, (2) indirectly, using other mechanism that gives axiality (for example, polarity-based axiality that operates a tissue-scale as proposed in Kennaway *et al.*, 2011, or stresses along the tissue that *per se* do not have directionality). Also, it is not clear if the mechanism that gives anisotropies also gives direction. The preliminary data suggest that they can also be separated (cells can be elongated, but have different direction as shown in Figure 6.4). Rotation at the cellular level might be also the result of connectivity of the tissue (see Kennaway *et al.*, 2011; Kuchen *et al.*, 2012 and *in silico* tissue simulations in Chapter 2). Figure modified from Coen *et al.*, 2004.

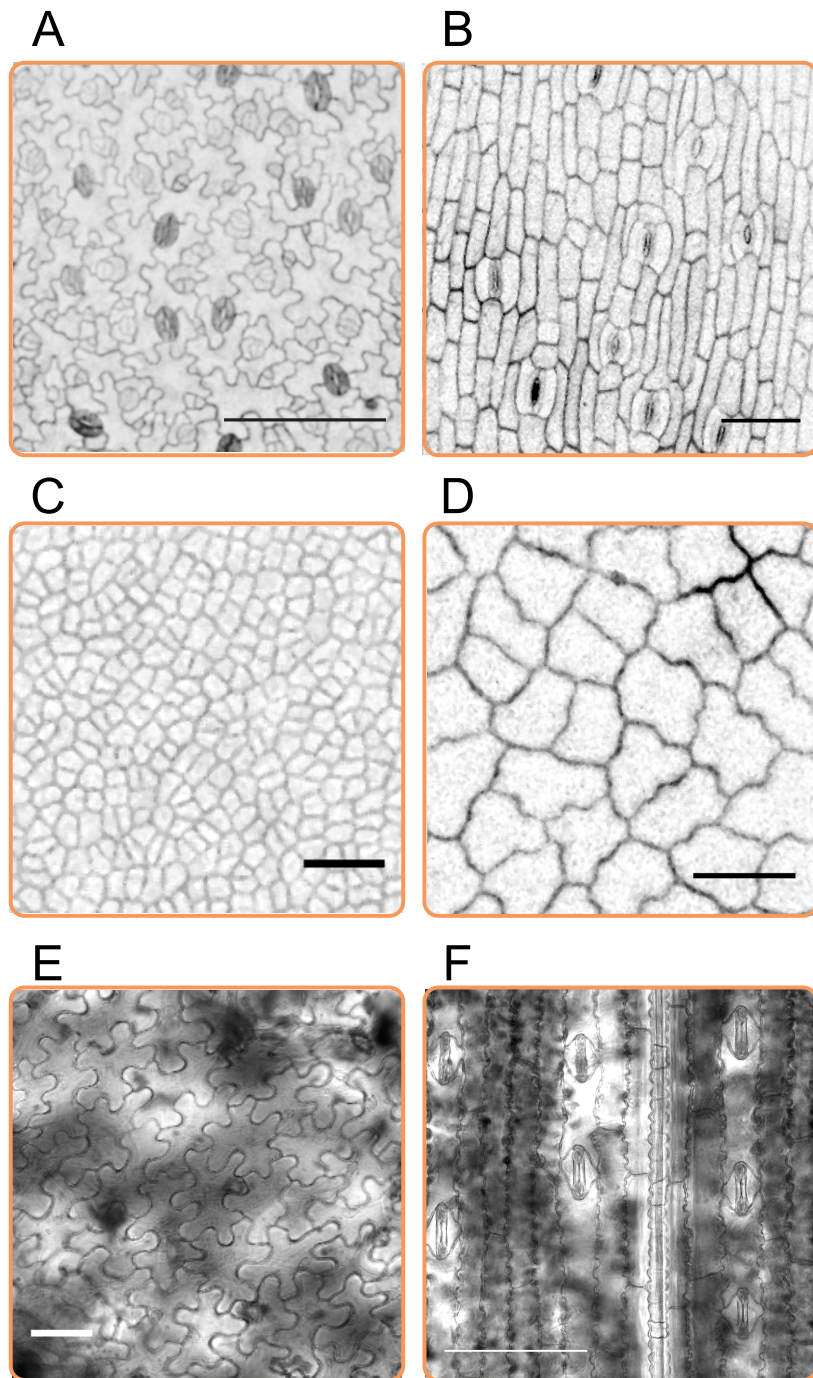


**Figure 6.6: Cell shape presents variations in different species.** A) First row shows a leaf impression of *Arabidopsis thaliana* showing the characteristic puzzle-like shape. B) The cells from the leaf of a banana plant are elongated along the proximodistal axis of the leaf, they show uniform direction and there is not a lobe and indentation pattern. C) An impression of a leaf of an orange shows that cells have “simple” shapes also without lobes and indentations but the anisotropy is very reduced compared with the other cases. D) An avocado leaf shows some pattern of lobe and indentations, but the amplitude of the lobes is very reduced compared with *Arabidopsis thaliana* (A). E) Cells of a crassulaceae plant also show a remarkable wavy outline, but there is not indication of secondary lobe formation. F) A maize leaf’s cells are elongated towards the proximodistal axis of the leaf and show a wavy outline just in the right and left sides of the cell. All scale bars represent  $100\mu\text{m}$ .

“If I have not done enough to pave the way for those who follow; if I have not cleared every obstacle from the path - nonetheless, I hope that this effort will not prove altogether fruitless.” Johann Wolfgang von Goethe (1790) in *The Metamorphosis of Plants*.

# Bibliography

- Abley, K., De Reuille, P. B., Strutt, D., Bangham, A., Prusinkiewicz, P., Mee, A. F., Grieneisen, V. A. & Coen, E. An intracellular partitioning-based framework for tissue cell polarity in plants and animals. *Development* 140: 2061–2074 (2013).
- Achard, P., Gusti, A., Cheminant, S., Alioua, M., Dhondt, S., Coppens, F., Beebe, G. T. & Genschik, P. Gibberellin signaling controls cell proliferation rate in *Arabidopsis*. *Curr. Biol.* 19: 1188–1193 (2009).
- Aloni, R., Schwalm, K., Langhans, M. & Ullrich, C. I. Gradual shifts in sites of free-auxin production during leaf-primordium development and their role in vascular differentiation and leaf morphogenesis in *Arabidopsis*. *Planta* 216: 841–853 (2003).
- Alvarez-Buylla, E. R., Benitez, M., Corvera-Poire, A., Chaos Cador, A., De Folter, S., Gamboa de Buen, A., Garay-Arroyo, A., Garcia-Ponce, B., Jaimes-Miranda, F., Perez-Ruiz, R. V., Pineyro-Nelson, A. & Sanchez-Corrales, Y. E. Flower development. *Arabidopsis. Book.* 8: e0127 (2010).
- Anastasiou, E., Kenz, S., Gerstung, M., MacLean, D., Timmer, J., Fleck, C. & Lenhard, M. Control of plant organ size by KLUH/CYP78A5-dependent intercellular signaling. *Dev. Cell* 13: 843–856 (2007).
- Andriankaja, M., Dhondt, S., De Bodt, S., Vanhaeren, H., Coppens, F., De Milde, L., Muhlenbock, P., Skirycz, A., Gonzalez, N., Beebe, G. T. & Inze, D. Exit from proliferation during leaf development in *Arabidopsis thaliana*: a not-so-gradual process. *Dev. Cell* 22: 64–78 (2012).
- Arnsdorf, E. J., Tummala, P., Kwon, R. Y. & Jacobs, C. R. Mechanically induced osteogenic differentiation—the role of RhoA, ROCKII and cytoskeletal dynamics. *J. Cell Sci.* 122: 546–553 (2009).
- Asl, L. K., Dhondt, S., Boudolf, V., Beebe, G. T., Beckman, T., Inze, D., Govaerts, W. & De Veylder, L. Model-based analysis of *Arabidopsis* leaf epidermal cells reveals distinct division and expansion patterns for pavement and guard cells. *Plant Physiol.* 156: 2172–2183 (2011).
- Asnacios, A. & Hamant, O. The mechanics behind cell polarity. *Trends Cell Biol.* 22: 584–591 (2012).
- Avery, G. Structure and development of the tobacco leaf. *American Journal of Botany* 20: O (1933).
- Bai, Y., Falk, S., Schnittger, A., Jakoby, M. J. & Hulskamp, M. Tissue layer specific regulation of leaf length and width in *Arabidopsis* as revealed by the cell autonomous action of ANGUSTIFOLIA. *Plant J.* 61: 191–199 (2010).
- Basu, D., Le, J., Zakharova, T., Mallery, E. L. & Szymanski, D. B. A SPIKE1 signaling complex controls actin-dependent cell morphogenesis through the heteromeric WAVE and ARP2/3 complexes. *Proc. Natl. Acad. Sci. U.S.A.* 105: 4044–4049 (2008).
- Beebe, G. T. & Baskin, T. I. Analysis of cell division and elongation underlying the developmental acceleration of root growth in *Arabidopsis thaliana*. *Plant Physiol.* 116: 1515–1526 (1998).

- Beemster, G. T., De Veylder, L., Vercruyse, S., West, G., Rombaut, D., Van Hummelen, P., Galichet, A., Gruissem, W., Inze, D. & Vuylsteke, M. Genome-wide analysis of gene expression profiles associated with cell cycle transitions in growing organs of *Arabidopsis*. *Plant Physiol.* 138: 734–743 (2005).
- Beemster, G. T., Vercruyse, S., De Veylder, L., Kuiper, M. & Inze, D. The *Arabidopsis* leaf as a model system for investigating the role of cell cycle regulation in organ growth. *J. Plant Res.* 119: 43–50 (2006).
- Ben-Zvi, D., Shilo, B. Z. & Barkai, N. Scaling of morphogen gradients. *Curr. Opin. Genet. Dev.* 21: 704–710 (2011).
- Ben-Zvi, D., Shilo, B. Z., Fainsod, A. & Barkai, N. Scaling of the BMP activation gradient in *Xenopus* embryos. *Nature* 453: 1205–1211 (2008).
- Benkova, E., Michniewicz, M., Sauer, M., Teichmann, T., Seifertova, D., Jurgens, G. & Friml, J. Local, efflux-dependent auxin gradients as a common module for plant organ formation. *Cell* 115: 591–602 (2003).
- Berken, A., Thomas, C. & Wittinghofer, A. A new family of RhoGEFs activates the Rop molecular switch in plants. *Nature* 436: 1176–1180 (2005).
- Besson, S. & Dumais, J. Universal rule for the symmetric division of plant cells. *Proc. Natl. Acad. Sci. U.S.A.* 108: 6294–6299 (2011).
- Blilou, I., Xu, J., Wildwater, M., Willemsen, V., Paponov, I., Friml, J., Heidstra, R., Aida, M., Palme, K. & Scheres, B. The PIN auxin efflux facilitator network controls growth and patterning in *Arabidopsis* roots. *Nature* 433: 39–44 (2005).
- Boehm, B., Westerberg, H., Lesnicar-Pucko, G., Raja, S., Rautschka, M., Cotterell, J., Swoger, J. & Sharpe, J. The role of spatially controlled cell proliferation in limb bud morphogenesis. *PLoS Biol.* 8: e1000420 (2010).
- Bowman, J. L., Eshed, Y. & Baum, S. F. Establishment of polarity in angiosperm lateral organs. *Trends Genet.* 18: 134–141 (2002).
- Breuninger, H. & Lenhard, M. Control of tissue and organ growth in plants. *Curr. Top. Dev. Biol.* 91: 185–220 (2010).
- Brown, G. C. & Kholodenko, B. N. Spatial gradients of cellular phospho-proteins. *FEBS Lett.* 457: 452–454 (1999).
- Carabelli, M., Possenti, M., Sessa, G., Ciolfi, A., Sassi, M., Morelli, G. & Ruberti, I. Canopy shade causes a rapid and transient arrest in leaf development through auxin-induced cytokinin oxidase activity. *Genes Dev.* 21: 1863–1868 (2007).
- Carlsbecker, A., Lee, J. Y., Roberts, C. J., Dettmer, J., Lehesranta, S., Zhou, J., Lindgren, O., Moreno-Risueno, M. A., Vaten, A., Thitamadee, S., Campilho, A., Sebastian, J., Bowman, J. L., Helariutta, Y. & Benfey, P. N. Cell signalling by microRNA165/6 directs gene dose-dependent root cell fate. *Nature* 465: 316–321 (2010).
- Carol, R. J., Takeda, S., Linstead, P., Durrant, M. C., Kakesova, H., Derbyshire, P., Drea, S., Zarsky, V. & Dolan, L. A RhoGDP dissociation inhibitor spatially regulates growth in root hair cells. *Nature* 438: 1013–1016 (2005).
- Caudron, M., Bunt, G., Bastiaens, P. & Karsenti, E. Spatial coordination of spindle assembly by chromosome-mediated signaling gradients. *Science* 309: 1373–1376 (2005).
- Chen, C. S., Mrksich, M., Huang, S., Whitesides, G. M. & Ingber, D. E. Geometric control of cell life and death. *Science* 276: 1425–1428 (1997).
- Clement, R., Blanc, P., Mauroy, B., Sapin, V. & Douady, S. Shape self-regulation in early lung morphogenesis. *PLoS One.* 7: e36925 (2012a).
- Clement, R., Douady, S. & Mauroy, B. Branching geometry induced by lung self-regulated growth. *Phys. Biol.* 9: 066006 (2012b).
- Coen, E., Rolland-Lagan, A. G., Matthews, M., Bangham, J. A. & Prusinkiewicz, P. The genetics of geometry. *Proc. Natl. Acad. Sci. U.S.A.* 101: 4728–4735 (2004).
- Cookson, S. J., Chenu, K. & Granier, C. Day length affects the dynamics of leaf expansion and cellular development in *Arabidopsis thaliana* partially through floral transition timing. *Ann. Bot.* 99: 703–711 (2007).

- Corbin, B. D., Yu, X. C. & Margolin, W. Exploring intracellular space: function of the Min system in round-shaped *Escherichia coli*. *EMBO J.* 21: 1998–2008 (2002).
- Craddock, C., Lavagi, I. & Yang, Z. New insights into Rho signaling from plant ROP/Rac GTPases. *Trends Cell Biol.* 22: 492–501 (2012).
- Cruz-Ramirez, A., Diaz-Trivino, S., Blilou, I., Grieneisen, V. A., Sozzani, R., Zamioudis, C., Miskolczi, P., Nieuwland, J., Benjamins, R., Dhonukshe, P., Caballero-Perez, J., Horvath, B., Long, Y., Mahonen, A. P., Zhang, H., Xu, J., Murray, J. A., Benfey, P. N., Bako, L., Maree, A. F. & Scheres, B. A bistable circuit involving SCARECROW-RETINOBLASTOMA integrates cues to inform asymmetric stem cell division. *Cell* 150: 1002–1015 (2012).
- Cunha, A., Tarr, P. T., Roeder, A. H., Altinok, A., Mjolsness, E. & Meyerowitz, E. M. Computational analysis of live cell images of the *Arabidopsis thaliana* plant. *Methods Cell Biol.* 110: 285–323 (2012).
- Day, S. J. & Lawrence, P. A. Measuring dimensions: the regulation of size and shape. *Development* 127: 2977–2987 (2000).
- De Reuille, P. B., Bohn-Courseau, I., Godin, C. & Traas, J. A protocol to analyse cellular dynamics during plant development. *Plant J.* 44: 1045–1053 (2005).
- De Veylder, L., Beeckman, T., Beemster, G. T., Krols, L., Terras, F., Landrieu, I., Van der Schueren, E., Maes, S., Naudts, M. & Inze, D. Functional analysis of cyclin-dependent kinase inhibitors of *Arabidopsis*. *Plant Cell* 13: 1653–1668 (2001).
- Dewitte, W., Riou-Khamlichi, C., Scofield, S., Healy, J. M., Jacquard, A., Kilby, N. J. & Murray, J. A. Altered cell cycle distribution, hyperplasia, and inhibited differentiation in *Arabidopsis* caused by the D-type cyclin CYCD3. *Plant Cell* 15: 79–92 (2003).
- Dewitte, W., Scofield, S., Alcasabas, A. A., Maughan, S. C., Menges, M., Braun, N., Collins, C., Nieuwland, J., Prinsen, E., Sundaresan, V. & Murray, J. A. *Arabidopsis* CYCD3 D-type cyclins link cell proliferation and endocycles and are rate-limiting for cytokinin responses. *Proc. Natl. Acad. Sci. U.S.A.* 104: 14537–14542 (2007).
- Dhondt, S., Coppens, F., De Winter, F., Swarup, K., Merks, R. M., Inze, D., Bennett, M. J. & Beemster, G. T. SHORT-ROOT and SCARECROW regulate leaf growth in *Arabidopsis* by stimulating S-phase progression of the cell cycle. *Plant Physiol.* 154: 1183–1195 (2010).
- Diaz, G., Quacci, D. & Dell’Orbo, C. Recognition of cell surface modulation by elliptic Fourier analysis. *Comput. Methods Programs. Biomed.* 31: 57–62 (1990).
- Dong, J., MacAlister, C. A. & Bergmann, D. C. BASL controls asymmetric cell division in *Arabidopsis*. *Cell* 137: 1320–1330 (2009).
- Donnelly, P. M., Bonetta, D., Tsukaya, H., Dengler, R. E. & Dengler, N. G. Cell cycling and cell enlargement in developing leaves of *Arabidopsis*. *Dev. Biol.* 215: 407–419 (1999).
- Dupont, S., Morsut, L., Aragona, M., Enzo, E., Giulitti, S., Cordenonsi, M., Zanconato, F., Le Digabel, J., Forcato, M., Bicciato, S., Elvassore, N. & Piccolo, S. Role of YAP/TAZ in mechanotransduction. *Nature* 474: 179–183 (2011).
- Efroni, I., Blum, E., Goldshmidt, A. & Eshed, Y. A protracted and dynamic maturation schedule underlies *Arabidopsis* leaf development. *Plant Cell* 20: 2293–2306 (2008).
- Efroni, I., Eshed, Y. & Lifschitz, E. Morphogenesis of simple and compound leaves: a critical review. *Plant Cell* 22: 1019–1032 (2010).
- Efroni, I., Han, S. K., Kim, H. J., Wu, M. F., Steiner, E., Birnbaum, K. D., Hong, J. C., Eshed, Y. & Wagner, D. Regulation of leaf maturation by chromatin-mediated modulation of cytokinin responses. *Dev. Cell* 24: 438–445 (2013).
- Elsner, J., Michalski, M. & Kwiatkowska, D. Spatiotemporal variation of leaf epidermal cell growth: a quantitative analysis of *Arabidopsis thaliana* wild-type and triple cyclinD3 mutant plants. *Ann. Bot.* 109: 897–910 (2012).
- Eriksson, S., Stransfeld, L., Adamski, N. M., Breuninger, H. & Lenhard, M. KLUH/CYP78A5-dependent growth signaling coordinates floral organ growth in *Arabidopsis*. *Curr. Biol.* 20: 527–532 (2010).
- Etienne-Manneville, S. & Hall, A. Rho GTPases in cell biology. *Nature* 420: 629–635 (2002).
- F., Kuhl & C., Giardina. Elliptic Fourier features of a closed contour. *Computer Graphics and Image*

- Processing* 18: 236–258 (1982).
- Federici, F., Dupuy, L., Laplaze, L., Heisler, M. & Haseloff, J.** Integrated genetic and computation methods for in planta cytometry. *Nat. Methods* 9: 483–485 (2012).
- Friess, M. & Baylac, M.** Exploring artificial cranial deformation using elliptic Fourier analysis of Procrustes aligned outlines. *Am. J. Phys. Anthropol.* 122: 11–22 (2003).
- Fu, Y., Gu, Y., Zheng, Z., Wasteneys, G. & Yang, Z.** *Arabidopsis* interdigitating cell growth requires two antagonistic pathways with opposing action on cell morphogenesis. *Cell* 120: 687–700 (2005).
- Fu, Y., Li, H. & Yang, Z.** The ROP2 GTPase controls the formation of cortical fine F-actin and the early phase of directional cell expansion during *Arabidopsis* organogenesis. *Plant Cell* 14: 777–794 (2002).
- Fu, Y., Xu, T., Zhu, L., Wen, M. & Yang, Z.** A ROP GTPase signaling pathway controls cortical microtubule ordering and cell expansion in *Arabidopsis*. *Curr. Biol.* 19: 1827–1832 (2009).
- Fu, Y. & Yang, Z.** Rop GTPase: a master switch of cell polarity development in plants. *Trends Plant Sci.* 6: 545–547 (2001).
- Fujikura, U., Horiguchi, G., Ponce, M. R., Micol, J. L. & Tsukaya, H.** Coordination of cell proliferation and cell expansion mediated by ribosome-related processes in the leaves of *Arabidopsis thaliana*. *Plant J.* 59: 499–508 (2009).
- Galinha, C., Hofhuis, H., Luijten, M., Willemsen, V., Blilou, I., Heidstra, R. & Scheres, B.** PLETHORA proteins as dose-dependent master regulators of *Arabidopsis* root development. *Nature* 449: 1053–1057 (2007).
- Gielis, J.** A generic geometric transformation that unifies a wide range of natural and abstract shapes. *Am. J. Bot.* 90: 333–338 (2003).
- Glazier, J. A. & Graner, F.** Simulation of the differential adhesion driven rearrangement of biological cells. *Phys. Rev. E* 47: 2128–2154 (1993).
- Goehring, N. W. & Grill, S. W.** Cell polarity: mechanochemical patterning. *Trends Cell Biol.* 23: 72–80 (2013).
- Gonzalez, N., Vanhaeren, H. & Inze, D.** Leaf size control: complex coordination of cell division and expansion. *Trends Plant Sci.* 17: 332–340 (2012).
- Grandjean, O., Vernoux, T., Laufs, P., Belcram, K., Mizukami, Y. & Traas, J.** In vivo analysis of cell division, cell growth, and differentiation at the shoot apical meristem in *Arabidopsis*. *Plant Cell* 16: 74–87 (2004).
- Graner, F. & Glazier, J. A.** Simulation of biological cell sorting using a two-dimensional extended Potts model. *Phys. Rev. Lett.* 69: 2013–2016 (1992).
- Granier, C. & Tardieu, F.** Spatial and temporal analyses of expansion and cell cycle in sunflower leaves. A common pattern of development for all zones of a leaf and different leaves of a plant. *Plant Physiol.* 116: 991–1001 (1998).
- Gray, D., Plusa, B., Piotrowska, K., Na, J., Tom, B., Glover, D. M. & Zernicka-Goetz, M.** First cleavage of the mouse embryo responds to change in egg shape at fertilization. *Curr. Biol.* 14: 397–405 (2004).
- Green, A. A., Kennaway, J. R., Hanna, A. I., Bangham, J. A. & Coen, E.** Genetic control of organ shape and tissue polarity. *PLoS Biol.* 8: e1000537 (2010).
- Gregor, T., Bialek, W., De Ruyter van Steveninck, R. R., Tank, D. W. & Wieschaus, E. F.** Diffusion and scaling during early embryonic pattern formation. *Proc. Natl. Acad. Sci. U.S.A.* 102: 18403–18407 (2005).
- Gregor, T., Tank, D. W., Wieschaus, E. F. & Bialek, W.** Probing the limits to positional information. *Cell* 130: 153–164 (2007a).
- Gregor, T., Wieschaus, E. F., McGregor, A. P., Bialek, W. & Tank, D. W.** Stability and nuclear dynamics of the bicoid morphogen gradient. *Cell* 130: 141–152 (2007b).
- Grieneisen, V. A., van Berkel, K., Xu, T., Scheres, B., Hogeweg, P., Yang, Z. & Maree, A.F.M.** Intracellular rop partitioning and auxin-mediated indirect cell-cell communication can explain interdigitation of pavement cells. *in press* (2013a).
- Grieneisen, V. A., Maree, A. F. & Ostergaard, L.** Juicy stories on female reproductive tissue

- development: coordinating the hormone flows. *J. Integr. Plant Biol.* 55: 847–863 (2013b).
- Grieneisen, V. A., Scheres, B., Hogeweg, P. & M Maree, A. F.** Morphogengineering roots: comparing mechanisms of morphogen gradient formation. *BMC Syst. Biol.* 6: 37 (2012).
- Grieneisen, V. A., Xu, J., Maree, A. F., Hogeweg, P. & Scheres, B.** Auxin transport is sufficient to generate a maximum and gradient guiding root growth. *Nature* 449: 1008–1013 (2007).
- Guenot, B., Bayer, E., Kierzkowski, D., Smith, R. S., Mandel, T., Zadnikova, P., Benkova, E. & Kuhlemeier, C.** Pin1-independent leaf initiation in *Arabidopsis*. *Plant Physiol.* 159: 1501–1510 (2012).
- Guo, X., Lu, W., Ma, Y., Qin, Q. & Hou, S.** The BIG gene is required for auxin-mediated organ growth in *Arabidopsis*. *Planta* 237: 1135–1147 (2013).
- Hamant, O., Heisler, M. G., Jonsson, H., Krupinski, P., Uyttewaal, M., Bokov, P., Corson, F., Sahlin, P., Boudaoud, A., Meyerowitz, E. M., Couder, Y. & Traas, J.** Developmental patterning by mechanical signals in *Arabidopsis*. *Science* 322: 1650–1655 (2008).
- Hamant, O., Traas, J. & Boudaoud, A.** Regulation of shape and patterning in plant development. *Curr. Opin. Genet. Dev.* 20: 454–459 (2010).
- Haswell, E. S., Peyronnet, R., Barbier-Brygoo, H., Meyerowitz, E. M. & Frachisse, J. M.** Two MscS homologs provide mechanosensitive channel activities in the *Arabidopsis* root. *Curr. Biol.* 18: 730–734 (2008).
- Heisler, M. G., Hamant, O., Krupinski, P., Uyttewaal, M., Ohno, C., Jonsson, H., Traas, J. & Meyerowitz, E. M.** Alignment between PIN1 polarity and microtubule orientation in the shoot apical meristem reveals a tight coupling between morphogenesis and auxin transport. *PLoS Biol.* 8: e1000516 (2010).
- Hirashima, T., Iwasa, Y. & Morishita, Y.** Mechanisms for split localization of Fgf10 expression in early lung development. *Dev. Dyn.* 238: 2813–2822 (2009).
- Holmes, R. M. & Loew, L. M.** Geometry shapes cell signaling network output. *Chem. Biol.* 15: 523–524 (2008).
- Horiguchi, G., Kim, G. T. & Tsukaya, H.** The transcription factor AtGRF5 and the transcription coactivator AN3 regulate cell proliferation in leaf primordia of *Arabidopsis thaliana*. *Plant J.* 43: 68–78 (2005).
- Horiguchi, G. & Tsukaya, H.** Organ size regulation in plants: insights from compensation. *Front. Plant Sci.* 2: 24 (2011).
- Howard, M.** Cell division: experiments and modelling unite to resolve the middle. *Curr. Biol.* 19: R67–R69 (2009).
- Hu, Y., Xie, Q. & Chua, N. H.** The *Arabidopsis* auxin-inducible gene ARGOS controls lateral organ size. *Plant Cell* 15: 1951–1961 (2003).
- Ibanes, M., Kawakami, Y., Rasskin-Gutman, D. & Izpisua Belmonte, J. C.** Cell lineage transport: a mechanism for molecular gradient formation. *Mol. Syst. Biol.* 2: 57 (2006).
- Iber, D. & Menshykau, D.** The control of branching morphogenesis. *Open. Biol.* 3: 130088 (2013).
- Ingber, D. E.** Cellular tensegrity: defining new rules of biological design that govern the cytoskeleton. *J. Cell Sci.* 104: 613–627 (1993a).
- Ingber, D. E.** The riddle of morphogenesis: a question of solution chemistry or molecular cell engineering? *Cell* 75: 1249–1252 (1993b).
- Iwata, H., Ebana, K., Uga, Y., Hayashi, T. & Jannink, J.** Genome-wide association study of grain shape variation among *oryza sativa* l. germplasms based on elliptic Fourier analysis. *Molecular Breeding* 25: 203–215 (2010).
- Iwata, H., S., Nikura, S., Matsuura, Y., Takano & Y., Ukai.** Evaluation of variation of root shape of japanese radish (*raphanus sativus* l.) based on image analysis using elliptic Fourier descriptors. *Euphytica* 102: 143–149 (1998).
- Jaeger, J., Irons, D. & Monk, N.** Regulative feedback in pattern formation: towards a general relativistic theory of positional information. *Development* 135: 3175–3183 (2008).
- Johnson, K. & Lenhard, M.** Genetic control of plant organ growth. *New Phytol.* 191: 319–333 (2011).
- Jones, M. A., Shen, J. J., Fu, Y., Li, H., Yang, Z. & Grierson, C. S.** The *Arabidopsis* Rop2 GTPase is

- a positive regulator of both root hair initiation and tip growth. *Plant Cell* 14: 763–776 (2002).
- Jonsson, H., Heisler, M. G., Shapiro, B. E., Meyerowitz, E. M. & Mjolsness, E.** An auxin-driven polarized transport model for phyllotaxis. *Proc. Natl. Acad. Sci. U.S.A.* 103: 1633–1638 (2006).
- Jorgensen, P. & Tyers, M.** How cells coordinate growth and division. *Curr. Biol.* 14: R1014–R1027 (2004).
- Kafri, R., Levy, J., Ginzberg, M. B., Oh, S., Lahav, G. & Kirschner, M. W.** Dynamics extracted from fixed cells reveal feedback linking cell growth to cell cycle. *Nature* 494: 480–483 (2013).
- Kalab, P., Weis, K. & Heald, R.** Visualization of a Ran-GTP gradient in interphase and mitotic *Xenopus* egg extracts. *Science* 295: 2452–2456 (2002).
- Kawade, K., Horiguchi, G. & Tsukaya, H.** Non-cell-autonomously coordinated organ size regulation in leaf development. *Development* 137: 4221–4227 (2010).
- Kawade, K., Horiguchi, G., Usami, T., Hirai, M. Y. & Tsukaya, H.** ANGUSTIFOLIA3 signaling coordinates proliferation between clonally distinct cells in leaves. *Curr. Biol.* 23: 788–792 (2013).
- Kazama, T., Ichihashi, Y., Murata, S. & Tsukaya, H.** The mechanism of cell cycle arrest front progression explained by a KLUH/CYP78A5-dependent mobile growth factor in developing leaves of *Arabidopsis thaliana*. *Plant Cell Physiol.* 51: 1046–1054 (2010).
- Kennaway, R., Coen, E., Green, A. & Bangham, A.** Generation of diverse biological forms through combinatorial interactions between tissue polarity and growth. *PLoS Comput. Biol.* 7: e1002071 (2011).
- Kicheva, A., Pantazis, P., Bollenbach, T., Kalaidzidis, Y., Bittig, T., Julicher, F. & Gonzalez-Gaitan, M.** Kinetics of morphogen gradient formation. *Science* 315: 521–525 (2007).
- Kierzkowski, D., Nakayama, N., Routier-Kierzkowska, A. L., Weber, A., Bayer, E., Schorderet, M., Reinhardt, D., Kuhlemeier, C. & Smith, R. S.** Elastic domains regulate growth and organogenesis in the plant shoot apical meristem. *Science* 335: 1096–1099 (2012).
- Kilian, K. A., Bugarija, B., Lahn, B. T. & Mrksich, M.** Geometric cues for directing the differentiation of mesenchymal stem cells. *Proc. Natl. Acad. Sci. U.S.A.* 107: 4872–4877 (2010).
- Klahre, U. & Kost, B.** Tobacco RhoGTPase ACTIVATING PROTEIN1 spatially restricts signaling of RAC/Rop to the apex of pollen tubes. *Plant Cell* 18: 3033–3046 (2006).
- Kondo, S. & Miura, T.** Reaction-diffusion model as a framework for understanding biological pattern formation. *Science* 329: 1616–1620 (2010).
- Kosugi, S. & Ohashi, Y.** PCF1 and PCF2 specifically bind to cis elements in the rice proliferating cell nuclear antigen gene. *Plant Cell* 9: 1607–1619 (1997).
- Kramer, E. M.** Auxin-regulated cell polarity: an inside job? *Trends Plant Sci.* 14: 242–247 (2009).
- Kuchen, E. E., Fox, S., De Reuille, P. B., Kennaway, R., Bensmihen, S., Avondo, J., Calder, G. M., Southam, P., Robinson, S., Bangham, A. & Coen, E.** Generation of leaf shape through early patterns of growth and tissue polarity. *Science* 335: 1092–1096 (2012).
- Lancaster, O. M., Le Berre, M., Dimitracopoulos, A., Bonazzi, D., Zlotek-Zlotkiewicz, E., Picone, R., Duke, T., Piel, M. & Baum, B.** Mitotic Rounding Alters Cell Geometry to Ensure Efficient Bipolar Spindle Formation. *Dev Cell* 0: O (2013).
- Lander, A. D.** How cells know where they are. *Science* 339: 923–927 (2013).
- Laskowski, M., Grieneisen, V. A., Hofhuis, H., Hove, C. A., Hogeweg, P., Marée, A. F. M. & Scheres, B.** Root system architecture from coupling cell shape to auxin transport. *PLoS Biol.* 6: e307 (2008).
- Le, J., Mallery, E. L., Zhang, C., Brankle, S. & Szymanski, D. B.** *Arabidopsis* BRICK1/HSPC300 is an essential WAVE-complex subunit that selectively stabilizes the Arp2/3 activator SCAR2. *Curr. Biol.* 16: 895–901 (2006).
- Lenhard, M.** All’s well that ends well: arresting cell proliferation in leaves. *Dev. Cell* 22: 9–11 (2012).
- Li, C., Potuschak, T., Colon-Carmona, A., Gutierrez, R. A. & Doerner, P.** *Arabidopsis* TCP20 links regulation of growth and cell division control pathways. *Proc. Natl. Acad. Sci. U.S.A.* 102: 12978–12983 (2005).
- Li, H., Lin, D., Dhonukshe, P., Nagawa, S., Chen, D., Friml, J., Scheres, B., Guo, H. & Yang, Z.** Phosphorylation switch modulates the interdigitated pattern of PIN1 localization and cell

- expansion in *Arabidopsis* leaf epidermis. *Cell Res.* 21: 970–978 (2011).
- Lin, D., Nagawa, S., Chen, J., Cao, L., Chen, X., Xu, T., Li, H., Dhonukshe, P., Yamamuro, C., Friml, J., Scheres, B., Fu, Y. & Yang, Z. A ROP GTPase-dependent auxin signaling pathway regulates the subcellular distribution of PIN2 in *Arabidopsis* roots. *Curr. Biol.* 22: 1319–1325 (2012).
- Lincoln, C., Britton, J. H. & Estelle, M. Growth and development of the *axr1* mutants of *Arabidopsis*. *Plant Cell* 2: 1071–1080 (1990).
- Liu, M., Yadav, R. K., Roy-Chowdhury, A. & Reddy, G. V. Automated tracking of stem cell lineages of *Arabidopsis* shoot apex using local graph matching. *Plant J.* 62: 135–147 (2010).
- Lu, P. & Werb, Z. Patterning mechanisms of branched organs. *Science* 322: 1506–1509 (2008).
- MacAlister, C. A., Ohashi-Ito, K. & Bergmann, D. C. Transcription factor control of asymmetric cell divisions that establish the stomatal lineage. *Nature* 445: 537–540 (2007).
- Marée, A. F. M., Grieneisen, V. A. & Edelstein-Keshet, L. How cells integrate complex stimuli: the effect of feedback from phosphoinositides and cell shape on cell polarization and motility. *PLoS Comput. Biol.* 8: e1002402 (2012).
- Marshall, W. F., Young, K. D., Swaffer, M., Wood, E., Nurse, P., Kimura, A., Frankel, J., Wallingford, J., Walbot, V., Qu, X. & Roeder, A. H. What determines cell size? *BMC Biol.* 10: 101 (2012).
- Martin-Trillo, M. & Cubas, P. TCP genes: a family snapshot ten years later. *Trends Plant Sci.* 15: 31–39 (2010).
- Matthews, H. K., Delabre, U., Rohn, J. L., Guck, J., Kunda, P. & Baum, B. Changes in Ect2 localization couple actomyosin-dependent cell shape changes to mitotic progression. *Dev. Cell* 23: 371–383 (2012).
- McBeath, R., Pirone, D. M., Nelson, C. M., Bhadriraju, K. & Chen, C. S. Cell shape, cytoskeletal tension, and RhoA regulate stem cell lineage commitment. *Dev. Cell* 6: 483–495 (2004).
- Megason, S. G. & Fraser, S. E. Imaging in systems biology. *Cell* 130: 784–795 (2007).
- Meinhardt, H. & Gierer, A. Applications of a theory of biological pattern formation based on lateral inhibition. *J. Cell Sci.* 15: 321–346 (1974).
- Mendez, M. G. & Janmey, P. A. Transcription factor regulation by mechanical stress. *Int. J. Biochem. Cell Biol.* 44: 728–732 (2012).
- Menshykau, D., Kraemer, C. & Iber, D. Branch mode selection during early lung development. *PLoS Comput. Biol.* 8: e1002377 (2012).
- Metzger, R. J., Klein, O. D., Martin, G. R. & Krasnow, M. A. The branching programme of mouse lung development. *Nature* 453: 745–750 (2008).
- Meyerowitz, E. M. Plant development: local control, global patterning. *Curr. Opin. Genet. Dev.* 6: 475–479 (1996).
- Meyers, J., Craig, J. & Odde, D. J. Potential for control of signaling pathways via cell size and shape. *Curr. Biol.* 16: 1685–1693 (2006).
- Micol, J. L. Leaf development: time to turn over a new leaf? *Curr. Opin. Plant Biol.* 12: 9–16 (2009).
- Minc, N., Burgess, D. & Chang, F. Influence of cell geometry on division-plane positioning. *Cell* 144: 414–426 (2011).
- Mizukami, Y. & Fischer, R. L. Plant organ size control: AINTEGUMENTA regulates growth and cell numbers during organogenesis. *Proc. Natl. Acad. Sci. U.S.A.* 97: 942–947 (2000).
- Monshausen, G. B. & Gilroy, S. Feeling green: mechanosensing in plants. *Trends Cell Biol.* 19: 228–235 (2009).
- Mori, Y., Jilkine, A. & Edelstein-Keshet, L. Wave-pinning and cell polarity from a bistable reaction-diffusion system. *Biophys. J.* 94: 3684–3697 (2008).
- Moseley, J. B. & Nurse, P. Cell division intersects with cell geometry. *Cell* 142: 184–188 (2010).
- Muller, P. & Schier, A. F. Extracellular movement of signaling molecules. *Dev. Cell* 21: 145–158 (2011).
- Nakayama, N., Smith, R. S., Mandel, T., Robinson, S., Kimura, S., Boudaoud, A. & Kuhlemeier, C. Mechanical regulation of auxin-mediated growth. *Curr. Biol.* 22: 1468–1476 (2012).
- Nalbant, P., Hodgson, L., Kraynov, V., Touthkine, A. & Hahn, K. M. Activation of endogenous

- Cdc42 visualized in living cells. *Science* 305: 1615–1619 (2004).
- Nath, U., Crawford, B. C., Carpenter, R. & Coen, E.** Genetic control of surface curvature. *Science* 299: 1404–1407 (2003).
- Nelissen, H., Rymen, B., Coppens, F., Dhondt, S., Fiorani, F. & Beemster, G. T.** Kinematic analysis of cell division in leaves of mono- and dicotyledonous species: a basis for understanding growth and developing refined molecular sampling strategies. *Methods Mol. Biol.* 959: 247–264 (2013).
- Nelson, B. K., Cai, X. & Nebenfuhr, A.** A multicolored set of in vivo organelle markers for co-localization studies in *Arabidopsis* and other plants. *Plant J.* 51: 1126–1136 (2007).
- Nelson, W. J.** Adaptation of core mechanisms to generate cell polarity. *Nature* 422: 766–774 (2003).
- Neto, J., Meyer, G., Jones, D. & Samal, A.** Plant species identification using elliptic Fourier leaf shape analysis. *Computers and Electronics in Agriculture* 50: 121–134 (2006).
- Neufeld, T. P. & Edgar, B. A.** Connections between growth and the cell cycle. *Curr. Opin. Cell Biol.* 10: 784–790 (1998).
- Neves, S. R., Tsokas, P., Sarkar, A., Grace, E. A., Rangamani, P., Taubenfeld, S. M., Alberini, C. M., Schaff, J. C., Blitzer, R. D., Moraru, I. I. & Iyengar, R.** Cell shape and negative links in regulatory motifs together control spatial information flow in signaling networks. *Cell* 133: 666–680 (2008).
- Niethammer, P., Bastiaens, P. & Karsenti, E.** Stathmin-tubulin interaction gradients in motile and mitotic cells. *Science* 303: 1862–1866 (2004).
- O’Connell, C. B. & Wang, Y. L.** Mammalian spindle orientation and position respond to changes in cell shape in a dynein-dependent fashion. *Mol. Biol. Cell* 11: 1765–1774 (2000).
- Oda, Y. & Fukuda, H.** Initiation of cell wall pattern by a Rho- and microtubule-driven symmetry breaking. *Science* 337: 1333–1336 (2012).
- Oh, S., Brammer, K. S., Li, Y. S., Teng, D., Engler, A. J., Chien, S. & Jin, S.** Stem cell fate dictated solely by altered nanotube dimension. *Proc. Natl. Acad. Sci. U.S.A.* 106: 2130–2135 (2009).
- Palatnik, J. F., Allen, E., Wu, X., Schommer, C., Schwab, R., Carrington, J. C. & Weigel, D.** Control of leaf morphogenesis by microRNAs. *Nature* 425: 257–263 (2003).
- Payne, R. J. & Grierson, C. S.** A theoretical model for ROP localisation by auxin in *Arabidopsis* root hair cells. *PLoS One.* 4: e8337 (2009).
- Perilli, S., Di Mambro, R. & Sabatini, S.** Growth and development of the root apical meristem. *Curr. Opin. Plant Biol.* 15: 17–23 (2012).
- Peterson, S. V., Johansson, A. I., Kowalczyk, M., Makoveychuk, A., Wang, J. Y., Moritz, T., Grebe, M., Benfey, P. N., Sandberg, G. & Ljung, K.** An auxin gradient and maximum in the *Arabidopsis* root apex shown by high-resolution cell-specific analysis of IAA distribution and synthesis. *Plant Cell* 21: 1659–1668 (2009).
- Pincus, Z. & Theriot, J. A.** Comparison of quantitative methods for cell-shape analysis. *J. Microsc.* 227: 140–156 (2007).
- Powell, A. E. & Lenhard, M.** Control of organ size in plants. *Curr. Biol.* 22: R360–R367 (2012).
- Pullen, N., Jaeger, K. E., Wigge, P. A. & Morris, R. J.** Simple network motifs can capture key characteristics of the floral transition in *Arabidopsis*. *Plant Signal. Behav.* 8: 24–30 (2013).
- Qiu, J. L., Jilk, R., Marks, M. D. & Szymanski, D. B.** The *Arabidopsis* SPIKE1 gene is required for normal cell shape control and tissue development. *Plant Cell* 14: 101–118 (2002).
- R., Erickson & K., Silk.** The kinematics of plant growth. *Scientific American* 242: 134–151 (1980).
- Reddy, G. V., Gordon, S. P. & Meyerowitz, E. M.** Unravelling developmental dynamics: transient intervention and live imaging in plants. *Nat. Rev. Mol. Cell Biol.* 8: 491–501 (2007).
- Reinhardt, D., Mandel, T. & Kuhlemeier, C.** Auxin regulates the initiation and radial position of plant lateral organs. *Plant Cell* 12: 507–518 (2000).
- Remmler, L. & Rolland-Lagan, A. G.** Computational method for quantifying growth patterns at the adaxial leaf surface in three dimensions. *Plant Physiol.* 159: 27–39 (2012).
- Riou-Khamlichi, C., Huntley, R., Jacquard, A. & Murray, J. A.** Cytokinin activation of *Arabidopsis* cell division through a D-type cyclin. *Science* 283: 1541–1544 (1999).
- Robinson, S., Barbier de Reuille, P., Chan, J., Bergmann, D., Prusinkiewicz, P. & Coen, E.** Gen-

- eration of spatial patterns through cell polarity switching. *Science* 333: 1436–1440 (2011).
- Rodriguez, R. E., Mecchia, M. A., Debernardi, J. M., Schommer, C., Weigel, D. & Palatnik, J. F.** Control of cell proliferation in *Arabidopsis thaliana* by microRNA miR396. *Development* 137: 103–112 (2010).
- Roeder, A. H., Chickarmane, V., Cunha, A., Obara, B., Manjunath, B. S. & Meyerowitz, E. M.** Variability in the control of cell division underlies sepal epidermal patterning in *Arabidopsis thaliana*. *PLoS Biol.* 8: e1000367 (2010).
- Roeder, A. H., Cunha, A., Burl, M. C. & Meyerowitz, E. M.** A computational image analysis glossary for biologists. *Development* 139: 3071–3080 (2012a).
- Roeder, A. H., Cunha, A., Ohno, C. K. & Meyerowitz, E. M.** Cell cycle regulates cell type in the *Arabidopsis* sepal. *Development* 139: 4416–4427 (2012b).
- van Rooij, J.A., Hartley, M., Sanchez-Corrales, Y.E, Sablowski, R., Grieneisen, V.A. & Maree, AFM.** The segmentation potts model: extracting quantitative cell information from 2d and 3d confocal microscopy images. *to be resubmitted* (2013a).
- van Rooij, J.A., Magno, R. & Maree, AFM.** Capturing complex cell shape in the cellular potts model framework. *in preparation* (2013b).
- Roskelley, C. D., Desprez, P. Y. & Bissell, M. J.** Extracellular matrix-dependent tissue-specific gene expression in mammary epithelial cells requires both physical and biochemical signal transduction. *Proc. Natl. Acad. Sci. U.S.A.* 91: 12378–12382 (1994).
- Rupes, I.** Checking cell size in yeast. *Trends Genet.* 18: 479–485 (2002).
- Russ, John C.** *The Image Processing Handbook*. SPRINGER, 3rd edition (2000).
- Sachs, Tsvi.** *Pattern Formation in Plant Tissue*. Cambridge University Press, 1st edition (1991).
- Sappl, P. G. & Heisler, M. G.** Live-imaging of plant development: latest approaches. *Curr. Opin. Plant Biol.* 16: 33–40 (2013).
- Saunders, T. E., Pan, K. Z., Angel, A., Guan, Y., Shah, J. V., Howard, M. & Chang, F.** Noise reduction in the intracellular pom1p gradient by a dynamic clustering mechanism. *Dev. Cell* 22: 558–572 (2012).
- Sauret-Gueto, S., Calder, G. & Harberd, N. P.** Transient gibberellin application promotes *Arabidopsis thaliana* hypocotyl cell elongation without maintaining transverse orientation of microtubules on the outer tangential wall of epidermal cells. *Plant J.* 69: 628–639 (2012).
- Savaldi-Goldstein, S. & Chory, J.** Growth coordination and the shoot epidermis. *Curr. Opin. Plant Biol.* 11: 42–48 (2008).
- Sawchuk, M. G., Edgar, A. & Scarpella, E.** Patterning of leaf vein networks by convergent auxin transport pathways. *PLoS Genet.* 9: e1003294 (2013).
- Schiessl, K., Kausika, S., Southam, P., Bush, M. & Sablowski, R.** JAGGED controls growth anisotropy and coordination between cell size and cell cycle during plant organogenesis. *Curr. Biol.* 22: 1739–1746 (2012).
- Schmittbuhl, M., Allenbach, B., Le Minor, J. & Schaaf, A.** Elliptical descriptors: Some simplified morphometric parameters for the quantification of complex outlines. *Mathematical Geology* 35: 853–871 (2003).
- Schmundt, D., Stitt, M., Jahne, B. & Ulrich, S.** Quantitative analysis of the local rates of growth of dicot leaves at a high temporal and spatial resolution, using image sequence analysis. *The Plant J.* 16: 505–514 (1998).
- Schwank, G. & Basler, K.** Regulation of organ growth by morphogen gradients. *Cold. Spring. Harb. Perspect. Biol.* 2: a001669 (2010).
- Schweizer, J., Loose, M., Bonny, M., Kruse, K., Monch, I. & Schwille, P.** Geometry sensing by self-organized protein patterns. *Proc. Natl. Acad. Sci. U.S.A.* 109: 15283–15288 (2012).
- Serralbo, O., Perez-Perez, J. M., Heidstra, R. & Scheres, B.** Non-cell-autonomous rescue of anaphase-promoting complex function revealed by mosaic analysis of HOBBIT, an *Arabidopsis* CDC27 homolog. *Proc. Natl. Acad. Sci. U.S.A.* 103: 13250–13255 (2006).
- Sharpe, J.** Two ways to use imaging: focusing directly on mechanism, or indirectly via behaviour? *Curr. Opin. Genet. Dev.* 21: 523–529 (2011).
- Shpak, E. D., Berthiaume, C. T., Hill, E. J. & Torii, K. U.** Synergistic interaction of three ERECTA-

- family receptor-like kinases controls *Arabidopsis* organ growth and flower development by promoting cell proliferation. *Development* 131: 1491–1501 (2004).
- Silk, W. K. & Erickson, R. O.** Kinematics of plant growth. *J. Theor. Biol.* 76: 481–501 (1979).
- Smith, R. S., Guyomarç'h, S., Mandel, T., Reinhardt, D., Kuhlemeier, C. & Prusinkiewicz, P.** A plausible model of phyllotaxis. *Proc. Natl. Acad. Sci. U.S.A.* 103: 1301–1306 (2006).
- Sorek, N., Gutman, O., Bar, E., Abu-Abied, M., Feng, X., Running, M. P., Lewinsohn, E., Ori, N., Sadot, E., Henis, Y. I. & Yalovsky, S.** Differential effects of prenylation and s-acylation on type I and II ROPS membrane interaction and function. *Plant Physiol.* 155: 706–720 (2011).
- Staff, L., Hurd, P., Reale, L., Seoighe, C., Rockwood, A. & Gehring, C.** The hidden geometries of the *Arabidopsis thaliana* epidermis. *PLoS One.* 7: e43546 (2012).
- Steiner, E., Yanai, O., Efroni, I., Ori, N., Eshed, Y. & Weiss, D.** Class I TCPs modulate cytokinin-induced branching and meristematic activity in tomato. *Plant Signal. Behav.* 7: 807–810 (2012).
- Steinmann, T., Geldner, N., Grebe, M., Mangold, S., Jackson, C. L., Paris, S., Galweiler, L., Palme, K. & Jurgens, G.** Coordinated polar localization of auxin efflux carrier PIN1 by GNOM ARF GEF. *Science* 286: 316–318 (1999).
- Su, T. T. & O'Farrell, P. H.** Size control: cell proliferation does not equal growth. *Curr. Biol.* 8: R687–R689 (1998).
- Sugimoto-Shirasu, K. & Roberts, K.** "Big it up": endoreduplication and cell-size control in plants. *Curr. Opin. Plant Biol.* 6: 544–553 (2003).
- Sukharev, S. & Sachs, F.** Molecular force transduction by ion channels: diversity and unifying principles. *J. Cell Sci.* 125: 3075–3083 (2012).
- Takai, Y., Sasaki, T. & Matozaki, T.** Small GTP-binding proteins. *Physiol. Rev.* 81: 153–208 (2001).
- Tao, Y., Ferrer, J. L., Ljung, K., Pojer, F., Hong, F., Long, J. A., Li, L., Moreno, J. E., Bowman, M. E., Ivans, L. J., Cheng, Y., Lim, J., Zhao, Y., Ballare, C. L., Sandberg, G., Noel, J. P. & Chory, J.** Rapid synthesis of auxin via a new tryptophan-dependent pathway is required for shade avoidance in plants. *Cell* 133: 164–176 (2008).
- Thery, M. & Bornens, M.** Cell shape and cell division. *Curr. Opin. Cell Biol.* 18: 648–657 (2006).
- Tisne, S., Barbier, F. & Granier, C.** The ERECTA gene controls spatial and temporal patterns of epidermal cell number and size in successive developing leaves of *Arabidopsis thaliana*. *Ann. Bot.* 108: 159–168 (2011).
- Torii, K. U., Mitsukawa, N., Oosumi, T., Matsuura, Y., Yokoyama, R., Whittier, R. F. & Komeda, Y.** The *Arabidopsis* ERECTA gene encodes a putative receptor protein kinase with extracellular leucine-rich repeats. *Plant Cell* 8: 735–746 (1996).
- Tostevin, F., Ten Wolde, P. R. & Howard, M.** Fundamental limits to position determination by concentration gradients. *PLoS Comput. Biol.* 3: e78 (2007).
- Tsou, M. F., Ku, W., Hayashi, A. & Rose, L. S.** PAR-dependent and geometry-dependent mechanisms of spindle positioning. *J. Cell Biol.* 160: 845–855 (2003).
- Tsuge, T., Tsukaya, H. & Uchimiya, H.** Two independent and polarized processes of cell elongation regulate leaf blade expansion in *Arabidopsis thaliana* (L.) Heynh. *Development* 122: 1589–1600 (1996).
- Tsukaya, H.** Interpretation of mutants in leaf morphology: genetic evidence for a compensatory system in leaf morphogenesis that provides a new link between cell and organismal theories. *Int. Rev. Cytol.* 217: 1–39 (2002).
- Tsukaya, H.** Leaf development. *Arabidopsis. Book.* 11: e0163 (2013).
- Turing, A. M.** The chemical basis of morphogenesis. 1953. *Bull. Math. Biol.* 52: 153–197 (1990).
- Turner, J. J., Ewald, J. C. & Skotheim, J. M.** Cell size control in yeast. *Curr. Biol.* 22: R350–R359 (2012).
- Tzur, A., Kafri, R., LeBleu, V. S., Lahav, G. & Kirschner, M. W.** Cell growth and size homeostasis in proliferating animal cells. *Science* 325: 167–171 (2009).
- Uhrig, J. F., Mutondo, M., Zimmermann, I., Deeks, M. J., Machesky, L. M., Thomas, P., Uhrig, S., Rambke, C., Hussey, P. J. & Hulskamp, M.** The role of *Arabidopsis* SCAR genes in ARP2-ARP3-dependent cell morphogenesis. *Development* 134: 967–977 (2007).
- Uyttewaal, M., Burian, A., Alim, K., Landrein, B., Borowska-Wykret, D., Dedieu, A., Peaucelle,**

- A., Ludynia, M., Traas, J., Boudaoud, A., Kwiatkowska, D. & Hamant, O. Mechanical stress acts via katanin to amplify differences in growth rate between adjacent cells in *Arabidopsis*. *Cell* 149: 439–451 (2012).
- Van Berkel, K., De Boer, R. J., Scheres, B. & Ten Tusscher, K. Polar auxin transport: models and mechanisms. *Development* 140: 2253–2268 (2013).
- Vanderlei, B., Feng, J. J. & Edelstein-Keshet, L. A computational model of cell polarization and motility coupling mechanics and biochemistry. *Multiscale. Model. Simul.* 9: 1420–1443 (2011).
- Varma, A., Huang, K. C. & Young, K. D. The Min system as a general cell geometry detection mechanism: branch lengths in Y-shaped *Escherichia coli* cells affect Min oscillation patterns and division dynamics. *J. Bacteriol.* 190: 2106–2117 (2008).
- Versaevel, M., Grevesse, T. & Gabriele, S. Spatial coordination between cell and nuclear shape within micropatterned endothelial cells. *Nat. Commun.* 3: 671 (2012).
- Wachsman, G., Heidstra, R. & Scheres, B. Distinct cell-autonomous functions of RETINOBLASTOMA-RELATED in *Arabidopsis* stem cells revealed by the Brother of Rainbow clonal analysis system. *Plant Cell* 23: 2581–2591 (2011).
- Wartlick, O. & Gonzalez-Gaitan, M. The missing link: implementation of morphogenetic growth control on the cellular and molecular level. *Curr. Opin. Genet. Dev.* 21: 690–695 (2011).
- Wartlick, O., Kicheva, A. & Gonzalez-Gaitan, M. Morphogen gradient formation. *Cold. Spring. Harb. Perspect. Biol.* 1: a001255 (2009).
- Wartlick, O., Mumcu, P., Kicheva, A., Bittig, T., Seum, C., Julicher, F. & Gonzalez-Gaitan, M. Dynamics of Dpp signaling and proliferation control. *Science* 331: 1154–1159 (2011).
- Watt, F. M., Jordan, P. W. & O'Neill, C. H. Cell shape controls terminal differentiation of human epidermal keratinocytes. *Proc. Natl. Acad. Sci. U.S.A.* 85: 5576–5580 (1988).
- Weimer, A. K., Nowack, M. K., Bouyer, D., Zhao, X., Harashima, H., Naseer, S., De Winter, F., Dismeyer, N., Geldner, N. & Schnittger, A. Retinoblastoma related1 regulates asymmetric cell divisions in *Arabidopsis*. *Plant Cell* 24: 4083–4095 (2012).
- Wellmer, F., Alves-Ferreira, M., Dubois, A., Riechmann, J. L. & Meyerowitz, E. M. Genome-wide analysis of gene expression during early *Arabidopsis* flower development. *PLoS Genet.* 2: e117 (2006).
- White, D. W. PEAPOD regulates lamina size and curvature in *Arabidopsis*. *Proc. Natl. Acad. Sci. U.S.A.* 103: 13238–13243 (2006).
- Wolpert, L. Positional information and the spatial pattern of cellular differentiation. *J. Theor. Biol.* 25: 1–47 (1969).
- Wolpert, L. Positional information and pattern formation in development. *Dev. Genet.* 15: 485–490 (1994).
- Wolpert, L. The progress zone model for specifying positional information. *Int. J. Dev. Biol.* 46: 869–870 (2002).
- Wolters, H. & Jurgens, G. Survival of the flexible: hormonal growth control and adaptation in plant development. *Nat. Rev. Genet.* 10: 305–317 (2009).
- Wuyts, N., Massonnet, C., Dautzat, M. & Granier, C. Structural assessment of the impact of environmental constraints on *Arabidopsis thaliana* leaf growth: a 3D approach. *Plant Cell Environ.* 35: 1631–1646 (2012).
- Xu, T., Nagawa, S. & Yang, Z. Uniform auxin triggers the Rho GTPase-dependent formation of interdigitation patterns in pavement cells. *Small. GTPases.* 2: 227–232 (2011).
- Xu, T., Wen, M., Nagawa, S., Fu, Y., Chen, J. G., Wu, M. J., Perrot-Rechenmann, C., Friml, J., Jones, A. M. & Yang, Z. Cell surface- and rho GTPase-based auxin signaling controls cellular interdigitation in *Arabidopsis*. *Cell* 143: 99–110 (2010).
- Yang, Z. Cell polarity signaling in *Arabidopsis*. *Annu. Rev. Cell Dev. Biol.* 24: 551–575 (2008).
- Yoshioka, Y., Iwata, H., Ohsawa, R. & Ninomiya, S. Quantitative evaluation of the petal shape variation in *Primula sieboldii* caused by breeding process in the last 300 years. *Heredity (Edinb.)* 94: 657–663 (2005).
- Zhang, C., Halsey, L. E. & Szymanski, D. B. The development and geometry of shape change in *Arabidopsis thaliana* cotyledon pavement cells. *BMC Plant Biol.* 11: 27 (2011).

**Zhiponova, M. K., Vanhoutte, I., Boudolf, V., Betti, C., Dhondt, S., Coppens, F., Mylle, E., Maes, S., Gonzalez-Garcia, M. P., Cano-Delgado, A. I., Inze, D., Beemster, G. T., De Veylder, L. & Russinova, E.** Brassinosteroid production and signaling differentially control cell division and expansion in the leaf. *New Phytol.* 197: 490–502 (2013).

